UNIVERSIDADE DE LISBOA
FACULDADE DE CIÊNCIAS
DEPARTAMENTO DE FÍSICA

Characterization of the turbulent transport in the edge plasma of the tokamak ISTTOK

Sara Vaz Mendes

Mestrado Integrado em Engenharia Física

Dissertação orientada por:
Carlos Alberto Nogueira Garcia da Silva
Olinda Maria Quelhas Fernandes Conde

2019

Acknowledgments

This thesis presents an effort as a master student to participate in the large effort of the fusion community in trying to understand the major challenges of terrestrial fusion. I am really grateful for the opportunity of finishing my masters in this subject of studies. More than anything, I would like to thank the availability and kindness of my supervisor, Dr. Carlos Silva. The opportunity to analyze and perform a characterization of the turbulence in the edge of the ISTTOK tokamak, along with all the knowledge about fusion devices that I got to take a first look at has been more than I could have hoped for the end of my master program. Thank you to Dr. Carlos Silva, here as a professor, for helping me in spite of my almost a year-long absence through Erasmus. Thanks to the IPFN team at IST for creating the space and means for an academic Fusion program in Lisbon.

A very special gratitude goes out to all responsible for my student internships at ENEA and CCFE for the great experiences to further my knowledge in Fusion diagnostics. These opportunities were only possible because of the great research conditions and hospitality at both institutions. Thanks to professor Guiomar Evans for the availability and guidance through our most pessimist times at the faculty. Thanks to both professors Guiomar Evans and Olinda Conde for the help in solving the not so straight forward administration procedures and allowing me to follow the last master subjects in this area.

Lastly, I also have to thank all my colleagues and family for the last years hearing my pessimist self, while still encouraging me about all the work ahead. Thank you all for the patient

Abstract

A major challenge in the realization of fusion power plants will be to overcome the dominant confinement losses induced by turbulence. The performance of current experiments is strongly influenced by these mechanisms. Turbulence considerably increases the transport of particles and energy in the edge, being the dominant source of losses in fusion devices. This work aims at contributing to the understanding of the turbulence induced by blob-filaments, trough a multi-scale investigation of the induced fluctuations on plasma quantities and ultimately the resultant transport of particles and energy in the edge of the ISTTOK (IST tokamak) experiment. It was intended to carry a detailed analysis of turbulence physics at various scales, from their origin to the impact on plasma confinement. ISTTOK is an ideal experiment to carry a study related to the edge plasma since it is compact, flexible and allows rapid installation of diagnostics. A multi-pin array of Langmuir probes allowed to carry bi-dimensional measurements of the structure of plasma fluctuations, and revealed to be ideal in determining the induced particle transport.

The different analysis techniques applied in this work revealed that the turbulent structures in the edge of the ISTTOK tokamak have a time scale of the order of $\sim 2-10$ μs, propagating poloidally with $v_\theta = 5-10$ km/s and having a poloidal dimension of $\sim 2-6$ cm. Fluctuation levels from 25% in the edge plasma to 150% in the far scrape-off layer (SOL) of ISTTOK revealed that the region is dominated by fluctuations, which are probably induced by the turbulence resulting in blob-filaments. The remaining statistical properties of the fluctuations also indicated that the edge and SOL of ISTTOK are dominated by fluctuations, where intermittency in plasma quantities results in probability distributions with high skewness and kurtosis. The statistical quantities of the fluctuations allowed to show the increase of the relative importance of the induced fluctuations with radius.

Further investigations were done on the properties of the edge/SOL fluctuations reveling broad power spectra, and coherent with structures of the order of $10-100$ μs. The power

spectra of the fluctuations when appropriately re-scaled to the standard deviation of the measurements shows a roughly universal shape in most fusion devices. The common result was also seen for the power spectra computed during this work, showing a modest decay with frequency until ~ 100 kHz, and a faster decay from this value with the power law of f^{-C}.

Lastly, the particle flux induced by the fluctuations in the edge and SOL was estimated to be in the order of $\sim 10^{21}\ m^{-2}s^{-1}$, and having the same order magnitude of the total particle losses at ISTTOK estimated from the measured particle confinement.

Keywords

Thermonuclear Fusion; Tokamak; Turbulence structures; Blob-filaments; Intermittent particle transport.

Resumo

Um enorme esforço por parte da comunidade de fusão nuclear tem vindo a reunir nas últimas décadas vários estudos sobre as principais dificuldades em construir futuros reatores baseados na fusão nuclear. Na actualidade, várias experiências espalhadas pelo globo têm como finalidade provar a eficiência de diferentes configurações para futuros reatores alimentados por reações de fusão nuclear. Uma das configurações mais promissoras para o sucesso da tecnologia de fusão nuclear na Terra é o Tokamak. Um dos principais obstáculos desta experiência deve-se a mecanismos de turbulência na periferia do plasma. De modo geral a eficiência das atuais experiências de fusão é fortemente influenciada por estes mecanismos de turbulência. A turbulência aumenta consideravelmente o transporte de partículas e energia no plasma periférico, sendo a fonte dominante de perdas em experiências de fusão nuclear. A turbulência verificada na região periférica resulta em filamentos de plasma (regiões de densidade superior). Estes filamentos nascem e propagam-se no plasma periférico. Um resultado fundamental da propagação de filamentos de plasma são as flutuações induzidas em parâmetros do plasma, tal como a densidade e o potencial.

Neste trabalho pretendeu-se compreender a física dos filamentos de plasma resultantes da turbulência, através de uma investigação das flutuações induzidas nos parâmetros do plasma e, finalmente, o transporte de partículas e energia resultante na perifería do ISTTOK (IST Tokamak). Executou-se uma análise detalhada da física da turbulência a várias escalas, desde a sua origem até ao impacto no confinamento do plasma. O ISTTOK é uma experiência ideal para realizar estudos relacionados com o plasma periférico, uma vez que é compacto, flexível e permite a instalação rápida de diagnósticos [1, 2]. Um extenso programa de Fusão Nuclear tem vindo a ser implementado no IST (Instituto Superior Técnico) com diversos diagnósticos instalados, entre os quais as sondas de Langmuir. As sondas de Langmuir consistem basicamente em eletrodos cilíndricos que podem ser inseridos no plasma periférico (até alguns centímetros dentro da última superfície de fluxo fechada). As sondas de Langmuir utilizadas no diagnóstico do plasma do ISTTOK têm uma elevada resolução espacial (de alguns milímetros) e temporal (na ordem de microsegundos). Adicionalmente, no ISTTOK diversos estudos foram implementados

ao longo dos anos com sistemas de múltiplas sondas de Langmuir [2–5]. Durante este trabalho foi usado um sistema de várias sondas separadas poloidalmente, permitindo determinar a estrutura poloidal das fluctuações. Este diagnóstico mostrou-se ideal na determinação do transporte de partículas induzido pelas estruturas de turbulência em propagação no plasma.
As sondas de Langmuir permitem traçar uma curva característica I-V (onde V é a diferença de potencial aplicada à sonda e I a corrente recolhida por esta). Em determinadas condições, aplicando uma alta diferença de potencial negativa, a corrente recolhida corresponde a uma corrente de saturação iónica I_{sat}^{+}. Por outro lado, pode não ser aplicada qualquer diferença de potencial à sonda de modo a medir o potencial flutuante V_f. As flutuações de I_{sat}^{+} permitem estimar as flutuações da densidade de plasma, enquanto as flutuações de V_f permitem estimar as flutuações do potencial de plasma.

Através da aplicação de diferentes técnicas de análise, desde análise estatística até técnicas de correlação e análise espectral, as flutuações foram caracterizadas, contribuindo assim para uma melhor compreensão da física associada aos filamentos do plasma e o seu impacto no transporte radial.

O ISTTOK pode operar com ciclos de corrente alternada, para os quais a direção da corrente de plasma é invertida periodicamente, permitindo obter descargas mais longas. Com a inversão entre ciclos positivos e negativos (direção da corrente de plasma) surgem também alterações na posição do plasma. Durante este trabalho a caracterização das flutuações e do transporte induzido no ISTTOK teve especial atenção a este facto. Foi analisada a importância das estruturas de turbulência ao longo de seis ciclos consecutivos de corrente alternada no ISTTOK.

As diversas propriedades estatísticas das flutuações aqui investigas permitiram concluir que o plasma periférico e a SOL do ISTTOK são dominados por flutuações. Os níveis de flutuações elevados, na orderm de 25% numa região dentro do limitador para 150% na SOL do ISTTOK, foi o primeiro resultado apresentado a comprovar que a região é dominada por flutuações, que são provavelmente induzidas pela turbulência. De seguida, os elevados valores de skewness e kurtosis da densidade e do potencial de plasma foram apresentados, de modo a indicar mais uma vez a importância das flutuações no plasma periférico do ISTTOK. Estas quantidades estatísticas permitiram mostrar o aumento da importância relativa das flutuações induzidas com o aumento do raio.
No capítulo 2 foram mencionados estudos anteriores sobre a importância das flutuações no plasma periférico. De um dos exemplos foi realçada a "universalidade" da Função Densidade de Probabilidade (FDP) para as flutuações do plasma periférico. Este resultado foi também concluído para as flutuações no plasma do ISTTOK, no capítulo 4.

Adicionalmente, o espectro de frequências das flutuações foi investigado. A análise espectral dos sinais de V_f e de I_{sat}^+ obtidos no ISTTOK revelaram que a potência espectral é dominada por frequências na gama 10-100 kHz, e que a amplitude diminui com a frequência de acordo com $1/f^C$, onde C é uma constante que varia nas diferentes regiões do espectro. De modo geral o espectrograma das flutuações do plasma periférico é largo em frequência. Os espectros de frequência tornam-se mais largos com o aumento do raio, indicando o aumento da importância relativa das altas frequências sobre as baixas frequências. Os espectrogramas obtidos assemelham-se ao espectro de *pink noise* que é bastante usual em sinais intermitentes, como o que se dá para os parâmetros do plasma devido a propagação das estruturas de turbulência.

O sistema de sondas utilizado permite determinar V_f e I_{sat}^+ para diferentes posições poloidais no ISTTOK. No total temos sete sondas espaçadas entre si por 2 mm. Os sinais obtidos para as diferentes posições foram comparados através da função correlação cruzada, de modo a determinar a velocidade de propagação, e as estruturas espacial e temporal das flutuações na direção poloidal. A correlação entre as medições nas diferentes posições poloidais é dependente da dimensão poloidal das estruturas intermitentes, assim como do tempo característico e velocidade de propagação destas através do plasma. Os resultados para a correlação cruzada entre dois sinais de V_f ou de I_{sat}^+ indicam a similaridade entre os sinais em função do desfasamento temporal entre os dois. As diferentes técnicas de análise aplicadas durante este trabalho revelaram que as estruturas de turbulência na periferia do tokamak ISTTOK têm uma estrutura temporal na ordem de $\sim 2-10$ μs, em propagação na direção poloidal com $v_\theta = 5-10$ km/s e dimensão poloidal na ordem de $\sim 2-6$ cm.

O fluxo médio de partículas que é induzido pelas flutuações pode ser estimado através das medições simultâneas das flutuações de densidade e de potencial. Tivemos durante este trabalho a oportunidade de enfatizar a grande influência deste fluxo induzido nas perdas totais no plasma periférico de um tokamak. O fluxo de partículas induzido pelas flutuações na periferia do ISTTOK encontra-se na ordem de 10^{21} $m^{-2}s^{-1}$, e apresenta a mesma ordem de grandeza das

perdas totais de partículas no ISTTOK estimadas a partir do confinamento de partículas medido.

Palavras Chave

Fusão Termonuclear; Tokamak; Estruturas de turbulência; Filamentos; Transporte intermitente de partículas.

Contents

List of Figures

List of Tables

Acronyms

ADC	Analog-to-digital converter
Asdex	Axially Symmetric Divertor Experiment
ATCA	Advanced Telecommunications Computing Architecture
BES	Beam emission spectroscopy
CODAS	Control and Data Acquisition System
DAC	Digital-to-analog converter
DAQ	Data Acquisition
GPI	Gas-puff imaging
IST	Instituto Superior Técnico
ISTTOK	IST Tokamak
ITER	International Thermonuclear Experimental Reactor
JET	Joint European Torus
LCFS	Last closed flux surface
LP	Langmuir Probe
MAST	Mega Ampere Spherical Tokamak
MHD	Magnetohydrodynamics
PDF	Probability distribution function
PFCs	Plasma facing components

RAM Random-Access Memory

SDAS Shared DataAccess System

SOL Scrape-off layer

Chapter 1

Thermonuclear fusion

1.1 Introduction

To start the current work we present a simple fusion reaction

$$ {}^{2}_{1}H + {}^{3}_{1}H \rightarrow {}^{4}_{2}He(3.5MeV) + {}^{1}_{0}n(14.1MeV) \tag{1.1} $$

, that could be the solution to the energetic needs of the world. However, how simple it may look, to efficiently harness the energy of this reaction in a continuous and stable mode of operation on earth is not that easy. As it seems to always be fifty years way from taking place. The reaction presented on (1.1) for deuterium (${}^{2}_{1}H$) and tritium (${}^{3}_{1}H$) corresponds to a light element fusion reaction, in which these nuclei fuse to generate heavier α particles (${}^{4}_{2}He$), relishing a great amount of energy. In general a nuclear reaction (fusion and fission) releases about a factor of one million more energy when compared to the energy released in a chemical reaction, such as the ones involved in the combustion of fossil fuels.

Fossil fuels have been the main driver for the civilization's growth and development into a more scientific and technological era. However, with the increase use of fossil fuels came an increase in the emission of green house gases well above the natural production range, busting from the Industrial Revolution, which was marked by a large combustion of coal. Coal has been the prevailing source of electricity and overall energy supply, not only when compared to the remaining fossil fuels, but to all energy sources. It was responsible for 39% of the world's total electricity production in 2014, as shown for the most recent inquires of [18]. Furthermore, in 2014, the remaining electricity production was achieved 22% by gas, 17% by hydroelectric generation, 11% through nuclear sources, 5% through oil, and finally renewable energy sources

entered with various others in a participation of only 7%, [18].

The repercussions on the environment that follow from carbon dioxide and other green house emissions have resulted in the increase of the average global temperatures. Followed by this came the raise in sea levels with growing rates, and on other climate changes that have imposed a large conscience about the use of fossil fuels. Although society has understood the repercussions of fossil fuel usage, major obstacles are still present for the remaining energy options. For example, renewable sources overall present efficiency instabilities based on the oscillations of the meteorologic conditions. Also require a large area to increase the environmental condition's exploitation. On the other hand, present nuclear fission power plants not only require high investments for construction, but are also involved in political conflicts. For these reasons fossil fuels will remain the main source of electricity production in the next years to come. In particular coal, whose world's reserve could be used to produce electricity for another hundreds of years, given current world rate of consumption. Nevertheless, even before the limits of fossil fuel reserves are reached, given the environmental repercussions mentioned above, this source of energy production will have to be eventually reduced. Since the current options to fossil fuels don't present to be efficient alternatives for the long run, a new scientific effort must be done to keep up with the seemingly never-ending growing needs of society. Not just in an economically positive way, but also presenting to be a less harmful alternative to the environment.

Thermonuclear fusion presents to be a very attractive option for producing uninterrupted electricity, with even higher gain in comparison to fission technology. In fission the bombardment of ${}^{235}_{92}U$ with a neutron results in 0.88 MeV per nucleon ([19]), macroscopically equivalent to 84×10^6 MJ/kg. During the fusion of D-T nuclei the energy relished per reaction corresponds to 3.52 MeV per nucleon, which is macroscopically equivalent to 338×10^6 MJ/kg ([19]). While deuterium nuclei are naturally abundant in earth's oceans, there is no natural tritium on earth. It's possible, however, to breed tritium using lithium. Very attractive and simple numbers presented by Dr Ian Chapman from the Culham Center for Fusion energy at the Royal Institution illustrated how one mole of the D-T nuclei could be used to produce about 10^{12} J of energy. The D-T nuclei are relatively abundant, and one mole (equivalent to a few grams of the reactants) found for example in a bathtub of water along with the lithium found in two laptop batteries. This rather accessible amount of reactants would nearly sustain the energy of one person for his entire adult life, assuming already a very high consumption lifestyle. The 17.6 MeV from the resulting products in (1.1), considering now 1 mol (6.03×10^{23} particles), would result in about 1.65×10^{12} J, and as suggested by Dr Ian Chapman to a 60 years energy supply

of one person, assuming a 20 KWh/day consumption rate.

The understanding of the current limitations in achieving uninterrupted reactions in present thermonuclear devices is fundamental. It should provide the start for a path in the construction of economically feasible reactors with high power gain. Although a safe guess is that the costs of a fusion facility should be higher than current alternatives given the complex, and some, still undeveloped technology needed. However, still laying in a competitive range. Projects involving experimental machines designed to explore fusion, such as ISTTOK (the fusion experiment at Instituto Superior Técnico) and, in preparation, the big collaboration in ITER (which will count with 35 nations to build the world's largest tokamak in southern France) will contribute in this understanding. Making possible in the future the incorporation of the improved technology in complete electrical power plants (maybe just another fifty years).

Along with the great benefits attractive to fusion comes tremendous challenges to the physics and engineering communities, from plasma physics, transport theories, to material and electrical engineering. Nuclear fusion is an never-ending challenge provider.
In order for the positively charged nuclei to overcome the Coulomb repulsion among them and fuse, they will have to possess extremely high kinetic energies. The reaction presented on (1.1) is one of a couple of options for a device based on fusion reactions between light elements, and should be the main focus for fusion power plants. Mainly given to its higher cross-section at lower temperatures. In particular, temperatures of about 20 keV (over 200 million Kelvin (k)) are necessary for the reactants on (1.1) to fuse in a continuous and self-sustained state of ignition. Starting with an initial fuel of atomic deuterium and tritium, in the necessary kinetic energy conditions for the positive nuclei of the two species to come close and undergo a fusion reaction, the fuel will have then become a plasma, presenting outstanding temperatures way above the core of stars.

1.2 Thermonuclear Ignition

Great efforts have been done to construct a device capable of reaching stable thermonuclear ignition. Ignition implies maintaining a significant amount of plasma confined at the high temperatures needed, and during a sufficient time to result in a positive power balance. When these features have been achieved a fusion device could operate uninterruptedly being fed at a given rate with fuel. The Lawson criterion [19] and later the "triple product", given as

$$nT\tau_E \geq f_{D-T} \sim (3-5) \times 10^{21} sm^{-3} keV, \qquad \text{"triple product"} \tag{1.2}$$

for the D-T reaction, express the conditions on plasma density ($n_{e,i} \sim n$), temperature ($T_{e,i} \sim T$) and energy confinement time (τ_e) in order for a magnetic fusion device to reach thermonuclear ignition. For a plasma in ignition (satisfying the criteria) the alpha power balances the energy sinks in the plasma, such as the irreducible Bremsstrahlung losses, [19]. Therefore, the fusion reactions in the plasma are self-sustained by one of the products they originate. These highly energetic alpha particles allow to maintain the plasma's energy requirements through multiple collisions with the D and T nuclei.
For the D-T reaction the minimum of the triplet criterion occurs for temperatures around the $T = 20$ keV reference. Commonly, to reach ignition, a combination of ohmic and external auxiliary heating are used in the initial transient phase until a transition temperature. Previous to the transition temperature, the alpha heating is negligible against the losses due to thermal conduction and Bremsstrahlung radiation. Above it the alpha heating power becomes more significant and eventually rises the temperature to satisfy the "triple product", according to the value of the two remaining quantities. Nonetheless, various combinations of the three parameters in the "triple product" are considered among the fusion community to reach plasma ignition. Current devices have not yet been able to sustain simultaneously the parameters in order to reach and maintain a steady and continuous mode of operation with an ignited plasma. However, ITER is expected to exceed all current results.

1.3 Tokamak Principles

There are different experimental configurations still in consideration to reach on earth the plasma confinement requirements that allow to generate thermonuclear fusion power.
Far in the run are magnetic confinement devices, such as tokamaks (experiments as ISTTOK, ITER, JET, Asdex Upgrade, DIII-D, Tore Supra and Alcator C-Mod), stellarators (TJ-II and Wendelstein 7-X, for example) and also spherical torus (as MAST). The main principle of these devices is a system of magnetic fields responsible for the confinement of the plasma charged particles in a vacuum chamber.

The charged alpha particles that result from (1.1) are confined in the chamber by the magnetic fields, and their power should sustain the ignited plasma. On the other hand, the neutrons

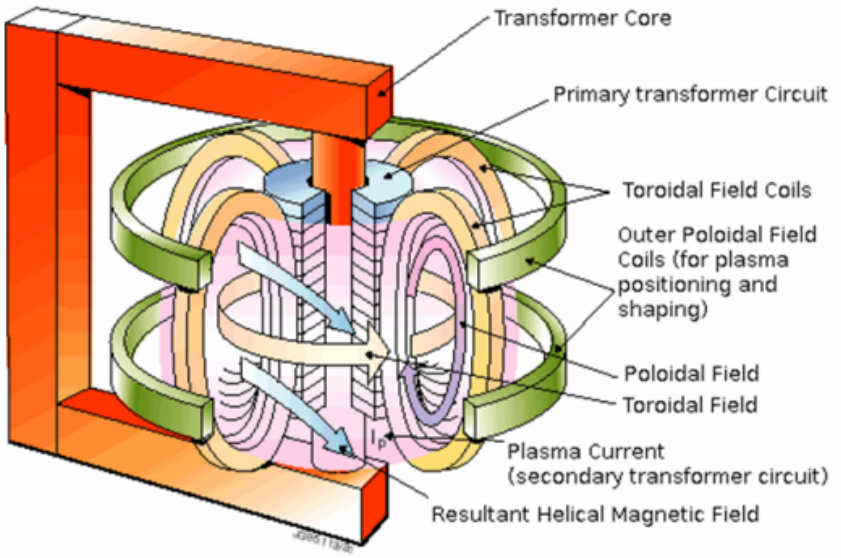

Figure 1.1 General scheme of a typical tokamak. [Adapted figure from [6]].

escape the magnetic fields and the plasma providing the main source of heat in material structures (the blanket), and are ultimately responsible for the production of electricity as commonly seen for other electricity sources, via restive heating, water vessels and turbines.
The tokamak is the most promising fusion configuration. Leading the run to understand and achieve fusion power in a controlled manner, and also in one that will allow to obtain a considerable positive gain in the approaching ITER experiment. In a tokamak the plasma is kept in a vacuum chamber with the shape of a torus (toroidal magnetic chamber), as in the scheme on Fig. 1.1. The acronym comes from the Russian designation *Toroidalnaya Kamera Magnitnaya*. The device was first introduced in 1950's by the work of Soviet physicists, [20].

The charged particles are kept in toroidal motion due to the Lorentz force. That causes the particles to orbit (with Larmor radius) along the toroidal magnetic field lines. The choice of a plasma vessel shaped as a torus is in order to avoid particle losses at the end of the fields lines. The radius of the center of the torus $R = R_0$ is referred to as the major radius, and the radius of the torus cross section $r = a$ as the minor radius. Finally, R/a is referred to as the aspect ratio R_0/a.

The toroidal field B_ϕ is generated by the coils that contour the chamber's cross section, the toroidal magnetic coils, in Figs. 1.1 and 1.2. Nevertheless, the particles must spin along helical field lines, to balance overall velocity drift components that arise from the toroidal geometry of

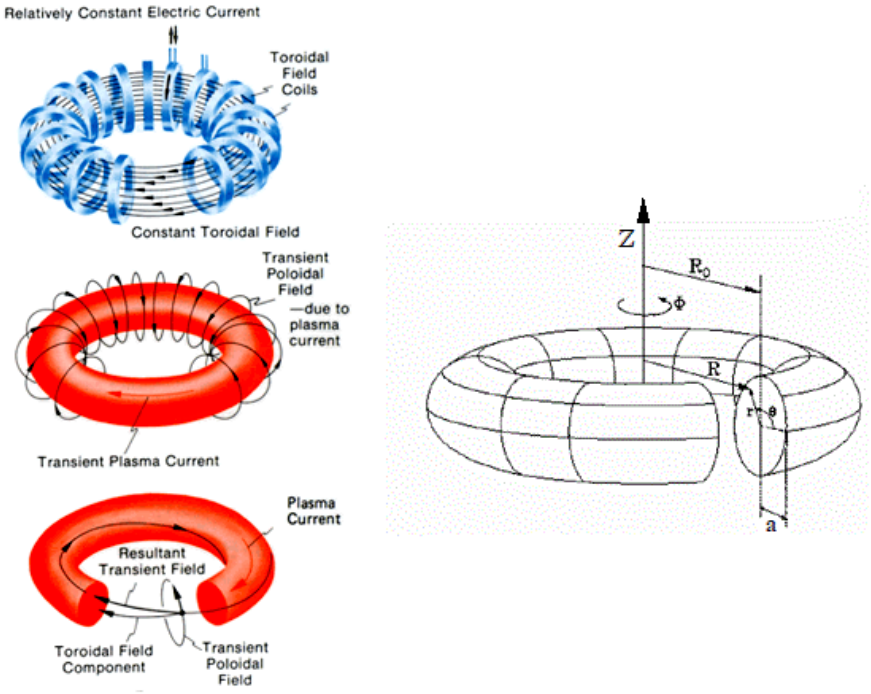

Figure 1.2 General scheme of the toroidal and poloidal directions and fields in a tokamak device. Main geometric parameters of the device. [Adapted figure from [7]].

the magnetic field and therefore avoid an unstable assemble.

The geometry of the toroidal field results in vertical velocity drifts (sec. 1.4), namely the $\nabla\vec{B}$ and curvature drifts. That arise due to the field's dependence on the major radius ($|\vec{B_\phi}| \propto 1/R$) and due to the curvature of the field lines, respectively. The components of these vertical drifts in opposite directions for ions and electrons establish a vertical electrical field that ultimately results in the $\vec{E} \times \vec{B}$ drift. The $\vec{E} \times \vec{B}$ is radially outwards for both ions and electrons, and therefore causes a coherent displacement of the plasma outwards into the vessel's walls.

This setback for an initial toroidal field scheme (also known as the pure toroidal θ-pinch configuration) provides therefore an unstable confinement. To balance these vertical drifts of ions and electrons the field lines must wrap around the torus, as shown in Fig. 1.2. The particles in turn will still possess the vertical $\nabla\vec{B}$ and curvature drifts. However, as they move along helical field lines for a significant number of toroidal turns, the vertical $\nabla\vec{B}$ and curvature drifts are averaged out.

The helical magnetic field is attained (in a configuration known as the screw pinch) by the combination of the toroidal magnetic field B_ϕ with a small poloidal magnetic field B_θ. The B_θ field results from a toroidal current circulating on the plasma (usually $B_\theta \sim B_\phi/10$). This current corresponds to the secondary winding of a transformer, which has a solenoid in the center of the torus as primary winding, seen in Fig. 1.1.
The safety factor, q, primarily represents the number of toroidal turns required for any given field line to perform one full poloidal turn. In the picture of macroscopic stability based on the MHD (Magnetohydrodynamics) model q is given by 1.3,

$$q(r) = \frac{rB_\phi(r)}{R_0 B_\theta(r)}. \tag{1.3}$$

This estimation holds for most axisymmetric toroidal configurations (and considering a cylindrical, large aspect ratio approximation), [19]. Configurations with $q > 2$ at the edge tend to be more stable.

The toroidal, poloidal and radial directions for a tokamak plasma can be better understood in Fig. 1.2, respectively, along ϕ, θ and $\vec{r}$. It is often referred to the direction along the magnetic field lines as simply the parallel direction, and perpendicularly to the magnetic field lines as just the perpendicular direction.

The shaping and positioning of the plasma is still managed by an external vertical field,

which is established by a system of coils often located outside the first wall. These coils are referred to as the outer poloidal coils on Fig. 1.1, (in some schemes, can be also found a set of inner poloidal coils).

1.3.1 Scrape-off layer

The magnetic field lines and the current lines lie on surfaces of constant pressure. A set of nested toroidal surfaces in a well-confined MHD plasma equilibrium, [19]. Both the magnetic field and current lines have no component perpendicular to these nested surfaces, thus they are also commonly referred to as flux surfaces. The flux surfaces should be closed surfaces in the vacuum chamber to avoid particle loss. Nonetheless, in the exterior region they are interrupted by components of the chamber's walls. The outer region of the chamber characteristic of having open magnetic surfaces (opened magnetic field lines) is usually referred to as scrape-off layer (SOL). The screw pinch configuration, used to confine particles along the helical field lines, should limit particle loss to result only from particle collisions along the radial direction. However, as desired to discuss in this work a solid understanding through the last decades has revealed that more complex plasma mechanisms such as high density plasma features (known as filaments or blob-filaments) appear and propagate in the SOL region of fusion plasmas. It is experimentally observed that plasma losses are up to 100 times larger than the expected to occur by particle collisions, most probably due to the filamentary structures. In fact these plasma blobs are also strongly influenced by the $\nabla\vec{B}$ and curvature drifts. Polarized blob structures occur in the plasma outer regions with the electric field on these structures providing a mechanism for their convective $\vec{E} \times \vec{B}$ drift.

The division between the core plasma (confined inside the closed flux surfaces) an the SOL is marked by the last closed flux surface (LCFS) in limited machines, or by the magnetic separatrix in diverted machines. On Fig. 1.3 are presented general schemes of the LCFS or separatrix considering the two common scenarios for the plasma-wall interface (limiter or divertor).
A limiter is simply a material structure interrupting the field lines before the actual chamber walls, and therefore determining the LCFS. Limiters can be installed in various geometries. Commonly seen are poloidal limiters, which can be a material with the shape of the vacuum vessel, but having a smaller diameter, and extending completely along the poloidal perimeter. Could also have an interrupted structure (rail limiters). Limiters can even be assembled as just a localized solid component in the vessel. Moreover a material interface placed in a certain local

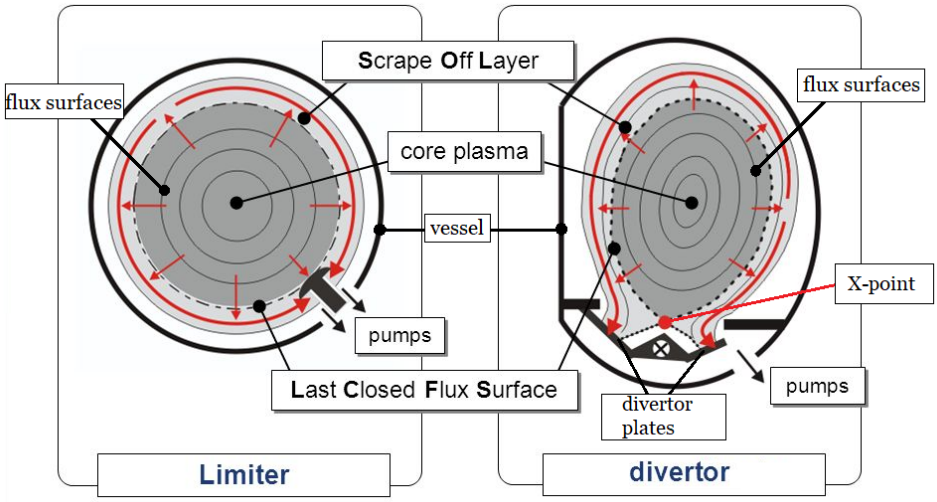

Figure 1.3 General schemes for the cross section of a tokamak with a divertor or with a magnetic separatrix. Common scenarios for the plasma-material interface. For devices with a divertor the plasma-material interaction takes place further away from the confined plasma, in a localized region on the vessel's edge (the divertor target plates). Extra coils are responsible for producing the X-point in the poloidal magnetic field. Near the X-point are the divertor target plates, set to better withstand plasma interactions. [Adapted figure from [8]].

position of the vessel but extending along the toroidal direction corresponds to a toroidal limiter. In the second common configuration for the plasma-material interface, the divertor, extra coils are responsible for producing a null point in the poloidal magnetic field, which is also referred to as an X-point, localized in the edge as in Fig. 1.3, [8]. Near the null point are the plasma facing components for this assemble, the divertor target plates. For this configuration the plasma-material interaction takes place much further away from the plasma confinement region on the closed flux surfaces. As a consequence, is reduced the probability of contamination of the plasma core with impurities that result from the interaction between the plasma and the plasma facing components. Also reduces the probabilities on wall damage, due to the lost of particles and energy outwards to the walls. Therefore a divertor is often seen in use for the majority of tokamaks.

1.4 Introduction to Plasma Physics

As previously mentioned, the positive nuclei have to overcome the Coulomb repulsion among them to be found in the short-range cross-section corresponding to the fusion reaction. The conditions of kinetic energy require very high values of temperature, for which ions are found in the tail of the Maxwellian energy distribution. Near the temperature of $T \sim 100$ keV the cross-

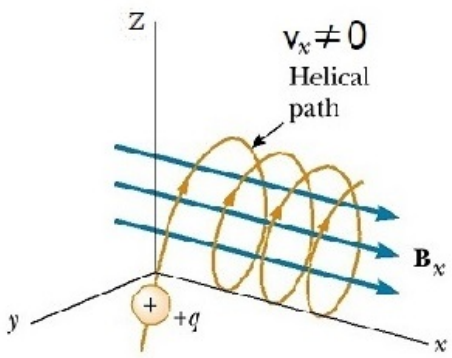

Figure 1.4 Lorentz force and Larmor motion. Uniform circular motion in the plane perpendicular to the magnetic field, with r_L and w_L. Helical path for charged particles with a velocity parallel to the magnetic field. [Adapted figure from [9]].

section of the reaction on 1.1 approaches a maximum. However, such high temperatures are not required to initialize the reactions. The reference value is around $T = 20$ keV. Under these conditions the fuel becomes a plasma consisting of an ionized gas composed by two independent species of charged particles: the positive ions (both deuterium an tritium nuclei) and a separate specie of electrons, where a quasi-neutrality condition holds for the ion and electron densities, i.e. $n_i \sim n_e$. Also an important general characteristic is the dominance of long range electromagnetic forces over short range collisions, and it has a major role in the collective behavior displayed by plasmas.

The Debye length, λ_D, in (1.4), corresponds to the characteristic decay length of charge density and potential in a plasma, and should be smaller than the plasma size L_p, i.e. $\lambda_D << L_p$, in order for the collective behavior to be dominate. In a 3-d approach of the problem (Debye shielding, [19]) the condition on (1.6) arises, [19]. The parameter in (1.6) is usually incorporated in the plasma description in order to ensure that collective behavior is dominant over collisions.

$$\lambda_D = \left(\frac{\epsilon_0 T_e}{e^2 n_\infty}\right)^2. \tag{1.4}$$

$$N_D = n\frac{4\pi}{3}\lambda_D^3. \tag{1.5}$$

$$N_D >> 1. \tag{1.6}$$

1.4.1 Guiding center drifts

Let us start by focusing on the confinement established by an imposed magnetic field, considered to be constant and uniform in both time and space, B. Due to the Lorentz force, particles are forced to rotate around the the magnetic field lines with

$$r_{L_{e,i}} = \frac{v_\perp m_{e,i}}{|Q|B} \tag{1.7}$$

, and

$$w_{L_{e,i}} = \frac{|Q|B}{m_{e,i}} \tag{1.8}$$

, where $r_{L_{e,i}}$ corresponds to the Larmor radius (or gyro-radius) for electrons and ions, $w_{L_{e,i}}$ to the cyclotron frequency (or gyro-frequency), $m_{e,i}$ to the particles mass, and Q to their respective charges. Finally, $v_\perp$ corresponds to the particles velocity in the direction perpendicular to the magnetic field. Moreover, if the particles are moving in the direction parallel to the magnetic field, i.e. $v_\parallel \neq 0$, the result is a helical orbit as in Fig. 1.4, [9]. In a tokamak device, in particular, the thermal velocity of the high energy particles allows them to move freely parallel to the magnetic field lines, while confined by the Lorentz force in the perpendicular direction. The gyro-motion around the field lines corresponds to the fastest motion (shortest time scale, $\propto 1/w_{L_{e,i}}$) and the solutions listed below correspond to slower drifts of the center of the gyro-motion (guiding center) of each particle.

1. $\vec{E} \times \vec{B}$ drift

   The presence of any force perpendicular to $\vec{B}$, as the electric force that results from $\vec{E}_\perp \neq 0$, origins a drift of the guiding center in the plane perpendicular to $\vec{B}$. The acceleration due to an electric force on the perpendicular plane causes $r_{L_{e,i}}$ to be bigger when $v_{L_{e,i}}$ increases. The end result is a drift in the direction perpendicular to both the electric and magnetic fields. Both ions and electrons have the same $\vec{E} \times \vec{B}$ velocity drift, independently of their values of charge and mass,

$$\vec{v}_{\vec{E}\times\vec{B}} = \frac{\vec{E} \times \vec{B}}{B^2}. \tag{1.9}$$

   In general a force $\vec{F}_\perp$ perpendicular to the magnetic field results in a perturbation term $\vec{v}_{\vec{F}_\perp \times \vec{B}}$ from the Larmor motion, perpendicular to both the field and the force,

$$\vec{v}_{\vec{F_\perp}\times\vec{B}} = \frac{1}{q}\frac{\vec{F_\perp}\times\vec{B}}{B^2}. \tag{1.10}$$

2. $\vec{\nabla}B$ drift

   If the magnetic field is not uniform in space the Larmor motion varies $\propto 1/B$ in such a way that the guiding center drift is according to the approximate term,

$$\vec{v}_{\vec{\nabla}B} = \frac{m_j v_\perp^2}{2qB}\frac{\vec{B}\times\vec{\nabla}B}{B^2}. \tag{1.11}$$

3. Curvature drift

   For curved magnetic field lines a centrifugal force acts on the particles as a result of the curvilinear movement along the field direction. As mentioned before, the presence of a perpendicular force results in a drift perpendicular to both the magnetic field and the force. The curvature drift adds to the $\vec{\nabla}B$ drift and both occur in opposite directions for charges of opposing signs.

4. Diamagnetic fluid drift

   The diamagnetic drift isn't perceptible in the single particle picture. It can't be account for single particle motion as it is not a guiding center drift. However, in the fluid picture, in the presence of a pressure gradient the fact that their are more particles moving in one direction implies a drift for the averaged velocity value of the fluid element. The perturbation from the fluid Larmor motion that results from $\vec{\nabla}P \neq 0$, is given by

$$\vec{v}_D = -\frac{\vec{\nabla}P\times\vec{B}}{n_j q_j B^2}. \tag{1.12}$$

   The ion diamagnetic drift direction is a common reference in fusion devices.

In general different values of charge, mass and temperature (kinetic energies) may lead to different velocity drifts between the plasma species, resulting in electric currents and fields.

1.4.2 Fluid description and fluid drifts

Whether the approach is to study plasmas considering single particle motion, through kinetic equations, or to simplify the problem describing the plasma as a Two Fluid Model, as represented below (equations (1.13) to (1.22)), a consistent result arises from every approach. Characterizing in a similar matter several particle drifts that result for charged particles in the presence of electromagnetic fields.

$$\frac{\partial n_j}{\partial t} + \vec{\nabla}(n_j \vec{v}_j) = 0 \tag{1.13}$$

Continuity Equation

$$n_j m_j \left[\frac{\partial \vec{v}_j}{\partial t} + (\vec{v}_j \cdot \vec{\nabla})\vec{v}_j\right] = n_j q_j \left[\vec{E} + \vec{v}_j \times \vec{B}\right] - \vec{\nabla} P_j - \bar{\nu}_{jk} n_j m_j (\vec{v}_j - \vec{v}_k) \tag{1.14}$$

Force Equation

$$P_j n_j^{-\gamma} = cte. \tag{1.15}$$

Energy/Equation of State

Maxwell's Equations

$$\vec{\nabla} \cdot \vec{B} = 0 \tag{1.16}$$

$$\vec{\nabla} \cdot \vec{E} = \frac{\rho}{\epsilon_0} \tag{1.17}$$

$$\vec{\nabla} \times \vec{B} = \mu_0 \vec{J} + \frac{1}{e^2} \frac{\partial \vec{E}}{\partial t} \tag{1.18}$$

$$\vec{\nabla} \times \vec{E} = -\frac{\partial \vec{B}}{\partial t} \tag{1.19}$$

where,

$$\rho = \sum_j q_j n_j \tag{1.20}$$

$$\vec{J} = \sum_j q_j n_j \vec{v}_j \tag{1.21}$$

$$\tag{1.22}$$

The model presented above is a Self Consistent Two Fluid Model that describes several

averaged macroscopic parameters such as density, velocity, temperature and pressure of the independent species composing the plasma, [19]. It provides a description of the plasma as a mixture of different fluids j, usually, found to be $j = e$ (electorns) and i (ions) for fully ionized plasmas. However, a third specie could be considered for partially ionized plasmas still containing a considerable density of neutrals. In that case $j = e, i$ and n. It is referred to as a Self Consistent Model, since it not only accounts for how electrons and ions respond in the presence of electric and magnetic fields, but then also to how these densities (n_e, n_i), and therefore the charge and current densities riposte on the value of the fields. In this way the model accounts for the self consistent loop of dependencies occurring in the ionized plasma medium.

Each equation in the model holds for an individual species j. The first equation (1.13) is the well known Continuity equation, that corresponds to the particle conservation equation. The second equation of the model (1.14) arises from the momentum conservation for each species, commonly referred to as the Force Equation. It accounts for the momentum exchange due to the Lorentz Force acting on the particles, also due to a Pressure Force (for an isotropic medium), and finally the exchange of momentum that results from collisions between the different species in the medium. In the Force equation the last term represents the overall loss of momentum by species j when colliding with particles from species k. Seeing that ν_{jk} corresponds to the rate of collisions between the two species, the corresponding term in 1.14 can be referred to as the rate of momentum loss by species j thanks to collisions with species k. The collisions between like particles are neglected since the total momentum for the species is conserved, given the overall averaged values. The third equation of the Two Fluid Model (1.15) for energy conservation is taken as an Equation of State.

The validation of the Fluid Description for a fusion plasma mainly relies on the fact that in a (toroidal) magnetic confinement device particles are trapped in the parallel direction because of the gyro-motion along the magnetic field lines, Fig. 1.2. In the perpendicular direction to the field lines this guaranties that the $N_j = n_j \Delta V$ particles in a fluid element ΔV act like the particles in a highly collisional gas. The particles in a given fluid element move coherently together. Each individual particle stays confined in a physical space always within short distances relative to its neighboring particles (admitting an approximately constant Larmor radius). Each fluid element in the model is described by the macroscopic averaged parameters $g_j(\vec{r}, t)$. The macroscopic parameters correspond to the average of all the individual particles' values for that same property over the velocity space. In general $g_j(\vec{r}, t)$ for a fluid element centered at $\vec{r}$ at a time instant t is given by

$$g_j(\vec{r},t) = \frac{\int g_j \cdot f_j(\vec{r},t) dv_j}{\int f_j(\vec{r},t) dv_j}. \tag{1.23}$$

Therefore loosing the need to have a detailed track of each particle's in the velocity space.

Relative to the present work the Two Fluid Model is a good approach to further understand important velocity drifts (away from the gyro-motion along the toroidal magnetic field lines), for both electron and ion species. The velocity drifts are not only fundamental in understanding several characteristics necessary in the design of fusion devices, but also in comprehending the origin and radial convection of coherent plasma structures (called "blob-filaments").
Taking advantage of a simplification of the Force Equation, in which we neglected the momentum transfer due to all collisions, equation (1.24) below,

$$n_j m_j \frac{d\vec{v}_j}{dt} = n_j q_j \vec{E} + n_j q_j \left[\vec{v}_j \times \vec{B}\right] - \vec{\nabla} P_j \tag{1.24}$$

Force Equation

$$\begin{cases} \frac{d\vec{v}_{L_j}}{dt} = \frac{q_j}{m_j}\left[\vec{v}_{L_j} \times \vec{B}\right] & \text{Larmor motion } \vec{v}_L \\ \frac{d\vec{v}_{\vec{E}\times\vec{B}_j}}{dt} = \frac{q_j}{m_j}\vec{E} & \vec{E}\times\vec{B} \text{ drift } \vec{v}_{\vec{E}\times\vec{B}} \\ \frac{d\vec{v}_{D_j}}{dt} = \frac{1}{n_j m_j} - \vec{\nabla} P_j & \text{Diamagnetic drift } \vec{v}_D \end{cases} \tag{1.25}$$

, it is easy to highlight some aspects on the right hand-side that are helpful in comprehending the velocity drifts. In (1.24) the second term in the right-hand side corresponds to the fluid gyro-motion $\propto d\vec{v}_{L_j}/dt$. Still on the right-hand side it's represented the velocity drift that arises from perpendicular magnetic and electric fields (first term), the $\vec{E}\times\vec{B}$ drift $\vec{v}_{\vec{E}\times\vec{B}}$. The third term corresponds to the diamagnetic drift due to the presence of a pressure gradient $\vec{\nabla}P$.

From the Two Fluid Model can be derived the single-fluid model MHD (magnetohydrodynamics). The MHD model is more often found to analyze the macroscopic equilibrium and stability of a fusion plasma than the previous Two Fluid Model. The MHD model can be obtained from the two-fluid analysis by reducing to single-fluid variables, while considering the length and time scales that characterize macroscopic plasma behavior, [13]. Such as the radius

(a) of a plasma volume being used to define the appropriate length scale L, ($L \sim a$), while the ion thermal transit time (a/v_{Ti}) across the plasma being taken as the the appropriate time scale τ, ($\tau \sim a/v_{Ti}$).

As previously mentioned, there are a couple of approaches to study and describe fusion plasmas providing similar results as the ones introduced in section 1.4 for guiding center and fluid drifts. The expressions provided through 1.4 are analyzed with more care in [19] and [21], accompanied with extended information on the approximations and considerations taken in their derivations.

Chapter 2

Edge turbulence in fusion devices

2.1 Introduction

In the edge of tokamaks and general fusion devices a major challenge is faced regarding enhanced losses of particles and energy. The performance of tokamaks drastically diminishes as enhanced losses at the edge degrade the confinement conditions.
The edge plasma is generally understood as starting a few centimeters inside the last closed flux surface (LCFS) (in limited devices) or magnetic separatrix (in diverted machines), where still lays the confined plasma on closed flux surfaces. The region extends up to the scrape-off layer plasma (SOL), where opened field lines are seen to be interrupted by material structures, (chapter 1). In the edge plasma the neutral particle density is not negligible and therefore atomic processes strongly influence the local particle and energy balance.

It has been understood from experimental investigations, mainly over the last couple of decades, that highly localized density structures are frequently born near the LCFS. A strong theoretical hypothesis is that it is due to the nonlinear saturation of turbulence (i.e. small-scale instabilities) in the tokamak plasma boundary.
Turbulence induced structures and associated electrostatic fluctuations of plasma quantities are routinely observed in the edge and SOL plasma, this phenomenon dominates the particle and energy losses and greatly limits the overall confinement conditions. In this sense, numerous edge studies, in distinctively parameterized devices, aim to gadder a solid understanding of the physics processes in the origin of the edge turbulence and the limitations that they set on plasma confinement. An effort to also prevent the enhanced plasma interaction and damaging on plasma facing components (PFCs), contamination of the vessel with impurities, and the influence on the

particle recycling and plasma exhaust processes. Several investigations have already determined that losses in tokamak devices are not continuous, but, instead, take place in an intermittent manner due to the radial convection of turbulent induced structures known as filaments (or blobs), [12, 13, 22–24].

The study of different experimental configurations in which turbulence arises can also give an insight on the instability mechanisms in its origin, therefore helping to understand how to reduce the dominant losses.
Conjointly with the time and space structure of turbulent filaments, a large body of work have been dedicated into characterizing their statistical distributions. In both subjects a wide set of results has been gathered showing a large coherency of the edge turbulence characteristics for most fusion devices. Previous results can be found from [14] to [25].

This chapter will reference a basic model for the convected particle losses by turbulence induced structures, [14]. In order to clarify the physics mechanisms in which the filament structures degrade the performance of fusion plasmas. It is also presented general plasma properties that should be expected in turbulence dominant regions, setting a useful background for the results presented and discussed in chapters 4 and 5.

2.2 Review on edge turbulence properties

The experimental investigations of the turbulence induced structures will provide a picture on the conditions in which these mechanisms dominate in the edge plasma. However, the multitude of plasma instability mechanisms driving turbulent regions is not thoroughly scooped in this study.

The induced filaments are generally characterized as magnetic-field-aligned plasma structures, [14], which present considerable higher density than that of the background plasma. They are very localized in the perpendicular direction (having perpendicular scale lengths intermediate between the ion gyro radius and macroscopic machine dimensions), while extending along the parallel direction. On [14] a working definition can be found that tries to encompass the theoretical and experimental investigations focused on the blob objects. From which it is worth to add that the plasma blob-filaments have a single-picked density distribution, with a maximum typically 2–3 higher than the surrounding rms fluctuations of the background plasma. Secondly, the filament variation along the magnetic field, to which they are highly align to, is

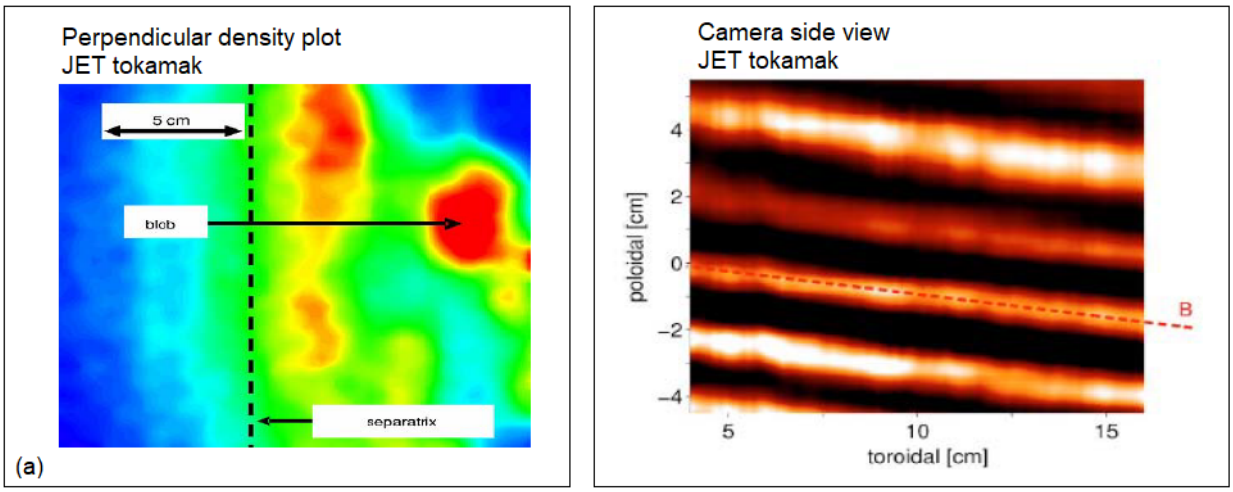

Figure 2.1 Results from cameras installed in the JET tokamak. In the left is showing a 2D density plot (intensity map) in the perpendicular plane. In the perpendicular view, high density blob-like structures are shown just outside the separatrix (dashed black line). On the right, the high density structures at the JET tokamak are seen as brighter filaments, extending along the toroidal field (dashed red line). [Adapted figure from [10]].

much weaker than the variation taking place in the perpendicular direction. At last, the blob motion is dominated by a convective $\vec{E} \times \vec{B}$ velocity component as a result of a charge polarizing force.

2.2.1 Spatial and temporal structures

The large number of edge investigations have been a great lever in clarifying the previous spatial picture of highly localized structures in the perpendicular plane, having a blob-like two-dimensional (2D) spatial structure, while extending over the torus, in the parallel direction, with a filament three-dimensional (3D) structure. The temporal and spatial structures of the "blob-filaments", as named on [14], have been interpreted using various different diagnostics and analysis techniques. Langmuir Probes, which consist in electrodes inserted in the edge plasma, are the most common and simplest diagnostic used in edge/SOL studies. Nonetheless, with the pressing need into understanding the edge turbulence processes, a large number of imaging diagnostics such as beam emission spectroscopy (BES), gas-puff imaging (GPI), and fast cameras have been well developed, and provide an intuitive and clarifying picture of the blob-filament structures.

From the imaging results shown as example on Fig. 2.1 it is observable on the perpendicular

plane (2D density plot) the resembling "blob" objects of higher density over the surrounding background plasma. The example is obtained from imaging diagnostics in the Joint European Torus (JET) experiment, [10]. On the 3D image, also obtained from the JET tokamak, the 3D filament structures from the extended blobs along the parallel direction are shown.
On camera images from the Mega Amp Spherical Tokamak (MAST) experiment, Fig. 2.2, edge filaments of higher density are evidenced through brighter pixels in the images. The filament structures not only show to extend around the chamber, but also to be highly aligned with the magnetic field, having the same helical geometry along the torus. The helical geometry of the magnetic field was introduced on chapter 1, Fig. 1.2.

Additional observations of 2D blob structures in the perpendicular plane are shown in Fig. 2.3 and Fig. 2.4. The former from the GPI diagnostic in the National Spherical Torus Experiment (NSTX tokamak), [11], an the latter obtained with the BES diagnostic on the edge of the DIII-D tokamak, [12, 26]. The high density 2D blob structures, coherently seen in these measurements, generally fall between 1–3 cm (along $\vec{r}$), [14] and are seen to propagate radially with typical velocities of $\sim$ 0.5–2 km/s.

On the other hand, theory predicts that while the higher density blobs are convected from the edge of the confined plasma through the SOL, regions of reduced density (density holes) propagate in the opposite direction (inward into the confinement region), as evidenced in the references [126, 129, 130, 144, 158, 159, 169, and 180] from [14]. To corroborate the theoretical scenario of plasma holes, simulations with seeded holes can be used to illustrate their inward motion, [27]. The formation of density holes and blobs due to plasma instabilities near the edge of the confined plasma can be read in more detail in [28, 29].
On Fig. 2.4, showing the example from the BES diagnostic obtained at the DIII-D tokamak [12, 26], it's seen not only the high density features corresponding to the blob-like structures (in red), but also low density features near the LCFS (in blue). The image shows two frames, with a time difference of 6 μs. In the figure it is seen a radial and poloidal displacement of the high density blobs, which are marked by a dashed circle in both frames.

2.2.2 Propagation mechanism by a charge polarizing force

The plasma filaments provide a mechanism for the radial outwards transport of particles and energy, resulting in losses from the edge boundary region in which they are born. A blob trans-

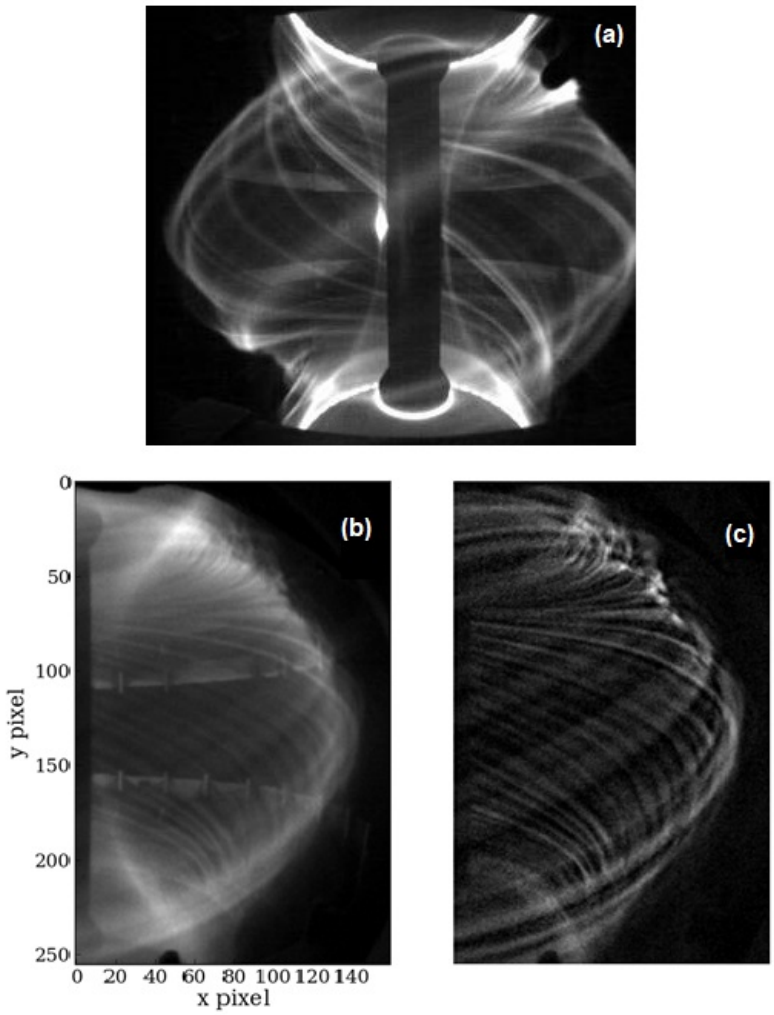

Figure 2.2 (a, b) Camera Image from the MAST tokamk. Images obtained from the MAST tokamak (a,b) are processed in order to evidence the high density filament structures corresponding to brighter pixels (c).
The filament structures not only show to extended onward in the chamber, but also to be highly aligned with the toroidal magnetic field, having the same helical geometry along the torus. [This figure is a cortesy of Tom Farley (MAST, CCFE), 2019].

port mechanism originated by a polarizing force is summarized in [14]. The overall idea is that an external polarizing force ultimately results in an $\vec{E}\times\vec{B}$ velocity drift that drives the filaments.

To begin, radial or outwards expansion forces result in a poloidal $\vec{F}\times\vec{B}$ particle drift. This mechanism is in the origin of the vertical $\nabla\vec{B}$ and curvature drifts explained in chapter 1. Any force $\vec{F}$ in the perpendicular plane results in $\vec{F}\times\vec{B}$ drifts also along the perpendicular plane. In the particular cases of the $\nabla\vec{B}$ and the curvature drifts the displacement of ions an electrons is unequal (and have opposing signs) according to the definition on (1.10), which is dependent

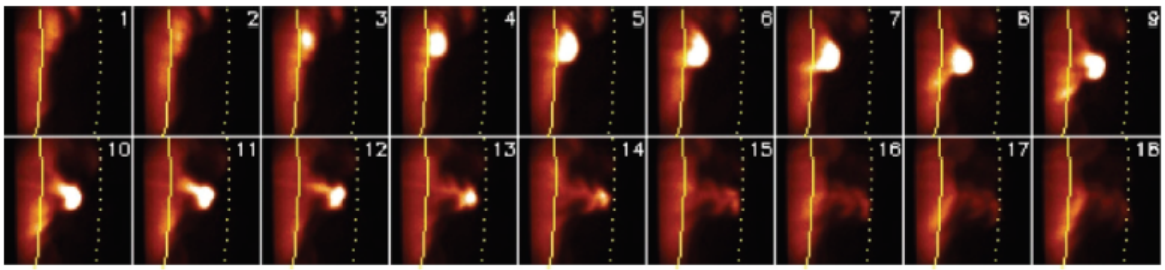

Figure 2.3 Gas-puff imaging (GPI) frames from the NSTX tokamak, taken near the outer midplane separatrix (solid line). The frames, with a frame rate of 7.5 μs/frame and a $\sim 25 \times 25$ cm^2 field of view, show the formation of a density blob (brighter feature) near the separatrix and its subsequent propagation radially outwards with $\sim V_r = 1$ km/s. A poloidal motion is also observable, although more subtle. [Figure from [11]].

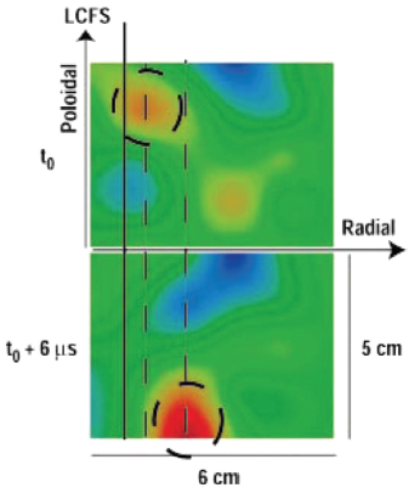

Figure 2.4 2D density plots from the edge of the DIII-D tokamak, obtained with the beam emission spectroscopy (BES) diagnostic. The Fig. shows two frames, where the frame rate is 6 μs, and each frame covers a 6×5 cm^2 area at the edge plasma of the DIII-D tokamak. While red indicates high density features, blue indicates low density ones. In the frames a high density feature of spatial structure of $\sim 2 \times 2$ cm^2, marked with a dashed circle, shows to propagate both poloidally and radially over the 2D perpendicular plane, with $\sim V_r = 1.5$ Km/s and $\sim V_\theta = 5$ Km/s. [Figure from [12, 13]].

of the value of $\vec{F}$ for each species. These forces (or drifts) polarize the plasma regions where they are observed. In the edge the filaments can be polarized in this way. A final consequence is a coherent $\vec{E} \times \vec{B}$ drift of the filaments in the perpendicular plane (chapter 1). On Fig. 2.5 it is illustrated the resultant radial outwards $\vec{E} \times \vec{B}$ velocity component ($\vec{V}_E$) arising from an external polarizing force, $\vec{F}$, directed radially outwards.

An experimental result arising from an estimation of the $\vec{E} \times \vec{B}$ blob's velocity component

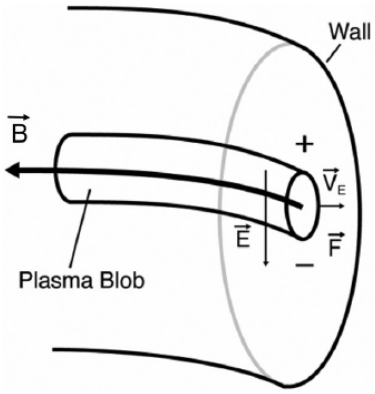

Figure 2.5 Scheme of the convective radial drift of a blob filament, resulting from the charge polarization mechanism. A $\vec{E} \times \vec{B}$ velocity component ($\vec{V}_{\vec{E}\times\vec{B}} \equiv \vec{V}_{\vec{E}} \equiv \vec{V}_r$) dominates the propagation of plasma filaments. The dominant radial component is induced by a charge polarizing force ($\vec{F}$) in the same direction. [Illustration from [14]].

is that blobs show to propagate with higher radial velocities over the surrounding background plasma. Different analysis proposed for an analytic blob model, more robust than the introductory scheme on Fig. 2.5, [14], often estimate an expected range for the magnitude of the radial velocity around $0.01 - 0.1\ C_s$ (where C_s corresponds to the ion acoustic speed). This estimated range is in the same order of magnitude as experimental results, found [26,28,30,31]. Meanwhile in the poloidal direction (i.e., the direction of the electric field, $\vec{E}$, on Fig. 2.5) filaments rotate along with the background plasma, having the same poloidal velocity component.

2.2.3 Transport induced by fluctuations

Electrostatic fluctuations of a multitude of plasma quantities in the SOL have been extensively documented in the bibliography to show a spatial and temporal intermittency, i.e., showing frequent burst-like events above the signal's mean value. These observations can be explained by the formation and propagation of the blob-filaments.

The electrostatic fluctuations derive from the filaments' distinct properties over the background plasma, along with their small temporal and spatial structures (of a few centimeters and a few microseconds) in comparison to machine dimensions. The filaments display an intermittent character themselves, having short life times they can grow and disappear in the edge plasma in a time scale of a few microseconds. The formation and propagation of the blob-filaments results in the electrostatic fluctuations of several plasma quantities. Such as the density $\tilde{n}(t)$ and the

plasma potential $\tilde{V_p}(t)$, where $\tilde{\cdot}$ denotes the fluctuations of a given quantity in time.
Anomalous net transport levels ($\bar{\Gamma}_r$) arise from correlated fluctuations of plasma density $\tilde{n}(t)$ and radial velocity $\tilde{\vec{v}}_r(t)$ (and/or temperature $\tilde{T_e}$ or $\tilde{T_i}$). The radial velocity component follows from the radial $\vec{E}_\theta \times \vec{B}_\phi$ drift, $\vec{v}_r \equiv \vec{v}_{\vec{E}\times\vec{B}}$. The expression for $\bar{\Gamma}_r$ is given on 2.1.

$$\bar{\Gamma}_r =< \tilde{n}(t) \cdot \tilde{\vec{v}}_r(t) >, \tag{2.1}$$

$$\|\vec{v}_r\| \equiv \|\vec{v}_{\vec{E}_\theta\times\vec{B}_\phi}\| = E_\theta/B_\phi, \tag{2.2}$$

where the the angular brackets denote a time average. In a scenario in which these quantities are uncorrelated, at any given time interval, the induced radial transport would average to zero. A result of an equivalent random distribution along $\eta\vec{ds}$ and $-\eta\vec{ds}$ for a given local flux surface.

The time signal of the induced transport, $\Gamma_r(t)$, displays an intermittent character with burst-like events, analogous to what is known for the fluctuating density and plasma potential in the edge/SOL plasma. Near the walls, region which is commonly referred to as the far-SOL, the filaments convective transport can account for a unit order factor of the total transport in some devices, [14], even up to 50%, as observed in [32, 33] for the TJ-II stellarator.

The transport by intermittent convection is a strong hypothesis to explain the flat profiles observed in the far-SOL of some diverted devices. In such scenarios, at the edge an SOL, the conduction and convection of heat to the divertor, in balance with the parallel transport, does not result in the expected results. Those being a thin SOL (when compared to its length) and exponential profiles with short decay lengths of typically 1-3 cm, [12]. Observations of wider and non-exponential SOL profiles, [34–36], implies an unexpectedly larger perpendicular transport of particles and heat towards the walls.

A common SOL diagnostic, to be soon discussed on section 3.2.1, Langmuir Probes, is mainly used to record two quantities which are the fluctuating ion saturation current, $\tilde{I}^+_{sat}(t)$, and the fluctuating floating potential, $\tilde{V}_f(t)$. The first is proportional to the plasma density fluctuations, $\tilde{n}(t)$, while the second proportional to the fluctuations of the plasma potential, $\tilde{V}_p(t)$. Both $\tilde{I}^+_{sat}(t)$ and $\tilde{V}_f(t)$ are better explained on section 3.2.1, but are now used as scalable examples of the SOL fluctuations of plasma density and potential, respectively. On Fig. 2.6 are shown examples of 1 ms probe signals for the time recording of these two properties, from measure-

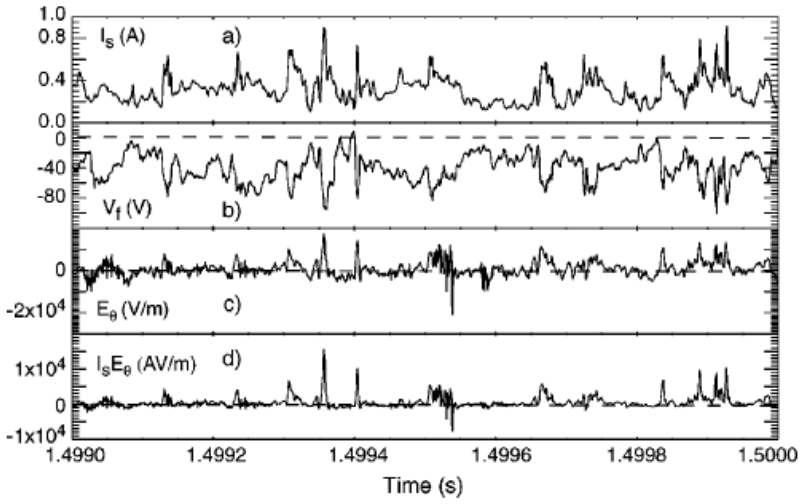

Figure 2.6 Langmuir Probe measurements obtained from the DIII-D tokamak. 1 ms time recordings of the $I^+_{sat}(t)$ ($\tilde{I}^+_{sat}(t) \propto \tilde{n}(t)$), $V_f(t)$ ($\tilde{V}_f(t) \propto \tilde{V}_p(t)$), and poloidal electric field E_θ. The results display frequent burst-like events above the signals rms. Finally it is also shown a sample of the product $I_{sat}E_\theta$ which is scalable with the intermittent radial particle flux ($\vec{n}_e\vec{V}_r = n_\theta/B_\phi$). [Figure from [12]].

ments carried at the DIII-D tokamak, [12]. It is also shown the probe signals of the poloidal electric field E_θ, and the product $I_{sat}E_\theta$. The latter is computed since it is scalable with the intermittent particle flux, $\Gamma_r = nv_r = nE_\theta/B_\phi$.

The intermittency in SOL fluctuations has been amply characterize through conditional averaging techniques of the burst-events above a rms-level threshold [14, 37]. The threshold is computed to discriminate the intermittency induced by turbulence. It varies for the conditions of each study, and is usually applied to the fluctuating density (often used a 2-3 rms-level threshold), [14, 37].

For the results of SOL fluctuations in the DIII-D tokamak showing on Fig. 2.6, a 2.5 rms-level threshold was set to discriminate the intermittent bursts in the ion saturation current fluctuations $\tilde{I}^+_{sat}(t) \propto \tilde{n}(t)$, [12]. The intermittent features were then binned for windows of 100 μs, centered around the maximum of each event, and averaged over about 20-40 events (or time recordings of 2-5 ms). For these results ([12]) was concluded that the intermittent bursts appear at a rate of $1-4\ 10^3 s^-1$. The windows determined from the $I^+_{sat}(t)$ signal were later used to identify the intermittent events' windows in the remaining quantities. Nevertheless, on [12], conditional averaging techniques with different rms-level thresholds and starting with E_θ to determine the appropriate windows culminated in coherent results. This example threshold is

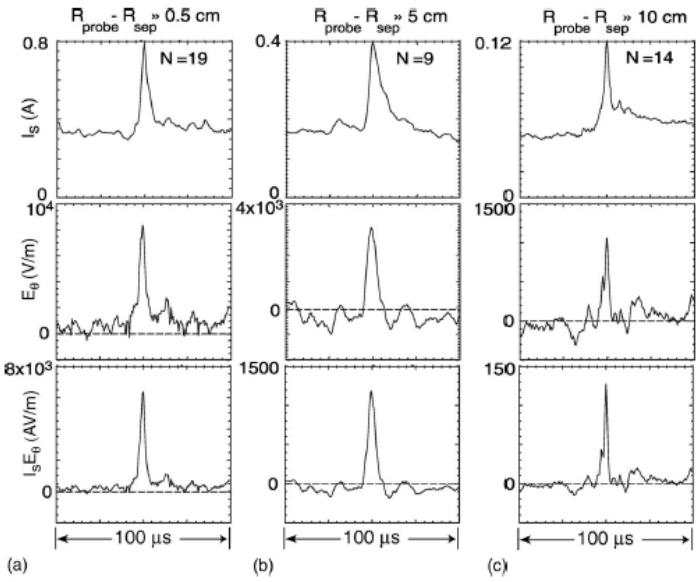

Figure 2.7 Conditional averaging results for Langmuir Probe measurements obtained from the DIII-D tokamak. The intermittent bursts on measurements taken at different radius in the scrape-off layer plasma are shown. Within (a) 0.5 cm, (b) 5 cm and (c) 10 cm of the LCFS at $r = R_{sep}$. Averaging over 20-40 events in each signal was taken for events over a 2.5 rms-level threshold (set initially to discriminate the bursts in the ion saturation current fluctuations). [Figure from [12]].

not universal and results from attempts on this specific experiment. However holds substantial similar conclusions taken in other tokamak experiments.

The time windows used in the conditional averaging technique in [12] are equivalent to averaging over structures smaller than ~ 2 cm. Scale which is associated to frequencies higher then $1/(100\ \mu s)$.

The observation of time structures between $10-100\ \mu$s, as evidenced in the example on Fig. 2.6, is a good reference for the range of results obtained for blob-filaments in most fusion plasmas. The conditional averaging results of the fluctuations in the DIII-D tokamak [12] are shown in Fig. 2.7. As can be seen the intensity of the bursts decreases with radius for the three positions probed in the SOL of DIII-D, with an attenuation factor of ~ 7 away from the LCFS, as referred on [12].

These examples, once again, call attention to the fact that the discrimination of the intermittent bursts that result from the filaments formation and propagation through the edge/SOL is not universally quantified. Neither is the scaling of the filament structures with fusion plasma parameters (density, plasma current, etc.). Nevertheless, evidence of the formation and propa-

gation of blob-filaments can be taken from investigations on the edge/SOL fluctuations of the spatial and time signals of various plasma quantities. The time recording of the fluctuations and subsequent discrimination of the intermittent events, from the average signals, allows to determine the spatial and temporal structures of the blobs (and their propagation through the SOL). Different analysis techniques applied to not only Langmuir probe data, but probing diagnostics such as the Neutral Beam Injector and Thomson Scattering have been used to establish coherent results to those determined from the optical diagnostics previously mentioned.

2.2.4 Statistical evidence for blob-filaments

Often the characterization of the edge/SOL intermittent fluctuations includes the probability distribution function (PDF), constructed by means of the terms of $P_f(x)$ over the range of values taken by a fluctuating quantity f, and where $P_f(x)$ expresses the probability of f falling between $f = x$ and $f = x + dx$. The third and fourth momentums which are used to compute the skewness and kurtosis, respectively, also hold relevant information about the presence and propagation of blob structures over the background plasma.

To facilitate the interpretation of the results the normalized form of the PDF is often used given by the terms of $\bar{P}_f(y)$, where y corresponds to $y = (x - \bar{f})/\sigma_f$. Lastly, σ_f represents the standard deviation of the series. The normalized form of the PDF, presents a similar behavior in the edge and SOL of most fusion devices when simultaneously evaluated for some quantities, [15]. In the far SOL where the intermittency in the electrostatic fluctuations is dominant, the PDF behavior of given quantities seem to be independent of the device and its parameters, displaying a roughly "universal" shape. The results present in general to be a deviation from a Gaussian distribution with high skewness. More into the confinement plasma boundary (i.e., LCFS) the deviation from a Gaussian distribution is usually smaller, and near Gaussian distributions are often observed. However, in the far SOL if there is a region where blobs propagate in a purely ballistic way, the PDFs may show to be approximately independent of the radius with properties that are related to their formation, as mentioned on [14]. On Fig. 2.8, are given examples of the normalized form of the PDF. The examples are computed for time signals of the ion saturation current, taken at four different experiments. Although correspondent to observations at different radial positions of four different fusion devices, they were all taken far enough in the SOL were the intermittency in the fluctuations should be significant. The identical character of the computed PDFs on Fig. 2.8 pictures well the aforementioned that the intermittency in the

electrostatic fluctuations, arising from turbulence processes in the far SOL, presents a coherent character among different devices and different device/plasma parameters.

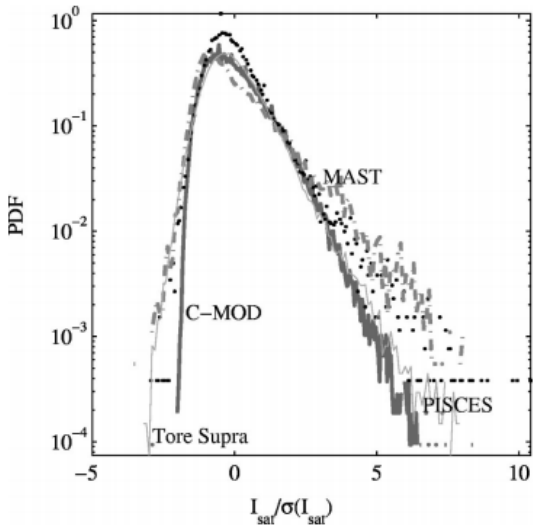

Figure 2.8 Semilogarithmic plot of the PDFs of the ion saturation current, normalized to the standard deviation. Results determined on the Tore Supra (solid line), Alcator C-Mod (thick solid line), MAST (dashed–dotted line), and PISCES (dots). [Figure from [15]].

For different quantities the deviation from Gaussian statistics may not evolve in the same way with radius. For example, the density PDF is often observed to be more tailed than the potential PDF at any radius. To paraphrase [14], the PDF result depends of the quantity being characterized. This calls attention to the fact that different quantities associated with the propagating blobs differ from the background plasma with different magnitudes. The intermittent bursts on the signals of distinct quantities will have different amplitudes. This fact was observed in Figs. 2.6 and 2.7.
The characteristics of the PDF described in this section are often seen for the fluctuating ion saturation current, $\propto n$, and the fluctuating particle flux in the far SOL. The PDFs of these quantities often have a positive tail, indicating a contribution of high density structures propagating in the plasma.

Further into the SOL the absolute magnitude of the blobs studied in DIII-D showed to rapidly decrease with radius, as just shown from results of [12]. Conjointly with a faster decay of the background plasma density, higher values of the skewness of the density PDF result. The observed correlation in DIII-D is a general hypothesis to explain a characteristic result for most fusion plasmas, which states that going further into the SOL the skewness profile of the density

PDF increases with radius. Positive density blobs are usually observed to be dominant in the far SOL, causing the density PDF to have a bigger positive tail, which is equivalent to higher values of skewness.

2.2.5 Frequency resolved measurements

The fluctuations generally display a broad frequency spectra, with most of the spectral power located bellow $\sim$ 100 kHz. The spectra decays towards higher frequencies with $1/f^c$, where c is a constant that varies in different frequency ranges. Usually c ranges from ~ -1 to ~ -2 at high frequencies, [14]. This decay index increases from $\sim$ 100 kHz, above which a quicker decay is observed with f.

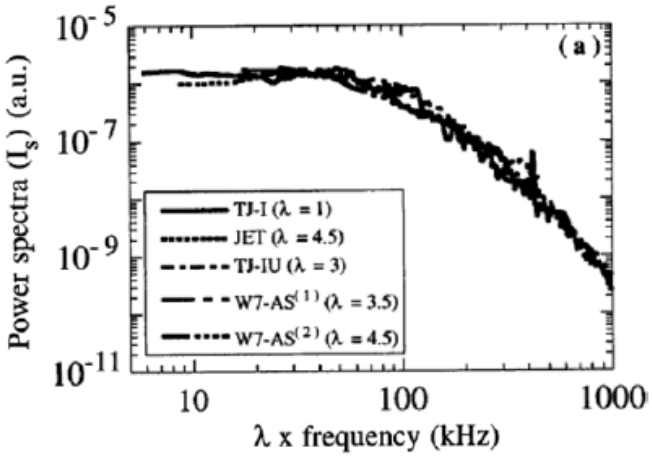

Figure 2.9 Power Spectra of the density intermittency obtained in the edge of various stellarator and tokamak devices. [Figure from [16]]. Results taken from Langmuir Probe measurements at the radius where the poloidal turbulence flow speed was near zero, [16]. In order to reveal that all curves have nearly the same shape, the factors presented in the legend were used to re-scaled the frequencies, and the amplitudes normalized.

The spectra of the fluctuations also shows a roughly "universal" behavior in most fusion experiments if re-scaled properly. Usually taking in consideration the standard deviation of the fluctuating series. This case is shown on Fig. 2.9, for investigations on different fusion devices, [16]. The results from [16] are as obtained in the JET tokamak, [25], where a decay with $1/f$ is seen in the spectral region where the intermittent transport is dominant.

Chapter 3

Experiment and diagnostic setup

3.1 Description of the experiment

3.1.1 ISTTOK

Turbulence studies were carried out on the edge and SOL plasma of the ISTTOK tokamak, which is shown on Fig. 3.1. The ISTTOK tokamak is a small circular cross-section device, with a large aspect ratio, having minor radius $a = 8.5$ cm and major radius $R_0 = 46$ cm. Information on the ISTTOK experiment and fusion program at IST can be found in [2,38,39]. ISTTOK has a poloidal graphite limiter, electrically connected to the vessel, is set at $r_L \simeq 8.5$ cm (see Fig. 3.3). The malleable structure is inserted on the vessel through one of the ports shown on Fig. 3.2, and after it is adjusted to take the circular shape of the vessel. As one can see on Fig. 3.3, the limiter installed at ISTTOK is a poloidal rail limiter, that is, a material extending along the poloidal perimeter with an interrupted structure (12 blocks of graphite). The smaller diameter of the limiter will interrupt the magnetic field lines trajectory, in an attempt to prevent the plasma from reaching the walls.

The vacuum chamber of this device is made by two half torus connected with insulating material, where each half torus structure is composed by six individual rigid sections of inox, which are in its turn connected by thin inconel bellows (0.15 mm). The vacuum system is made of a magnetic levitation turbo molecular pump supported by rotary pumps. In ISTTOK it is possible to measure the residual ($\sim 2 \times 10^{-7}$ torr) and also the work (2×10^{-4} torr) pressure by both ionisation and capacitance manometers. ISTTOK has installed a gas injection system made of several electromagnetic and pneumatic valves that allows to initially fill the vacuum chamber, and also for additional gas injections in a pulsed regime by means of a piezoelectric

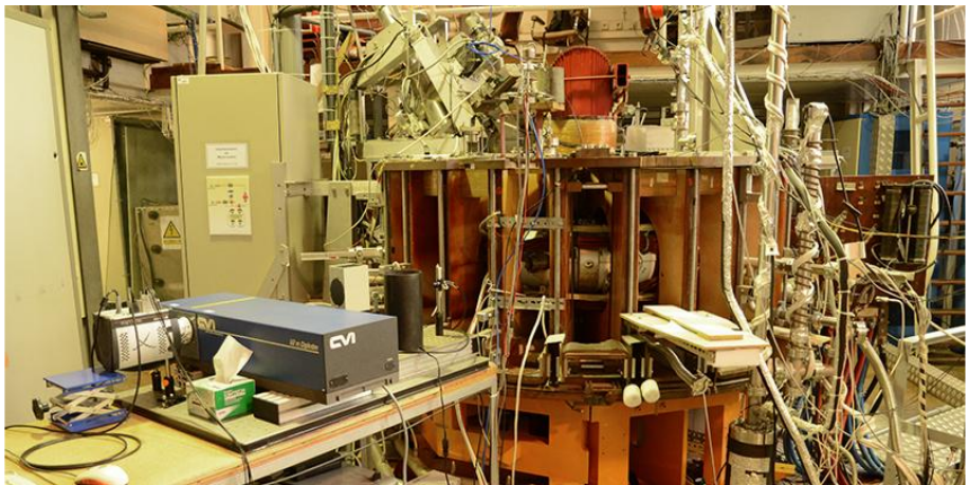

Figure 3.1 The ISTTOK tokamak experiment at IST. A small circular cross-section device, with a large aspect ratio, having minor radius $a = 8.5$ cm and major radius $R = 46$ cm, and a graphite limiter set at $r_L \simeq 8.5$ cm. An extensive scientific programme is carried at the the ISTTOK tokamak with the various diagnostics seen in the image.

valve.

ISTTOK usually operates with a toroidal magnetic filed between $B_T \simeq 0.4 - 0.7$ T. Although the toroidal field on ISTTOK could go up to 2.8 T by means of a set of 24 water cooled coils, power limitations (1 MW) obligate the operation with lower magnetic fields. In particular $B_T \simeq 0.5$ T is set during most discharges.

An iron core transformer with a primary winding of 2×20 spires at the central post and an auxiliary winding with $20 + 10$ spires in the external post, is installed in ISTTOK. The current applied to the transformer is provided by condenser banks. Usual operation is set for plasma current values of $I_p \leq 7$ kA.
ISTTOK can operate with both alternate current (AC) and direct current (DC) modes. For the former the plasma current direction is reversed several times, as illustrated in [40]. The plasma direction (positive or negative plasma current) is kept for around ~ 25 ms cycles, making each AC full-cycle last ~ 50 ms (both current signs). The AC mode of operation allows to obtain discharges with longer duration. The frequent change in the plasma current direction avoids the saturation of the iron core transformer.

Both vertical and horizontal positions of the plasma column are governed in real-time, using vertical equilibrium coils controlled by a magnetic feedback, with an accuracy of 5 mm, [39].

The remaining geometric parameters of the ISTTOK tokamak, along with the usual discharge parameters used on its operation can be found in table 3.1.

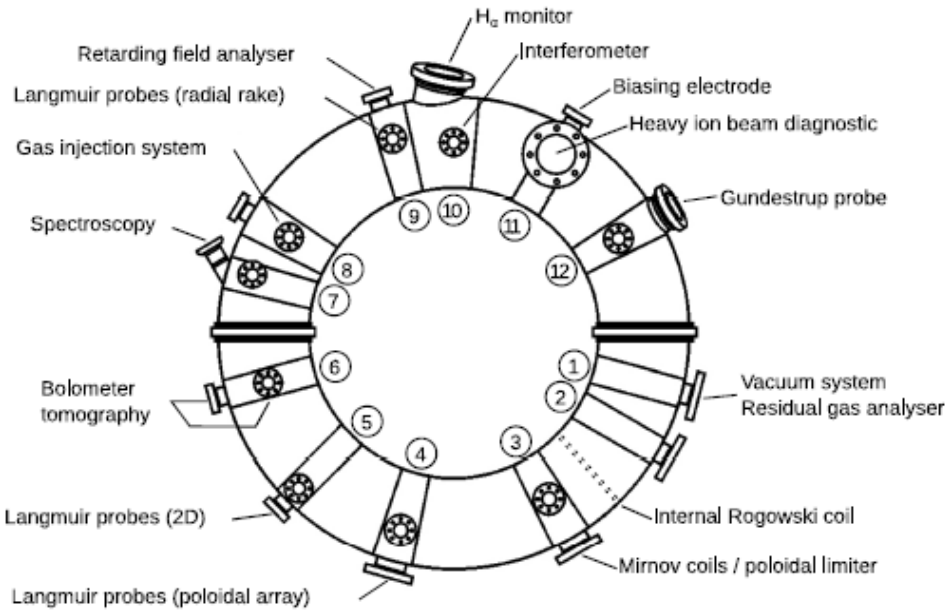

Figure 3.2 Scheme of the main diagnostics installed at ISTTOK, along with their toroidal positions. The ports used in the diagnosis of the plasma are also shown.

There are several diagnostics at ISTTOK that allow to carry an extensive Fusion programme at IST. On Fig. 3.2 one can find how most of them are placed in the experiment (toroidal positions), with complementary information found on [2] and [39]. The main diagnostic used in this thesis is described with some extent on the following section 3.2.1. Meanwhile, it is worth to briefly describe a few of the remaining diagnostics. Namely those used to determine the following quantities, which are referred in this study:

Plasma current: The plasma current at ISTTOK can be determined with the Rogowski coils diagnostics. Two Rogowski coils are installed at poloidal planes in ISTTOK. They allow to measure the plasma current and also the total toroidal current. The latter includes the currents on the vacuum vessel. The coils at ISTTOK are composed with 500 spires, each having 3.25 mm in diameter. An analog integrator is used along with coils to determined the currents.

Density: A microwave interferometer (100 GHz) is installed to determine the line integrated plasma density. The phase shift of the interferometer is determined between a probing beam that crosses the vacuum vessel, and a reference beam propagating in a controlled environment outside. The probing beam crosses the plasma vertically, at the geometric center of the vacuum vessel. The phase shift allows to determine the line inte-

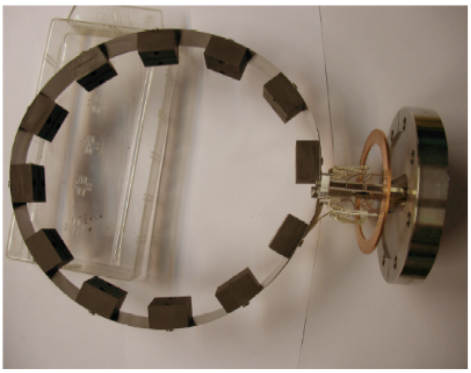

Figure 3.3 Poloidal rail limiter installed at ISTTOK (at $r_L \simeq 8.5$ cm). A graphite material with the shape of the vacuum vessel, that extends along the poloidal perimeter with an interrupted structure. The smaller diameter of the limiter will interrupt the magnetic field lines trajectory, in an attempt to prevent the conduction of plasma particles towards the walls.

grated plasma density along the probing path.

Plasma position: A set of 12 Mirnov coils, uniformly distributed along a poloidal plane are used to determine the plasma column position. The set of coils is used to determine the magnetic flux resulting from the plasma current, which in turns enables to determine the position of the column.

Loop voltage: A single loop installed around the iron core is used to measure the loop voltage, V_{loop}. The V_{loop} refers to the induced electromotive force (ε), and allows to compute the toroidal electric field driving the plasma current. The location of the diagnostics is due to the fact that at ISTTOK the majority of the flux is through the iron core.

3.1.2 Data Acquisition System

The Control and Data Acquisition System (CODAS) at ISTTOK is divided in two control subsystems and two data acquisition systems. The CODAS at ISTTOK has been often used with the purpose of testing new systems to install in other fusion experiments, as one can find on [39],

"ISTTOK has served as a test bed for new hardware and software developments that later were exported to other fusion devices.".

The experiment is now equipped with a Data Acquisition (DAQ) subsystem based on the Advanced Telecommunications Computing Architecture (ATCA). A more detailed description

Table 3.1 ISTTOK geometric and usual discharge parameters.

Parameters	Value
Major radius (R)	46 cm
Minor radius (a)	8.5 cm
Vessel radius (r_{vessel})	10 cm
Aspect ratio	5.75
Maximum toroidal magnetic field ($B_{T_{max}}$)	0.4-0.7 T
Plasma current (I_p)	$\leq$ 7 kA
Discharge duration	$\simeq$ 45 ms
Plasma density at r=0	$\simeq 5{\times}10^{18}$ m^{-3}
Electron temperature at r=0	$\simeq$ 120 eV
Energy confinement time	$\simeq$ 0.8 ms
Safety factor q(0)	$\simeq$ 1
Safety factor q(a)	$\simeq$ 5-8

of this computer architecture can be found from [39]. In the rest of this section its briefly described the main characteristics of the subsystems at ISTTOK. It is also mentioned their main advantages for the data acquisition in this experiment.

The installation of an ATCA subsystem is more recent at ISTTOK, and its boards were developed by members of IPFN (Instituto de Plasmas e Fusão Nuclear, at IST), in order to now allow sampling rates of 2 MSamples s^{-1}. The ATCA subsystem is the one used in the acquisitions of the edge/SOL fluctuations at ISTTOK. The main characteristics of the ATCA subsystem are as follows,

- The input is an analog to digital converter (ADC) modules, responsible for acquiring the raw data.
- The output consists of digital to analog converters (DACs).
- Can communicate with the computer via Peripheral Component Interconnect express (PCIe).
- Saves the data in the computer memory (Random-Access Memory, RAM) over direct memory access (DMA).

Each ATCA board operates with 32 ADC modules and 10 DACs. ISTTOK is equipped with six boards, equally divided for data acquisition and control. For the three DAQ boards, the ADC modules acquire the raw data and store it in the inboard RAM during discharges.

Table 3.2 Names of the diagnostics channels used during this thesis to access data from the SDAS server. Its is also listed the quantities measured using this channels.

Diagnostics channel	Abbreviation	Measurement
PCIE_ATCA_ADC_16.BOARD_1.CHANNEL_011	ch 11	I_{sat}^{+} [mA]
PCIE_ATCA_ADC_16.BOARD_1.CHANNEL_012	ch 12	I_{sat}^{+} [mA]
PCIE_ATCA_ADC_16.BOARD_1.CHANNEL_013	ch 13	V_f [V]
PCIE_ATCA_ADC_16.BOARD_1.CHANNEL_014	ch 14	V_f [V]
PCIE_ATCA_ADC_16.BOARD_1.CHANNEL_015	ch 15	V_f [V]
MARTE_NODE_IVO3.DataCollection.Channel_081	ch 81	Plasma position R [mm]
MARTE_NODE_IVO3.DataCollection.Channel_082	ch 82	plasma position Z [mm]
MARTE_NODE_IVO3.DataCollection.Channel_095	ch 95	V_{Loop} [V]
MARTE_NODE_IVO3.DataCollection.Channel_100	ch 100	Plasma current (I_p) [kA]
POST.PROCESSED.DENSITY	ch density	Density (n) [m^{-3}]

Later an appropriate software is responsible for reading the data and saving it in the ISTTOK database.

On the other hand, a real time control system is implemented using the three control boards. These boards acquire raw data from the ADC modules, to then be implemented in the real time control system running at ISTTOK, [2, 39]. The control boards are strictly used for diagnosis of quantities which are useful in the real-time control of the plasma, as for example the plasma position from the Mirnov Coils diagnostics.

The ISTTOK's digitized data for each shot can be remotely accessed using the Shared Data Access System (SDAS) server. This server takes as some of the inputs a shot number and the specific diagnostics channel. The names of the channels used during this thesis to access data from the SDAS server are enumerated on 3.2, along with the quantities measured by each channel.

3.1.3 Set of discharges

The current investigation on edge turbulence at ISTTOK was achieved through the time recording of different plasma quantities with Langmuir probes. The results are presented as a function of different plasma current values, and also for different pressure values. Simulta-

neously, throughout the entire analysis the measurements are interpreted as a function of the alternated current regimes that ISTTOK operates on.

An initial study was carried as a function of the plasma current (shot lists A and B). During which measurements were taken at different radial positions across the ISTTOK boundary plasma, from $r = 70$ mm to $r = 105$ mm. For the discharges on shot list A the plasma current was set as $I_p = 4$ kA, while for the ones enumerated on shot list B we had $I_p = 4.7$ kA. The value of the plasma current used during these discharges, along with the radial positions of the probe is according to the what is shown on Fig. 3.4. For shot list B measurements were taken around radial positions as close as possible to the ones used in shot list A, using the same discharge parameters except for the value of plasma current.

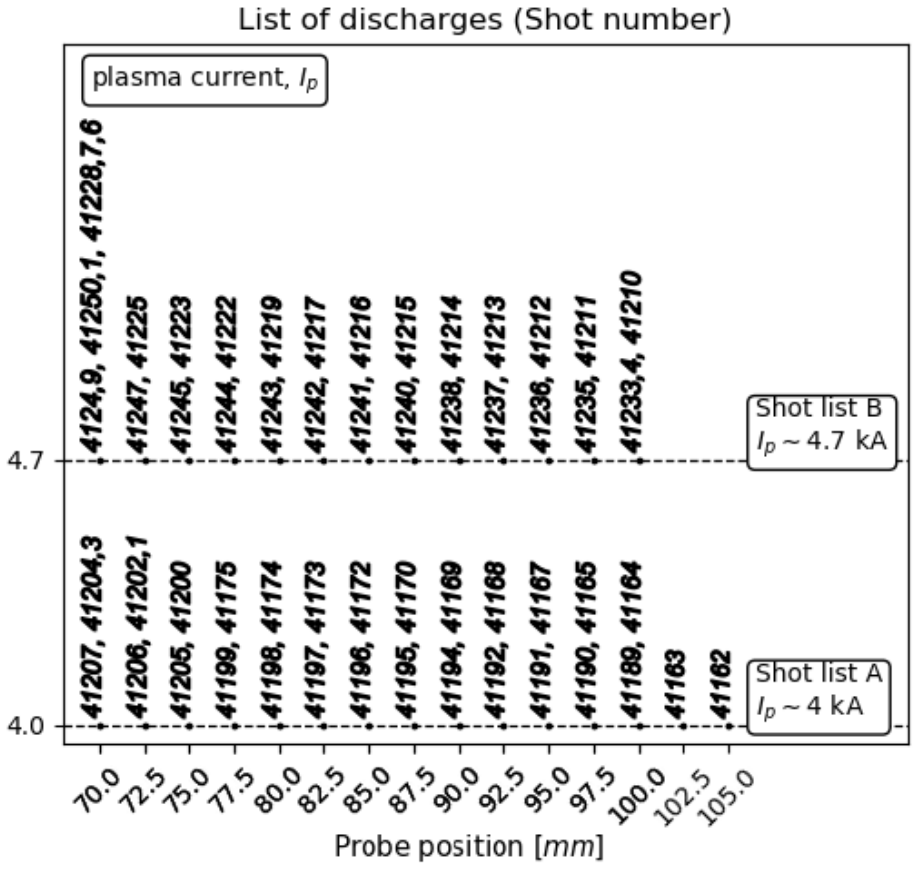

Figure 3.4 Shot lists for the initial study of the intermittent fluctuations carried at the ISTTOK tokamak. Analysis for two different plasma current values, $I_{p_A} = 4$ kA (shot list A) and $I_{p_B} = 4.7$ kA (shot list B). Measurements were taken at different radial positions across the ISTTOK boundary plasma, from $r = 70$ mm to $r = 105$ mm.

An experimental investigation was also carried on the electrostatic fluctuations as a function of the work pressure, as shown for the list of discharges on Fig. 3.5.

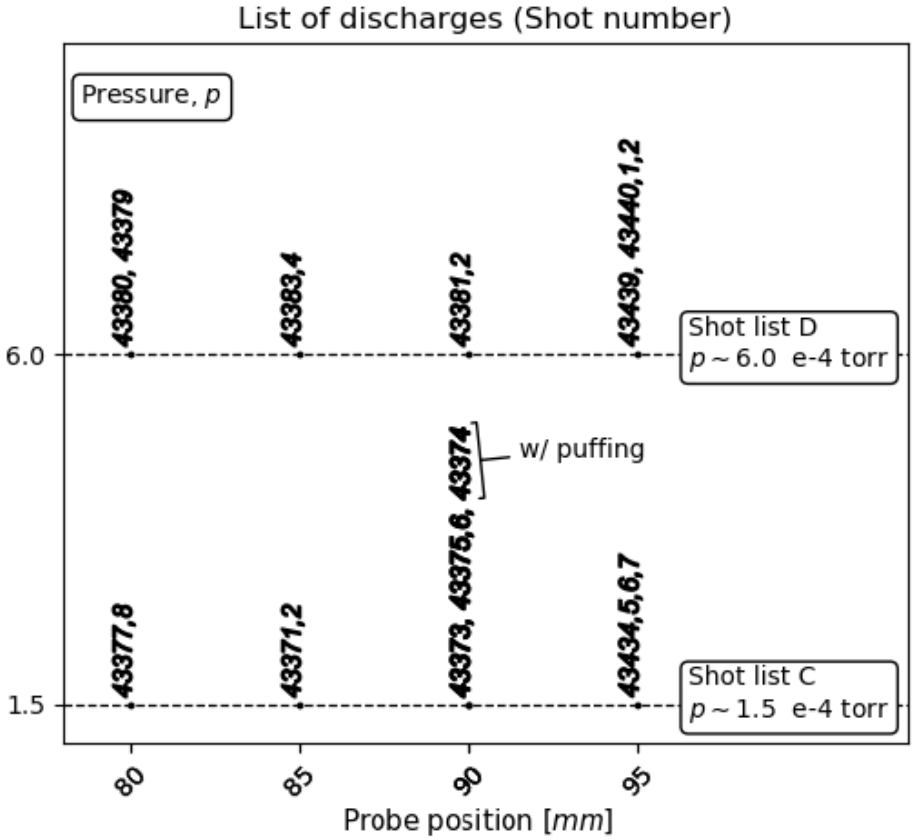

Figure 3.5 Shot lists for a second study of the intermittent fluctuations carried at the ISTTOK tokamak (shot list C and shot list D). Analysis for different pressure values and gas injection regimes. Measurements were taken at different radial positions across the ISTTOK boundary plasma, from $r = 80$ mm to $r = 95$ mm, with $B_\phi \simeq 0.5$ T $I_{p_{C,D}} \sim 4$ kA.

The investigations carried on the next sections will take a special attention on the operation of ISTTOK as a function of the multi-cycle alternating plasma current regimes. With this mode of operation, discharges of ~ 1 s have been previously obtained at ISTTOK, having 20 full AC plasma current cycles, [39, 40].

For the discharges analyzed on lists A and B a total of six alternating cycles (positive or negative current) allowed to obtain coherent 160 ms discharges, with individual cycles having flat top regimes of ~ 20 ms. On Fig. 3.6 an example is shown of the plasma current signal

during a full discharge on ISTTOK lasting ~ 160 ms.

For all discharges (on the lists A, B, C and D) the toroidal magnetic field was set as $B_\phi \simeq 0.5$ T. Usual discharges on ISTTOK are characterized by density values of $n = (0.5 - 1) \times 10^{18} m^{-3}$ around the limiter radius. Fig. 3.6 shows the average density along the probing path of the microwave interferometer, (of about $n = 4.5 \times 10^{18} m^{-3}$) which is much higher than the density value at the edge (near the limiter). The example is for a discharge belonging to list A. The example on Fig. 3.6 also sets a coherent picture for the density, plasma current and V_{loop} values across the AC regimes during the discharges on the lists A, B, C and D. Finally, on Fig. 3.7 one can see the consistent evolution of the plasma position in-between positive and negative cycles.

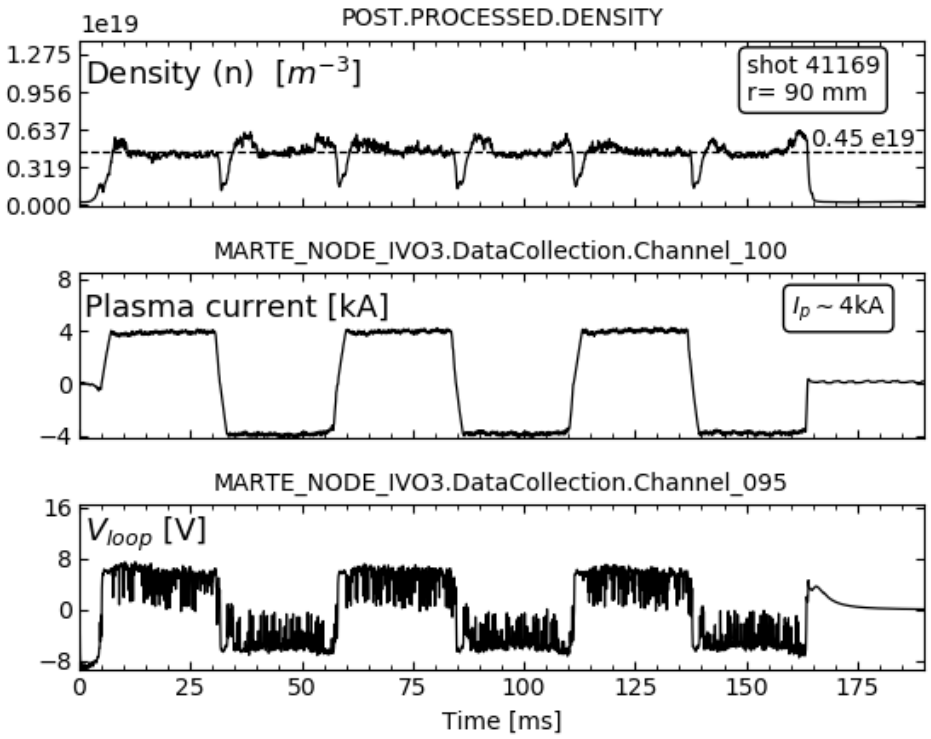

Figure 3.6 Time recordings of the density, plasma current and V_{loop} signals during a full discharge on tokamak ISTTOK (shot 41169, at $r = 90$ mm). A total of six alternating current cycles allowed to obtain coherent discharges (of ~ 160 ms), with individual cycles having flat top regimes of ~ 20 ms.

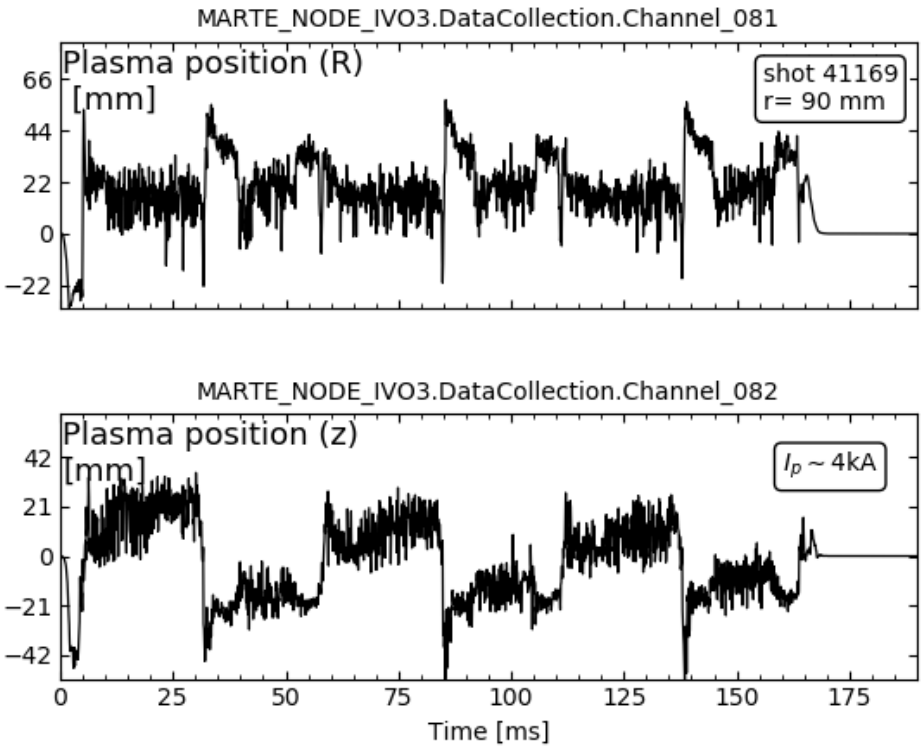

Figure 3.7 Time recordings of the plasma position during a full discharge on tokamak ISTTOK (for the discharge shown in Fig. 3.6). A total of six alternating current cycles allowed to obtain coherent discharges (of ~ 160 ms), with individual cycles having flat top regimes of ~ 20 ms.

3.2 Measurement technique

3.2.1 Diagnosis of the plasma edge by Langmuir probes

Langmuir probes (LPs) are usually cylindrical pin electrodes that are polarized by an external circuit and inserted into the plasma, as in the scheme illustrated in Fig. 3.9. Langmuir probes have been commonly used to study low temperature plasmas ($T_e \lesssim 100$ eV), and remain a widely used diagnostic in fusion devices. The disadvantages of this diagnostic come mainly from a substantial plasma perturbation from probe insertion, and the fact that probe theory is still a subject in need of development. Despite these obstacles LPs have been a highly used diagnostic to help to understand the fluctuations and the associated particle transport in the periphery. They make part of a broad list of diagnostics that provide complementary and most often coherent results of the plasma quantities.

In characterizing SOL fluctuations, LPs offer easy access to the edge plasma, up to a few cen-

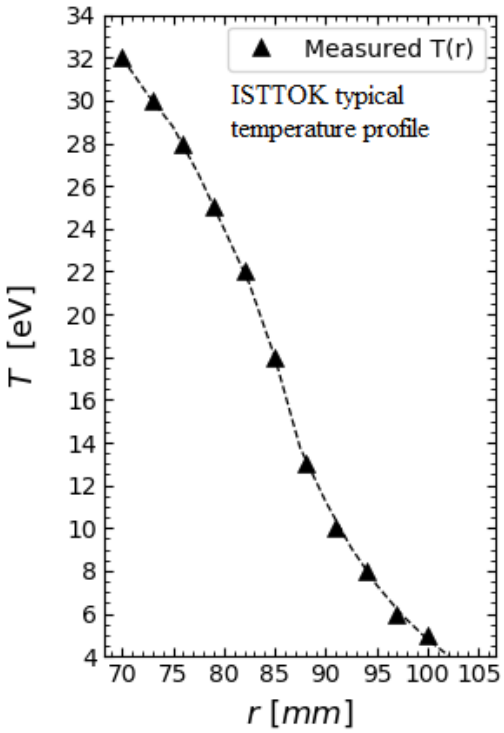

Figure 3.8 Radial profile for the electronic temperature, T_e, on the ISTTOK tokamak. Previous measurements for established radial positions (black triangles), along with an exponential interpolation for the remaining edge/SOL locations in study on chapter 4.

timeters inside the LCFS. In addition, this diagnostic presents high spatial and time resolutions, capable of resolving the fast edge/SOL fluctuations of quantities such as the fluctuating plasma density $\tilde{n}$ and potential $\tilde{V_p}$.

As described previously, plasma turbulence is characterized by structures with a fine spatial variation (in the order of few millimeters) and a fast temporal variation (a few microseconds). The characterization of turbulence is therefore very demanding for plasma diagnostics. Langmuir probes can have dimensions in the millimeter scale and permit the construction of probe arrays, being therefore ideal to resolve the turbulence complex structure. When operated in I_{sat}^{+} or V_f mode, the time resolution of the LPs is typically only limited by the resolution of the data acquisition system, that on ISTTOK is below the microsecond.

The obtained fluctuating parameters allow to determine the statistical characterization of the blobs in the SOL and calculate the induced radial particle transport. Among other possible information obtained from this diagnostic, one can also determine the spatial and temporal

structures of the blobs, followed by an understanding of their propagation in the SOL plasma.

3.2.2 Langmuir Probe Theory

An electrostatic sheath (Debye sheath) is formed in front of any material surface in contact with the plasma, such as the inserted probes. From the knowledge of the physical mechanisms taking place on the sheath region plasma parameters such as temperature and density can be determined.

In front of any plasma facing component it's observable a potential drop, starting from the plasma bulk and decreasing towards the surface, in the sheath region. As the lighter electrons move faster towards the surface of PFCs, leaving the ions behind, the material surface is left with a negative potential relative to the bulk plasma, a floating potential, V_f. In a region called the pre-sheath it is established a small electric field in order to balance the flux of electrons and ions into the sheath region, and restoring in the plasma bulk the quasi-neutrality condition ($n_e \simeq n_i$).
The formation of the sheath region is what allows the plasma to coexist with the floating surface. It is the transitional area from the floating surface to the unperturbed plasma in which the quasi-neutrality condition holds again. Meanwhile in the sheath $n_i > n_e$. The potential drop through the region adjusts in a way to equalize the lost of ions and electrons from the bulk plasma. The sheath has usual thickness of $\sim 10\lambda_D$.
A density decrease in the sheath implies that in order to maintain stability the fluid velocity must increase towards the material surface. In this case the gain in dynamic pressure due to the fluid momentum contrasts the loss in static pressure, which is proportional to n. The Bohm criteria states that the fluid velocity entering the sheath must reach the minimum value of the ion sound speed c_s,

$$c_s = \sqrt{\frac{k_\beta(T_e + T_i)}{m_i}}. \tag{3.1}$$

When a probe is inserted in the plasma, the resultant mechanism is in the same general way as described for the formation of the sheath and pre-sheath regions. The faster electrons move out of the plasma-probe interface towards the surface of the probe. If the inserted probe is not biased, its surface gets charged at the floating potential. The floating potential is given according to the electron temperature, T_e, and plasma potential, V_p, as follows

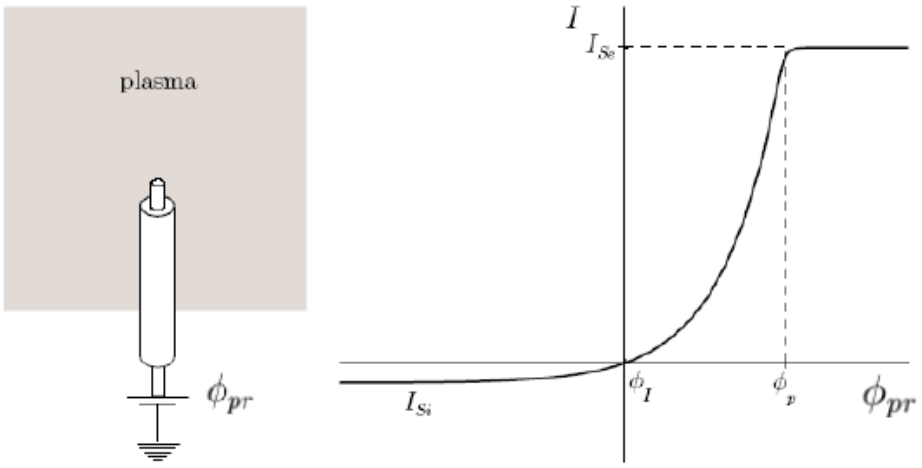

Figure 3.9 On the left its shown an illustrative scheme of the diagnosis of the plasma with Langmuir probes. Usually a cylindrical pin electrode that is polarized by an external circuit, and then inserted in the plasma. On the right, presented the characteristic I-V curve between the collected current by the probe, I_{pr}, and the potential applied to it, V_{pr}. From which it is possible to determine local plasma quantities, such as the electron temperature, T_e, electron density, $n_e \simeq n$, and plasma potential, V_p.

$$V_f \approx V_p - 3K_\beta T_e. \tag{3.2}$$

One the other hand, the probe can be biased by an external potential, V_{pr}. In this way the the current flow into the sheath region allows to obtain a characteristic I-V curve. The current is given as a function of the voltage drop across the sheath, and subsequently, as a function of the potential applied to the probe, V_{pr}. However in some cases the perturbations to the plasma by the inserted probe can be more significant and, simultaneously, very hard to estimate.

From the characteristic I-V curve between the collected current by the probe, I_{pr}, and the potential applied to it, V_{pr}, it is possible to determine local quantities such as the electron temperature T_e, electron density $n_e \simeq n$, and plasma potential V_p. The characteristic I-V curve is distinguished by three intervals corresponding to the regions of electron saturation, transition and ion saturation, Fig. 3.9.

In the presence of magnetic fields difficulties arise in the analysis of the electronic part of the I-V characteristic, due to a distortion of this region as a result of the influence of the magnetic field on the lighter electrons. The common procedure is to use measures in the transition and ion saturation regions, where the probe current as a function of the applied potential is approximately obtained through (3.3),

$$I(V_{pr}) = I_{sat}^{+} \cdot \left(1 - e^{\frac{V_{pr}-V_f}{k_\beta T_e}}\right). \tag{3.3}$$

Probe I-V characteristic

In general a three parameter fit is then applied to the experimental probe characteristics in this regime, according to (3.3), in order to determine the local values of T_e, I_{sat}^{+} and V_f.

In the ion saturation regime, the collected current takes the value of I_{sat}^{+} when the probe is biased to a large enough negative potential. In this regime the electrons are completely repelled and the restricted ion flux to the probe sheath becomes independent of the applied potential, resulting in the constant I_{sat}^{+} given by

$$I_{sat}^{+} = j_{sat}^{+} A_{pr} = \frac{e n_e c_s A_{pr}}{2} \tag{3.4}$$

, where A_{pr} is the effective probe area, and j_{sat}^{+} the ion current density, given by the parameters at the sheath edge. The usual consideration of isothermal plasmas $T_e = T_i$ is taken. The expressions on (3.4) and (3.1) allow to determined the local value of the electron density through the previous determine values of I_{sat}^{+} and T_e. Finally, the plasma potential is determined according to the approximation in (3.2), using the estimations on V_f and T_e.

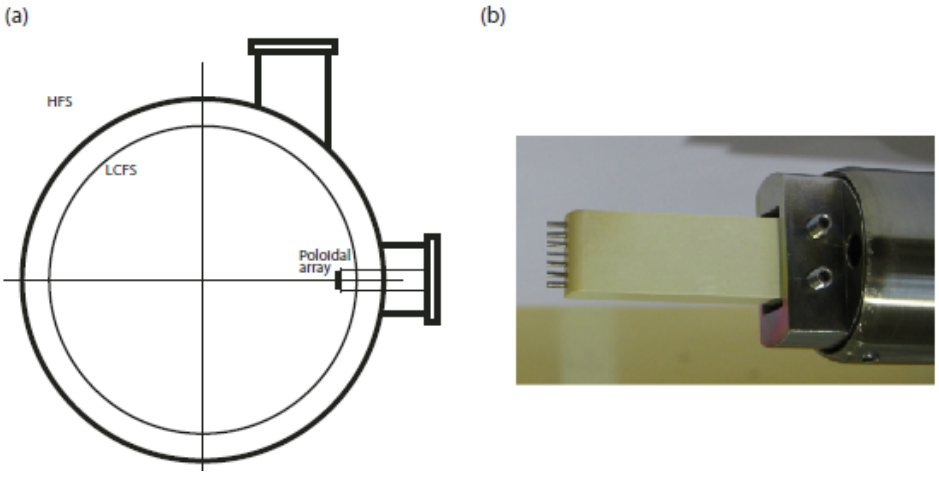

Figure 3.10 (a) Scheme of the insertion of the poloidal array of Langmuir probes on ISTTOK. Trough a port that allows to diagnose the edge plasma with the possibility to radially shift the probe systems from shot to shot by means of a drive mechanism. (b) Photograph of the probe system. Consisting of a 7-pin poloidal array of probes, sequentially separate by 2 mm. Probes with 0.75 mm of diameter and 2 mm of length.

3.2.3 Approximations

During this work the plasma density and potential fluctuations were estimated neglecting the influence of the temperature fluctuations, which are difficult to resolve. The two quantities were determined from the fluctuating ion saturation current and floating potential, respectively. From the measurements of ion saturation current, where $I_{sat}^{+} \propto n\sqrt{2T}$ (3.1 and 3.4), it is made the assumption for the fluctuations of density that $\tilde{n} \approx \tilde{I}_{sat}^{+}$. Similarly, from the floating potential recordings, where $V_f \approx V_p - 3K_\beta T_e$ (3.2), it is considered $\tilde{V}_p \approx \tilde{V}_f$. In addition, the poloidal electric field fluctuations are estimated from two floating potential measurements. Here we have $\tilde{E}_\theta \approx (\tilde{V}_{f_1} - \tilde{V}_{f_2})/d$.

The simultaneous analysis of the fluctuations of plasma potential and density allow to determine the radial transport induced by the cross-field fluctuations. This quantity is estimated according to 2.1, $\bar{\Gamma}_r =< \tilde{n}(t) \cdot \tilde{\vec{v}}_r(t) >=< \tilde{n}(t) \cdot \tilde{E}_\theta(t) > /B$. Note that $\tilde{\vec{v}}_r$ corresponds to the $\vec{E} \times \vec{B}$ radial drift fluctuations.

Good estimations are obtained for the fluctuations of the ion saturation current, despite neglecting the temperature fluctuations. However, a more severe error is introduce on the plasma potential fluctuations when neglecting the temperature fluctuations, [41].

3.2.4 Poloidal probe array

On the tokamak ISTTOK experiment the two ports schemed on Fig. 3.10 allow to diagnose the edge plasma through the use of multiple-Langmuir probe systems. With the possibility to radially shift the probe systems from shot to shot by means of a drive mechanism. The drive mechanism provides access to a larger range of radial locations in-between shots. Furthermore, the use of multi-pin array systems grants simultaneous measurements of close (few millimeters apart) plasma positions, either radially or poloidally shifted.
The Langmuir probe system used during this study is also shown on Fig. 3.10. It consists of a 7-pin poloidal array of Langmuir probes. The probes are sequentially separate by 2 mm, and have 0.75 mm of diameter and 2 mm of length. The poloidal array was installed in the tokamak equatorial port, as schemed on Fig. 3.10.

The array operated in a simultaneous mixed mode of pins recording floating potential and ion saturation current. The measurements of floating potential were taken by the three most inner pins (sequentially 2 mm apart), while two outer pins (8 mm apart) were set to measure

the ion saturation current, as shown in Fig. 3.11.

The inner pins of the probe array were not biased, in order to measure the floating potential. On the other hand, the pins programmed to measure the ion saturation current were biased by a constant potential of −180 V with respect to the vessel. This negative potential is chosen in order to guarantee that the current to the probe equals I_{sat}^{+}, see Fig. 3.9.

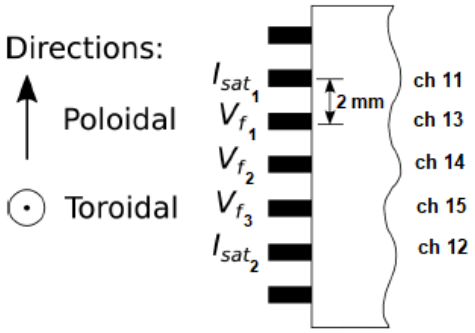

Figure 3.11 Scheme of the poloidal probe array operations mode. The channels from table 3.2 are also identified.

3.3 Signal analysis

A characterization of the induced plasma fluctuations and turbulent transport in the edge of ISTTOK is shown on chapter 4 using the different analysis methods explained on this section.

3.3.1 Determination of the plasma fluctuations

Fluctuations in the different quantities are estimated by subtracting to the signals its average value. Directly acquired Langmuir probe signals $y(t)$ are first filtered with a Moving Average smoothing technique. The smooth result of $y(t)$ is determined for samples of N data points, a sliding average $\bar{y}_N(t)$. Typically N is chosen so that the averages are calculated in a time scale of 1 ms, which is larger than the time scales of interest.

On Fig. 3.12 it's shown an example of the Moving Average smoothing result for a standard I_{sat}^{+} signal from ISTTOK with N=1000.

The determined fluctuations $\tilde{y}(t) = y(t) - \bar{y}_N(t)$ have important and distinctive characteris-

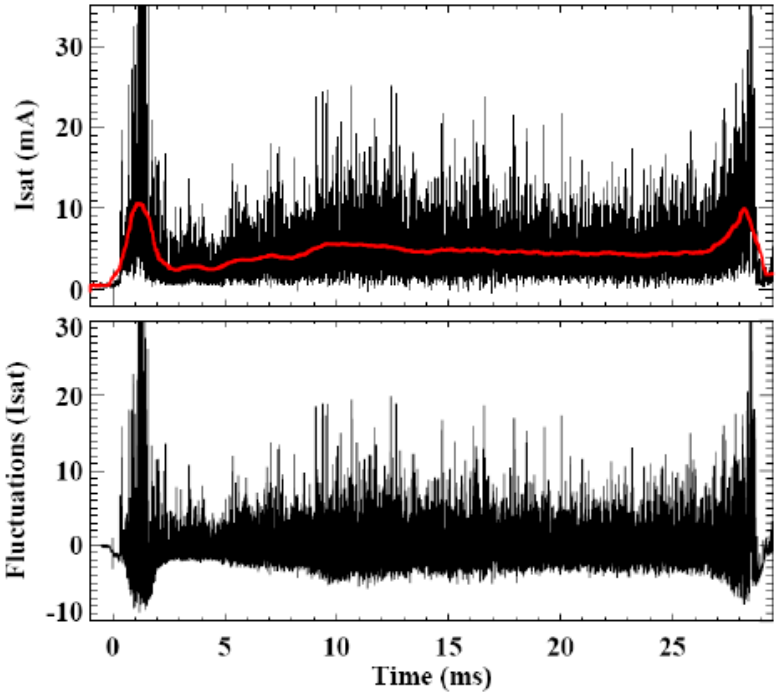

Figure 3.12 Example of the determination of the I_{sat}^{+} fluctuations. Moving Average smoothing result for a standard I_{sat}^{+} signal from ISTTOK with N=1000. The smoothed trend for a time scale of ~ 1 ms is shown in red. [Figure from [17]].

tics resulting from the intermittent structures propagating through the plasma.

3.3.2 Statistics

The probability density function (PDF) of the temporal evolution of the ion saturation current and floating potential were computed. Along with quantities such as the standard deviation (σ_y), fluctuation level (relative level of the fluctuations, $\sigma_y/\bar{y}$), and third and fourth central moments used, respectively, to define the skewness and kurtosis.

The skewness gives a measure of the distribution's asymmetry and should be zero for a normal distribution (and near zero for any symmetric data set), while negative for a left skewed distribution, and positive for a right skewed distribution. For a left skewed distribution a longer left tail is shown while the bulk of the distribution in concentrated on the right, and, inversely, for a right skewed distribution a longer tail is observed on the right while the bulk of the distribution is concentrated on the left.

The Fisher-Pearson coefficient of skewness, (3.5), gives the common definition of the quantity for an univariate data set, such as the time signals in analysis throughout this work. On (3.5), $\bar{y}$

corresponds to the mean value of the data set, σ_y to the standard deviation given here by (3.6), and, finally, N to the number of points in the data.

$$skewness = \frac{1}{N}\sum_{j=1}^{N}\frac{(y_j - \bar{y})^3}{\sigma_y^3}, \tag{3.5}$$

$$\sigma_y^2 = \frac{1}{N}\sum_{j=1}^{N}(y_j - \mu)^2. \tag{3.6}$$

The Kurtosis, determined through the fourth central momentum of the distribution, measures the weight of the outliers (i.e. the weight of the distribution's tail) relative to a normal distribution. For the adjusted version of Pearson's definition for kurtosis, the excess kurtosis on (3.7), the constant 3 is subtracted from the general result to give a zero value of kurtosis for a normal distribution. Moreover, according to (3.7) positive kurtosis indicates a "heavy tailed" distribution and negative kurtosis indicates a "light tailed" distribution, meaning that the distribution produces fewer and less extreme outliers relative to the standard normal distribution.

$$excess\ kurtosis = \frac{1}{N}\sum_{j=1}^{N}\frac{(y_j - \bar{y})^4}{\sigma_y^4} - 3. \tag{3.7}$$

3.3.3 Cross Correlation

The cross correlation between two signals measures the similarity of the two as a function of the time shift (time lag) among them. The general definition for the cross correlation between two continuous functions is determined according to the sliding inner product between the two,

$$(f \star g)(\tau) = \int_{-\infty}^{+\infty} f^*(t)g(t+\tau)dt, \tag{3.8}$$

where $f^*(t)$ corresponds to the complex conjugate function of $f(t)$, and τ to the time lag between the two. A maximum value is obtained when the functions have a similar and synchronous pattern, and contrarily, a minimum when functions have a similar but out-of-phase pattern.
From (3.8), follows for discrete data series the expression on (3.9), where n is the lag between

the discrete data indexes.

$$(f \star g)[n] = \sum_{k=-\infty}^{+\infty} f^*[k]g[k+n]. \tag{3.9}$$

An analysis of the time delay between measurements taken in different locations can be used to determine the velocity of propagation of coherent components (structures) in the signals. The velocity of propagation is simply the ratio between the distance among the locations and the time delay. On Fig. 3.13 it's shown a scheme exemplifying the time delay analysis for two sensors poloidally shifted. The distance between the two sensors acquiring $f[n]$ and $g[n]$ divided by the time delay between $f[n]$ and $g[n]$ corresponds to the velocity of propagation of the similar feature (or features) belonging to both $f[n]$ and $g[n]$.

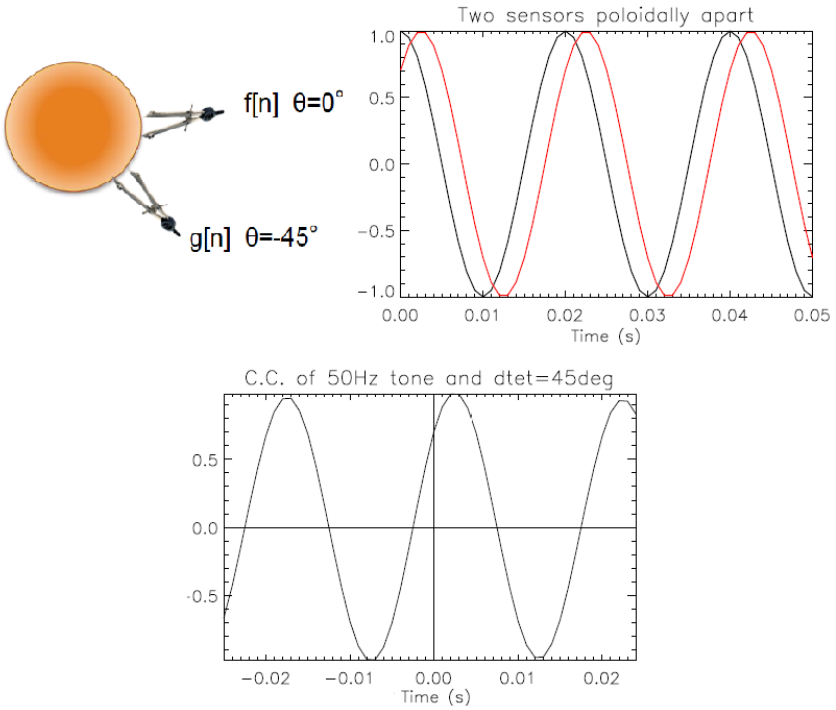

Figure 3.13 Time delay analysis. Example scheme of the correlation for two signals taken in poloidally shifted positions. [Adapted figure from [17]].

In Fig. 3.14 is shown an example of the cross correlation between V_f signals measured at ISTTOK. The measurements were simultaneously acquired according to the probe-system configuration on Fig. 3.14. The cross correlations between the poloidally shifted ($\Delta\phi \sim 2$mm) probe measurements should be fairly independent from the approximately constant background

plasma conditions (removed smoothed result), and considerably affected by the propagation of the intermittent turbulence structures in the plasma.

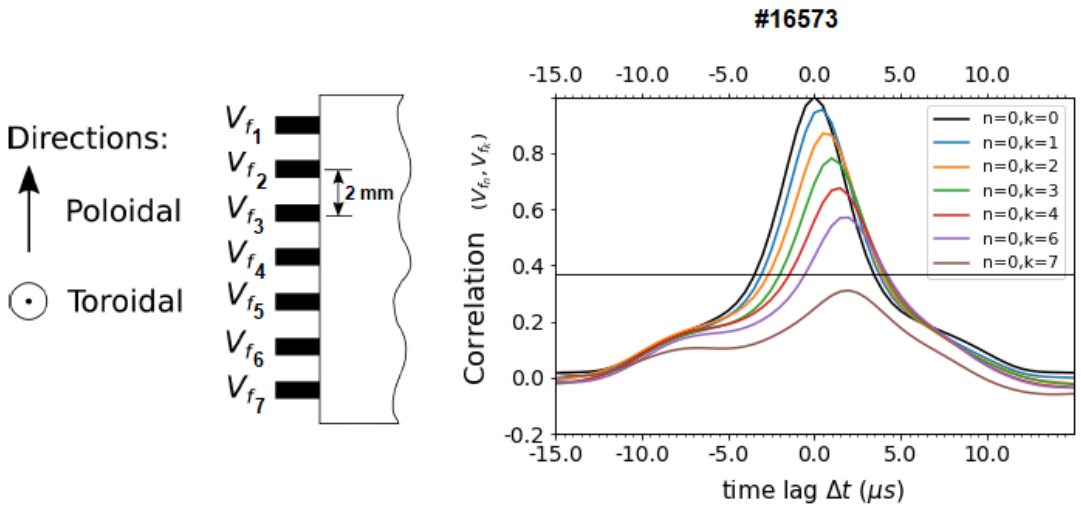

Figure 3.14 Scheme a probe system configuration used to previously measure V_f signals. Correlation between the signals acquired by the 7 poloidally shifted probes.

Chapter 4

Experimental results

4.1 Introduction

The results discussed in this chapter follow from several measurements of ion saturation current and floating potential, taken at different radial locations in the edge and SOL of the ISTTOK tokamak. As explained in the previous chapter 3, time signals of the two quantities were recorded with a multi-pin Langmuir probe system (poloidal array, 3.2.4). The probe system was set to record on channels 11 and 12 I_{sat}^{+}, and on channels 13, 14 and 15 V_f. The pins in I_{sat}^{+} mode were biased at constant potential (-180 V), in order to be in the ion saturation current regime through the entire acquisition time. On the other hand, the pins in V_f mode were unbiased, allowing their surfaces to be at the floating potential. In this way all pins in I_{sat}^{+} or V_f mode could continuously measure one of the specific quantities. The time resolution of the measurements is only limited by the sampling frequency of the acquisition system. In this case of 2 MHz for the ATCA system at ISTTOK.
The measurements during the discharges on shot lists A, B, C and D (Figs. 3.4 and 3.5) were after accessed through the SDAS server.

The definitions below,

$$I_{sat}^{+} = j_{sat}^{+} A_{pr} = \frac{e n_e c_s A_{pr}}{2}, \tag{4.1}$$

$$c_s = \sqrt{\frac{k_\beta(T_e + T_i)}{m_i}}, \tag{4.2}$$

$$V_p \approx V_f + 3K_\beta T_e. \tag{4.3}$$

, which were previously discussed on chapter 3, depend on several estimations. In particular the 1/2 factor on (4.1). In this sense different expressions of the aforementioned quantities may be seen through the bibliography. Nevertheless, we want to point for now that $I_{sat}^{+} \propto n\sqrt{T_e}$ (4.1 and 4.2), and that $V_f \approx V_p - 3K_\beta T_e$ (4.3).

Fig. 4.1 shows samples of measured signals (during the flat top of the first cycle of alternating current regimes) for I_{sat}^{+} and V_f. Both signals were probed at r=80 mm.

In the remaining of this chapter it's presented the average radial profiles of I_{sat}^{+}, V_f and V_p on 4.2. On 4.3 an initial characterization of the fluctuations, followed by a frequency resolved analysis on 4.4. Finally, on sections 4.5 and 4.6 it's computed the fluctuations poloidal velocity and the induced particle flux, respectively. For every discharge (radial location), an individual study of the previous subjects was done in six individual alternating current cycles (positive or negative I_p). This analysis builds on previous works on ISTTOK where the boundary plasma was characterized [2–5], with a significantly extended analysis performed in this thesis.

4.2 Average profiles

This section presents the radial profiles of I_{sat}^{+}, V_f and V_p (mean values) at the edge/SOL of ISTTOK. The radial profiles are computed with measurements taken during different discharges, in-between each the probe system is radially displaced by a driving mechanism.
The profiles were determined first from the discharges characterized on Fig. 3.4 (shot lists A and B) and secondly for the ones in Fig. 3.5 (shot lists C and D). The first figure referring to two shot lists in which the dependency on the plasma current value was studied. While the second referred to discharges for which the dependency on the neutral density and gas puffing conditions was observed.

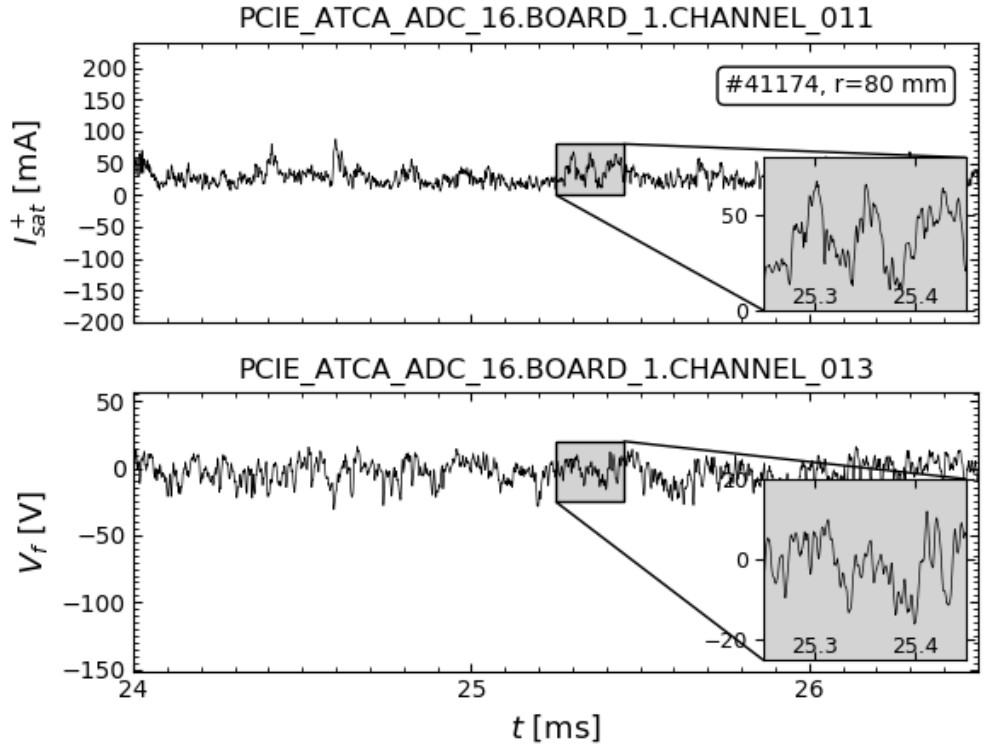

Figure 4.1 Langmuir Probe time recordings of the ion saturation current and floating potential, at the edge of the ISTTOK tokamak (r = 80 mm), for #41174. The time series were obtained with the sampling rate of 2 MHz. It is shown the overall intermittent character of the edge fluctuations in the ISTTOK tokamak, and an enlargement on the burst-events temporal structures.

On Figs. 4.2, 4.3, 4.4 are computed the I_{sat}^{+}, V_f and Vp radial profiles for discharges with $I_p = 4$ kA (shot list A) and $I_p = 4.7$ kA (shot list B). The plasma potential is determined from the definition on 4.3, using the floating potential profile on Fig. 4.3 and ISTTOK's temperature profile on Fig. 3.8 (previously obtained).

Tokamak plasmas tend to be hot and dense in the core with values decreasing towards the walls. In the SOL the plasma temperature and density profiles are expected to decrease exponentially mainly due to the strong parallel losses to the limiter, if assuming a simple SOL model. One can see from the I_{sat}^{+} radial profile on Fig. 4.2 that in the SOL ($r \geq r_L = 85$ mm) I_{sat}^{+} decreases with radius. However an exponential decay may no apply to the entire SOL region. An exponential fit to the data from shot list A (where $I_p = 4$ kA), can be seen in the figure along with the determined radial decay constants, τ. There is a fair agreement with an expo-

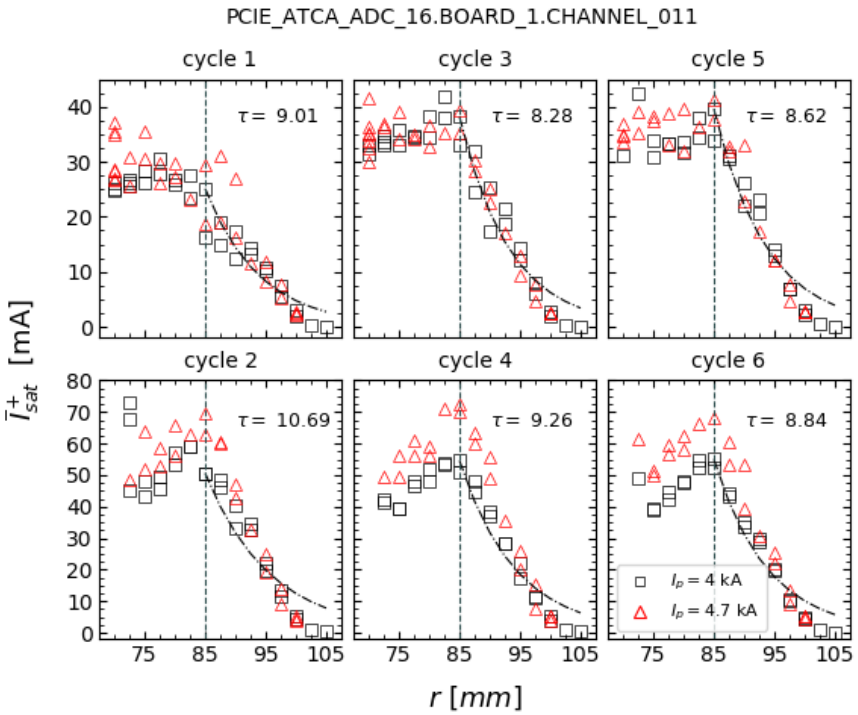

Figure 4.2 Radial profile of the ion saturation current (mean values), taken with Langmuir probe recordings at the edge and SOL of the ISTTOK tokamak. The radial measurements represent the mean values for probe samples of about $\sim 3-5$ ms, with the sampling rate of 2 MHz. The results from shot list A (black squares) were taken for $I_p = 4$ kA, while the results from shot list B (red triangles) with $I_p = 4.7$ kA, Fig. 3.4. The remaining device/plasma parameters were kept for all discharges.

nential decay of I^+_{sat} while $r \lesssim 100$ mm. From this position outwards I^+_{sat} decreases much faster, which is understandable given that it's the location of the wall. The exponential decay length determined, $0.9 \lesssim \lambda \lesssim 1.2$ cm, is according to what is expected for the SOL length at ISTTOK.

The plasma potential has a maximum just before the limiter, as seen on Fig. 4.4. For positive cycles it is observed $V_{p_{max}} \sim 80$ V around r=75 mm, and for negative cycles $V_{p_{max}} \sim 43$ V near r=80 mm. During positive plasma current cycles it is observed a near linear decrease towards both the confined and the SOL regions. The inversion of the slop of V_p corresponds to the change in the sign of the radial electric field E_r. From the plot in Fig. 4.4 the magnitude of E_r seems to be similar in the confined region and in the SOL, and in the order of 2.5 kV/m. For negative plasma cycles the plasma potential maximum is slightly lower and all probing positions have the same sign for E_r in Fig. 4.4. For negative cycles one sees only a decrease from the maximum towards the SOL. The profile of V_p was determined with previous radial temperature measurements of ISTTOK. The temperature was measured for positive cycles and

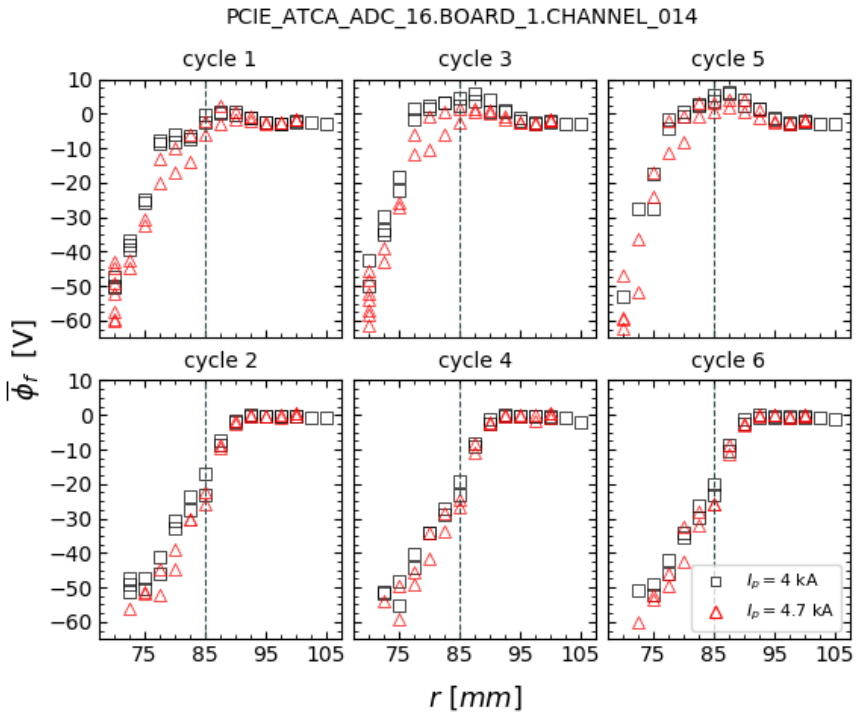

Figure 4.3 Radial profile of the floating potential (mean values), taken with Langmuir probe recordings at the edge and SOL of the ISTTOK tokamak. The radial profiles are computed in the same way as proceeded for the plots in Fig. 4.2. The results from shot list A (black squares) were taken for $I_p = 4$ kA, while the results from shot list B (red triangles) with $I_p = 4.7$ kA, Fig. 3.4.

therefore may not be suitable for the negative ones. The profile computed for positive cycles is very coherent with the inversion of the poloidal velocity of fluctuations.

On the other hand, the radial profiles of the floating potential are coherent to expected results on ISTTOK, [5], and independent of temperature estimations. The radial profile of the floating potential is typically observed to reach a maximum near the limiter's position, decreasing slowly towards the SOL and sharply towards the core plasma, as observed in Fig. 4.3. As expected from the changes in the radial plasma position, the V_f profiles for negative current cycles start to decay slightly further out than for positive cycles.

4.2.1 Alternating current regimes

In this subsection the aim is to consider the radial profiles computed on Figs. 4.2, 4.3 and 4.4 independently of the magnitude of I_p. In order to observe for the same shot list (A or B), in which the same plasma/device parameters are taken, the dependency on the plasma current regime (direction of I_p).

As illustrated in Fig. 3.7, the plasma position typically moves down by about 3 cm from positive to negative cycles, and radially slightly further out by ~ 5 mm. As will be seen, the measurements for negative current cycles have always a very systematic result among themselves, and for most parameters a very distinctive behavior is shown from positive current cycle measurements (also showing a very systematic behavior among themselves).

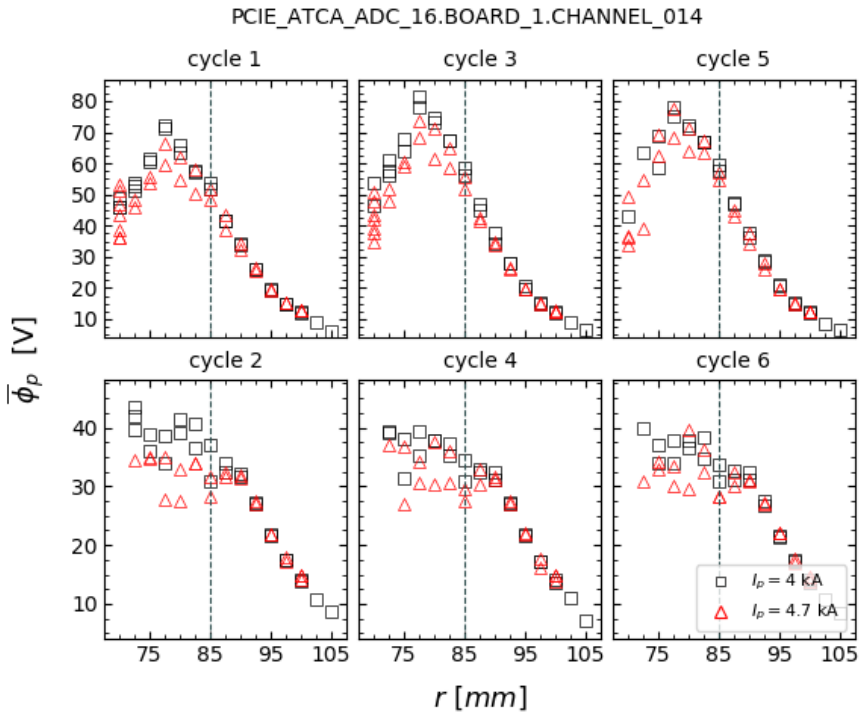

Figure 4.4 Radial profile of plasma potential. Computed from the measurements of the floating potential profile on Fig. 4.3 along with the temperature profile for typical ISTTOK discharges, on Fig. 3.8, according to 3.2.. The results from shot list A (black squares) were taken for $I_p = 4$ kA, while the results from shot list B (red triangles) with $I_p = 4.7$ kA, Fig. 3.4.

Individual analysis for every current regime of each discharge were determined taking time periods of ∼3-5 ms. The time periods were chosen in the discharges flat top in stationary phases, avoiding therefore transient periods. Since the data set of probe measurements used here includes a large number of discharges, the selected time intervals may vary from discharge to discharge. The intervals were carefully chosen for more steady plasma conditions. While corroborating general results of tokamak devices, the analysis throughout the AC cycles of ISTTOK gives an understanding of edge plasma physics on the operation of a tokamak in an alternating plasma current regime.

On Fig. 4.2, during both positive and negative cycles the ion saturation current mean value decreases as expected with radial position in the SOL ($r \gtrsim r_L$). However, the measurements taken also suggest a considerable decrease of the ion saturation current mean value ($\Delta I_{sat}^{+} \sim 30$ mA) for negative cycles, and a slight one for positive cycles ($\Delta I_{sat}^{+} \lesssim 20$ mA), for $r \lesssim r_L$, thus implying a decrease in density into the core (about 1.5 cm) of ISTTOK.
The local maximum exhibit on the radial profiles of density is not anticipated and contradicts the expected plasma losses towards the wall. This result may be explained by the large negative values of floating potential (-60 V) in the innermost positions, Fig. 4.3. As the floating potential takes these large negative values the applied voltage to the probes (-180 V) may not be large enough to completely repel the electrons and drive the probe current into the ion saturation mode. In this case the flux into the probe is not restrictive to ions, but instead results in a net of both ion and electron currents, and therefore for $r \lesssim r_L$ there is no guaranties that the probe current corresponds to a correct measurement of I_{sat}^{+}. It is observed an increase in the maximum value of I_{sat}^{+} between cycles having a positive current regime relative to cycles having a negative current regime ($\Delta I_{max} \sim 30$ mA). This is most probably due to the fact that the plasma position is further out in negative cycles than in positive ones, leading to larger density and temperatures values near the limiter's position ($r_L = 85$ mm). However the exponential decay in the SOL ($r \gtrsim r_L$) is identical for both positive and negative cycles, with exponential decay lengths of $0.9 \lesssim \lambda \lesssim 1.2$ cm.

Overall, the main cause of the differences observed in the averaged radial profiles on Figs. 4.2 to 4.4, across cycles having either positive or negative plasma current regimes, is due to the evolution of the plasma position. The radially outwards displacement of the plasma column during negative cycles is reflected on an increase of the plasma density further out.

4.2.2 Dependency on plasma current

Concerning the dependency on the plasma current (Figs. 4.2 and 4.4), during positive cycles no significant changes are seen for either I_{sat}^{+} and V_p between measurements taken with $I_p = 4$ kA or $I_p = 4.7$ kA. For negative cycles I_{sat}^{+} presents a small increase, and V_p a small decrease with plasma current. These differences may be justified by the fact that on ISTTOK only ohmic heating is available. Therefore as the plasma current is increased the heating power is also typically increased leading to larger temperatures, more ionization and higher densities.

4.2.3 Dependency on the neutral density

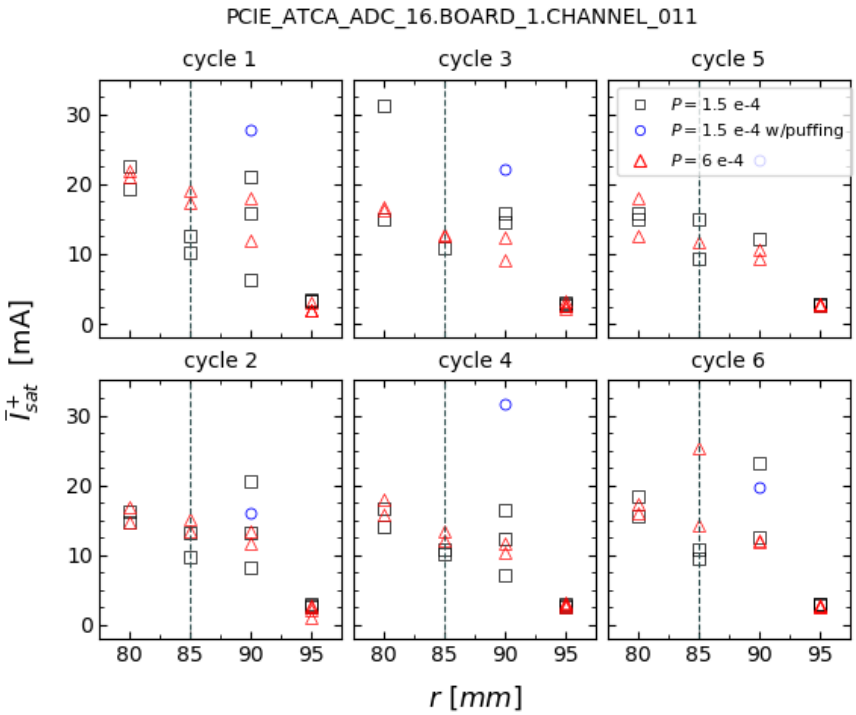

Figure 4.5 Radial profile of the ion saturation current (mean values) for shot lists C and D. The radial profiles are computed in the same way explained for Fig.4.2. The results from shot list C (black squares and blue circles) were taken for $p \sim 1.5e^{-4}$ torr, while the results from shot list D (red triangles) with $p \sim 6.0e^{-4}$ torr, Fig. 3.5.

Tokamaks are often characterized by having a large clearance between the plasma and the wall, achieved for instance by the shaping of the magnetic field surfaces. In the far SOL filaments propagate into a region where the background plasma density is very low but with a high neutral pressure. The interaction of the filaments with neutrals may lead to changes in the properties of the filaments. The plasma ionization source is partially defined by the neutral density. By changing the neutral pressure in the vacuum chamber the density of the neutrals in contact with the plasma can be modified. This is a new research topic with very little information available in the literature, stressing the relevance of this study.

The dependency on the neutral denstity at ISTTOK was studied trough the work pressure estabished during discharges. For shot list C was taken $p \sim 1.5 \times 10^{-4}$ torr, while for shot list D $p \sim 6.0 \times 10^{-4}$ torr, Fig. 3.5. The remaining device/plasma parameters were kept for all discharges. The data set on shot list C still includes a discharge with additional gas puffing injections. On Figs. 4.5 and 4.6 are shown the radial profiles of I^{+}_{sat} and V_f mean values for

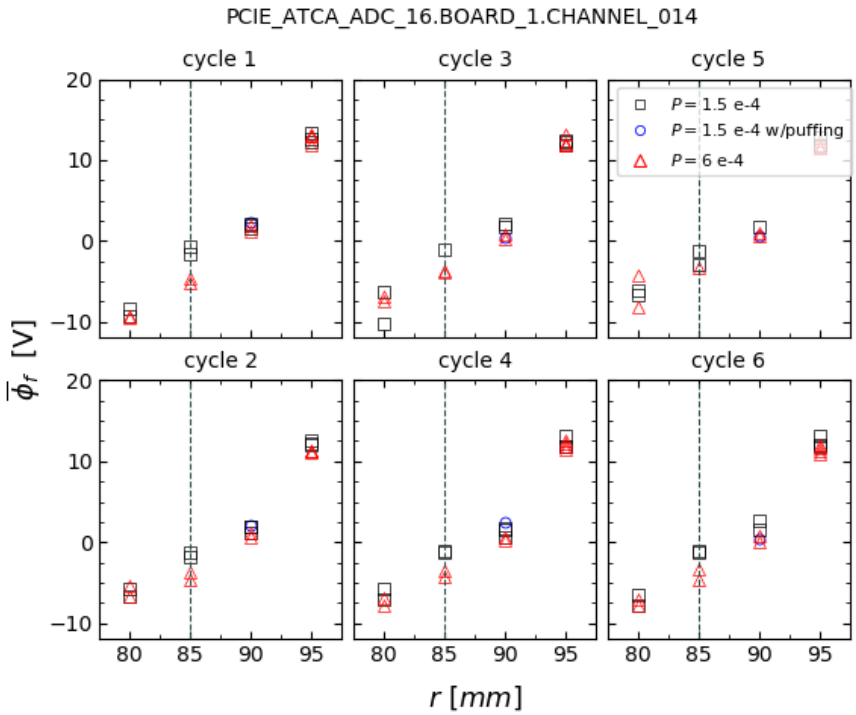

Figure 4.6 Radial profile of the floating potential (mean values) for shot lists C and D. The radial profiles are computed in the same way explained for Fig.4.2. The results from shot list C (black squares and blue circles) were taken for $p \sim 1.5e^{-4}$ torr, while the results from shot list D (red triangles) with $p \sim 6.0e^{-4}$ torr, Fig. 3.5.

shot lists C+D.

As illustrated in Figs. 4.5 and 4.6, the neutral pressure does not seem to change significantly the SOL profiles, although results suggest that the scatter of the data increases at low pressures. Only when gas is puffed along the discharge (large amounts of gas injected for short periods, ~ 2 ms, along the discharge) a clear change in the plasma parameters is observed. In tokamaks the neutral fluxes are defined mainly by the fuel externally injected in the vacuum vessel. However, a particle flux from the wall (limiter and vacuum vessel) also exists (resulting from the fuel retained in the plasma facing components). The flux from the wall will have a direct impact on the ionization sources. However, the particle fluxes from the wall are difficult to control, as they depend on the wall particle inventory that is defined by the history of the previous discharges and cleaning process in between discharges. On ISTTOK the plasma extends all the way until the wall and therefore the ionization sources will be strongly influenced by the particle fluxes from the limiter and vacuum vessel. The fact that no significant change of the plasma properties is seen with neutral pressure may indicate that the fluxes from the wall are dominant on ISTTOK. This is consistent with the observation of a larger data scatter at low pressure, as the wall fluxes may vary significantly from discharge to discharge.

4.3 Properties of the fluctuations

Given that $I_{sat}^{+} \propto n\sqrt{T_e}$ (4.1 and 4.2), and also that $V_f \approx V_p - 3K_\beta T_e$ (4.3) it's assumed that the fluctuations of plasma density $\tilde{n}$ and potential $\tilde{V}_p$ are given by,

$$\tilde{n} \approx \tilde{I}_{sat}^{+} \tag{4.4}$$

$$\tilde{V}_p \approx \tilde{V}_f \tag{4.5}$$

, neglecting the temperature fluctuations, as previously discussed in chapter 3.

Finally, the fluctuations are obtained from the directly acquired probe data, $y(t)$, by subtracting the averaged value of the signals $\bar{y}_N$,

$$\tilde{y}(t) \approx y(t) - \bar{y}_N(t) \tag{4.6}$$

, where the mean signal in time $\bar{y}_N(t)$ is determined by a Moving Average technique, which creates a series of averages of different subsets of the full data set (N data points). The subset averages are calculated typically in a time scale in the order of 1 ms. In this study was set $\Delta t = 0.5$ ms so that there were considered 1000 points for every subset (given the sampling frequency of 2MHz).

The fluctuations statistical properties have been studied with results presented trough Figs. 4.7-4.11. First it is shown the standard deviation for I_{sat}^{+} ($\sigma_{I_{sat}^{+}}$) along with the fluctuation levels ($\sigma_{I_{sat}^{+}}/\bar{I}_{sat}^{+}$, where $\bar{I}_{sat}^{+}$ is the time average) in Fig. 4.7 for shot lists A+B. In Figs. 4.8 and 4.9 are considered the skewness and kurtosis of I_{sat}^{+} and V_f for the same discharges. Lastly, the discrete probability density function is computed for I_{sat}^{+} and V_f on Figs. 4.10 and 4.11, respectively. The PDFs along with the values of skewness and kurtosis will give a broader understanding of the distinct statistical characteristics of turbulent plasma regions.

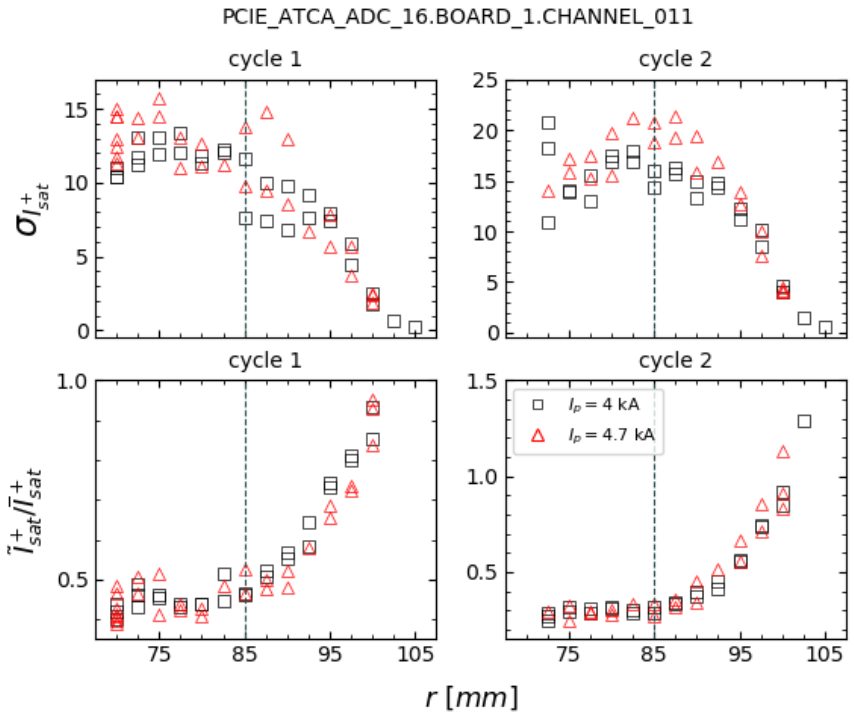

Figure 4.7 Radial profile of the standard deviation ($\sigma_{I_{sat}^+}$) and fluctuation level ($\sigma_{I_{sat}^+}/\bar{I}_{sat}^+$) of the fluctuating ion saturation current. The results from shot list A (black squares) were taken for $I_p = 4$ kA, while the results from shot list B (red triangles) with $I_p = 4.7$ kA, Fig. 3.4.

On Fig. 4.7 one can see that the standard deviation of the I_{sat}^+ fluctuations decreases with radius as for the mean values, because filaments also exhibit losses by parallel transport to the limiter's structures. However, this radial variation is slower than for the mean values (Fig. 4.2), leading to an increase of the fluctuation level with radius. This is a typical result observed in most devices where fluctuation levels in the order of 100% are observed at the far SOL, although on ISTTOK values are often even larger, with fluctuation levels up to 150% observed (see Fig. 4.7). This result indicates that the SOL plasma is dominated by fluctuations and most probably induced by the filamentary structures.

As referred on chapter 2 the intermittent fluctuations of plasma quantities are reflected in a deviation from a Gaussian distribution for the quantities' time series. For the plasma density fluctuations, the higher density blob-filaments result in positive bursts, which are reflected in positive skewness with increasing values towards more turbulent plasma regions in the far-SOL. Similar observations made for the distribution of $\tilde{V}_p$ could indicate overall higher values of the filament's potential, when compared to the background plasma.

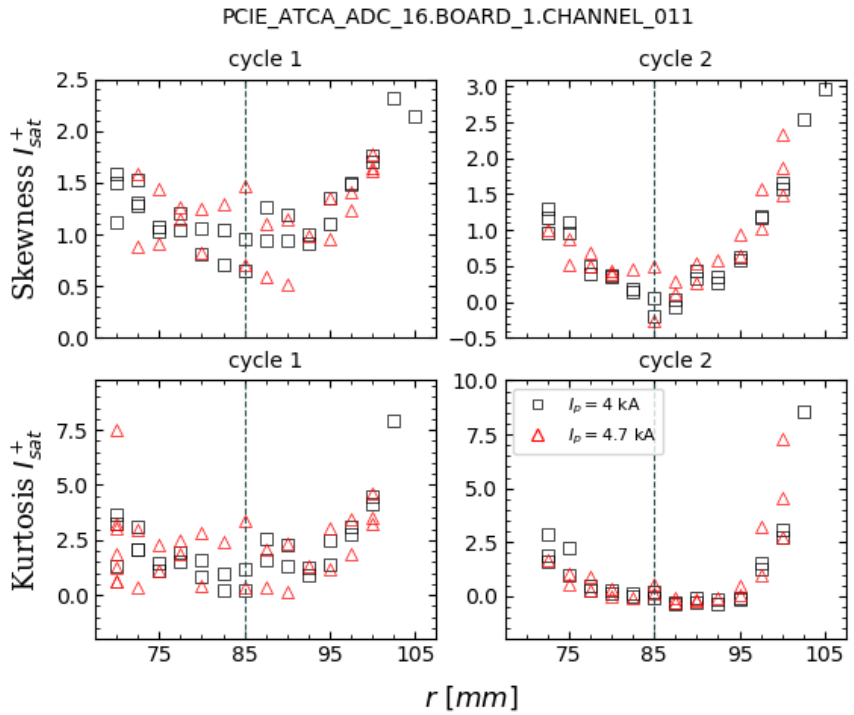

Figure 4.8 Radial profile of the skewness and kurtosis of the ion saturation current. The results from shot list A (black squares) were taken for $I_p = 4$ kA, while the results from shot list B (red triangles) with $I_p = 4.7$ kA, Fig. 3.4.

The skewness and kurtosis should increase with radius at the edge/SOL since the importance of the filaments increases as well. This fact is corroborated in this work for ISTTOK SOL studies. In Figs. 4.8 and 4.9 are computed the skewness and kurtosis radial profiles for both I_{sat}^{+} and V_f, where it's observed an increase with radius at the SOL ($r \geq 85$ mm). A minimum in the skewness is typically observed near the limiter and an increase inwards. The minimum observed may be related to the velocity shear layer position, which can possibly influence the filaments and their propagation.

The higher asymmetry and peakeness of the distributions (measured by the skewness and kurtosis, respectively) are graphically shown by the discrete PDFs on Figs. 4.10 and 4.11. Fig. 4.10 illustrates clearly that the PDF of the I_{sat}^{+} fluctuations in the far SOL is peaked and exhibits a long positive tail, confirming that fluctuations are dominated by intermittent structures.

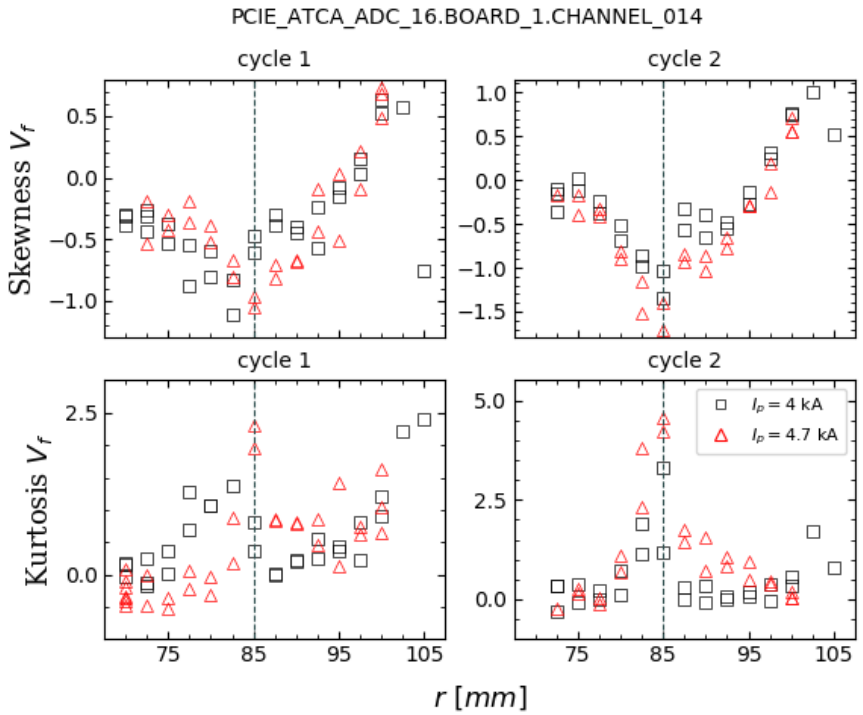

Figure 4.9 Radial profile of the skewness and kurtosis of the floating potential. The results from shot list A (black squares) were taken for $I_p = 4$ kA, while the results from shot list B (red triangles) with $I_p = 4.7$ kA, Fig. 3.4.

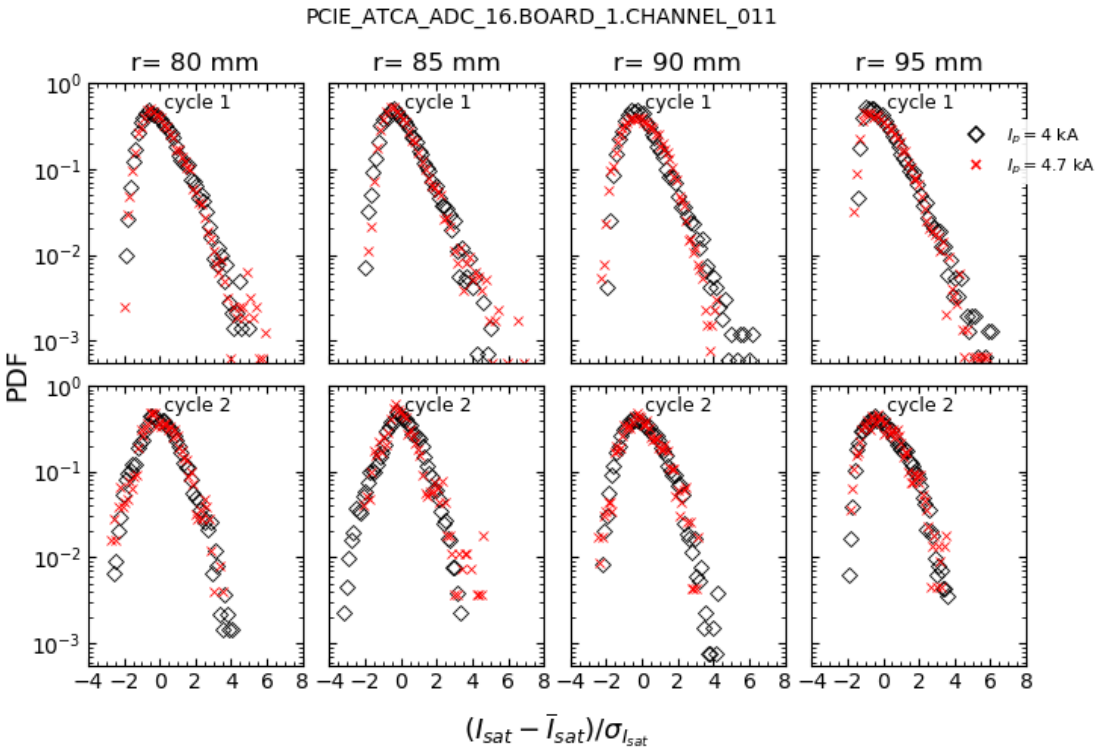

Figure 4.10 PDF of the ion saturation current time series. The distributions were computed for Langmuir probe recordings of about $\sim 3-5$ ms. The results presented were taken for the discharges #41174, #41172, #41169 and #41167, with $I_p = 4$ kA from list A, and #41219, #41216, #41214, and #41212 with $I_p = 4.7$ kA from list B, Fig.3.4.

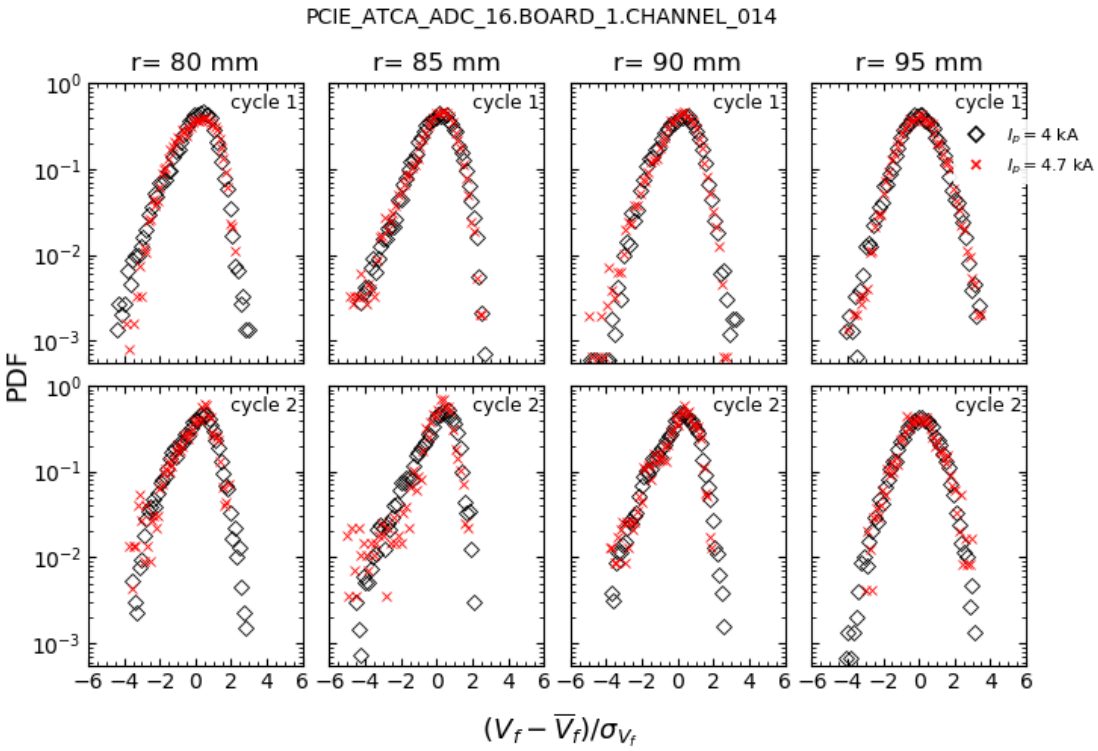

Figure 4.11 PDF of the floating potential time series. The distributions were computed for Langmuir probe recordings of about $\sim 3-5$ ms. The results presented were taken for the discharges #41174, #41172, #41169 and #41167, with $I_p = 4$ kA from list A, and #41219, #41216, #41214 and #41212 with $I_p = 4.7$ kA from list B, Fig.3.4.

4.4 Frequency resolved measurements

To further characterize the fluctuations properties the frequency power spectra of the $\tilde{I}^+_{sat}$ and $\tilde{V}_f$ signals has been computed for the different radial locations r=80, 85, 90 and 95 mm, with $I_p = 4$ kA (discharges #41174, #41172, #41169 and #41167 from list A).
The frequency power spectra is very broad extending above 100 kHz, generally not exhibiting any coherent structure (not clear frequency component), with the power displaying a small variation with frequency up to ~ 100 kHz, and then a fast decay often with a power law of f^{-C}.

For each of the four locations, the spectra of both I^+_{sat} and V_f were constructed from time periods of about $\sim 3-5$ ms. During this section it will be considered the first and second plasma current cycles, therefore having the characterization for a positive and negative plasma current cycle, respectively. The spectras were determined using the Welch method, and finally the frequencies were normalized according to the σ of each series.

In Fig. 4.12 the computed power spectra for I^+_{sat} and V_f (from list A with $I_p = 4$ kA)

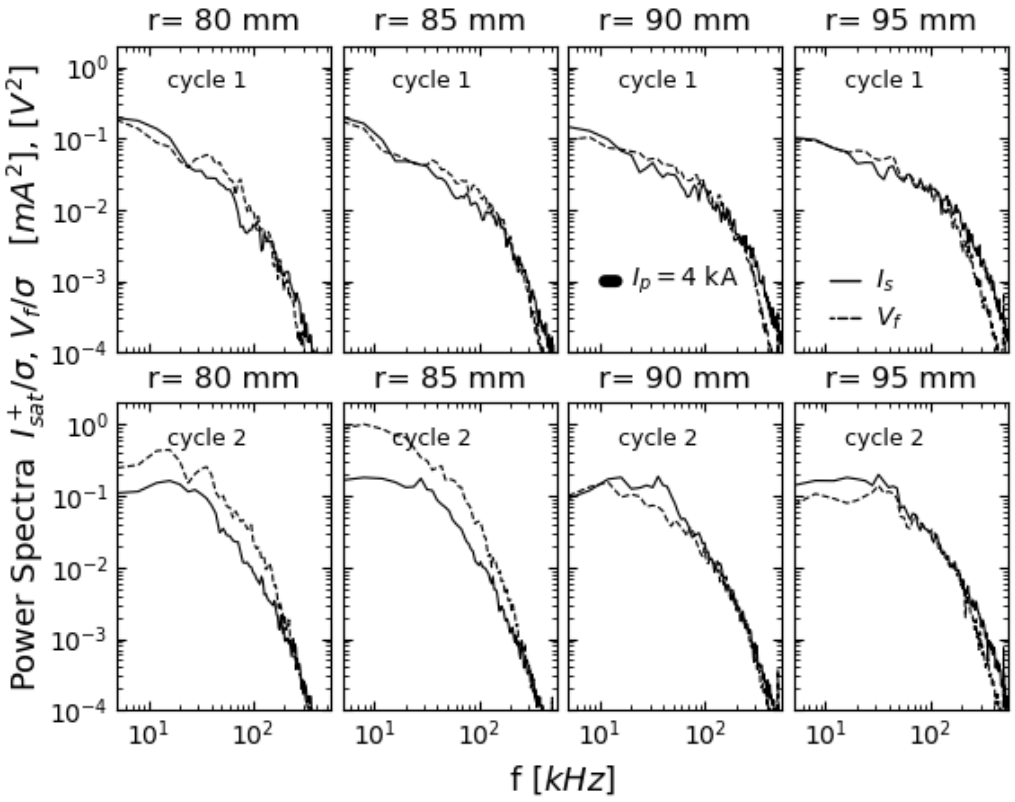

Figure 4.12 power spectra (PS) of the ion saturation current (solid lines) and floating potential (dashed lines) time series at the edge/SOL of the ISTTOK tokamak. For each quantity was computed the PS for $I_p = 4$ kA (#41174, #41172, #41169 and #41167 from list A, Fig.3.4). The frequencies were normalized according to the factor $1/\sigma$ of each time series. The PSs' shape supports what was described in chapter 2 (see Fig.2.9).

display a similar shape, despite having a broader range of dominant frequencies and a higher power amplitude maximum for I_{sat}^+. This fact is coherent with the overall higher intermittent character of the ion saturation current signals.

Outside the confined region the differences between the power spectra computed for the two quantities shows to be more contrasting with each other. Nevertheless, both power spectra exhibit a strong dependence on frequency at high frequencies, rapidly decaying with $1/f^C$, where C is a constant that varies for the different segments of the power spectra.

The value of the constant C has been determine for the I_{sat}^+ spectra on Fig. 4.12 (at r=80 mm, during cycle 1), taken the frequency intervals shown on table 4.1. The faster decay for higher frequencies, is shown by higher values for C on table 4.1. At lower frequencies the spectral power shows a more modest dependency on frequency. This can be concluded both from Fig. 4.12 and the power law f^{-C} dependency on table 4.1.

Table 4.1 Determination of the decay with f^{-C} for the I_{sat}^{+} spectra on Fig. 4.12 (at r=80 mm, during cycle 1). The constant C has been seen to take different values in different segments of the curve.

Δ_f (kHz)		f^{-C} fit to PS(I_{sat}^{+}/σ) (mA^2)
f_i	f_f	C
20	50	0.304 ±0.005
50	100	0.372 ±0.006
100	150	0.422 ±0.004
150	200	0.462 ±0.004
200	250	0.513 ±0.004

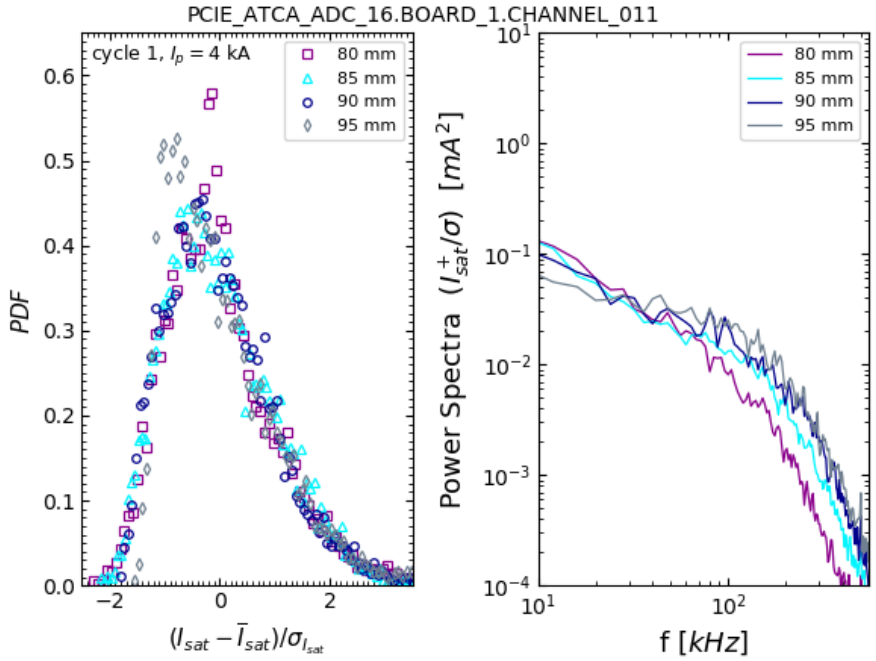

Figure 4.13 PDF and PS of the I_{sat}^{+} fluctuations. Comparison of the PDF and power spectra results shown on Fig.4.10, Fig.4.11 and Fig.4.12. The fluctuations PDF shows a higher asymmetry (higher skewness) for the outwards locations. Most clrear for r=95 mm. While for the PS, the relative importance of the lower frequencies decreases with radius and broader spectras are observed.

Still from Fig. 4.12, and clearly on Fig. 4.14, one can see that the fluctuations' power spectra has a broader extent for outer positions r=90, 95 mm, which indicates an increase of the higher frequency components of the fluctuations near the wall. For outer radial locations the relative

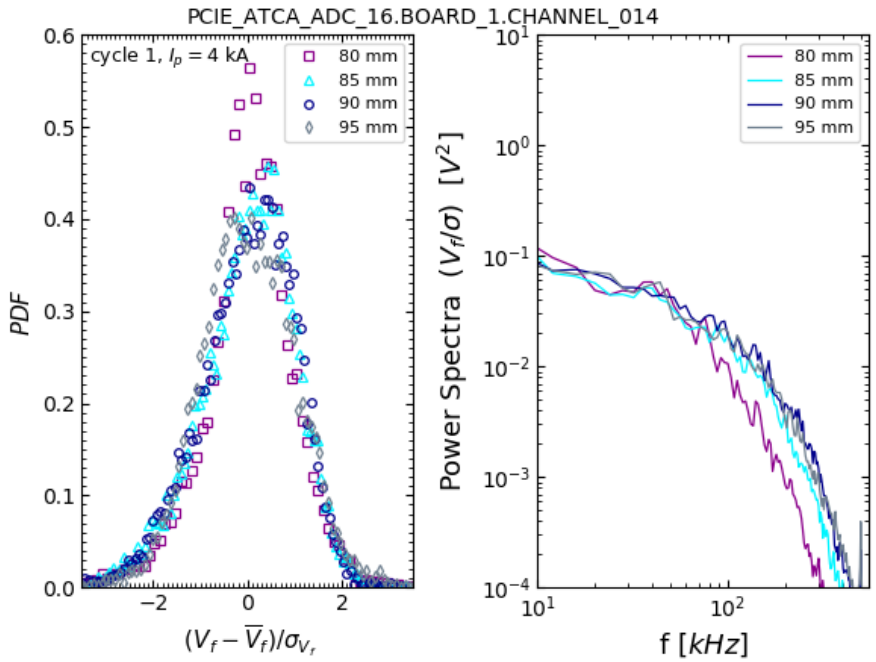

Figure 4.14 PDF and PS of the V_f fluctuations. Comparison of the PDF and power spectra results shown on Fig.4.10, Fig.4.11 and Fig.4.12. The relative importance of the lower frequencies decreases with radius and broader spectras are observed.
Its known from Fig. 4.9 that the asymmetry of the PDF of $\tilde{V}_f$ increases with radius, although the changes are not very perceptible in this figure.

importance of the lower frequencies decreases.

The evolution of the fluctuations with a time scale smaller than 1 ms was studied by applying a Savitzky-Golay (SG) filter ([42, 43]) to the original signals of I_{sat}^{+} and V_f. The method uses a sliding window of $n = L + R + 1$ points, with L and R being the left and right neighbors of a center point x_i. For each iteration i a polynomial of order M, f_M, is approximated to the n data points. The smoothed value at x_i corresponds to the result of the fit, $f_M(x_i)$. On the other hand, the remaining values of f_M are discarded for the i^{th} iteration. It was taken $n = 1001$ in order to consider the fluctuations evolution with time scale of ~ 0.5 ms (signals with sampling frequency of 2 MHz). The SG filter choice of appropriate parameters is not usually obvious, and some visual optimization was needed in choosing M=4. In Fig. 4.15 its shown the SG filter result for I_{sat}^{+} and V_f.
This smoothing technique of the fluctuating signals was introduced with the aim of suppressing the highest frequencies of the fluctuations, but not so severe that we would completely lose track of the intermittency appearing in the data. SG filters are commonly used to smooth signals with

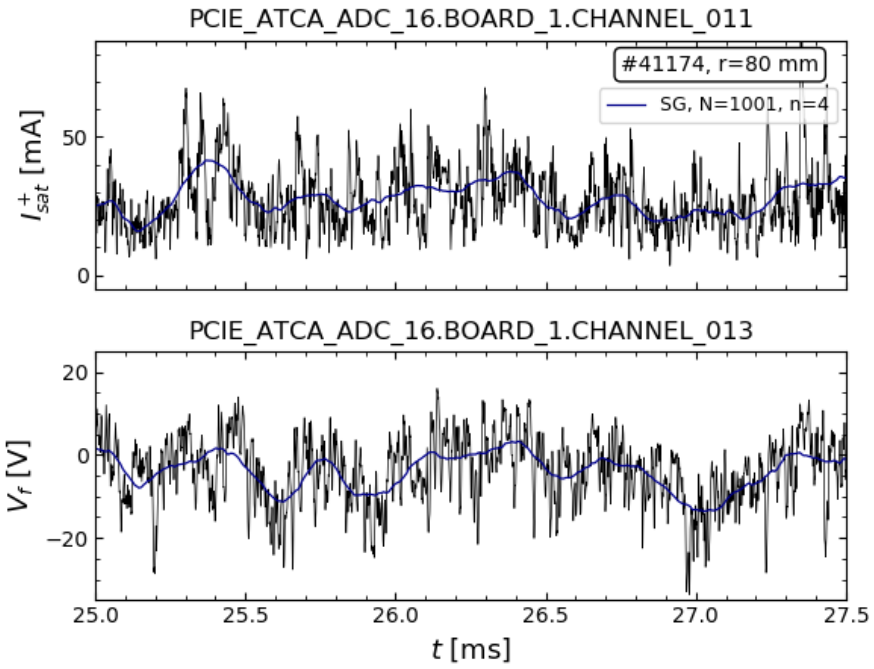

Figure 4.15 Smoothing result of a Savitzky-Golay filter (n=1001, M=4) on the initial recordings of the ion saturation current and floating potential ($r = 80$ mm, $f = 2$ MHz), for #41174. The technique ended up revealing in this case a possible trend for the structures first introduced in the zoom-in in Fig. 4.1 (at r=80 mm).

a large frequency span, as for the broad PS seen for the edge/SOL fluctuations.

The technique ended up revealing in this case a possible trend for the structures first introduced in the zoom-in in Fig. 4.1 (at r=80 mm). Filaments with usual structures around $10 - 100$ μs ($10 - 100$ kHz) are in good agreement with the observed PS of fluctuations. Furthermore, we can see that the intensity of these bursts is modulated in a time scale $0.1 - 1$ ms ($1 - 10$ kHz), Fig. 4.15. The apparent modulation of the intermittency intensity is probably associated with a variation in the mechanisms driving the filaments at ISTTOK.

4.5 Cross-correlation

Electrostatic probes allow the measurement of the velocity of the turbulence moving in the plasma, along with their characteristic time and spatial structures. The correlations between different pin measurements are strongly influenced by the propagation and characteristic structures of the turbulence. The correlations between the several pin measurements allow to determine the velocity of the induced fluctuation structures in the direction of the probe array. For the

set-up in this experiment it will allow to determine the poloidal velocity. Simultaneously, one can approximate the characteristic time of the fluctuations by taking the auto-correlation time (time for which the auto-correlations decays by 1/e). The determination of the poloidal velocity along with the temporal structure of the fluctuations are finally used to estimate their spatial structure in the poloidal direction.

4.5.1 Poloidal velocity of the fluctuations

To determine the poloidal velocities were taken from two different probe pins (of either I_{sat}^{+} or V_f) measurements with the same time period (typically $\sim$ 5 ms), for each location. The time lag of the maximum value of the cross correlation between two poloidally shifted probe measurements i and j, $n_{\max_{i,j}}$, has been used to determine the poloidal propagation velocity of the fluctuations as defined bellow,

$$v_\theta = \frac{n_{\max_{i,j}}}{\Delta\phi_{i,j}}, \tag{4.7}$$

$$n_{\max_{i,j}} = lag \text{ for } \max(f[k]_{\text{probe i}} \star g[k]_{\text{probe j}}), \tag{4.8}$$

where $\Delta\phi_{i,j}$ corresponds to the poloidal shift between the considered pin probes, i and j.
The cross correlation between the time series of one pin by itself, i.e., the auto-correlation, has a maximum value at lag=0, and was used as a reference when determining the lag between the cross correlations of different pin signals.

The poloidal velocities determined are shown on Fig. 4.16 using the cross correlations of both ion saturation current and floating potential signals, and show the reverse of the filaments poloidal velocity around the limiter. The slope of the plasma potential radial profile changes sign around the limiter's position (Fig. 4.3) so we expect the plasma rotation due to the $\vec{E_r} \times \vec{B}_\phi$ drift to reverse around the same position, usually referred to as the velocity shear layer.

As illustrated in Fig. 4.16 in both sides of the velocity shear layer are seen similar magnitudes of v_θ, in the order of 5-10 km/s. The cross-correlation gives the similarity between the signals of two different pins in function of the time delay between them. Here the time delay between the series is limited to multiples of the acquisition system resolution. The filaments poloidal

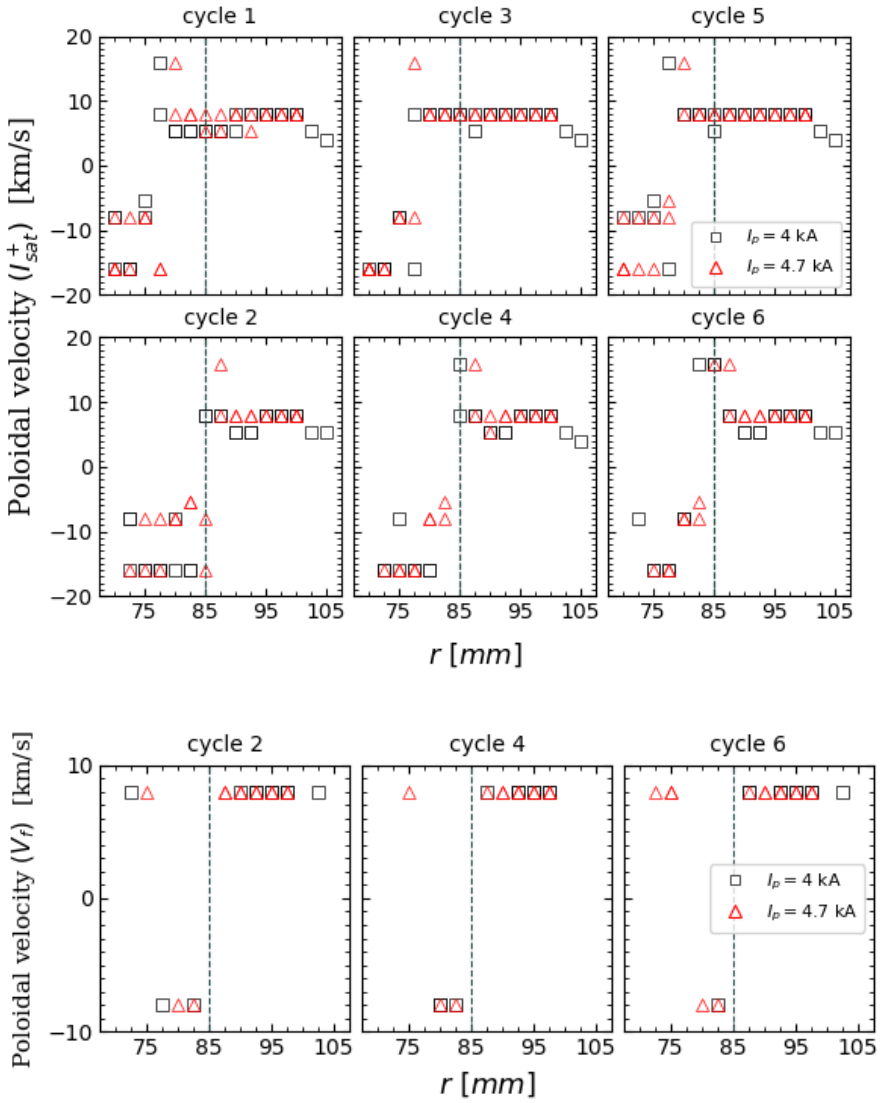

Figure 4.16 Radial profile of the blobs' poloidal velocity, $\|\vec{v}_\theta\|$, determined according to (4.7), where it is used the cross correlations of both ion saturation current and floating potential signals. The blob-filaments propagate with opposing direction across the shear layer ($\sim r_L$), however in both sides of the velocity shear layer are seen similar magnitudes.

propagation and time structures can be smaller than the discrete time delays that arise from the finite resolution of the acquisition system (0.5 μs). In this sense, the discrete time delays possible may not be enough to resolve the poloidal displacement of the filaments, resulting in similar determinations through the SOL.

The propagation velocity of the fluctuations is generally small in the plasma frame and therefore the $\vec{E}_r \times \vec{B}_\phi$ velocity should dominate the measurements. To confirm this assumption,

the $\vec{E_r} \times \vec{B_\phi}$ drift velocity can be estimated from the plasma potential profile at both sides of the limiter (see Fig. 4.4) and compared with the poloidal velocity obtained here. From Fig. 4.4 a radial electric field in the order of 2.5 kV/m is obtained both in the SOL and in the confined region resulting in a drift velocity of 5 km/s. This is in reasonable agreement with the estimate obtained from the plasma fluctuations taking into account the limitations of the cross-correlation method. The plasma potential profile has a similar decay on both sides of the shear layer with a near constant decay, which should also be a major factor in the similar results obtained.

4.5.2 Characteristic structure of the fluctuations

The auto-correlation time (for which the auto-correlations falls by 1/e) gives an approximation of the characteristic temporal structure of the filaments (locally). It is assumed here that the living time of the turbulent structures is larger than the time taken by the filaments to cross a probe, and therefore the filament duration as seen by the Langmuir pin will be given by its poloidal dimension and velocity.

The example on Fig. 4.17 shows the auto-correlation for an I_{sat}^{+} measurement from ch 11 at $r = 80$ mm. From this example it's concluded that the characteristic time of the fluctuations at $r = 80$ mm is ~ 7.3 μs. On Fig. 4.17 it's shown a radial profile of the duration of the turbulent structures, estimated from the remaining discharges in shot list A (for cycles 3 (pos.) and 4 (neg.)). The remaining data is computed in the same way for the auto-correlation of the measurements of ch 11. It's not shown in the figure, but the results using measurements from ch 12 (also I_{sat}^{+}) have the same exact values. The distance between the two pins (8 mm) is relatively smaller that the characteristic spatial structure of the fluctuations (a few centimeters).

It is observed that structures have a duration of ~ 5 μs from $r = 70$ mm growing until ~ 13 μs just inside the limiter during positive cycles. For negative cycles the growth for the temporal structures is slightly lower from ~ 5 μs to ~ 9 μs. Further out the auto-correlation time decreases from ~ 5 μ at the limiter to $2 - 3$ μs at $r = 105$ mm.
The smaller correlation times in the far-SOL probably result from the fact that the plasma is more turbulent near the wall than inside the limiter. More turbulent plasma regions display smaller time structures (as seen by the probes), i.e., higher intermittency.

The profiles of the characteristic time structures, along with the poloidal velocities (Fig. 4.16) were used to estimate the characteristic poloidal spatial structures, 4.18.
During both negative and positive current cycles are seen in the SOL poloidal structures ranging

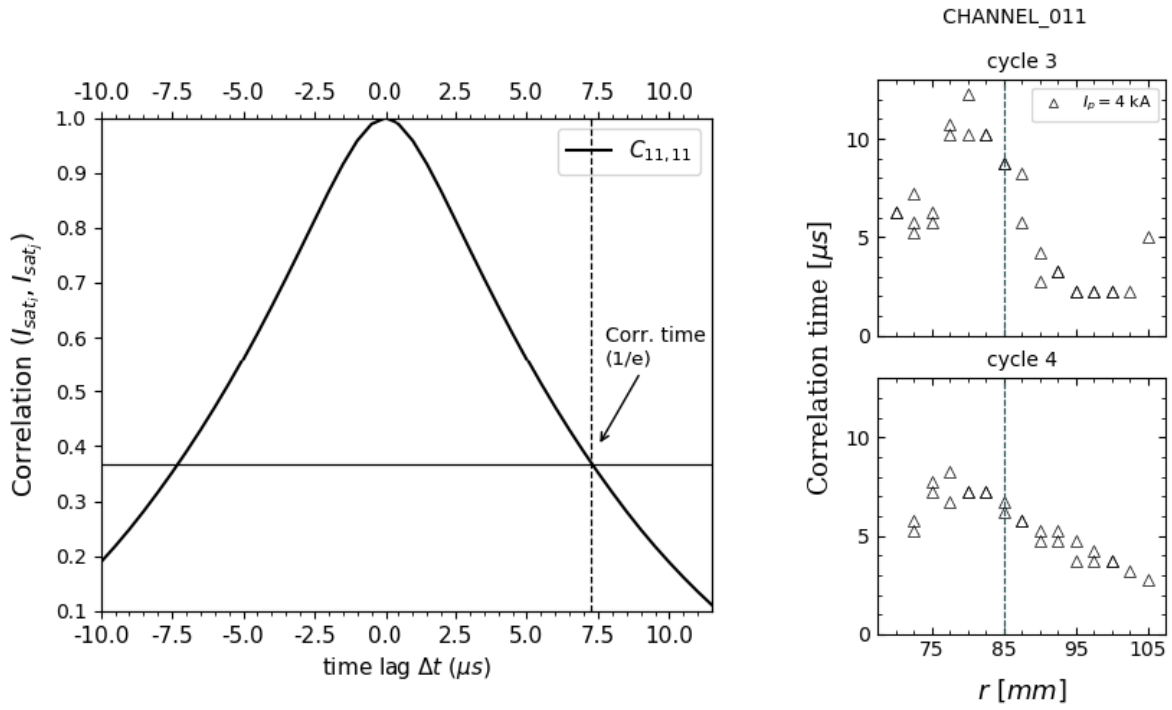

Figure 4.17 Time delay analysis. The auto-correlation time for the I_{sat}^{+} measurements from ch 11 were used to estimate the characteristic time structures of the fluctuations.

from $\sim 1-6$ cm. The decrease of the poloidal dimension of the turbulent structures from the edge to the SOL confirms again that the SOL plasma is dominated by filamentary structures, with a poloidal dimension in the order of a few centimeters.

4.6 Transport induced by fluctuations

In this section we hope to further emphasize the consequences of the fluctuations on the edge and SOL of ISTTOK by determining the radial profile of the induced particle transport, $\bar{\Gamma}_r$. The radial profile of $\bar{\Gamma}_r$ (mean values), was determined for the positions listed on Fig. 3.4 (shot lists A and B). Once again the profile is computed for the individual alternating plasma current cycles. The results for each location represent the mean values for time periods of about $\sim 3-5$ ms, during stationary periods of the flat top of each plasma current cycle.

As expressed on 2.1 the turbulent particle flux is given by $\bar{\Gamma}_r =< \tilde{n}(t) \cdot \tilde{\vec{E}}_\theta(t) > /B$ (where the angular brackets denote a time average). The plasma density fluctuations are estimated from the fluctuating ion saturation current, 4.4. The poloidal electric field fluctuations, $\tilde{\vec{E}}_\theta$, estimated from two floating potential signals, 4.5.

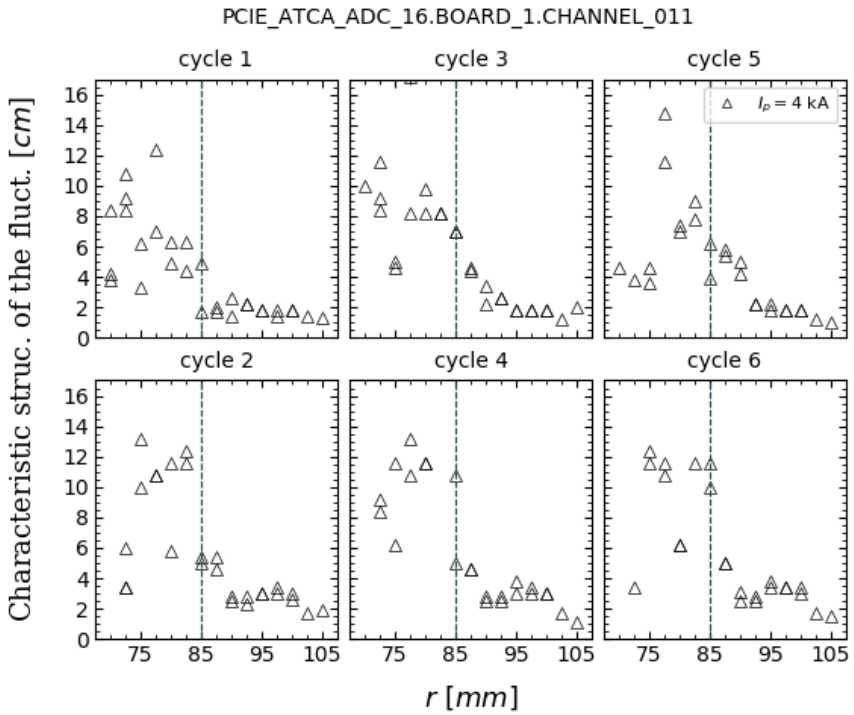

Figure 4.18 Characteristic spatial structures of the fluctuations.

Recall that $I_{sat}^{+} = en_e c_s A_{pr}/2$, 4.1. Given the probe area of $A_{pr} = 1 \times 10^{-6}$ m^2, and $C_s = \sqrt{2T_e/m_i} = 1 \times 10^4 \sqrt{T_e}$ (hydrogen nuclei), follows for the fluctuating density

$$\tilde{n} = \frac{1.25 \times 10^{21}}{\sqrt{T_e}} \tilde{I}_{sat}^{+}. \tag{4.9}$$

It has been used the ion saturation signal obtained from channel 11, and the temperature is determined in function of r from 3.8.

The fluctuating poloidal field is determined from two floating potential signals $\Delta_\theta = 2$ mm apart, measurements from channels 13 and 14,

$$\tilde{E}_\theta(t) = \frac{\tilde{V}_{f1} - \tilde{V}_{f2}}{2 \times 10^{-3}}. \tag{4.10}$$

Finally the toroidal magnetic field is $B = 0.5$ T.

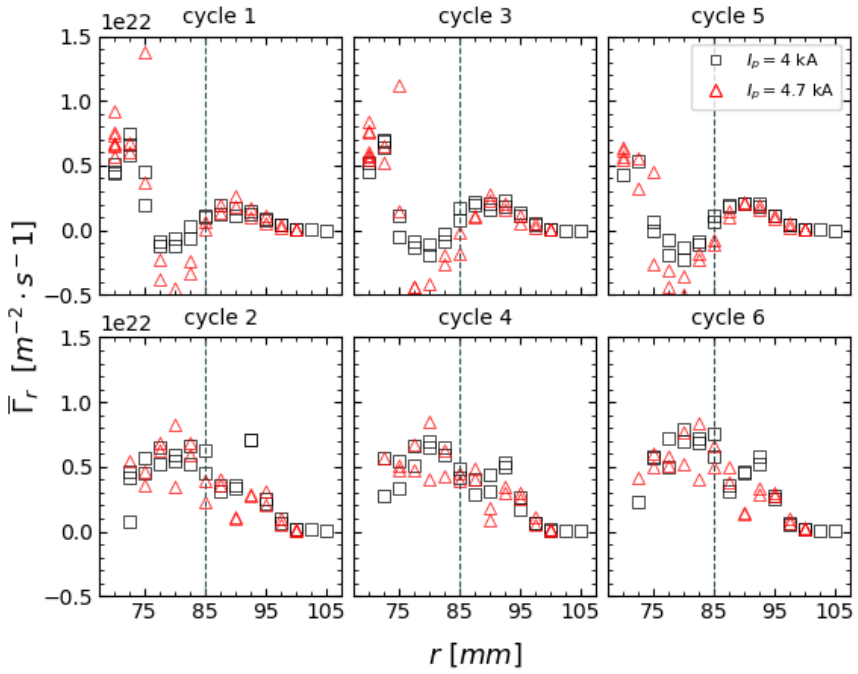

Figure 4.19 Radial profile of the turbulent particle flux, $\bar{\Gamma}_r =< \tilde{n}(t) \cdot \tilde{\vec{E}}_\theta(t) > /B$. The plasma density is estimated from fluctuating ion saturation current (channel 11), and the poloidal electric field fluctuations, $\tilde{\vec{E}}_\theta$, estimated from two floating potential signals $\Delta_\theta = 2$ mm apart, (measurements from channels 13 and 14).

In this way,

$$\bar{\Gamma}_r = 1.25 \times 10^{24} \frac{< \tilde{I}^{+}_{sat}(t) \cdot (\tilde{V}_{f2}(t) - \tilde{V}_{f1}(t)) >}{\sqrt{T_e}}. \tag{4.11}$$

On Fig. 4.19 is shown the profile of the turbulent particle flux computed as just explained, for $[\bar{\Gamma}_r] = m^{-2}s^{-1}$.
The profile shows an increase from the confined region towards the inner SOL. For the negative AC cycles the induced transport shows a systematic maximum just around the limiter's position, and rapidly decreasing towards the wall, since the density should be considerably smaller.
The inner displacement of the plasma for the positive cycles, is shown on Fig. 4.19 as a inner displacement of the behavior profile observed for the negative cycles. The maximum induced transport is seen around $r = 70$ mm, while around the wall position the decreasing profile takes values near zero.

Fluctuations induce by plasma turbulence, and in particular by filaments, cause radial trans-

port. In the SOL, apart from radial transport, there are fast parallel losses to the limiter surfaces and therefore it is expected that the turbulence flux decay radially as observed. In the confined region the ionization sources may exist but because there are no parallel losses (field lines are closed) the particle flux should increase with radius up to the limiter position. This is observed in the region just inside the limiter but not for $r < 80$ mm, suggesting again that I_{sat}^{+} data may not be valid in this region.

At ISTTOK the particle confinement time is in the order of $\tau = 0.2$ ms, [3]. The confinement time can be estimated from 4.12.

$$\tau = \frac{N}{\bar{\Gamma}_T A}, \tag{4.12}$$

where $N = \bar{n}V$ is the total number of particles in the chamber, Γ_T the total particle flux ($\bar{n}$ and V are the average density, and volume of the torus), and A the surface of the torus. At ISTTOK follows that,

$$\begin{cases} \bar{n} \sim 4 \times 10^{18} & [m^{-3}], \\ V = 2a^2\pi^2 R_0 \sim 0.066 & [m^3], \\ S = 4a\pi^2 R_0 \sim 1.544 & [m^2]. \end{cases} \tag{4.13}$$

From the quantities at 4.13 and the expression on 4.12 one estimates that the total particle flux at ISTTOK is in the order of $10^{21} m^{-2} s^{-1}$. The average particle flux induced by the edge/SOL fluctuations, estimated in Fig. 4.19, is in the same order of magnitude as the total flux at ISTTOK, of $\sim 10^{21} m^{-2} s^{-1}$. As mentioned throughout this work the particle transport induced by the edge/SOL fluctuations dominates the losses in most fusion devices. Here at ISTTOK we have estimated the losses induced by fluctuations to be in the same order of magnitude than the total particle flux (given by the measured confinement time).

Chapter 5
Conclusions & Future Work

5.1 Conclusions

This thesis aimed to further understand the presence of blob-filaments and the induced fluctuations on plasma quantities at the boundary plasma of the ISTTOK experiment, while emphasizing the major importance of the radial transport induced by fluctuations.
The diagnosis of the plasma edge/SOL (up to 1.5 cm inside the LCFS) is achieved with high resolution at ISTTOK with a Langmuir probe system coupled to a ATCA DAQ system.

An initial assessment for discharges with two distinct plasma current values $I_p = 4$, 4.7 kA showed slightly higher values for the average $I_{sat}^{+} \propto n$ (chapter 4) and slightly lower values for the average V_p in the same conditions. This observation (clear during negative plasma current cycles) may result from the fact that only Ohmic heating is available on ISTTOK. The gain in plasma current usually sets a gain in the heating power leading to larger temperatures, more ionizations and higher densities. During the characterization of the fluctuations no relevant differences were seen, with neither a suppression or a more intermittent character with the 0.7 kA gain in I_p.

It also was intended to investigate how the properties of filaments were influenced by the interactions with the neutrals by changing the neutrals pressure. It's a new research topic and little was known to start with. The results for discharges with the different work pressure values $p = 1.5$, 6×10^{-4} torr didn't show a significant change for the average SOL profiles (on chapter 4). More important, for the different values of p, the characterization of the fluctuations showed similar results (from the fluctuation levels, skewness, kurtosis and PDF of these discharges).

During this work we didn't got to realize discharges with a broader range of either plasma current or neutral pressure values. However, an extensive and comprehensive characterization of the plasma fluctuations was carried out. Density and potential fluctuations measurements were performed with a high radial (2 mm) and temporal (0.5 μs) resolution. By applying different analysis techniques, ranging from statistical analysis to correlation techniques and spectral analysis, the fluctuations where characterized with a contribution to a better understanding of the physics associated with the plasma filaments and its impact on the radial transport.

We have seen in chapter 4 edge/SOL fluctuation levels increasing from $\sim 25\%$ inside the LCFS to $\sim 150\%$ at the far SOL, which indicates that the SOL plasma is dominated by fluctuations and most probably induced by the filamentary structures. The SOL fluctuations were shown to have a distribution consistent with a high presence of intermittent events. The filamentary structures in the SOL should result in the intermittency of plasma quantities and a deviation from a Gaussian distribution, due to their different properties from the background plasma. High skewness values should be seen for the density fluctuations, for example, given the higher density of the filaments. We concluded in this work this hypothesis for the negative and positive plasma current cycles that ISTTOK operates on. Longer positive tails were also found in the density fluctuations ($\tilde{I}^{+}_{sat}$) PDF at the far SOL (r=95 mm), confirming that fluctuations are dominated by intermittent structures at this region.
Overall the fluctuation levels, skewness and kurtosis should increase with radius at the edge/SOL, since the importance of the filaments increases as well. The importance of the induced fluctuations in the edge region near the limiter has severe consequences in degrading the plasma confinement, therefore restraining the machine performance.

We were able to show the frequency resolved fluctuation measurements at the edge and SOL of ISTTOK, and corroborate a common result in most fusion devices. The computed power spectra (using the Welch method) as expected showed to be very broad extending above 100 kHz. It was seen that the relative importance on the lower frequencies decreases going near the wall, where there is an increase of the higher frequency components of the fluctuations. Therefore, at the far SOL are seen even broader spectras. Overall the fluctuations power shows a modest dependency with frequency for $f \lesssim 100$ kHz, and then a fast decay often with a power law f^{-C}. The faster decay of the power from $f \sim 100$ varies for different frequency ranges, as displayed for the values of C estimated on chapter 4.

Filaments with usual structures around $10 - 100$ μs ($10 - 100$ kHz) are in good agreement

with the observed PS of fluctuations. In addition a Savitzky-Golay smoothing technique end up revealing that the intensity of these bursts may be modulated in a time scale $0.1 - 1$ ms ($1 - 10$ kHz), Fig. 4.15, probably associated with a variation in the mechanisms driving the filaments.

Afterwards, the poloidal velocities of the fluctuations were determined. In the poloidal direction the filaments are expected to rotated along with the background plasma, since the $E_r \times B_\phi$ drift should be dominant over the smaller velocity of the fluctuations. This hypothesis is in good agreement with our observation as the poloidal velocity derived both from the fluctuation and the radial electric field profile are in the order of 5-10 km/s. Similar magnitudes were obtained in both sides of the velocity shear layer, coherent with similar magnitudes of the radial electric field.

The probe array system installed at ISTTOK allowed to determine the induced particle flux from simultaneous measurements of the ion saturation and poloidal electric field fluctuations. We have concluded an induced particle flux in the same order of magnitude as the total particle losses of ISTTOK, of $10^{21} m^{-2} s^{-1}$. The flux showed to increase in the edge boundary plasma, from $r = 75$ mm to $r \sim 85$ mm. These observations are of major importance in the performance of devices such as ISTTOK, where the turbulence in the confined edge plasma (near the LCFS) results in dominant losses of particles and energy, degrading the confinement conditions and energy output. Hopefully the previous characterization of the turbulence induced fluctuations are a significant addition in understanding the conditions in which these mechanisms arise and in solving some of the constrains observed in the edge plasma of fusion devices.

The results through chapter 4 are in agreement with previous observations at ISTTOK, and are a good addition to the existent literature for the edge/SOL plasma not only at this experiment but for fusion devices in general. Given that ISTTOK operates with AC plasma current cycles to allow longer discharges, trough out this entire work we also added an analyses of the fluctuations and induced transport conditions in six consecutive AC cycles of the experiment.

5.2 System Limitations & Future Work

During this work the machine conditions did not allow to realize discharges with a broader range of either plasma current or neutral pressure values. For example, the maximum achievable plasma current on ISTTOK strongly depends on the machine vacuum and wall conditions. Following a ISTTOK shutdown, typically only after one month of operation plasma currents above 5 kA are achieved, requiring not only good vacuum condition (in the order of 2×10^{-7}

mbar) but also conditioned walls (low level of surface and retained impurities). In this condition, the low impurity content in the plasma will result in lower plasma resistivity, therefore offering the possibility to achieved higher plasma currents. As the machine was not fully conditioned during our experiments, the maximum achieved plasma current in stationary conditions was limited to about 4.7 kA. Future work to understand the influence of both the plasma current and neutral density on the plasma fluctuations would consist on performing more experiments in function of a broader range of these parameters, when the machine conditions permit so.

Across this work some uncertainties were mentioned about the I_{sat}^{+} measurements on chapter 4. In future experiments it is also necessary to make sure that the I_{sat}^{+} data is valid by applying a large bias voltage.

Bibliography

[1] H. Fernandes, J. Cabral, C. Varandas, and C. Silva, "20 years of isttok tokamak scientific activity," in *Presented at the 24th IAEA Fusion Energy Conference. San Diego, USA, October 8–13*, 2012.

[2] H. Fernandes, C. Varandas, and J. Cabral, "Role of the tokamak isttok on the euratom fusion programme," *Brazilian journal of physics*, vol. 32, no. 1, pp. 100–106, 2002.

[3] C. Silva, H. Figueiredo, I. Nedzelskiy, B. Gonçalves, and C. Varandas, "Control of the edge turbulent transport by emissive electrode biasing on the tokamak isttok," *Plasma physics and controlled fusion*, vol. 48, no. 6, p. 727, 2006.

[4] C. Silva, H. Figueiredo, P. Duarte, and H. Fernandes, "Characterization of the poloidal asymmetries in the isttok edge plasma," *Plasma Physics and Controlled Fusion*, vol. 53, no. 8, p. 085021, 2011.

[5] C. Silva, H. Fernandes, H. Figueiredo, C. Varandas, J. Cabral, C. Hidalgo, M. Pedrosa, and E. Sanchez, "Plasma fluctuations and reynolds stress measurements on the tokamak isttok," *Czechoslovak Journal of Physics*, vol. 49, no. suppl. S3, pp. 29–34, 1999.

[6] M. G. Sevillano, I. Garrido, and A. J. Garrido, "Sliding-mode loop voltage control using astra-matlab integration in tokamak reactors," *International Journal of Innovative Computing, Information and Control*, vol. 8, no. 9, pp. 6473–6489, 2012.

[7] "Tokamak- Wikipedia, the free encyclopedia," https://en.wikipedia.org/wiki/Tokamak, accessed: 2019-05-30.

[8] "An introduction to operational regimes in limiter and divertor tokamaks, Mitglied der Helmholtz-Gemeinschaft Institut für," https://slideplayer.com/slide/10998174/, accessed: 2019-05-30.

[9] "AP C - UNIT 9 Magnetic Fields and Forces," https://slideplayer.com/slide/273794/, accessed: 2019-05-30.

[10] A. A. m. i. t. J. b. Presented by GuoshengXu and transport teams, "Blob/hole formation and zonalflow generationin the jet edge plasma presentation, tfe meeting," 2009.

[11] R. Maqueda, D. Stotler, S. Zweben, and N. The, "Intermittency in the scrape-off layer of the national spherical torus experiment during h-mode confinement," *Journal of nuclear materials*, vol. 415, no. 1, pp. S459–S462, 2011.

[12] J. A. Boedo, D. Rudakov, R. Moyer, S. Krasheninnikov, D. Whyte, G. McKee, G. Tynan, M. Schaffer, P. Stangeby, P. West *et al.*, "Transport by intermittent convection in the boundary of the diii-d tokamak," *Physics of Plasmas*, vol. 8, no. 11, pp. 4826–4833, 2001.

[13] J. A. Boedo, D. L. Rudakov, R. A. Moyer, G. R. McKee, R. J. Colchin, M. J. Schaffer, P. Stangeby, W. West, S. L. Allen, T. E. Evans *et al.*, "Transport by intermittency in the boundary of the diii-d tokamak," *Physics of Plasmas*, vol. 10, no. 5, pp. 1670–1677, 2003.

[14] D. D'Ippolito, J. Myra, and S. Zweben, "Convective transport by intermittent blob-filaments: Comparison of theory and experiment," *Physics of Plasmas*, vol. 18, no. 6, p. 060501, 2011.

[15] G. Y. Antar, G. Counsell, Y. Yu, B. Labombard, and P. Devynck, "Universality of intermittent convective transport in the scrape-off layer of magnetically confined devices," *Physics of Plasmas*, vol. 10, no. 2, pp. 419–428, 2003.

[16] S. Zweben, J. Boedo, O. Grulke, C. Hidalgo, B. LaBombard, R. Maqueda, P. Scarin, and J. Terry, "Edge turbulence measurements in toroidal fusion devices," *Plasma Physics and Controlled Fusion*, vol. 49, no. 7, p. S1, 2007.

[17] C. Silva, "Plasma diagnostic techniques, lectures, ist," 2017.

[18] "The Shift Project, Breakdown of Electricity Generation by Energy Source," http://www.tsp-data-portal.org/Breakdown-of-Electricity-Generation-by-Energy-Source#tspQvChart, accessed: 2019-05-30.

[19] J. P. Freidberg, *Plasma physics and fusion energy*. Cambridge university press, 2008.

[20] "Iter: A brief history of fusion."

[21] F. F. Chen, *Introduction to plasma physics and controlled fusion*. Springer, 1984, vol. 1.

[22] D. Rudakov, J. Boedo, R. Moyer, S. Krasheninnikov, A. Leonard, M. Mahdavi, G. McKee, G. Porter, P. Stangeby, J. Watkins *et al.*, "Fluctuation-driven transport in the diii-d boundary," *Plasma physics and controlled fusion*, vol. 44, no. 6, p. 717, 2002.

[23] D. Rudakov, J. Boedo, R. Moyer, P. C. Stangeby, J. Watkins, D. Whyte, L. Zeng, N. Brooks, R. Doerner, T. Evans *et al.*, "Far sol transport and main wall plasma interaction in diii-d," *Nuclear fusion*, vol. 45, no. 12, p. 1589, 2005.

[24] J. Boedo, D. Rudakov, R. Colchin, R. Moyer, S. Krasheninnikov, D. Whyte, G. McKee, G. Porter, M. Schaffer, P. Stangeby *et al.*, "Intermittent convection in the boundary of diii-d," *Journal of nuclear materials*, vol. 313, pp. 813–819, 2003.

[25] I. Garcia-Cortes, R. Balbin, A. Loarte, J. Bleuel, A. Chankin, S. Davies, M. Endler, S. Erents, C. Hidalgo, G. Matthews *et al.*, "Turbulent transport studies in the jet edge plasmas in limiter configuration," *Plasma physics and controlled fusion*, vol. 42, no. 4, p. 389, 2000.

[26] J. A. Boedo, D. L. Rudakov, R. A. Moyer, G. R. McKee, R. J. Colchin, M. J. Schaffer, P. Stangeby, W. West, S. L. Allen, T. E. Evans *et al.*, "Transport by intermittency in the boundary of the diii-d tokamak," *Physics of Plasmas*, vol. 10, no. 5, pp. 1670–1677, 2003.

[27] D. D'Ippolito, J. Myra, and S. Zweben, "Convective transport by intermittent blob-filaments: Comparison of theory and experiment," *Physics of Plasmas*, vol. 18, no. 6, p. 060501, 2011.

[28] S. Krasheninnikov, D. D'ippolito, and J. Myra, "Recent theoretical progress in understanding coherent structures in edge and sol turbulence," *Journal of Plasma Physics*, vol. 74, no. 5, pp. 679–717, 2008.

[29] D. Russell, J. Myra, and D. D'Ippolito, "Collisionality and magnetic geometry effects on tokamak edge turbulent transport. ii. many-blob turbulence in the two-region model," *Physics of Plasmas*, vol. 14, no. 10, p. 102307, 2007.

[30] T. Carter, "Intermittent turbulence and turbulent structures in a linear magnetized plasma," *Physics of plasmas*, vol. 13, no. 1, p. 010701, 2006.

[31] O. Grulke, J. Terry, B. LaBombard, and S. Zweben, "Radially propagating fluctuation structures in the scrape-off layer of alcator c-mod," *Physics of Plasmas*, vol. 13, no. 1, p. 012306, 2006.

[32] A. Melnikov, L. Eliseev, T. Estrada, E. Ascasibar, A. Alonso, A. Chmyga, C. Hidalgo, A. Komarov, A. Kozachek, L. Krupnik *et al.*, "Changes in plasma potential and turbulent

particle flux in the core plasma measured by heavy ion beam probe during l–h transitions in the tj-ii stellarator," *Nuclear Fusion*, vol. 53, no. 9, p. 092002, 2013.

[33] A. Melnikov, L. Krupnik, L. Eliseev, J. Barcala, A. Bravo, A. Chmyga, G. Deshko, M. Drabinskij, C. Hidalgo, P. Khabanov *et al.*, "Heavy ion beam probing—diagnostics to study potential and turbulence in toroidal plasmas," *Nuclear Fusion*, vol. 57, no. 7, p. 072004, 2017.

[34] J. Boedo, D. Gray, L. Chousal, R. Conn, B. Hiller, and K. Finken, "Fast scanning probe for tokamak plasmas," *Review of scientific instruments*, vol. 69, no. 7, pp. 2663–2670, 1998.

[35] B. LaBombard, M. Umansky, R. Boivin, J. Goetz, J. Hughes, B. Lipschultz, D. Mossessian, C. Pitcher, J. Terry *et al.*, "Cross-field plasma transport and main-chamber recycling in diverted plasmas on alcator c-mod," *Nuclear Fusion*, vol. 40, no. 12, p. 2041, 2000.

[36] W. West, N. Brooks, G. Jackson, A. Leonard, M. Mahdavi, T. Osborne, T. Petrie, M. Schaffer, R. Stambaugh, M. Wade *et al.*, "Impurity enrichment and radiative enhancement using induced sol flow in diii-d," *Journal of nuclear materials*, vol. 266, pp. 44–50, 1999.

[37] A. Filippas, "Av filippas, rd bengtson, gx li, ma meier, cp ritz, and ej powers, phys. plasmas 2, 839 (1995)." *Phys. Plasmas*, vol. 2, p. 839, 1995.

[38] C. Varandas, J. Cabral, J. Mendonça, M. Alonso, P. Amorim, B. Carvalho, C. Correia, L. Cupido, M. Carvalho, J. Dias *et al.*, "Engineering aspects of the tokamak isttok," *Fusion Technology*, vol. 29, no. 1, pp. 105–115, 1996.

[39] "Isttok tokamak, cfn, ist."

[40] "Isttok: Real-time control of ac discharges."

[41] M. Endler, "Turbulent sol transport in stellarators and tokamaks," *Journal of nuclear materials*, vol. 266, pp. 84–90, 1999.

[42] H. H. Madden, "Comments on the savitzky-golay convolution method for least-squares-fit smoothing and differentiation of digital data," *Analytical chemistry*, vol. 50, no. 9, pp. 1383–1386, 1978.

[43] P. A. Gorry, "General least-squares smoothing and differentiation by the convolution (savitzky-golay) method," *Analytical Chemistry*, vol. 62, no. 6, pp. 570–573, 1990.

UNIVERSIDADE DE LISBOA
FACULDADE DE CIÊNCIAS
DEPARTAMENTO DE FÍSICA

Characterization of the turbulent transport in the edge plasma of the tokamak ISTTOK

Sara Vaz Mendes

Mestrado Integrado em Engenharia Física

Versão Provisória

Dissertação orientada por:
Carlos Alberto Nogueira Garcia da Silva
Olinda Maria Quelhas Fernandes Conde

2019

Acknowledgments

This thesis presents an effort as a master student to participate in the large effort of the fusion community in trying to understand the major challenges of terrestrial fusion. I am really grateful for the opportunity of finishing my masters in this subject of studies. More than anything, I would like to thank the availability and kindness of my supervisor, Dr. Carlos Silva. The opportunity to analyze and perform a characterization of the turbulence in the edge of the ISTTOK tokamak, along with all the knowledge about fusion devices that I got to take a first look at has been more than I could have hoped for the end of my master program. Thank you to Dr. Carlos Silva, here as a professor, for helping me in spite of my almost a year-long absence through Erasmus. Thanks to the IPFN team at IST for creating the space and means for an academic Fusion program in Lisbon.

A very special gratitude goes out to all responsible for my student internships at ENEA and CCFE for the great experiences to further my knowledge in Fusion diagnostics. These opportunities were only possible because of the great research conditions and hospitality at both institutions. Thanks to professor Guiomar Evans for the availability and guidance through our most pessimist times at the faculty. Thanks to both professors Guiomar Evans and Olinda Conde for the help in solving the not so straight forward administration procedures and allowing me to follow the last master subjects in this area.

Lastly, I also have to thank all my colleagues and family for the last years hearing my pessimist self, while still encouraging me about all the work ahead. Thank you all for the patient

Abstract

A major challenge in the realization of fusion power plants will be to overcome the dominant confinement losses induced by turbulence. The performance of current experiments is strongly influenced by these mechanisms. Turbulence considerably increases the transport of particles and energy in the edge, being the dominant source of losses in fusion devices. This work aims at contributing to the understanding of the turbulence induced by blob-filaments, trough a multi-scale investigation of the induced fluctuations on plasma quantities and ultimately the resultant transport of particles and energy in the edge of the ISTTOK (IST tokamak) experiment. It was intended to carry a detailed analysis of turbulence physics at various scales, from their origin to the impact on plasma confinement. ISTTOK is an ideal experiment to carry a study related to the edge plasma since it is compact, flexible and allows rapid installation of diagnostics. A multi-pin array of Langmuir probes allowed to carry bi-dimensional measurements of the structure of plasma fluctuations, and revealed to be ideal in determining the induced particle transport.

The different analysis techniques applied in this work revealed that the turbulent structures in the edge of the ISTTOK tokamak have a time scale of the order of $\sim 2-10$ μs, propagating poloidally with $v_\theta = 5-10$ km/s and having a poloidal dimension of $\sim 2-6$ cm. Fluctuation levels from 25% in the edge plasma to 150% in the far scrape-off layer (SOL) of ISTTOK revealed that the region is dominated by fluctuations, which are probably induced by the turbulence resulting in blob-filaments. The remaining statistical properties of the fluctuations also indicated that the edge and SOL of ISTTOK are dominated by fluctuations, where intermittency in plasma quantities results in probability distributions with high skewness and kurtosis. The statistical quantities of the fluctuations allowed to show the increase of the relative importance of the induced fluctuations with radius.

Further investigations were done on the properties of the edge/SOL fluctuations reveling broad power spectra, and coherent with structures of the order of $10-100$ μs. The power

spectra of the fluctuations when appropriately re-scaled to the standard deviation of the measurements shows a roughly universal shape in most fusion devices. The common result was also seen for the power spectra computed during this work, showing a modest decay with frequency until ~ 100 kHz, and a faster decay from this value with the power law of f^{-C}.

Lastly, the particle flux induced by the fluctuations in the edge and SOL was estimated to be in the order of $\sim 10^{21}\ m^{-2}s^{-1}$, and having the same order magnitude of the total particle losses at ISTTOK estimated from the measured particle confinement.

Keywords

Thermonuclear Fusion; Tokamak; Turbulence structures; Blob-filaments; Intermittent particle transport.

Resumo

Um enorme esforço por parte da comunidade de fusão nuclear tem vindo a reunir nas últimas décadas vários estudos sobre as principais dificuldades em construir futuros reatores baseados na fusão nuclear. Na actualidade, várias experiências espalhadas pelo globo têm como finalidade provar a eficiência de diferentes configurações para futuros reatores alimentados por reações de fusão nuclear. Uma das configurações mais promissoras para o sucesso da tecnologia de fusão nuclear na Terra é o Tokamak. Um dos principais obstáculos desta experiência deve-se a mecanismos de turbulência na periferia do plasma. De modo geral a eficiência das atuais experiências de fusão é fortemente influenciada por estes mecanismos de turbulência. A turbulência aumenta consideravelmente o transporte de partículas e energia no plasma periférico, sendo a fonte dominante de perdas em experiências de fusão nuclear. A turbulência verificada na região periférica resulta em filamentos de plasma (regiões de densidade superior). Estes filamentos nascem e propagam-se no plasma periférico. Um resultado fundamental da propagação de filamentos de plasma são as flutuações induzidas em parâmetros do plasma, tal como a densidade e o potencial.

Neste trabalho pretendeu-se compreender a física dos filamentos de plasma resultantes da turbulência, através de uma investigação das flutuações induzidas nos parâmetros do plasma e, finalmente, o transporte de partículas e energia resultante na perifería do ISTTOK (IST Tokamak). Executou-se uma análise detalhada da física da turbulência a várias escalas, desde a sua origem até ao impacto no confinamento do plasma. O ISTTOK é uma experiência ideal para realizar estudos relacionados com o plasma periférico, uma vez que é compacto, flexível e permite a instalação rápida de diagnósticos [1, 2]. Um extenso programa de Fusão Nuclear tem vindo a ser implementado no IST (Instituto Superior Técnico) com diversos diagnósticos instalados, entre os quais as sondas de Langmuir. As sondas de Langmuir consistem basicamente em eletrodos cilíndricos que podem ser inseridos no plasma periférico (até alguns centímetros dentro da última superfície de fluxo fechada). As sondas de Langmuir utilizadas no diagnóstico do plasma do ISTTOK têm uma elevada resolução espacial (de alguns milímetros) e temporal (na ordem de microsegundos). Adicionalmente, no ISTTOK diversos estudos foram implementados

ao longo dos anos com sistemas de múltiplas sondas de Langmuir [2–5]. Durante este trabalho foi usado um sistema de várias sondas separadas poloidalmente, permitindo determinar a estrutura poloidal das fluctuações. Este diagnóstico mostrou-se ideal na determinação do transporte de partículas induzido pelas estruturas de turbulência em propagação no plasma.
As sondas de Langmuir permitem traçar uma curva característica I-V (onde V é a diferença de potencial aplicada à sonda e I a corrente recolhida por esta). Em determinadas condições, aplicando uma alta diferença de potencial negativa, a corrente recolhida corresponde a uma corrente de saturação iónica I_{sat}^{+}. Por outro lado, pode não ser aplicada qualquer diferença de potencial à sonda de modo a medir o potencial flutuante V_f. As flutuações de I_{sat}^{+} permitem estimar as flutuações da densidade de plasma, enquanto as flutuações de V_f permitem estimar as flutuações do potencial de plasma.

Através da aplicação de diferentes técnicas de análise, desde análise estatística até técnicas de correlação e análise espectral, as flutuações foram caracterizadas, contribuindo assim para uma melhor compreensão da física associada aos filamentos do plasma e o seu impacto no transporte radial.

O ISTTOK pode operar com ciclos de corrente alternada, para os quais a direção da corrente de plasma é invertida periodicamente, permitindo obter descargas mais longas. Com a inversão entre ciclos positivos e negativos (direção da corrente de plasma) surgem também alterações na posição do plasma. Durante este trabalho a caracterização das flutuações e do transporte induzido no ISTTOK teve especial atenção a este facto. Foi analisada a importância das estruturas de turbulência ao longo de seis ciclos consecutivos de corrente alternada no ISTTOK.

As diversas propriedades estatísticas das flutuações aqui investigas permitiram concluir que o plasma periférico e a SOL do ISTTOK são dominados por flutuações. Os níveis de flutuações elevados, na orderm de 25% numa região dentro do limitador para 150% na SOL do ISTTOK, foi o primeiro resultado apresentado a comprovar que a região é dominada por flutuações, que são provavelmente induzidas pela turbulência. De seguida, os elevados valores de skewness e kurtosis da densidade e do potencial de plasma foram apresentados, de modo a indicar mais uma vez a importância das flutuações no plasma periférico do ISTTOK. Estas quantidades estatísticas permitiram mostrar o aumento da importância relativa das flutuações induzidas com o aumento do raio.
No capítulo 2 foram mencionados estudos anteriores sobre a importância das flutuações no plasma periférico. De um dos exemplos foi realçada a "universalidade" da Função Densidade de Probabilidade (FDP) para as flutuações do plasma periférico. Este resultado foi também concluído para as flutuações no plasma do ISTTOK, no capítulo 4.

Adicionalmente, o espectro de frequências das flutuações foi investigado. A análise espectral dos sinais de V_f e de I_{sat}^+ obtidos no ISTTOK revelaram que a potência espectral é dominada por frequências na gama 10-100 kHz, e que a amplitude diminui com a frequência de acordo com $1/f^C$, onde C é uma constante que varia nas diferentes regiões do espectro. De modo geral o espectrograma das flutuações do plasma periférico é largo em frequência. Os espectros de frequência tornam-se mais largos com o aumento do raio, indicando o aumento da importância relativa das altas frequências sobre as baixas frequências. Os espectrogramas obtidos assemelham-se ao espectro de *pink noise* que é bastante usual em sinais intermitentes, como o que se dá para os parâmetros do plasma devido a propagação das estruturas de turbulência.

O sistema de sondas utilizado permite determinar V_f e I_{sat}^+ para diferentes posições poloidais no ISTTOK. No total temos sete sondas espaçadas entre si por 2 mm. Os sinais obtidos para as diferentes posições foram comparados através da função correlação cruzada, de modo a determinar a velocidade de propagação, e as estruturas espacial e temporal das flutuações na direção poloidal. A correlação entre as medições nas diferentes posições poloidais é dependente da dimensão poloidal das estruturas intermitentes, assim como do tempo característico e velocidade de propagação destas através do plasma. Os resultados para a correlação cruzada entre dois sinais de V_f ou de I_{sat}^+ indicam a similaridade entre os sinais em função do desfasamento temporal entre os dois. As diferentes técnicas de análise aplicadas durante este trabalho revelaram que as estruturas de turbulência na periferia do tokamak ISTTOK têm uma estrutura temporal na ordem de $\sim 2-10$ μs, em propagação na direção poloidal com $v_\theta = 5-10$ km/s e dimensão poloidal na ordem de $\sim 2-6$ cm.

O fluxo médio de partículas que é induzido pelas flutuações pode ser estimado através das medições simultâneas das flutuações de densidade e de potencial. Tivemos durante este trabalho a oportunidade de enfatizar a grande influência deste fluxo induzido nas perdas totais no plasma periférico de um tokamak. O fluxo de partículas induzido pelas flutuações na periferia do ISTTOK encontra-se na ordem de 10^{21} $m^{-2}s^{-1}$, e apresenta a mesma ordem de grandeza das

perdas totais de partículas no ISTTOK estimadas a partir do confinamento de partículas medido.

Palavras Chave

Fusão Termonuclear; Tokamak; Estruturas de turbulência; Filamentos; Transporte intermitente de partículas.

Contents

List of Figures

List of Tables

Acronyms

ADC	Analog-to-digital converter
Asdex	Axially Symmetric Divertor Experiment
ATCA	Advanced Telecommunications Computing Architecture
BES	Beam emission spectroscopy
CODAS	Control and Data Acquisition System
DAC	Digital-to-analog converter
DAQ	Data Acquisition
GPI	Gas-puff imaging
IST	Instituto Superior Técnico
ISTTOK	IST Tokamak
ITER	International Thermonuclear Experimental Reactor
JET	Joint European Torus
LCFS	Last closed flux surface
LP	Langmuir Probe
MAST	Mega Ampere Spherical Tokamak
MHD	Magnetohydrodynamics
PDF	Probability distribution function
PFCs	Plasma facing components

RAM Random-Access Memory

SDAS Shared DataAccess System

SOL Scrape-off layer

Chapter 1

Thermonuclear fusion

1.1 Introduction

To start the current work we present a simple fusion reaction

$$ {}^{2}_{1}H + {}^{3}_{1}H \rightarrow {}^{4}_{2}He(3.5MeV) + {}^{1}_{0}n(14.1MeV) \tag{1.1} $$

, that could be the solution to the energetic needs of the world. However, how simple it may look, to efficiently harness the energy of this reaction in a continuous and stable mode of operation on earth is not that easy. As it seems to always be fifty years way from taking place. The reaction presented on (1.1) for deuterium (${}^{2}_{1}H$) and tritium (${}^{3}_{1}H$) corresponds to a light element fusion reaction, in which these nuclei fuse to generate heavier α particles (${}^{4}_{2}He$), relishing a great amount of energy. In general a nuclear reaction (fusion and fission) releases about a factor of one million more energy when compared to the energy released in a chemical reaction, such as the ones involved in the combustion of fossil fuels.

Fossil fuels have been the main driver for the civilization's growth and development into a more scientific and technological era. However, with the increase use of fossil fuels came an increase in the emission of green house gases well above the natural production range, busting from the Industrial Revolution, which was marked by a large combustion of coal. Coal has been the prevailing source of electricity and overall energy supply, not only when compared to the remaining fossil fuels, but to all energy sources. It was responsible for 39% of the world's total electricity production in 2014, as shown for the most recent inquires of [18]. Furthermore, in 2014, the remaining electricity production was achieved 22% by gas, 17% by hydroelectric generation, 11% through nuclear sources, 5% through oil, and finally renewable energy sources

entered with various others in a participation of only 7%, [18].

The repercussions on the environment that follow from carbon dioxide and other green house emissions have resulted in the increase of the average global temperatures. Followed by this came the raise in sea levels with growing rates, and on other climate changes that have imposed a large conscience about the use of fossil fuels. Although society has understood the repercussions of fossil fuel usage, major obstacles are still present for the remaining energy options. For example, renewable sources overall present efficiency instabilities based on the oscillations of the meteorologic conditions. Also require a large area to increase the environmental condition's exploitation. On the other hand, present nuclear fission power plants not only require high investments for construction, but are also involved in political conflicts. For these reasons fossil fuels will remain the main source of electricity production in the next years to come. In particular coal, whose world's reserve could be used to produce electricity for another hundreds of years, given current world rate of consumption. Nevertheless, even before the limits of fossil fuel reserves are reached, given the environmental repercussions mentioned above, this source of energy production will have to be eventually reduced. Since the current options to fossil fuels don't present to be efficient alternatives for the long run, a new scientific effort must be done to keep up with the seemingly never-ending growing needs of society. Not just in an economically positive way, but also presenting to be a less harmful alternative to the environment.

Thermonuclear fusion presents to be a very attractive option for producing uninterrupted electricity, with even higher gain in comparison to fission technology. In fission the bombardment of ${}^{235}_{92}U$ with a neutron results in 0.88 MeV per nucleon ([19]), macroscopically equivalent to 84×10^6 MJ/kg. During the fusion of D-T nuclei the energy relished per reaction corresponds to 3.52 MeV per nucleon, which is macroscopically equivalent to 338×10^6 MJ/kg ([19]). While deuterium nuclei are naturally abundant in earth's oceans, there is no natural tritium on earth. It's possible, however, to breed tritium using lithium. Very attractive and simple numbers presented by Dr Ian Chapman from the Culham Center for Fusion energy at the Royal Institution illustrated how one mole of the D-T nuclei could be used to produce about 10^{12} J of energy. The D-T nuclei are relatively abundant, and one mole (equivalent to a few grams of the reactants) found for example in a bathtub of water along with the lithium found in two laptop batteries. This rather accessible amount of reactants would nearly sustain the energy of one person for his entire adult life, assuming already a very high consumption lifestyle. The 17.6 MeV from the resulting products in (1.1), considering now 1 mol (6.03×10^{23} particles), would result in about 1.65×10^{12} J, and as suggested by Dr Ian Chapman to a 60 years energy supply

of one person, assuming a 20 KWh/day consumption rate.

The understanding of the current limitations in achieving uninterrupted reactions in present thermonuclear devices is fundamental. It should provide the start for a path in the construction of economically feasible reactors with high power gain. Although a safe guess is that the costs of a fusion facility should be higher than current alternatives given the complex, and some, still undeveloped technology needed. However, still laying in a competitive range. Projects involving experimental machines designed to explore fusion, such as ISTTOK (the fusion experiment at Instituto Superior Técnico) and, in preparation, the big collaboration in ITER (which will count with 35 nations to build the world's largest tokamak in southern France) will contribute in this understanding. Making possible in the future the incorporation of the improved technology in complete electrical power plants (maybe just another fifty years).

Along with the great benefits attractive to fusion comes tremendous challenges to the physics and engineering communities, from plasma physics, transport theories, to material and electrical engineering. Nuclear fusion is an never-ending challenge provider.
In order for the positively charged nuclei to overcome the Coulomb repulsion among them and fuse, they will have to possess extremely high kinetic energies. The reaction presented on (1.1) is one of a couple of options for a device based on fusion reactions between light elements, and should be the main focus for fusion power plants. Mainly given to its higher cross-section at lower temperatures. In particular, temperatures of about 20 keV (over 200 million Kelvin (k)) are necessary for the reactants on (1.1) to fuse in a continuous and self-sustained state of ignition. Starting with an initial fuel of atomic deuterium and tritium, in the necessary kinetic energy conditions for the positive nuclei of the two species to come close and undergo a fusion reaction, the fuel will have then become a plasma, presenting outstanding temperatures way above the core of stars.

1.2 Thermonuclear Ignition

Great efforts have been done to construct a device capable of reaching stable thermonuclear ignition. Ignition implies maintaining a significant amount of plasma confined at the high temperatures needed, and during a sufficient time to result in a positive power balance. When these features have been achieved a fusion device could operate uninterruptedly being fed at a given rate with fuel. The Lawson criterion [19] and later the "triple product", given as

$$nT\tau_E \geq f_{D-T} \sim (3-5) \times 10^{21} sm^{-3} keV, \qquad \text{"triple product"} \tag{1.2}$$

for the D-T reaction, express the conditions on plasma density ($n_{e,i} \sim n$), temperature ($T_{e,i} \sim T$) and energy confinement time (τ_e) in order for a magnetic fusion device to reach thermonuclear ignition. For a plasma in ignition (satisfying the criteria) the alpha power balances the energy sinks in the plasma, such as the irreducible Bremsstrahlung losses, [19]. Therefore, the fusion reactions in the plasma are self-sustained by one of the products they originate. These highly energetic alpha particles allow to maintain the plasma's energy requirements through multiple collisions with the D and T nuclei.
For the D-T reaction the minimum of the triplet criterion occurs for temperatures around the $T = 20$ keV reference. Commonly, to reach ignition, a combination of ohmic and external auxiliary heating are used in the initial transient phase until a transition temperature. Previous to the transition temperature, the alpha heating is negligible against the losses due to thermal conduction and Bremsstrahlung radiation. Above it the alpha heating power becomes more significant and eventually rises the temperature to satisfy the "triple product", according to the value of the two remaining quantities. Nonetheless, various combinations of the three parameters in the "triple product" are considered among the fusion community to reach plasma ignition. Current devices have not yet been able to sustain simultaneously the parameters in order to reach and maintain a steady and continuous mode of operation with an ignited plasma. However, ITER is expected to exceed all current results.

1.3 Tokamak Principles

There are different experimental configurations still in consideration to reach on earth the plasma confinement requirements that allow to generate thermonuclear fusion power.
Far in the run are magnetic confinement devices, such as tokamaks (experiments as ISTTOK, ITER, JET, Asdex Upgrade, DIII-D, Tore Supra and Alcator C-Mod), stellarators (TJ-II and Wendelstein 7-X, for example) and also spherical torus (as MAST). The main principle of these devices is a system of magnetic fields responsible for the confinement of the plasma charged particles in a vacuum chamber.

The charged alpha particles that result from (1.1) are confined in the chamber by the magnetic fields, and their power should sustain the ignited plasma. On the other hand, the neutrons

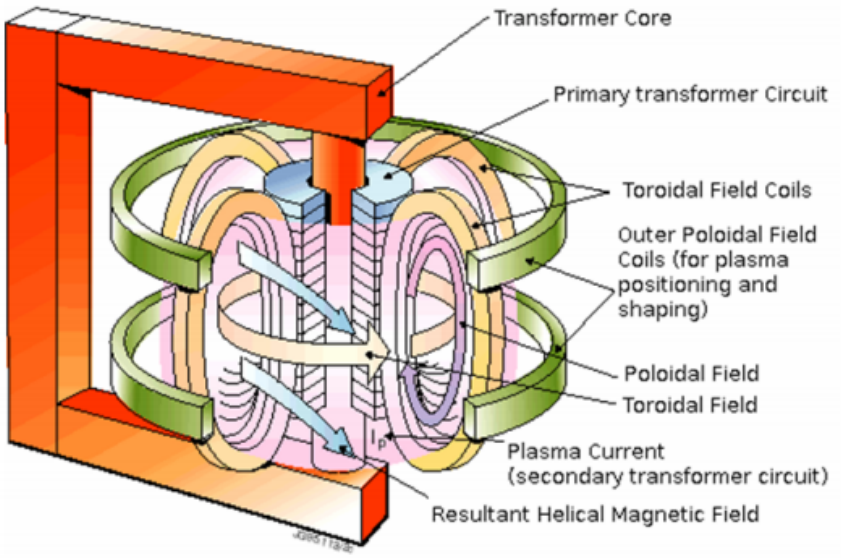

Figure 1.1 General scheme of a typical tokamak. [Adapted figure from [6]].

escape the magnetic fields and the plasma providing the main source of heat in material structures (the blanket), and are ultimately responsible for the production of electricity as commonly seen for other electricity sources, via restive heating, water vessels and turbines.
The tokamak is the most promising fusion configuration. Leading the run to understand and achieve fusion power in a controlled manner, and also in one that will allow to obtain a considerable positive gain in the approaching ITER experiment. In a tokamak the plasma is kept in a vacuum chamber with the shape of a torus (toroidal magnetic chamber), as in the scheme on Fig. 1.1. The acronym comes from the Russian designation *Toroidalnaya Kamera Magnitnaya*. The device was first introduced in 1950's by the work of Soviet physicists, [20].

The charged particles are kept in toroidal motion due to the Lorentz force. That causes the particles to orbit (with Larmor radius) along the toroidal magnetic field lines. The choice of a plasma vessel shaped as a torus is in order to avoid particle losses at the end of the fields lines. The radius of the center of the torus $R = R_0$ is referred to as the major radius, and the radius of the torus cross section $r = a$ as the minor radius. Finally, R/a is referred to as the aspect ratio R_0/a.

The toroidal field B_ϕ is generated by the coils that contour the chamber's cross section, the toroidal magnetic coils, in Figs. 1.1 and 1.2. Nevertheless, the particles must spin along helical field lines, to balance overall velocity drift components that arise from the toroidal geometry of

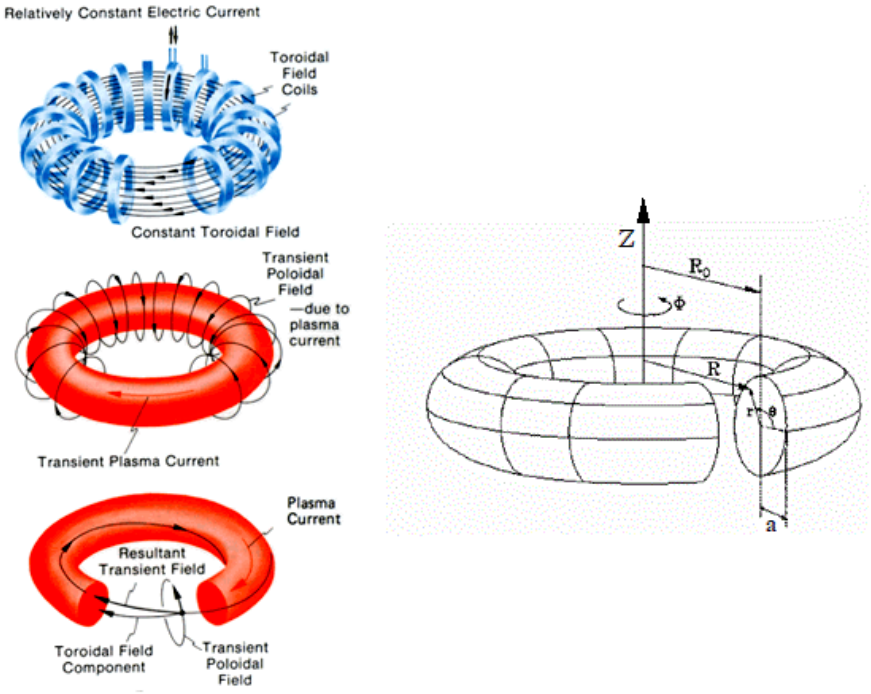

Figure 1.2 General scheme of the toroidal and poloidal directions and fields in a tokamak device. Main geometric parameters of the device. [Adapted figure from [7]].

the magnetic field and therefore avoid an unstable assemble.

The geometry of the toroidal field results in vertical velocity drifts (sec. 1.4), namely the $\nabla\vec{B}$ and curvature drifts. That arise due to the field's dependence on the major radius ($|\vec{B_\phi}| \propto 1/R$) and due to the curvature of the field lines, respectively. The components of these vertical drifts in opposite directions for ions and electrons establish a vertical electrical field that ultimately results in the $\vec{E} \times \vec{B}$ drift. The $\vec{E} \times \vec{B}$ is radially outwards for both ions and electrons, and therefore causes a coherent displacement of the plasma outwards into the vessel's walls.

This setback for an initial toroidal field scheme (also known as the pure toroidal θ-pinch configuration) provides therefore an unstable confinement. To balance these vertical drifts of ions and electrons the field lines must wrap around the torus, as shown in Fig. 1.2. The particles in turn will still possess the vertical $\nabla\vec{B}$ and curvature drifts. However, as they move along helical field lines for a significant number of toroidal turns, the vertical $\nabla\vec{B}$ and curvature drifts are averaged out.

The helical magnetic field is attained (in a configuration known as the screw pinch) by the combination of the toroidal magnetic field B_ϕ with a small poloidal magnetic field B_θ. The B_θ field results from a toroidal current circulating on the plasma (usually $B_\theta \sim B_\phi/10$). This current corresponds to the secondary winding of a transformer, which has a solenoid in the center of the torus as primary winding, seen in Fig. 1.1.
The safety factor, q, primarily represents the number of toroidal turns required for any given field line to perform one full poloidal turn. In the picture of macroscopic stability based on the MHD (Magnetohydrodynamics) model q is given by 1.3,

$$q(r) = \frac{rB_\phi(r)}{R_0 B_\theta(r)}. \tag{1.3}$$

This estimation holds for most axisymmetric toroidal configurations (and considering a cylindrical, large aspect ratio approximation), [19]. Configurations with $q > 2$ at the edge tend to be more stable.

The toroidal, poloidal and radial directions for a tokamak plasma can be better understood in Fig. 1.2, respectively, along ϕ, θ and $\vec{r}$. It is often referred to the direction along the magnetic field lines as simply the parallel direction, and perpendicularly to the magnetic field lines as just the perpendicular direction.

The shaping and positioning of the plasma is still managed by an external vertical field,

which is established by a system of coils often located outside the first wall. These coils are referred to as the outer poloidal coils on Fig. 1.1, (in some schemes, can be also found a set of inner poloidal coils).

1.3.1 Scrape-off layer

The magnetic field lines and the current lines lie on surfaces of constant pressure. A set of nested toroidal surfaces in a well-confined MHD plasma equilibrium, [19]. Both the magnetic field and current lines have no component perpendicular to these nested surfaces, thus they are also commonly referred to as flux surfaces. The flux surfaces should be closed surfaces in the vacuum chamber to avoid particle loss. Nonetheless, in the exterior region they are interrupted by components of the chamber's walls. The outer region of the chamber characteristic of having open magnetic surfaces (opened magnetic field lines) is usually referred to as scrape-off layer (SOL). The screw pinch configuration, used to confine particles along the helical field lines, should limit particle loss to result only from particle collisions along the radial direction. However, as desired to discuss in this work a solid understanding through the last decades has revealed that more complex plasma mechanisms such as high density plasma features (known as filaments or blob-filaments) appear and propagate in the SOL region of fusion plasmas. It is experimentally observed that plasma losses are up to 100 times larger than the expected to occur by particle collisions, most probably due to the filamentary structures. In fact these plasma blobs are also strongly influenced by the $\nabla\vec{B}$ and curvature drifts. Polarized blob structures occur in the plasma outer regions with the electric field on these structures providing a mechanism for their convective $\vec{E} \times \vec{B}$ drift.

The division between the core plasma (confined inside the closed flux surfaces) an the SOL is marked by the last closed flux surface (LCFS) in limited machines, or by the magnetic separatrix in diverted machines. On Fig. 1.3 are presented general schemes of the LCFS or separatrix considering the two common scenarios for the plasma-wall interface (limiter or divertor).
A limiter is simply a material structure interrupting the field lines before the actual chamber walls, and therefore determining the LCFS. Limiters can be installed in various geometries. Commonly seen are poloidal limiters, which can be a material with the shape of the vacuum vessel, but having a smaller diameter, and extending completely along the poloidal perimeter. Could also have an interrupted structure (rail limiters). Limiters can even be assembled as just a localized solid component in the vessel. Moreover a material interface placed in a certain local

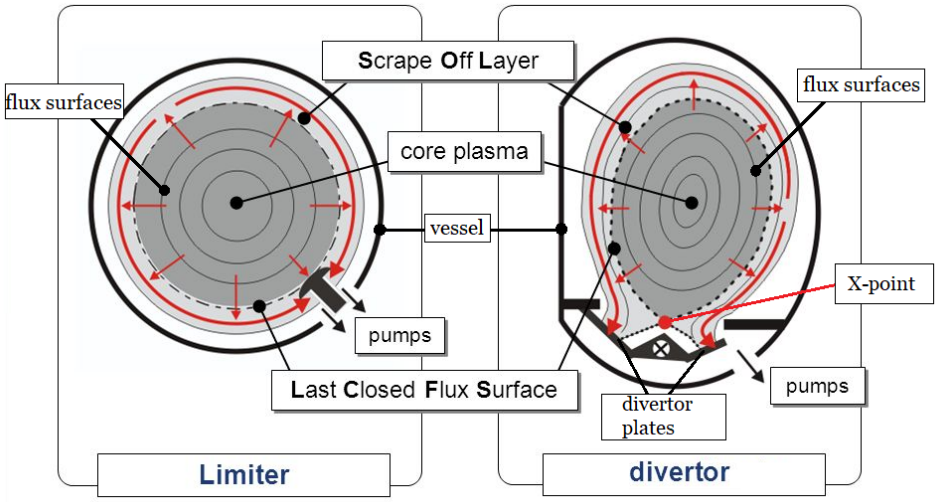

Figure 1.3 General schemes for the cross section of a tokamak with a divertor or with a magnetic separatrix. Common scenarios for the plasma-material interface. For devices with a divertor the plasma-material interaction takes place further away from the confined plasma, in a localized region on the vessel's edge (the divertor target plates). Extra coils are responsible for producing the X-point in the poloidal magnetic field. Near the X-point are the divertor target plates, set to better withstand plasma interactions. [Adapted figure from [8]].

position of the vessel but extending along the toroidal direction corresponds to a toroidal limiter. In the second common configuration for the plasma-material interface, the divertor, extra coils are responsible for producing a null point in the poloidal magnetic field, which is also referred to as an X-point, localized in the edge as in Fig. 1.3, [8]. Near the null point are the plasma facing components for this assemble, the divertor target plates. For this configuration the plasma-material interaction takes place much further away from the plasma confinement region on the closed flux surfaces. As a consequence, is reduced the probability of contamination of the plasma core with impurities that result from the interaction between the plasma and the plasma facing components. Also reduces the probabilities on wall damage, due to the lost of particles and energy outwards to the walls. Therefore a divertor is often seen in use for the majority of tokamaks.

1.4 Introduction to Plasma Physics

As previously mentioned, the positive nuclei have to overcome the Coulomb repulsion among them to be found in the short-range cross-section corresponding to the fusion reaction. The conditions of kinetic energy require very high values of temperature, for which ions are found in the tail of the Maxwellian energy distribution. Near the temperature of $T \sim 100$ keV the cross-

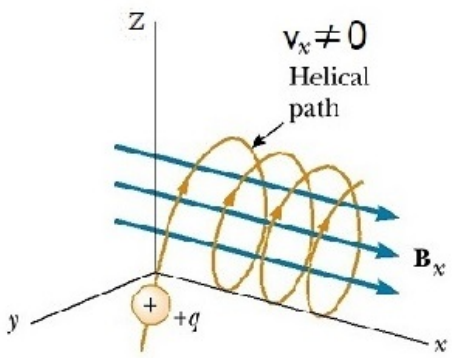

Figure 1.4 Lorentz force and Larmor motion. Uniform circular motion in the plane perpendicular to the magnetic field, with r_L and w_L. Helical path for charged particles with a velocity parallel to the magnetic field. [Adapted figure from [9]].

section of the reaction on 1.1 approaches a maximum. However, such high temperatures are not required to initialize the reactions. The reference value is around $T = 20$ keV. Under these conditions the fuel becomes a plasma consisting of an ionized gas composed by two independent species of charged particles: the positive ions (both deuterium an tritium nuclei) and a separate specie of electrons, where a quasi-neutrality condition holds for the ion and electron densities, i.e. $n_i \sim n_e$. Also an important general characteristic is the dominance of long range electromagnetic forces over short range collisions, and it has a major role in the collective behavior displayed by plasmas.

The Debye length, λ_D, in (1.4), corresponds to the characteristic decay length of charge density and potential in a plasma, and should be smaller than the plasma size L_p, i.e. $\lambda_D << L_p$, in order for the collective behavior to be dominate. In a 3-d approach of the problem (Debye shielding, [19]) the condition on (1.6) arises, [19]. The parameter in (1.6) is usually incorporated in the plasma description in order to ensure that collective behavior is dominant over collisions.

$$\lambda_D = \left(\frac{\epsilon_0 T_e}{e^2 n_\infty}\right)^2. \tag{1.4}$$

$$N_D = n\frac{4\pi}{3}\lambda_D^3. \tag{1.5}$$

$$N_D >> 1. \tag{1.6}$$

1.4.1 Guiding center drifts

Let us start by focusing on the confinement established by an imposed magnetic field, considered to be constant and uniform in both time and space, B. Due to the Lorentz force, particles are forced to rotate around the the magnetic field lines with

$$r_{L_{e,i}} = \frac{v_\perp m_{e,i}}{|Q|B} \tag{1.7}$$

, and

$$w_{L_{e,i}} = \frac{|Q|B}{m_{e,i}} \tag{1.8}$$

, where $r_{L_{e,i}}$ corresponds to the Larmor radius (or gyro-radius) for electrons and ions, $w_{L_{e,i}}$ to the cyclotron frequency (or gyro-frequency), $m_{e,i}$ to the particles mass, and Q to their respective charges. Finally, $v_\perp$ corresponds to the particles velocity in the direction perpendicular to the magnetic field. Moreover, if the particles are moving in the direction parallel to the magnetic field, i.e. $v_\parallel \neq 0$, the result is a helical orbit as in Fig. 1.4, [9]. In a tokamak device, in particular, the thermal velocity of the high energy particles allows them to move freely parallel to the magnetic field lines, while confined by the Lorentz force in the perpendicular direction. The gyro-motion around the field lines corresponds to the fastest motion (shortest time scale, $\propto 1/w_{L_{e,i}}$) and the solutions listed below correspond to slower drifts of the center of the gyro-motion (guiding center) of each particle.

1. $\vec{E} \times \vec{B}$ drift

   The presence of any force perpendicular to $\vec{B}$, as the electric force that results from $\vec{E}_\perp \neq 0$, origins a drift of the guiding center in the plane perpendicular to $\vec{B}$. The acceleration due to an electric force on the perpendicular plane causes $r_{L_{e,i}}$ to be bigger when $v_{L_{e,i}}$ increases. The end result is a drift in the direction perpendicular to both the electric and magnetic fields. Both ions and electrons have the same $\vec{E} \times \vec{B}$ velocity drift, independently of their values of charge and mass,

$$\vec{v}_{\vec{E}\times\vec{B}} = \frac{\vec{E} \times \vec{B}}{B^2}. \tag{1.9}$$

   In general a force $\vec{F}_\perp$ perpendicular to the magnetic field results in a perturbation term $\vec{v}_{\vec{F}_\perp \times \vec{B}}$ from the Larmor motion, perpendicular to both the field and the force,

$$\vec{v}_{\vec{F_\perp}\times\vec{B}} = \frac{1}{q}\frac{\vec{F_\perp}\times\vec{B}}{B^2}. \tag{1.10}$$

2. $\vec{\nabla}B$ drift

   If the magnetic field is not uniform in space the Larmor motion varies $\propto 1/B$ in such a way that the guiding center drift is according to the approximate term,

$$\vec{v}_{\vec{\nabla}B} = \frac{m_j v_\perp^2}{2qB}\frac{\vec{B}\times\vec{\nabla}B}{B^2}. \tag{1.11}$$

3. Curvature drift

   For curved magnetic field lines a centrifugal force acts on the particles as a result of the curvilinear movement along the field direction. As mentioned before, the presence of a perpendicular force results in a drift perpendicular to both the magnetic field and the force. The curvature drift adds to the $\vec{\nabla}B$ drift and both occur in opposite directions for charges of opposing signs.

4. Diamagnetic fluid drift

   The diamagnetic drift isn't perceptible in the single particle picture. It can't be account for single particle motion as it is not a guiding center drift. However, in the fluid picture, in the presence of a pressure gradient the fact that their are more particles moving in one direction implies a drift for the averaged velocity value of the fluid element. The perturbation from the fluid Larmor motion that results from $\vec{\nabla}P \neq 0$, is given by

$$\vec{v}_D = -\frac{\vec{\nabla}P\times\vec{B}}{n_j q_j B^2}. \tag{1.12}$$

   The ion diamagnetic drift direction is a common reference in fusion devices.

In general different values of charge, mass and temperature (kinetic energies) may lead to different velocity drifts between the plasma species, resulting in electric currents and fields.

1.4.2 Fluid description and fluid drifts

Whether the approach is to study plasmas considering single particle motion, through kinetic equations, or to simplify the problem describing the plasma as a Two Fluid Model, as represented below (equations (1.13) to (1.22)), a consistent result arises from every approach. Characterizing in a similar matter several particle drifts that result for charged particles in the presence of electromagnetic fields.

$$\frac{\partial n_j}{\partial t} + \vec{\nabla}(n_j \vec{v}_j) = 0 \tag{1.13}$$

Continuity Equation

$$n_j m_j \left[\frac{\partial \vec{v}_j}{\partial t} + (\vec{v}_j \cdot \vec{\nabla})\vec{v}_j\right] = n_j q_j \left[\vec{E} + \vec{v}_j \times \vec{B}\right] - \vec{\nabla} P_j - \bar{\nu}_{jk} n_j m_j (\vec{v}_j - \vec{v}_k) \tag{1.14}$$

Force Equation

$$P_j n_j^{-\gamma} = cte. \tag{1.15}$$

Energy/Equation of State

Maxwell's Equations

$$\vec{\nabla} \cdot \vec{B} = 0 \tag{1.16}$$

$$\vec{\nabla} \cdot \vec{E} = \frac{\rho}{\epsilon_0} \tag{1.17}$$

$$\vec{\nabla} \times \vec{B} = \mu_0 \vec{J} + \frac{1}{e^2} \frac{\partial \vec{E}}{\partial t} \tag{1.18}$$

$$\vec{\nabla} \times \vec{E} = -\frac{\partial \vec{B}}{\partial t} \tag{1.19}$$

where,

$$\rho = \sum_j q_j n_j \tag{1.20}$$

$$\vec{J} = \sum_j q_j n_j \vec{v}_j \tag{1.21}$$

$$\tag{1.22}$$

The model presented above is a Self Consistent Two Fluid Model that describes several

averaged macroscopic parameters such as density, velocity, temperature and pressure of the independent species composing the plasma, [19]. It provides a description of the plasma as a mixture of different fluids j, usually, found to be $j = e$ (electorns) and i (ions) for fully ionized plasmas. However, a third specie could be considered for partially ionized plasmas still containing a considerable density of neutrals. In that case $j = e, i$ and n. It is referred to as a Self Consistent Model, since it not only accounts for how electrons and ions respond in the presence of electric and magnetic fields, but then also to how these densities (n_e, n_i), and therefore the charge and current densities riposte on the value of the fields. In this way the model accounts for the self consistent loop of dependencies occurring in the ionized plasma medium.

Each equation in the model holds for an individual species j. The first equation (1.13) is the well known Continuity equation, that corresponds to the particle conservation equation. The second equation of the model (1.14) arises from the momentum conservation for each species, commonly referred to as the Force Equation. It accounts for the momentum exchange due to the Lorentz Force acting on the particles, also due to a Pressure Force (for an isotropic medium), and finally the exchange of momentum that results from collisions between the different species in the medium. In the Force equation the last term represents the overall loss of momentum by species j when colliding with particles from species k. Seeing that ν_{jk} corresponds to the rate of collisions between the two species, the corresponding term in 1.14 can be referred to as the rate of momentum loss by species j thanks to collisions with species k. The collisions between like particles are neglected since the total momentum for the species is conserved, given the overall averaged values. The third equation of the Two Fluid Model (1.15) for energy conservation is taken as an Equation of State.

The validation of the Fluid Description for a fusion plasma mainly relies on the fact that in a (toroidal) magnetic confinement device particles are trapped in the parallel direction because of the gyro-motion along the magnetic field lines, Fig. 1.2. In the perpendicular direction to the field lines this guaranties that the $N_j = n_j \Delta V$ particles in a fluid element ΔV act like the particles in a highly collisional gas. The particles in a given fluid element move coherently together. Each individual particle stays confined in a physical space always within short distances relative to its neighboring particles (admitting an approximately constant Larmor radius). Each fluid element in the model is described by the macroscopic averaged parameters $g_j(\vec{r}, t)$. The macroscopic parameters correspond to the average of all the individual particles' values for that same property over the velocity space. In general $g_j(\vec{r}, t)$ for a fluid element centered at $\vec{r}$ at a time instant t is given by

$$g_j(\vec{r},t) = \frac{\int g_j \cdot f_j(\vec{r},t) dv_j}{\int f_j(\vec{r},t) dv_j}. \tag{1.23}$$

Therefore loosing the need to have a detailed track of each particle's in the velocity space.

Relative to the present work the Two Fluid Model is a good approach to further understand important velocity drifts (away from the gyro-motion along the toroidal magnetic field lines), for both electron and ion species. The velocity drifts are not only fundamental in understanding several characteristics necessary in the design of fusion devices, but also in comprehending the origin and radial convection of coherent plasma structures (called "blob-filaments").
Taking advantage of a simplification of the Force Equation, in which we neglected the momentum transfer due to all collisions, equation (1.24) below,

$$n_j m_j \frac{d\vec{v}_j}{dt} = n_j q_j \vec{E} + n_j q_j \left[\vec{v}_j \times \vec{B}\right] - \vec{\nabla} P_j \tag{1.24}$$

Force Equation

$$\begin{cases} \frac{d\vec{v}_{L_j}}{dt} = \frac{q_j}{m_j}\left[\vec{v}_{L_j} \times \vec{B}\right] & \text{Larmor motion } \vec{v}_L \\ \frac{d\vec{v}_{\vec{E}\times\vec{B}_j}}{dt} = \frac{q_j}{m_j}\vec{E} & \vec{E}\times\vec{B} \text{ drift } \vec{v}_{\vec{E}\times\vec{B}} \\ \frac{d\vec{v}_{D_j}}{dt} = \frac{1}{n_j m_j} - \vec{\nabla} P_j & \text{Diamagnetic drift } \vec{v}_D \end{cases} \tag{1.25}$$

, it is easy to highlight some aspects on the right hand-side that are helpful in comprehending the velocity drifts. In (1.24) the second term in the right-hand side corresponds to the fluid gyro-motion $\propto d\vec{v}_{L_j}/dt$. Still on the right-hand side it's represented the velocity drift that arises from perpendicular magnetic and electric fields (first term), the $\vec{E}\times\vec{B}$ drift $\vec{v}_{\vec{E}\times\vec{B}}$. The third term corresponds to the diamagnetic drift due to the presence of a pressure gradient $\vec{\nabla}P$.

From the Two Fluid Model can be derived the single-fluid model MHD (magnetohydrodynamics). The MHD model is more often found to analyze the macroscopic equilibrium and stability of a fusion plasma than the previous Two Fluid Model. The MHD model can be obtained from the two-fluid analysis by reducing to single-fluid variables, while considering the length and time scales that characterize macroscopic plasma behavior, [13]. Such as the radius

(a) of a plasma volume being used to define the appropriate length scale L, ($L \sim a$), while the ion thermal transit time (a/v_{Ti}) across the plasma being taken as the the appropriate time scale τ, ($\tau \sim a/v_{Ti}$).

As previously mentioned, there are a couple of approaches to study and describe fusion plasmas providing similar results as the ones introduced in section 1.4 for guiding center and fluid drifts. The expressions provided through 1.4 are analyzed with more care in [19] and [21], accompanied with extended information on the approximations and considerations taken in their derivations.

Chapter 2

Edge turbulence in fusion devices

2.1 Introduction

In the edge of tokamaks and general fusion devices a major challenge is faced regarding enhanced losses of particles and energy. The performance of tokamaks drastically diminishes as enhanced losses at the edge degrade the confinement conditions.
The edge plasma is generally understood as starting a few centimeters inside the last closed flux surface (LCFS) (in limited devices) or magnetic separatrix (in diverted machines), where still lays the confined plasma on closed flux surfaces. The region extends up to the scrape-off layer plasma (SOL), where opened field lines are seen to be interrupted by material structures, (chapter 1). In the edge plasma the neutral particle density is not negligible and therefore atomic processes strongly influence the local particle and energy balance.

It has been understood from experimental investigations, mainly over the last couple of decades, that highly localized density structures are frequently born near the LCFS. A strong theoretical hypothesis is that it is due to the nonlinear saturation of turbulence (i.e. small-scale instabilities) in the tokamak plasma boundary.
Turbulence induced structures and associated electrostatic fluctuations of plasma quantities are routinely observed in the edge and SOL plasma, this phenomenon dominates the particle and energy losses and greatly limits the overall confinement conditions. In this sense, numerous edge studies, in distinctively parameterized devices, aim to gadder a solid understanding of the physics processes in the origin of the edge turbulence and the limitations that they set on plasma confinement. An effort to also prevent the enhanced plasma interaction and damaging on plasma facing components (PFCs), contamination of the vessel with impurities, and the influence on the

particle recycling and plasma exhaust processes. Several investigations have already determined that losses in tokamak devices are not continuous, but, instead, take place in an intermittent manner due to the radial convection of turbulent induced structures known as filaments (or blobs), [12, 13, 22–24].

The study of different experimental configurations in which turbulence arises can also give an insight on the instability mechanisms in its origin, therefore helping to understand how to reduce the dominant losses.
Conjointly with the time and space structure of turbulent filaments, a large body of work have been dedicated into characterizing their statistical distributions. In both subjects a wide set of results has been gathered showing a large coherency of the edge turbulence characteristics for most fusion devices. Previous results can be found from [14] to [25].

This chapter will reference a basic model for the convected particle losses by turbulence induced structures, [14]. In order to clarify the physics mechanisms in which the filament structures degrade the performance of fusion plasmas. It is also presented general plasma properties that should be expected in turbulence dominant regions, setting a useful background for the results presented and discussed in chapters 4 and 5.

2.2 Review on edge turbulence properties

The experimental investigations of the turbulence induced structures will provide a picture on the conditions in which these mechanisms dominate in the edge plasma. However, the multitude of plasma instability mechanisms driving turbulent regions is not thoroughly scooped in this study.

The induced filaments are generally characterized as magnetic-field-aligned plasma structures, [14], which present considerable higher density than that of the background plasma. They are very localized in the perpendicular direction (having perpendicular scale lengths intermediate between the ion gyro radius and macroscopic machine dimensions), while extending along the parallel direction. On [14] a working definition can be found that tries to encompass the theoretical and experimental investigations focused on the blob objects. From which it is worth to add that the plasma blob-filaments have a single-picked density distribution, with a maximum typically 2–3 higher than the surrounding rms fluctuations of the background plasma. Secondly, the filament variation along the magnetic field, to which they are highly align to, is

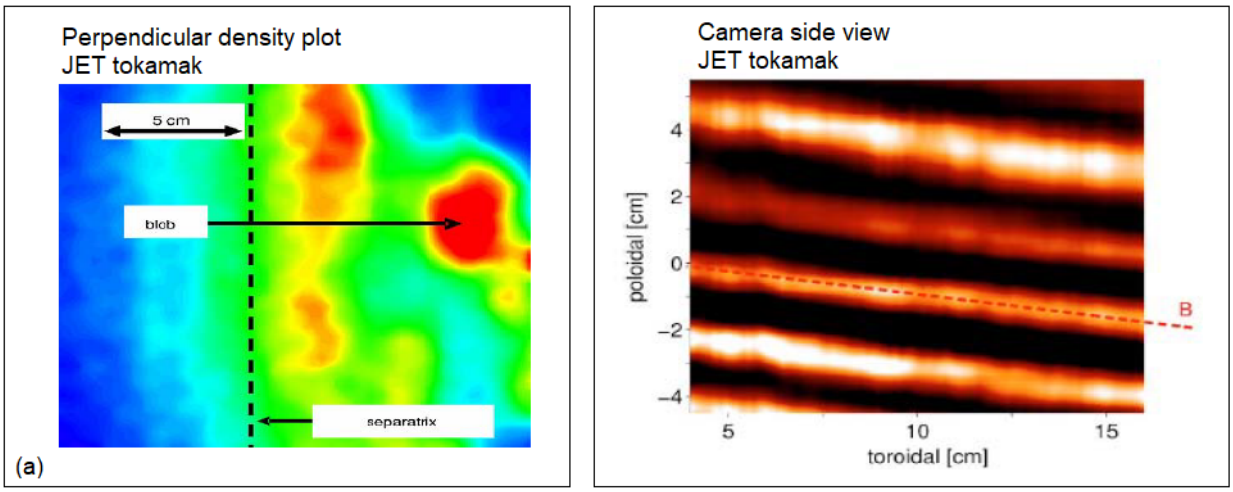

Figure 2.1 Results from cameras installed in the JET tokamak. In the left is showing a 2D density plot (intensity map) in the perpendicular plane. In the perpendicular view, high density blob-like structures are shown just outside the separatrix (dashed black line). On the right, the high density structures at the JET tokamak are seen as brighter filaments, extending along the toroidal field (dashed red line). [Adapted figure from [10]].

much weaker than the variation taking place in the perpendicular direction. At last, the blob motion is dominated by a convective $\vec{E} \times \vec{B}$ velocity component as a result of a charge polarizing force.

2.2.1 Spatial and temporal structures

The large number of edge investigations have been a great lever in clarifying the previous spatial picture of highly localized structures in the perpendicular plane, having a blob-like two-dimensional (2D) spatial structure, while extending over the torus, in the parallel direction, with a filament three-dimensional (3D) structure. The temporal and spatial structures of the "blob-filaments", as named on [14], have been interpreted using various different diagnostics and analysis techniques. Langmuir Probes, which consist in electrodes inserted in the edge plasma, are the most common and simplest diagnostic used in edge/SOL studies. Nonetheless, with the pressing need into understanding the edge turbulence processes, a large number of imaging diagnostics such as beam emission spectroscopy (BES), gas-puff imaging (GPI), and fast cameras have been well developed, and provide an intuitive and clarifying picture of the blob-filament structures.

From the imaging results shown as example on Fig. 2.1 it is observable on the perpendicular

plane (2D density plot) the resembling "blob" objects of higher density over the surrounding background plasma. The example is obtained from imaging diagnostics in the Joint European Torus (JET) experiment, [10]. On the 3D image, also obtained from the JET tokamak, the 3D filament structures from the extended blobs along the parallel direction are shown.
On camera images from the Mega Amp Spherical Tokamak (MAST) experiment, Fig. 2.2, edge filaments of higher density are evidenced through brighter pixels in the images. The filament structures not only show to extend around the chamber, but also to be highly aligned with the magnetic field, having the same helical geometry along the torus. The helical geometry of the magnetic field was introduced on chapter 1, Fig. 1.2.

Additional observations of 2D blob structures in the perpendicular plane are shown in Fig. 2.3 and Fig. 2.4. The former from the GPI diagnostic in the National Spherical Torus Experiment (NSTX tokamak), [11], an the latter obtained with the BES diagnostic on the edge of the DIII-D tokamak, [12, 26]. The high density 2D blob structures, coherently seen in these measurements, generally fall between 1–3 cm (along $\vec{r}$), [14] and are seen to propagate radially with typical velocities of $\sim$ 0.5–2 km/s.

On the other hand, theory predicts that while the higher density blobs are convected from the edge of the confined plasma through the SOL, regions of reduced density (density holes) propagate in the opposite direction (inward into the confinement region), as evidenced in the references [126, 129, 130, 144, 158, 159, 169, and 180] from [14]. To corroborate the theoretical scenario of plasma holes, simulations with seeded holes can be used to illustrate their inward motion, [27]. The formation of density holes and blobs due to plasma instabilities near the edge of the confined plasma can be read in more detail in [28, 29].
On Fig. 2.4, showing the example from the BES diagnostic obtained at the DIII-D tokamak [12, 26], it's seen not only the high density features corresponding to the blob-like structures (in red), but also low density features near the LCFS (in blue). The image shows two frames, with a time difference of 6 μs. In the figure it is seen a radial and poloidal displacement of the high density blobs, which are marked by a dashed circle in both frames.

2.2.2 Propagation mechanism by a charge polarizing force

The plasma filaments provide a mechanism for the radial outwards transport of particles and energy, resulting in losses from the edge boundary region in which they are born. A blob trans-

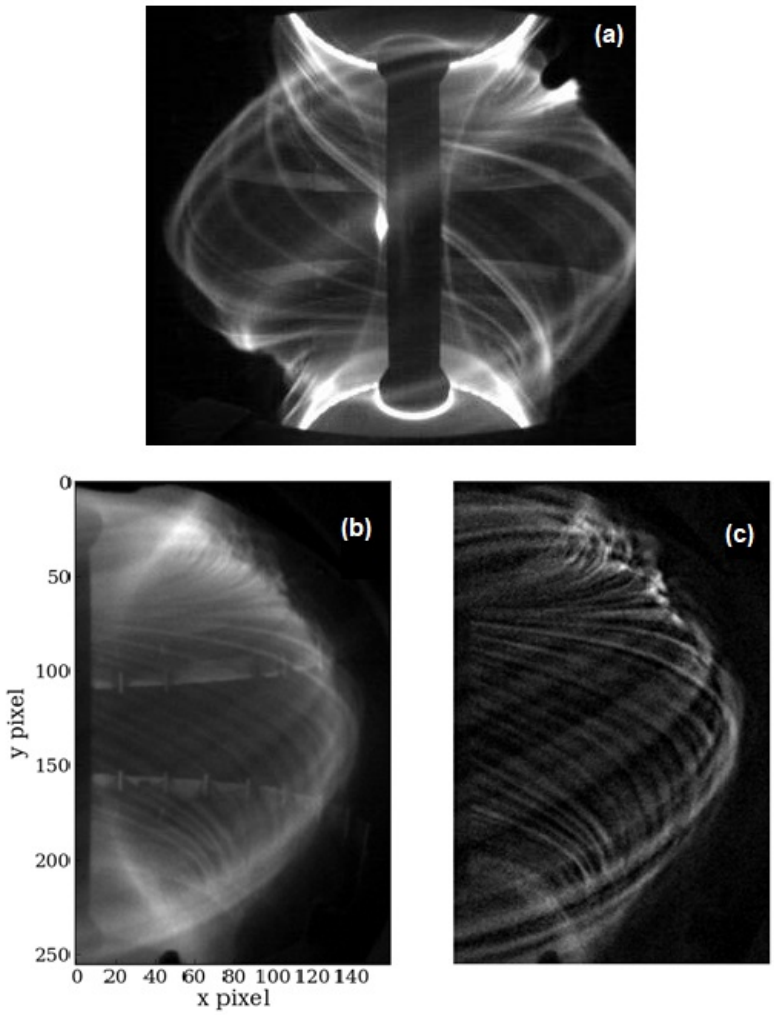

Figure 2.2 (a, b) Camera Image from the MAST tokamk. Images obtained from the MAST tokamak (a,b) are processed in order to evidence the high density filament structures corresponding to brighter pixels (c).
The filament structures not only show to extended onward in the chamber, but also to be highly aligned with the toroidal magnetic field, having the same helical geometry along the torus. [This figure is a cortesy of Tom Farley (MAST, CCFE), 2019].

port mechanism originated by a polarizing force is summarized in [14]. The overall idea is that an external polarizing force ultimately results in an $\vec{E}\times\vec{B}$ velocity drift that drives the filaments.

To begin, radial or outwards expansion forces result in a poloidal $\vec{F}\times\vec{B}$ particle drift. This mechanism is in the origin of the vertical $\nabla\vec{B}$ and curvature drifts explained in chapter 1. Any force $\vec{F}$ in the perpendicular plane results in $\vec{F}\times\vec{B}$ drifts also along the perpendicular plane. In the particular cases of the $\nabla\vec{B}$ and the curvature drifts the displacement of ions an electrons is unequal (and have opposing signs) according to the definition on (1.10), which is dependent

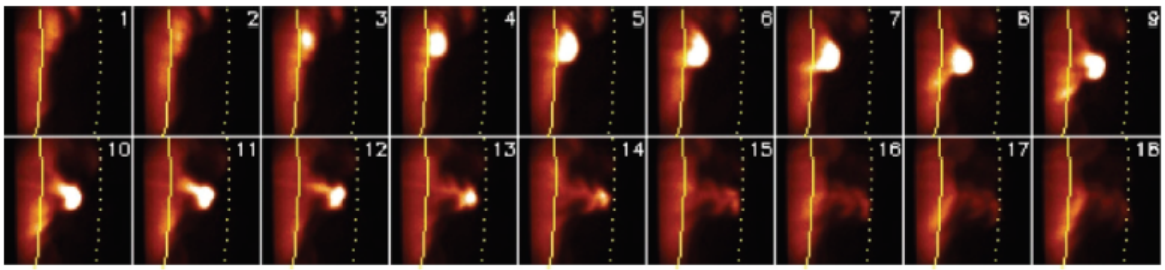

Figure 2.3 Gas-puff imaging (GPI) frames from the NSTX tokamak, taken near the outer midplane separatrix (solid line). The frames, with a frame rate of 7.5 μs/frame and a $\sim 25 \times 25$ cm^2 field of view, show the formation of a density blob (brighter feature) near the separatrix and its subsequent propagation radially outwards with $\sim V_r = 1$ km/s. A poloidal motion is also observable, although more subtle. [Figure from [11]].

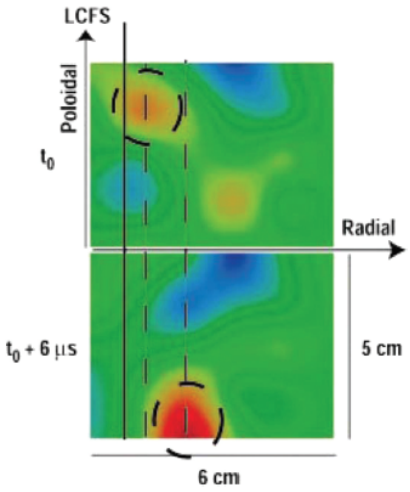

Figure 2.4 2D density plots from the edge of the DIII-D tokamak, obtained with the beam emission spectroscopy (BES) diagnostic. The Fig. shows two frames, where the frame rate is 6 μs, and each frame covers a 6×5 cm^2 area at the edge plasma of the DIII-D tokamak. While red indicates high density features, blue indicates low density ones. In the frames a high density feature of spatial structure of $\sim 2 \times 2$ cm^2, marked with a dashed circle, shows to propagate both poloidally and radially over the 2D perpendicular plane, with $\sim V_r = 1.5$ Km/s and $\sim V_\theta = 5$ Km/s. [Figure from [12, 13]].

of the value of $\vec{F}$ for each species. These forces (or drifts) polarize the plasma regions where they are observed. In the edge the filaments can be polarized in this way. A final consequence is a coherent $\vec{E} \times \vec{B}$ drift of the filaments in the perpendicular plane (chapter 1). On Fig. 2.5 it is illustrated the resultant radial outwards $\vec{E} \times \vec{B}$ velocity component ($\vec{V}_E$) arising from an external polarizing force, $\vec{F}$, directed radially outwards.

An experimental result arising from an estimation of the $\vec{E} \times \vec{B}$ blob's velocity component

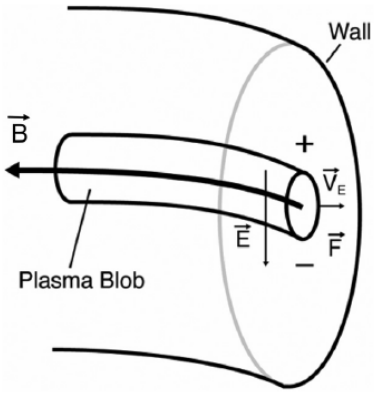

Figure 2.5 Scheme of the convective radial drift of a blob filament, resulting from the charge polarization mechanism. A $\vec{E} \times \vec{B}$ velocity component ($\vec{V}_{\vec{E}\times\vec{B}} \equiv \vec{V}_{\vec{E}} \equiv \vec{V}_r$) dominates the propagation of plasma filaments. The dominant radial component is induced by a charge polarizing force ($\vec{F}$) in the same direction. [Illustration from [14]].

is that blobs show to propagate with higher radial velocities over the surrounding background plasma. Different analysis proposed for an analytic blob model, more robust than the introductory scheme on Fig. 2.5, [14], often estimate an expected range for the magnitude of the radial velocity around $0.01 - 0.1\ C_s$ (where C_s corresponds to the ion acoustic speed). This estimated range is in the same order of magnitude as experimental results, found [26,28,30,31]. Meanwhile in the poloidal direction (i.e., the direction of the electric field, $\vec{E}$, on Fig. 2.5) filaments rotate along with the background plasma, having the same poloidal velocity component.

2.2.3 Transport induced by fluctuations

Electrostatic fluctuations of a multitude of plasma quantities in the SOL have been extensively documented in the bibliography to show a spatial and temporal intermittency, i.e., showing frequent burst-like events above the signal's mean value. These observations can be explained by the formation and propagation of the blob-filaments.

The electrostatic fluctuations derive from the filaments' distinct properties over the background plasma, along with their small temporal and spatial structures (of a few centimeters and a few microseconds) in comparison to machine dimensions. The filaments display an intermittent character themselves, having short life times they can grow and disappear in the edge plasma in a time scale of a few microseconds. The formation and propagation of the blob-filaments results in the electrostatic fluctuations of several plasma quantities. Such as the density $\tilde{n}(t)$ and the

plasma potential $\tilde{V_p}(t)$, where $\tilde{\cdot}$ denotes the fluctuations of a given quantity in time.
Anomalous net transport levels ($\bar{\Gamma}_r$) arise from correlated fluctuations of plasma density $\tilde{n}(t)$ and radial velocity $\tilde{\vec{v}}_r(t)$ (and/or temperature $\tilde{T_e}$ or $\tilde{T_i}$). The radial velocity component follows from the radial $\vec{E}_\theta \times \vec{B}_\phi$ drift, $\vec{v}_r \equiv \vec{v}_{\vec{E}\times\vec{B}}$. The expression for $\bar{\Gamma}_r$ is given on 2.1.

$$\bar{\Gamma}_r =< \tilde{n}(t) \cdot \tilde{\vec{v}}_r(t) >, \tag{2.1}$$

$$\|\vec{v}_r\| \equiv \|\vec{v}_{\vec{E}_\theta\times\vec{B}_\phi}\| = E_\theta/B_\phi, \tag{2.2}$$

where the the angular brackets denote a time average. In a scenario in which these quantities are uncorrelated, at any given time interval, the induced radial transport would average to zero. A result of an equivalent random distribution along $\eta\vec{ds}$ and $-\eta\vec{ds}$ for a given local flux surface.

The time signal of the induced transport, $\Gamma_r(t)$, displays an intermittent character with burst-like events, analogous to what is known for the fluctuating density and plasma potential in the edge/SOL plasma. Near the walls, region which is commonly referred to as the far-SOL, the filaments convective transport can account for a unit order factor of the total transport in some devices, [14], even up to 50%, as observed in [32, 33] for the TJ-II stellarator.

The transport by intermittent convection is a strong hypothesis to explain the flat profiles observed in the far-SOL of some diverted devices. In such scenarios, at the edge an SOL, the conduction and convection of heat to the divertor, in balance with the parallel transport, does not result in the expected results. Those being a thin SOL (when compared to its length) and exponential profiles with short decay lengths of typically 1-3 cm, [12]. Observations of wider and non-exponential SOL profiles, [34–36], implies an unexpectedly larger perpendicular transport of particles and heat towards the walls.

A common SOL diagnostic, to be soon discussed on section 3.2.1, Langmuir Probes, is mainly used to record two quantities which are the fluctuating ion saturation current, $\tilde{I}^+_{sat}(t)$, and the fluctuating floating potential, $\tilde{V}_f(t)$. The first is proportional to the plasma density fluctuations, $\tilde{n}(t)$, while the second proportional to the fluctuations of the plasma potential, $\tilde{V}_p(t)$. Both $\tilde{I}^+_{sat}(t)$ and $\tilde{V}_f(t)$ are better explained on section 3.2.1, but are now used as scalable examples of the SOL fluctuations of plasma density and potential, respectively. On Fig. 2.6 are shown examples of 1 ms probe signals for the time recording of these two properties, from measure-

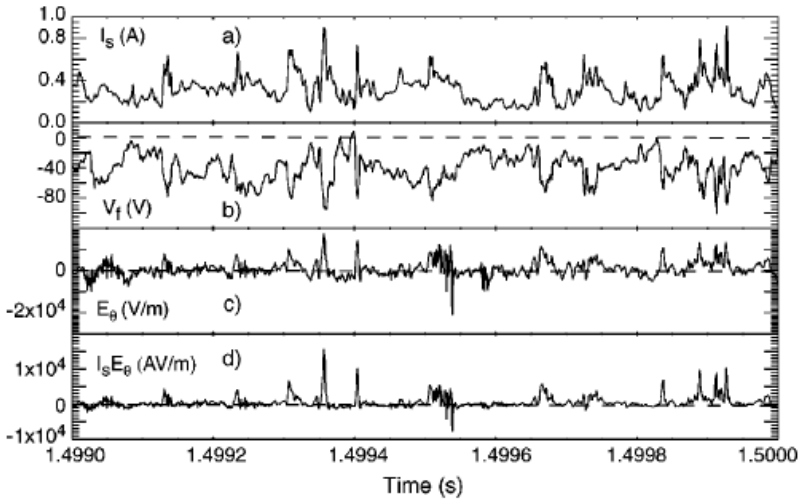

Figure 2.6 Langmuir Probe measurements obtained from the DIII-D tokamak. 1 ms time recordings of the $I^+_{sat}(t)$ ($\tilde{I}^+_{sat}(t) \propto \tilde{n}(t)$), $V_f(t)$ ($\tilde{V}_f(t) \propto \tilde{V}_p(t)$), and poloidal electric field E_θ. The results display frequent burst-like events above the signals rms. Finally it is also shown a sample of the product $I_{sat}E_\theta$ which is scalable with the intermittent radial particle flux ($\vec{n}_e\vec{V}_r = n_\theta/B_\phi$). [Figure from [12]].

ments carried at the DIII-D tokamak, [12]. It is also shown the probe signals of the poloidal electric field E_θ, and the product $I_{sat}E_\theta$. The latter is computed since it is scalable with the intermittent particle flux, $\Gamma_r = nv_r = nE_\theta/B_\phi$.

The intermittency in SOL fluctuations has been amply characterize through conditional averaging techniques of the burst-events above a rms-level threshold [14, 37]. The threshold is computed to discriminate the intermittency induced by turbulence. It varies for the conditions of each study, and is usually applied to the fluctuating density (often used a 2-3 rms-level threshold), [14, 37].

For the results of SOL fluctuations in the DIII-D tokamak showing on Fig. 2.6, a 2.5 rms-level threshold was set to discriminate the intermittent bursts in the ion saturation current fluctuations $\tilde{I}^+_{sat}(t) \propto \tilde{n}(t)$, [12]. The intermittent features were then binned for windows of 100 μs, centered around the maximum of each event, and averaged over about 20-40 events (or time recordings of 2-5 ms). For these results ([12]) was concluded that the intermittent bursts appear at a rate of $1-4\ 10^3 s^-1$. The windows determined from the $I^+_{sat}(t)$ signal were later used to identify the intermittent events' windows in the remaining quantities. Nevertheless, on [12], conditional averaging techniques with different rms-level thresholds and starting with E_θ to determine the appropriate windows culminated in coherent results. This example threshold is

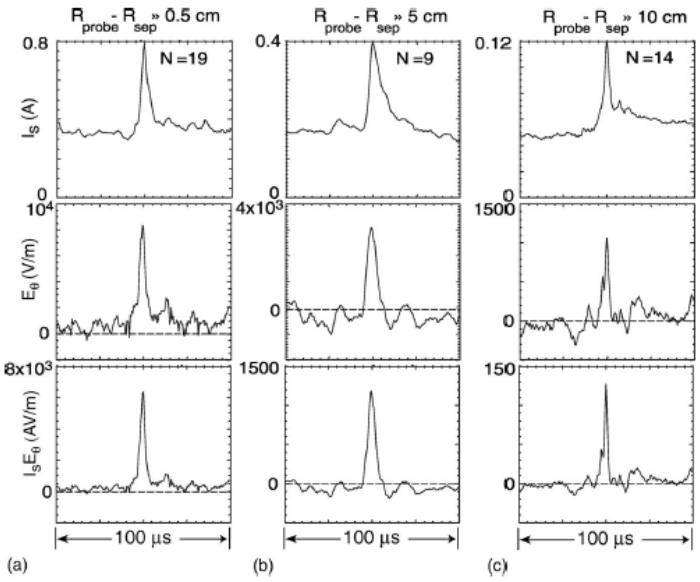

Figure 2.7 Conditional averaging results for Langmuir Probe measurements obtained from the DIII-D tokamak. The intermittent bursts on measurements taken at different radius in the scrape-off layer plasma are shown. Within (a) 0.5 cm, (b) 5 cm and (c) 10 cm of the LCFS at $r = R_{sep}$. Averaging over 20-40 events in each signal was taken for events over a 2.5 rms-level threshold (set initially to discriminate the bursts in the ion saturation current fluctuations). [Figure from [12]].

not universal and results from attempts on this specific experiment. However holds substantial similar conclusions taken in other tokamak experiments.

The time windows used in the conditional averaging technique in [12] are equivalent to averaging over structures smaller than ~ 2 cm. Scale which is associated to frequencies higher then $1/(100\ \mu s)$.

The observation of time structures between $10-100\ \mu$s, as evidenced in the example on Fig. 2.6, is a good reference for the range of results obtained for blob-filaments in most fusion plasmas. The conditional averaging results of the fluctuations in the DIII-D tokamak [12] are shown in Fig. 2.7. As can be seen the intensity of the bursts decreases with radius for the three positions probed in the SOL of DIII-D, with an attenuation factor of ~ 7 away from the LCFS, as referred on [12].

These examples, once again, call attention to the fact that the discrimination of the intermittent bursts that result from the filaments formation and propagation through the edge/SOL is not universally quantified. Neither is the scaling of the filament structures with fusion plasma parameters (density, plasma current, etc.). Nevertheless, evidence of the formation and propa-

gation of blob-filaments can be taken from investigations on the edge/SOL fluctuations of the spatial and time signals of various plasma quantities. The time recording of the fluctuations and subsequent discrimination of the intermittent events, from the average signals, allows to determine the spatial and temporal structures of the blobs (and their propagation through the SOL). Different analysis techniques applied to not only Langmuir probe data, but probing diagnostics such as the Neutral Beam Injector and Thomson Scattering have been used to establish coherent results to those determined from the optical diagnostics previously mentioned.

2.2.4 Statistical evidence for blob-filaments

Often the characterization of the edge/SOL intermittent fluctuations includes the probability distribution function (PDF), constructed by means of the terms of $P_f(x)$ over the range of values taken by a fluctuating quantity f, and where $P_f(x)$ expresses the probability of f falling between $f = x$ and $f = x + dx$. The third and fourth momentums which are used to compute the skewness and kurtosis, respectively, also hold relevant information about the presence and propagation of blob structures over the background plasma.

To facilitate the interpretation of the results the normalized form of the PDF is often used given by the terms of $\bar{P}_f(y)$, where y corresponds to $y = (x - \bar{f})/\sigma_f$. Lastly, σ_f represents the standard deviation of the series. The normalized form of the PDF, presents a similar behavior in the edge and SOL of most fusion devices when simultaneously evaluated for some quantities, [15]. In the far SOL where the intermittency in the electrostatic fluctuations is dominant, the PDF behavior of given quantities seem to be independent of the device and its parameters, displaying a roughly "universal" shape. The results present in general to be a deviation from a Gaussian distribution with high skewness. More into the confinement plasma boundary (i.e., LCFS) the deviation from a Gaussian distribution is usually smaller, and near Gaussian distributions are often observed. However, in the far SOL if there is a region where blobs propagate in a purely ballistic way, the PDFs may show to be approximately independent of the radius with properties that are related to their formation, as mentioned on [14]. On Fig. 2.8, are given examples of the normalized form of the PDF. The examples are computed for time signals of the ion saturation current, taken at four different experiments. Although correspondent to observations at different radial positions of four different fusion devices, they were all taken far enough in the SOL were the intermittency in the fluctuations should be significant. The identical character of the computed PDFs on Fig. 2.8 pictures well the aforementioned that the intermittency in the

electrostatic fluctuations, arising from turbulence processes in the far SOL, presents a coherent character among different devices and different device/plasma parameters.

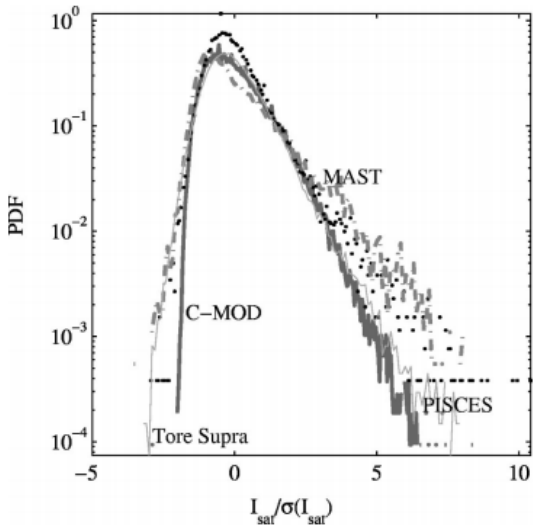

Figure 2.8 Semilogarithmic plot of the PDFs of the ion saturation current, normalized to the standard deviation. Results determined on the Tore Supra (solid line), Alcator C-Mod (thick solid line), MAST (dashed–dotted line), and PISCES (dots). [Figure from [15]].

For different quantities the deviation from Gaussian statistics may not evolve in the same way with radius. For example, the density PDF is often observed to be more tailed than the potential PDF at any radius. To paraphrase [14], the PDF result depends of the quantity being characterized. This calls attention to the fact that different quantities associated with the propagating blobs differ from the background plasma with different magnitudes. The intermittent bursts on the signals of distinct quantities will have different amplitudes. This fact was observed in Figs. 2.6 and 2.7.
The characteristics of the PDF described in this section are often seen for the fluctuating ion saturation current, $\propto n$, and the fluctuating particle flux in the far SOL. The PDFs of these quantities often have a positive tail, indicating a contribution of high density structures propagating in the plasma.

Further into the SOL the absolute magnitude of the blobs studied in DIII-D showed to rapidly decrease with radius, as just shown from results of [12]. Conjointly with a faster decay of the background plasma density, higher values of the skewness of the density PDF result. The observed correlation in DIII-D is a general hypothesis to explain a characteristic result for most fusion plasmas, which states that going further into the SOL the skewness profile of the density

PDF increases with radius. Positive density blobs are usually observed to be dominant in the far SOL, causing the density PDF to have a bigger positive tail, which is equivalent to higher values of skewness.

2.2.5 Frequency resolved measurements

The fluctuations generally display a broad frequency spectra, with most of the spectral power located bellow $\sim$ 100 kHz. The spectra decays towards higher frequencies with $1/f^c$, where c is a constant that varies in different frequency ranges. Usually c ranges from ~ -1 to ~ -2 at high frequencies, [14]. This decay index increases from $\sim$ 100 kHz, above which a quicker decay is observed with f.

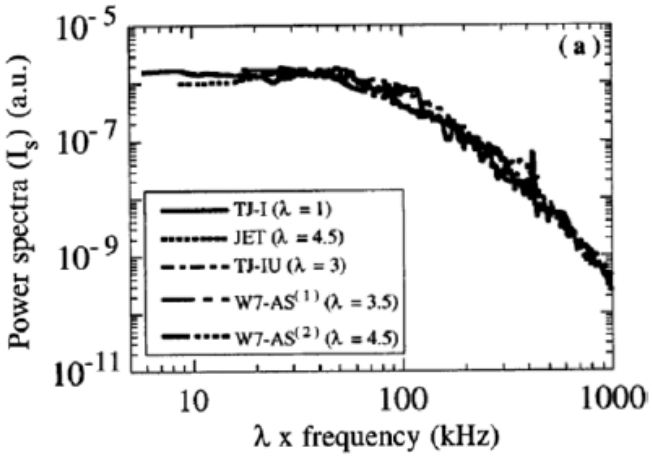

Figure 2.9 Power Spectra of the density intermittency obtained in the edge of various stellarator and tokamak devices. [Figure from [16]]. Results taken from Langmuir Probe measurements at the radius where the poloidal turbulence flow speed was near zero, [16]. In order to reveal that all curves have nearly the same shape, the factors presented in the legend were used to re-scaled the frequencies, and the amplitudes normalized.

The spectra of the fluctuations also shows a roughly "universal" behavior in most fusion experiments if re-scaled properly. Usually taking in consideration the standard deviation of the fluctuating series. This case is shown on Fig. 2.9, for investigations on different fusion devices, [16]. The results from [16] are as obtained in the JET tokamak, [25], where a decay with $1/f$ is seen in the spectral region where the intermittent transport is dominant.

Chapter 3

Experiment and diagnostic setup

3.1 Description of the experiment

3.1.1 ISTTOK

Turbulence studies were carried out on the edge and SOL plasma of the ISTTOK tokamak, which is shown on Fig. 3.1. The ISTTOK tokamak is a small circular cross-section device, with a large aspect ratio, having minor radius $a = 8.5$ cm and major radius $R_0 = 46$ cm. Information on the ISTTOK experiment and fusion program at IST can be found in [2,38,39]. ISTTOK has a poloidal graphite limiter, electrically connected to the vessel, is set at $r_L \simeq 8.5$ cm (see Fig. 3.3). The malleable structure is inserted on the vessel through one of the ports shown on Fig. 3.2, and after it is adjusted to take the circular shape of the vessel. As one can see on Fig. 3.3, the limiter installed at ISTTOK is a poloidal rail limiter, that is, a material extending along the poloidal perimeter with an interrupted structure (12 blocks of graphite). The smaller diameter of the limiter will interrupt the magnetic field lines trajectory, in an attempt to prevent the plasma from reaching the walls.

The vacuum chamber of this device is made by two half torus connected with insulating material, where each half torus structure is composed by six individual rigid sections of inox, which are in its turn connected by thin inconel bellows (0.15 mm). The vacuum system is made of a magnetic levitation turbo molecular pump supported by rotary pumps. In ISTTOK it is possible to measure the residual ($\sim 2 \times 10^{-7}$ torr) and also the work (2×10^{-4} torr) pressure by both ionisation and capacitance manometers. ISTTOK has installed a gas injection system made of several electromagnetic and pneumatic valves that allows to initially fill the vacuum chamber, and also for additional gas injections in a pulsed regime by means of a piezoelectric

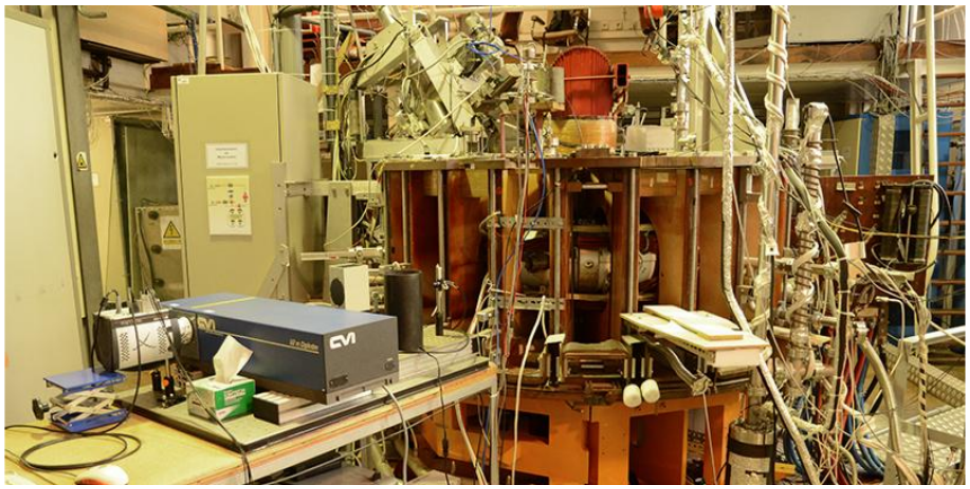

Figure 3.1 The ISTTOK tokamak experiment at IST. A small circular cross-section device, with a large aspect ratio, having minor radius $a = 8.5$ cm and major radius $R = 46$ cm, and a graphite limiter set at $r_L \simeq 8.5$ cm. An extensive scientific programme is carried at the the ISTTOK tokamak with the various diagnostics seen in the image.

valve.

ISTTOK usually operates with a toroidal magnetic filed between $B_T \simeq 0.4 - 0.7$ T. Although the toroidal field on ISTTOK could go up to 2.8 T by means of a set of 24 water cooled coils, power limitations (1 MW) obligate the operation with lower magnetic fields. In particular $B_T \simeq 0.5$ T is set during most discharges.

An iron core transformer with a primary winding of 2×20 spires at the central post and an auxiliary winding with $20 + 10$ spires in the external post, is installed in ISTTOK. The current applied to the transformer is provided by condenser banks. Usual operation is set for plasma current values of $I_p \leq 7$ kA.
ISTTOK can operate with both alternate current (AC) and direct current (DC) modes. For the former the plasma current direction is reversed several times, as illustrated in [40]. The plasma direction (positive or negative plasma current) is kept for around ~ 25 ms cycles, making each AC full-cycle last ~ 50 ms (both current signs). The AC mode of operation allows to obtain discharges with longer duration. The frequent change in the plasma current direction avoids the saturation of the iron core transformer.

Both vertical and horizontal positions of the plasma column are governed in real-time, using vertical equilibrium coils controlled by a magnetic feedback, with an accuracy of 5 mm, [39].

The remaining geometric parameters of the ISTTOK tokamak, along with the usual discharge parameters used on its operation can be found in table 3.1.

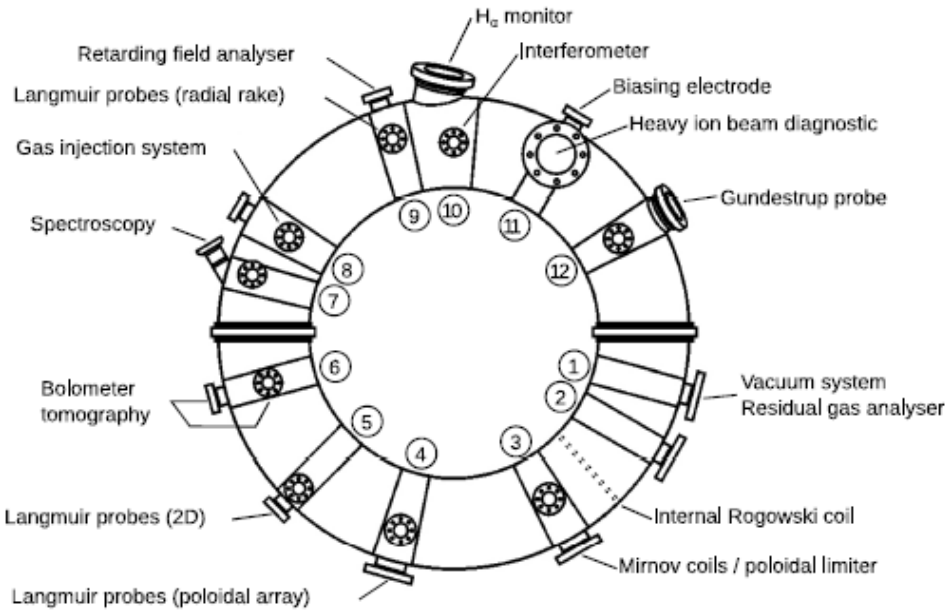

Figure 3.2 Scheme of the main diagnostics installed at ISTTOK, along with their toroidal positions. The ports used in the diagnosis of the plasma are also shown.

There are several diagnostics at ISTTOK that allow to carry an extensive Fusion programme at IST. On Fig. 3.2 one can find how most of them are placed in the experiment (toroidal positions), with complementary information found on [2] and [39]. The main diagnostic used in this thesis is described with some extent on the following section 3.2.1. Meanwhile, it is worth to briefly describe a few of the remaining diagnostics. Namely those used to determine the following quantities, which are referred in this study:

Plasma current: The plasma current at ISTTOK can be determined with the Rogowski coils diagnostics. Two Rogowski coils are installed at poloidal planes in ISTTOK. They allow to measure the plasma current and also the total toroidal current. The latter includes the currents on the vacuum vessel. The coils at ISTTOK are composed with 500 spires, each having 3.25 mm in diameter. An analog integrator is used along with coils to determined the currents.

Density: A microwave interferometer (100 GHz) is installed to determine the line integrated plasma density. The phase shift of the interferometer is determined between a probing beam that crosses the vacuum vessel, and a reference beam propagating in a controlled environment outside. The probing beam crosses the plasma vertically, at the geometric center of the vacuum vessel. The phase shift allows to determine the line inte-

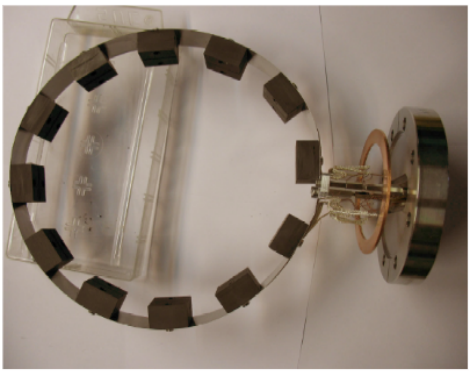

Figure 3.3 Poloidal rail limiter installed at ISTTOK (at $r_L \simeq 8.5$ cm). A graphite material with the shape of the vacuum vessel, that extends along the poloidal perimeter with an interrupted structure. The smaller diameter of the limiter will interrupt the magnetic field lines trajectory, in an attempt to prevent the conduction of plasma particles towards the walls.

grated plasma density along the probing path.

Plasma position: A set of 12 Mirnov coils, uniformly distributed along a poloidal plane are used to determine the plasma column position. The set of coils is used to determine the magnetic flux resulting from the plasma current, which in turns enables to determine the position of the column.

Loop voltage: A single loop installed around the iron core is used to measure the loop voltage, V_{loop}. The V_{loop} refers to the induced electromotive force (ε), and allows to compute the toroidal electric field driving the plasma current. The location of the diagnostics is due to the fact that at ISTTOK the majority of the flux is through the iron core.

3.1.2 Data Acquisition System

The Control and Data Acquisition System (CODAS) at ISTTOK is divided in two control subsystems and two data acquisition systems. The CODAS at ISTTOK has been often used with the purpose of testing new systems to install in other fusion experiments, as one can find on [39],

"ISTTOK has served as a test bed for new hardware and software developments that later were exported to other fusion devices.".

The experiment is now equipped with a Data Acquisition (DAQ) subsystem based on the Advanced Telecommunications Computing Architecture (ATCA). A more detailed description

Table 3.1 ISTTOK geometric and usual discharge parameters.

Parameters	Value
Major radius (R)	46 cm
Minor radius (a)	8.5 cm
Vessel radius (r_{vessel})	10 cm
Aspect ratio	5.75
Maximum toroidal magnetic field ($B_{T_{max}}$)	0.4-0.7 T
Plasma current (I_p)	$\leq$ 7 kA
Discharge duration	$\simeq$ 45 ms
Plasma density at r=0	$\simeq 5{\times}10^{18}$ m^{-3}
Electron temperature at r=0	$\simeq$ 120 eV
Energy confinement time	$\simeq$ 0.8 ms
Safety factor q(0)	$\simeq$ 1
Safety factor q(a)	$\simeq$ 5-8

of this computer architecture can be found from [39]. In the rest of this section its briefly described the main characteristics of the subsystems at ISTTOK. It is also mentioned their main advantages for the data acquisition in this experiment.

The installation of an ATCA subsystem is more recent at ISTTOK, and its boards were developed by members of IPFN (Instituto de Plasmas e Fusão Nuclear, at IST), in order to now allow sampling rates of 2 MSamples s^{-1}. The ATCA subsystem is the one used in the acquisitions of the edge/SOL fluctuations at ISTTOK. The main characteristics of the ATCA subsystem are as follows,

- The input is an analog to digital converter (ADC) modules, responsible for acquiring the raw data.
- The output consists of digital to analog converters (DACs).
- Can communicate with the computer via Peripheral Component Interconnect express (PCIe).
- Saves the data in the computer memory (Random-Access Memory, RAM) over direct memory access (DMA).

Each ATCA board operates with 32 ADC modules and 10 DACs. ISTTOK is equipped with six boards, equally divided for data acquisition and control. For the three DAQ boards, the ADC modules acquire the raw data and store it in the inboard RAM during discharges.

Table 3.2 Names of the diagnostics channels used during this thesis to access data from the SDAS server. Its is also listed the quantities measured using this channels.

Diagnostics channel	Abbreviation	Measurement
PCIE_ATCA_ADC_16.BOARD_1.CHANNEL_011	ch 11	I_{sat}^{+} [mA]
PCIE_ATCA_ADC_16.BOARD_1.CHANNEL_012	ch 12	I_{sat}^{+} [mA]
PCIE_ATCA_ADC_16.BOARD_1.CHANNEL_013	ch 13	V_f [V]
PCIE_ATCA_ADC_16.BOARD_1.CHANNEL_014	ch 14	V_f [V]
PCIE_ATCA_ADC_16.BOARD_1.CHANNEL_015	ch 15	V_f [V]
MARTE_NODE_IVO3.DataCollection.Channel_081	ch 81	Plasma position R [mm]
MARTE_NODE_IVO3.DataCollection.Channel_082	ch 82	plasma position Z [mm]
MARTE_NODE_IVO3.DataCollection.Channel_095	ch 95	V_{Loop} [V]
MARTE_NODE_IVO3.DataCollection.Channel_100	ch 100	Plasma current (I_p) [kA]
POST.PROCESSED.DENSITY	ch density	Density (n) [m^{-3}]

Later an appropriate software is responsible for reading the data and saving it in the ISTTOK database.

On the other hand, a real time control system is implemented using the three control boards. These boards acquire raw data from the ADC modules, to then be implemented in the real time control system running at ISTTOK, [2, 39]. The control boards are strictly used for diagnosis of quantities which are useful in the real-time control of the plasma, as for example the plasma position from the Mirnov Coils diagnostics.

The ISTTOK's digitized data for each shot can be remotely accessed using the Shared Data Access System (SDAS) server. This server takes as some of the inputs a shot number and the specific diagnostics channel. The names of the channels used during this thesis to access data from the SDAS server are enumerated on 3.2, along with the quantities measured by each channel.

3.1.3 Set of discharges

The current investigation on edge turbulence at ISTTOK was achieved through the time recording of different plasma quantities with Langmuir probes. The results are presented as a function of different plasma current values, and also for different pressure values. Simulta-

neously, throughout the entire analysis the measurements are interpreted as a function of the alternated current regimes that ISTTOK operates on.

An initial study was carried as a function of the plasma current (shot lists A and B). During which measurements were taken at different radial positions across the ISTTOK boundary plasma, from $r = 70$ mm to $r = 105$ mm. For the discharges on shot list A the plasma current was set as $I_p = 4$ kA, while for the ones enumerated on shot list B we had $I_p = 4.7$ kA. The value of the plasma current used during these discharges, along with the radial positions of the probe is according to the what is shown on Fig. 3.4. For shot list B measurements were taken around radial positions as close as possible to the ones used in shot list A, using the same discharge parameters except for the value of plasma current.

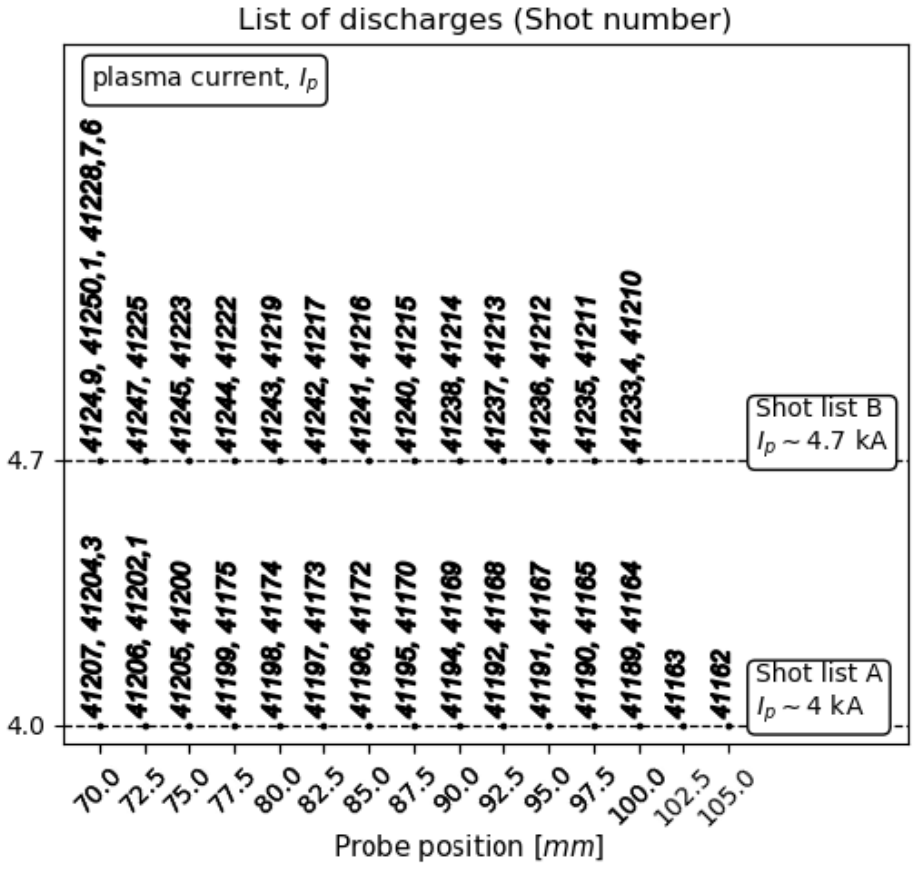

Figure 3.4 Shot lists for the initial study of the intermittent fluctuations carried at the ISTTOK tokamak. Analysis for two different plasma current values, $I_{p_A} = 4$ kA (shot list A) and $I_{p_B} = 4.7$ kA (shot list B). Measurements were taken at different radial positions across the ISTTOK boundary plasma, from $r = 70$ mm to $r = 105$ mm.

An experimental investigation was also carried on the electrostatic fluctuations as a function of the work pressure, as shown for the list of discharges on Fig. 3.5.

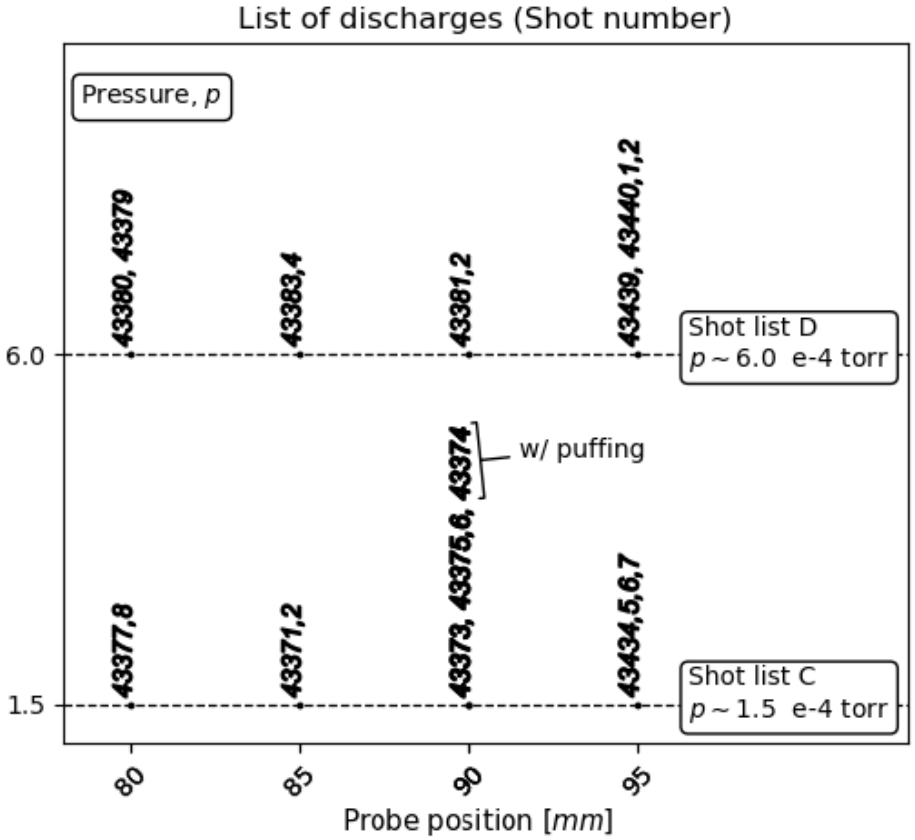

Figure 3.5 Shot lists for a second study of the intermittent fluctuations carried at the ISTTOK tokamak (shot list C and shot list D). Analysis for different pressure values and gas injection regimes. Measurements were taken at different radial positions across the ISTTOK boundary plasma, from $r = 80$ mm to $r = 95$ mm, with $B_\phi \simeq 0.5$ T $I_{p_{C,D}} \sim 4$ kA.

The investigations carried on the next sections will take a special attention on the operation of ISTTOK as a function of the multi-cycle alternating plasma current regimes. With this mode of operation, discharges of ~ 1 s have been previously obtained at ISTTOK, having 20 full AC plasma current cycles, [39, 40].

For the discharges analyzed on lists A and B a total of six alternating cycles (positive or negative current) allowed to obtain coherent 160 ms discharges, with individual cycles having flat top regimes of ~ 20 ms. On Fig. 3.6 an example is shown of the plasma current signal

during a full discharge on ISTTOK lasting ~ 160 ms.

For all discharges (on the lists A, B, C and D) the toroidal magnetic field was set as $B_\phi \simeq 0.5$ T. Usual discharges on ISTTOK are characterized by density values of $n = (0.5 - 1) \times 10^{18} m^{-3}$ around the limiter radius. Fig. 3.6 shows the average density along the probing path of the microwave interferometer, (of about $n = 4.5 \times 10^{18} m^{-3}$) which is much higher than the density value at the edge (near the limiter). The example is for a discharge belonging to list A. The example on Fig. 3.6 also sets a coherent picture for the density, plasma current and V_{loop} values across the AC regimes during the discharges on the lists A, B, C and D. Finally, on Fig. 3.7 one can see the consistent evolution of the plasma position in-between positive and negative cycles.

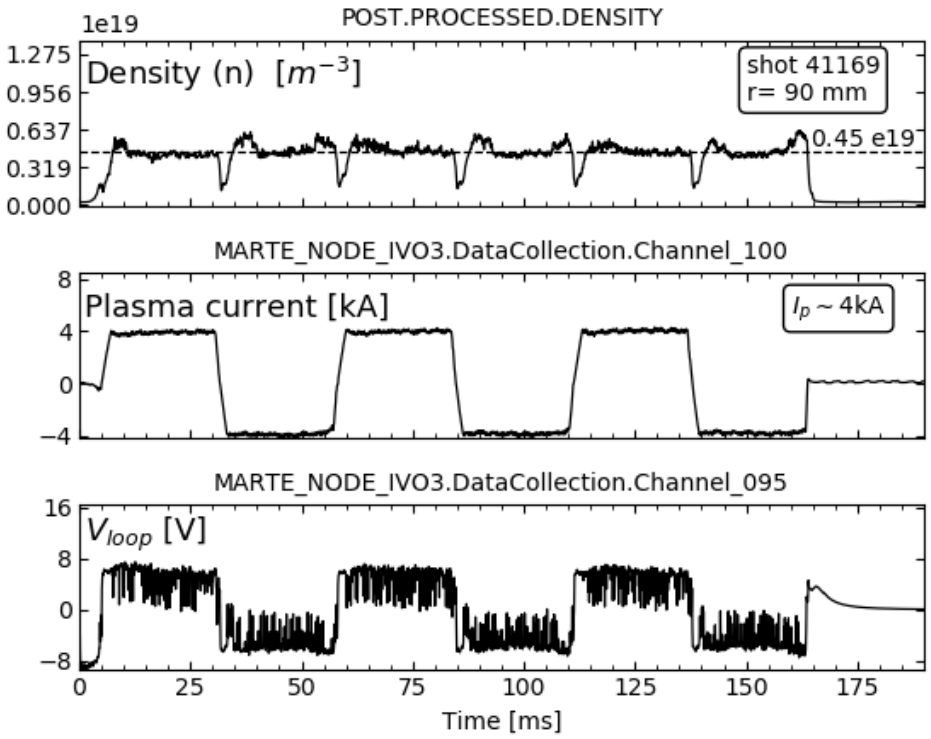

Figure 3.6 Time recordings of the density, plasma current and V_{loop} signals during a full discharge on tokamak ISTTOK (shot 41169, at $r = 90$ mm). A total of six alternating current cycles allowed to obtain coherent discharges (of ~ 160 ms), with individual cycles having flat top regimes of ~ 20 ms.

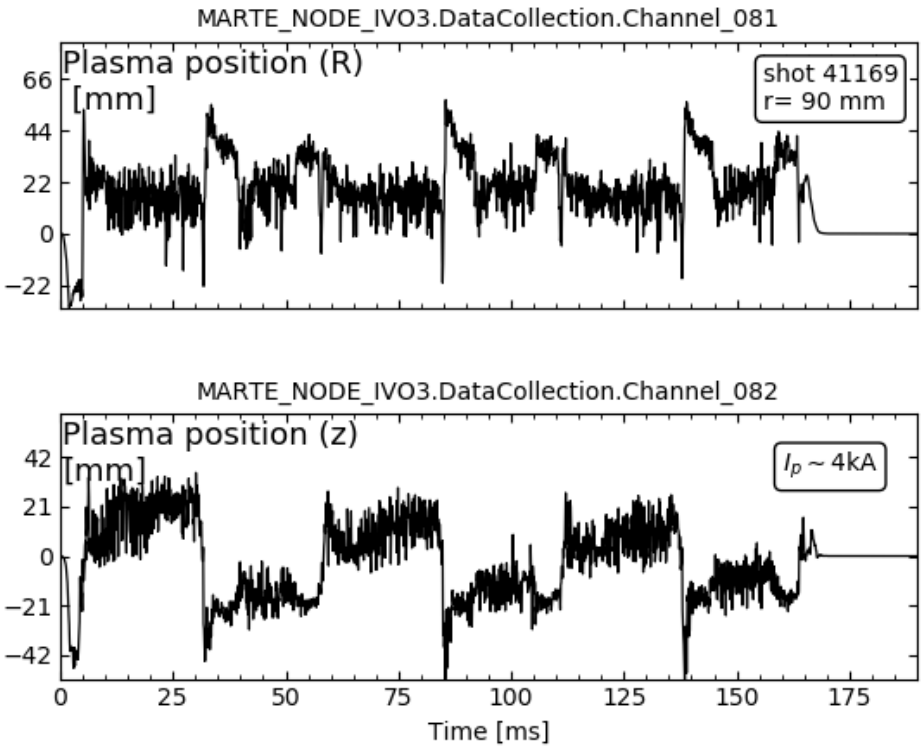

Figure 3.7 Time recordings of the plasma position during a full discharge on tokamak ISTTOK (for the discharge shown in Fig. 3.6). A total of six alternating current cycles allowed to obtain coherent discharges (of ~ 160 ms), with individual cycles having flat top regimes of ~ 20 ms.

3.2 Measurement technique

3.2.1 Diagnosis of the plasma edge by Langmuir probes

Langmuir probes (LPs) are usually cylindrical pin electrodes that are polarized by an external circuit and inserted into the plasma, as in the scheme illustrated in Fig. 3.9. Langmuir probes have been commonly used to study low temperature plasmas ($T_e \lesssim 100$ eV), and remain a widely used diagnostic in fusion devices. The disadvantages of this diagnostic come mainly from a substantial plasma perturbation from probe insertion, and the fact that probe theory is still a subject in need of development. Despite these obstacles LPs have been a highly used diagnostic to help to understand the fluctuations and the associated particle transport in the periphery. They make part of a broad list of diagnostics that provide complementary and most often coherent results of the plasma quantities.

In characterizing SOL fluctuations, LPs offer easy access to the edge plasma, up to a few cen-

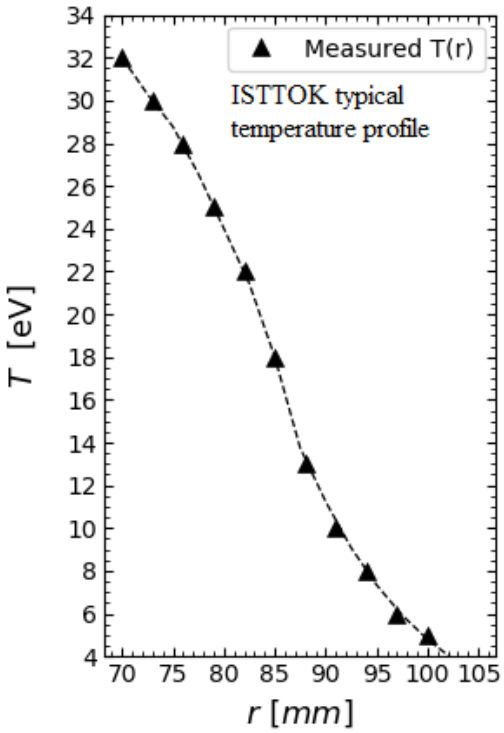

Figure 3.8 Radial profile for the electronic temperature, T_e, on the ISTTOK tokamak. Previous measurements for established radial positions (black triangles), along with an exponential interpolation for the remaining edge/SOL locations in study on chapter 4.

timeters inside the LCFS. In addition, this diagnostic presents high spatial and time resolutions, capable of resolving the fast edge/SOL fluctuations of quantities such as the fluctuating plasma density $\tilde{n}$ and potential $\tilde{V_p}$.

As described previously, plasma turbulence is characterized by structures with a fine spatial variation (in the order of few millimeters) and a fast temporal variation (a few microseconds). The characterization of turbulence is therefore very demanding for plasma diagnostics. Langmuir probes can have dimensions in the millimeter scale and permit the construction of probe arrays, being therefore ideal to resolve the turbulence complex structure. When operated in I_{sat}^{+} or V_f mode, the time resolution of the LPs is typically only limited by the resolution of the data acquisition system, that on ISTTOK is below the microsecond.

The obtained fluctuating parameters allow to determine the statistical characterization of the blobs in the SOL and calculate the induced radial particle transport. Among other possible information obtained from this diagnostic, one can also determine the spatial and temporal

structures of the blobs, followed by an understanding of their propagation in the SOL plasma.

3.2.2 Langmuir Probe Theory

An electrostatic sheath (Debye sheath) is formed in front of any material surface in contact with the plasma, such as the inserted probes. From the knowledge of the physical mechanisms taking place on the sheath region plasma parameters such as temperature and density can be determined.

In front of any plasma facing component it's observable a potential drop, starting from the plasma bulk and decreasing towards the surface, in the sheath region. As the lighter electrons move faster towards the surface of PFCs, leaving the ions behind, the material surface is left with a negative potential relative to the bulk plasma, a floating potential, V_f. In a region called the pre-sheath it is established a small electric field in order to balance the flux of electrons and ions into the sheath region, and restoring in the plasma bulk the quasi-neutrality condition ($n_e \simeq n_i$).
The formation of the sheath region is what allows the plasma to coexist with the floating surface. It is the transitional area from the floating surface to the unperturbed plasma in which the quasi-neutrality condition holds again. Meanwhile in the sheath $n_i > n_e$. The potential drop through the region adjusts in a way to equalize the lost of ions and electrons from the bulk plasma. The sheath has usual thickness of $\sim 10\lambda_D$.
A density decrease in the sheath implies that in order to maintain stability the fluid velocity must increase towards the material surface. In this case the gain in dynamic pressure due to the fluid momentum contrasts the loss in static pressure, which is proportional to n. The Bohm criteria states that the fluid velocity entering the sheath must reach the minimum value of the ion sound speed c_s,

$$c_s = \sqrt{\frac{k_\beta(T_e + T_i)}{m_i}}. \tag{3.1}$$

When a probe is inserted in the plasma, the resultant mechanism is in the same general way as described for the formation of the sheath and pre-sheath regions. The faster electrons move out of the plasma-probe interface towards the surface of the probe. If the inserted probe is not biased, its surface gets charged at the floating potential. The floating potential is given according to the electron temperature, T_e, and plasma potential, V_p, as follows

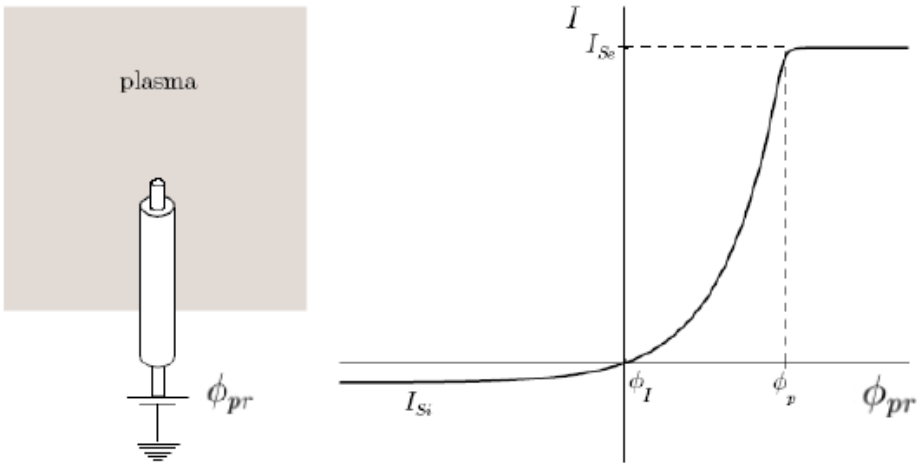

Figure 3.9 On the left its shown an illustrative scheme of the diagnosis of the plasma with Langmuir probes. Usually a cylindrical pin electrode that is polarized by an external circuit, and then inserted in the plasma. On the right, presented the characteristic I-V curve between the collected current by the probe, I_{pr}, and the potential applied to it, V_{pr}. From which it is possible to determine local plasma quantities, such as the electron temperature, T_e, electron density, $n_e \simeq n$, and plasma potential, V_p.

$$V_f \approx V_p - 3K_\beta T_e. \tag{3.2}$$

One the other hand, the probe can be biased by an external potential, V_{pr}. In this way the the current flow into the sheath region allows to obtain a characteristic I-V curve. The current is given as a function of the voltage drop across the sheath, and subsequently, as a function of the potential applied to the probe, V_{pr}. However in some cases the perturbations to the plasma by the inserted probe can be more significant and, simultaneously, very hard to estimate.

From the characteristic I-V curve between the collected current by the probe, I_{pr}, and the potential applied to it, V_{pr}, it is possible to determine local quantities such as the electron temperature T_e, electron density $n_e \simeq n$, and plasma potential V_p. The characteristic I-V curve is distinguished by three intervals corresponding to the regions of electron saturation, transition and ion saturation, Fig. 3.9.

In the presence of magnetic fields difficulties arise in the analysis of the electronic part of the I-V characteristic, due to a distortion of this region as a result of the influence of the magnetic field on the lighter electrons. The common procedure is to use measures in the transition and ion saturation regions, where the probe current as a function of the applied potential is approximately obtained through (3.3),

$$I(V_{pr}) = I_{sat}^{+} \cdot \left(1 - e^{\frac{V_{pr}-V_f}{k_\beta T_e}}\right). \tag{3.3}$$

Probe I-V characteristic

In general a three parameter fit is then applied to the experimental probe characteristics in this regime, according to (3.3), in order to determine the local values of T_e, I_{sat}^{+} and V_f.

In the ion saturation regime, the collected current takes the value of I_{sat}^{+} when the probe is biased to a large enough negative potential. In this regime the electrons are completely repelled and the restricted ion flux to the probe sheath becomes independent of the applied potential, resulting in the constant I_{sat}^{+} given by

$$I_{sat}^{+} = j_{sat}^{+} A_{pr} = \frac{e n_e c_s A_{pr}}{2} \tag{3.4}$$

, where A_{pr} is the effective probe area, and j_{sat}^{+} the ion current density, given by the parameters at the sheath edge. The usual consideration of isothermal plasmas $T_e = T_i$ is taken. The expressions on (3.4) and (3.1) allow to determined the local value of the electron density through the previous determine values of I_{sat}^{+} and T_e. Finally, the plasma potential is determined according to the approximation in (3.2), using the estimations on V_f and T_e.

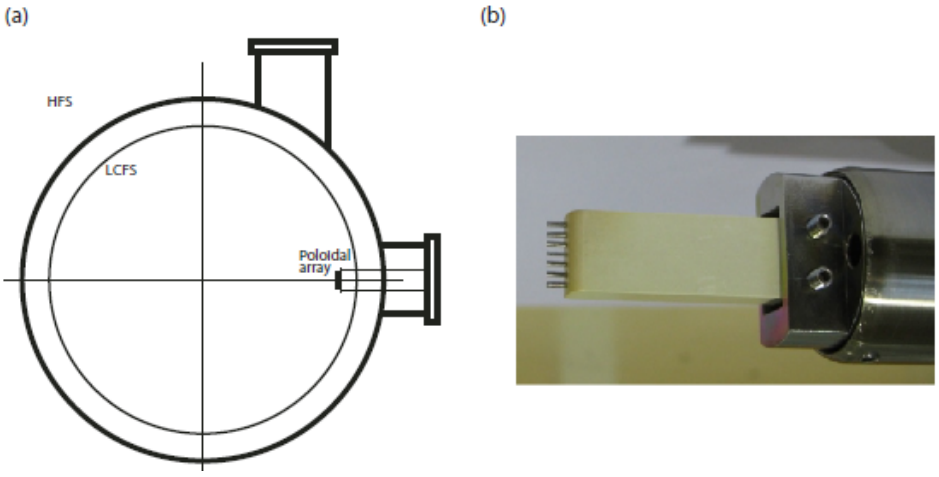

Figure 3.10 (a) Scheme of the insertion of the poloidal array of Langmuir probes on ISTTOK. Trough a port that allows to diagnose the edge plasma with the possibility to radially shift the probe systems from shot to shot by means of a drive mechanism. (b) Photograph of the probe system. Consisting of a 7-pin poloidal array of probes, sequentially separate by 2 mm. Probes with 0.75 mm of diameter and 2 mm of length.

3.2.3 Approximations

During this work the plasma density and potential fluctuations were estimated neglecting the influence of the temperature fluctuations, which are difficult to resolve. The two quantities were determined from the fluctuating ion saturation current and floating potential, respectively. From the measurements of ion saturation current, where $I_{sat}^{+} \propto n\sqrt{2T}$ (3.1 and 3.4), it is made the assumption for the fluctuations of density that $\tilde{n} \approx \tilde{I}_{sat}^{+}$. Similarly, from the floating potential recordings, where $V_f \approx V_p - 3K_\beta T_e$ (3.2), it is considered $\tilde{V}_p \approx \tilde{V}_f$. In addition, the poloidal electric field fluctuations are estimated from two floating potential measurements. Here we have $\tilde{E}_\theta \approx (\tilde{V}_{f_1} - \tilde{V}_{f_2})/d$.

The simultaneous analysis of the fluctuations of plasma potential and density allow to determine the radial transport induced by the cross-field fluctuations. This quantity is estimated according to 2.1, $\bar{\Gamma}_r =< \tilde{n}(t) \cdot \tilde{\vec{v}}_r(t) >=< \tilde{n}(t) \cdot \tilde{E}_\theta(t) > /B$. Note that $\tilde{\vec{v}}_r$ corresponds to the $\vec{E} \times \vec{B}$ radial drift fluctuations.

Good estimations are obtained for the fluctuations of the ion saturation current, despite neglecting the temperature fluctuations. However, a more severe error is introduce on the plasma potential fluctuations when neglecting the temperature fluctuations, [41].

3.2.4 Poloidal probe array

On the tokamak ISTTOK experiment the two ports schemed on Fig. 3.10 allow to diagnose the edge plasma through the use of multiple-Langmuir probe systems. With the possibility to radially shift the probe systems from shot to shot by means of a drive mechanism. The drive mechanism provides access to a larger range of radial locations in-between shots. Furthermore, the use of multi-pin array systems grants simultaneous measurements of close (few millimeters apart) plasma positions, either radially or poloidally shifted.
The Langmuir probe system used during this study is also shown on Fig. 3.10. It consists of a 7-pin poloidal array of Langmuir probes. The probes are sequentially separate by 2 mm, and have 0.75 mm of diameter and 2 mm of length. The poloidal array was installed in the tokamak equatorial port, as schemed on Fig. 3.10.

The array operated in a simultaneous mixed mode of pins recording floating potential and ion saturation current. The measurements of floating potential were taken by the three most inner pins (sequentially 2 mm apart), while two outer pins (8 mm apart) were set to measure

the ion saturation current, as shown in Fig. 3.11.

The inner pins of the probe array were not biased, in order to measure the floating potential. On the other hand, the pins programmed to measure the ion saturation current were biased by a constant potential of −180 V with respect to the vessel. This negative potential is chosen in order to guarantee that the current to the probe equals I_{sat}^{+}, see Fig. 3.9.

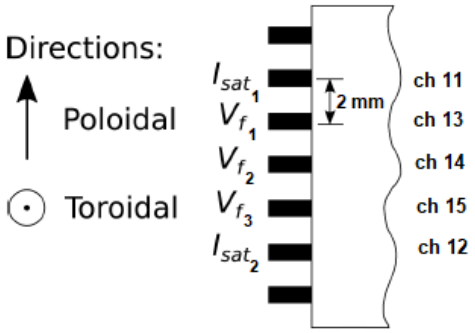

Figure 3.11 Scheme of the poloidal probe array operations mode. The channels from table 3.2 are also identified.

3.3 Signal analysis

A characterization of the induced plasma fluctuations and turbulent transport in the edge of ISTTOK is shown on chapter 4 using the different analysis methods explained on this section.

3.3.1 Determination of the plasma fluctuations

Fluctuations in the different quantities are estimated by subtracting to the signals its average value. Directly acquired Langmuir probe signals $y(t)$ are first filtered with a Moving Average smoothing technique. The smooth result of $y(t)$ is determined for samples of N data points, a sliding average $\bar{y}_N(t)$. Typically N is chosen so that the averages are calculated in a time scale of 1 ms, which is larger than the time scales of interest.

On Fig. 3.12 it's shown an example of the Moving Average smoothing result for a standard I_{sat}^{+} signal from ISTTOK with N=1000.

The determined fluctuations $\tilde{y}(t) = y(t) - \bar{y}_N(t)$ have important and distinctive characteris-

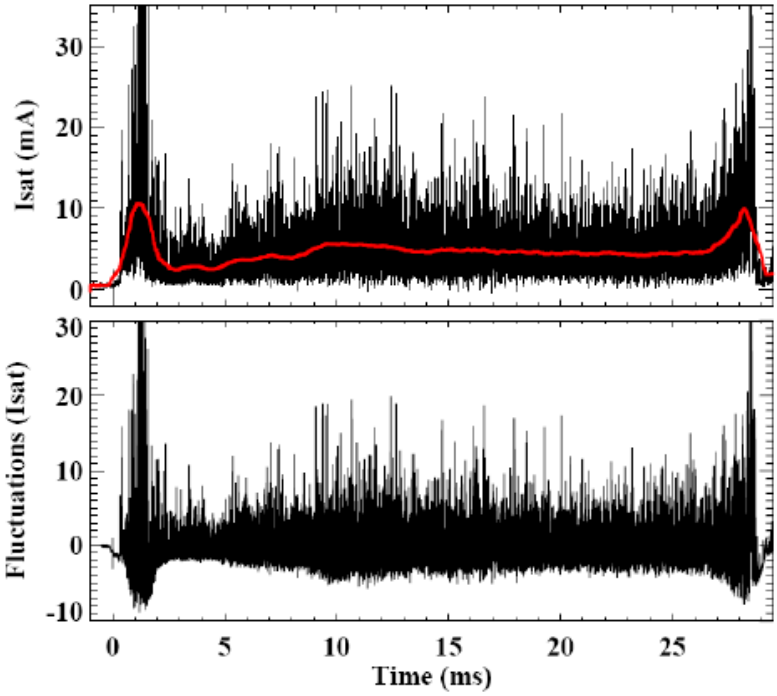

Figure 3.12 Example of the determination of the I_{sat}^{+} fluctuations. Moving Average smoothing result for a standard I_{sat}^{+} signal from ISTTOK with N=1000. The smoothed trend for a time scale of ~ 1 ms is shown in red. [Figure from [17]].

tics resulting from the intermittent structures propagating through the plasma.

3.3.2 Statistics

The probability density function (PDF) of the temporal evolution of the ion saturation current and floating potential were computed. Along with quantities such as the standard deviation (σ_y), fluctuation level (relative level of the fluctuations, $\sigma_y/\bar{y}$), and third and fourth central moments used, respectively, to define the skewness and kurtosis.

The skewness gives a measure of the distribution's asymmetry and should be zero for a normal distribution (and near zero for any symmetric data set), while negative for a left skewed distribution, and positive for a right skewed distribution. For a left skewed distribution a longer left tail is shown while the bulk of the distribution in concentrated on the right, and, inversely, for a right skewed distribution a longer tail is observed on the right while the bulk of the distribution is concentrated on the left.

The Fisher-Pearson coefficient of skewness, (3.5), gives the common definition of the quantity for an univariate data set, such as the time signals in analysis throughout this work. On (3.5), $\bar{y}$

corresponds to the mean value of the data set, σ_y to the standard deviation given here by (3.6), and, finally, N to the number of points in the data.

$$skewness = \frac{1}{N}\sum_{j=1}^{N}\frac{(y_j - \bar{y})^3}{\sigma_y^3}, \tag{3.5}$$

$$\sigma_y^2 = \frac{1}{N}\sum_{j=1}^{N}(y_j - \mu)^2. \tag{3.6}$$

The Kurtosis, determined through the fourth central momentum of the distribution, measures the weight of the outliers (i.e. the weight of the distribution's tail) relative to a normal distribution. For the adjusted version of Pearson's definition for kurtosis, the excess kurtosis on (3.7), the constant 3 is subtracted from the general result to give a zero value of kurtosis for a normal distribution. Moreover, according to (3.7) positive kurtosis indicates a "heavy tailed" distribution and negative kurtosis indicates a "light tailed" distribution, meaning that the distribution produces fewer and less extreme outliers relative to the standard normal distribution.

$$excess\ kurtosis = \frac{1}{N}\sum_{j=1}^{N}\frac{(y_j - \bar{y})^4}{\sigma_y^4} - 3. \tag{3.7}$$

3.3.3 Cross Correlation

The cross correlation between two signals measures the similarity of the two as a function of the time shift (time lag) among them. The general definition for the cross correlation between two continuous functions is determined according to the sliding inner product between the two,

$$(f \star g)(\tau) = \int_{-\infty}^{+\infty} f^*(t)g(t+\tau)dt, \tag{3.8}$$

where $f^*(t)$ corresponds to the complex conjugate function of $f(t)$, and τ to the time lag between the two. A maximum value is obtained when the functions have a similar and synchronous pattern, and contrarily, a minimum when functions have a similar but out-of-phase pattern.
From (3.8), follows for discrete data series the expression on (3.9), where n is the lag between

the discrete data indexes.

$$(f \star g)[n] = \sum_{k=-\infty}^{+\infty} f^*[k]g[k+n]. \tag{3.9}$$

An analysis of the time delay between measurements taken in different locations can be used to determine the velocity of propagation of coherent components (structures) in the signals. The velocity of propagation is simply the ratio between the distance among the locations and the time delay. On Fig. 3.13 it's shown a scheme exemplifying the time delay analysis for two sensors poloidally shifted. The distance between the two sensors acquiring $f[n]$ and $g[n]$ divided by the time delay between $f[n]$ and $g[n]$ corresponds to the velocity of propagation of the similar feature (or features) belonging to both $f[n]$ and $g[n]$.

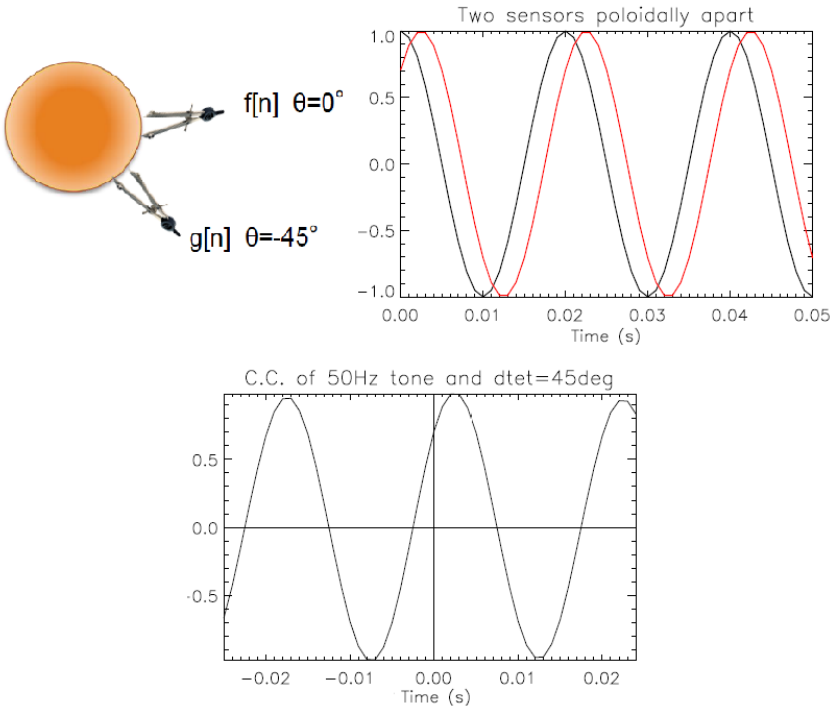

Figure 3.13 Time delay analysis. Example scheme of the correlation for two signals taken in poloidally shifted positions. [Adapted figure from [17]].

In Fig. 3.14 is shown an example of the cross correlation between V_f signals measured at ISTTOK. The measurements were simultaneously acquired according to the probe-system configuration on Fig. 3.14. The cross correlations between the poloidally shifted ($\Delta\phi \sim 2$mm) probe measurements should be fairly independent from the approximately constant background

plasma conditions (removed smoothed result), and considerably affected by the propagation of the intermittent turbulence structures in the plasma.

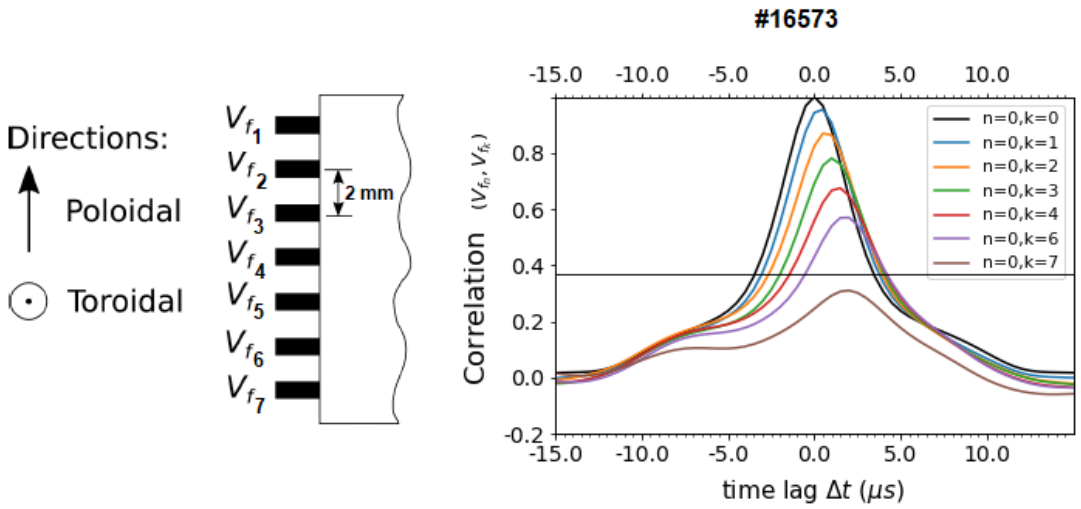

Figure 3.14 Scheme a probe system configuration used to previously measure V_f signals. Correlation between the signals acquired by the 7 poloidally shifted probes.

Chapter 4

Experimental results

4.1 Introduction

The results discussed in this chapter follow from several measurements of ion saturation current and floating potential, taken at different radial locations in the edge and SOL of the ISTTOK tokamak. As explained in the previous chapter 3, time signals of the two quantities were recorded with a multi-pin Langmuir probe system (poloidal array, 3.2.4). The probe system was set to record on channels 11 and 12 I_{sat}^{+}, and on channels 13, 14 and 15 V_f. The pins in I_{sat}^{+} mode were biased at constant potential (-180 V), in order to be in the ion saturation current regime through the entire acquisition time. On the other hand, the pins in V_f mode were unbiased, allowing their surfaces to be at the floating potential. In this way all pins in I_{sat}^{+} or V_f mode could continuously measure one of the specific quantities. The time resolution of the measurements is only limited by the sampling frequency of the acquisition system. In this case of 2 MHz for the ATCA system at ISTTOK.
The measurements during the discharges on shot lists A, B, C and D (Figs. 3.4 and 3.5) were after accessed through the SDAS server.

The definitions below,

$$I_{sat}^{+} = j_{sat}^{+} A_{pr} = \frac{e n_e c_s A_{pr}}{2}, \tag{4.1}$$

$$c_s = \sqrt{\frac{k_\beta(T_e + T_i)}{m_i}}, \tag{4.2}$$

$$V_p \approx V_f + 3K_\beta T_e. \tag{4.3}$$

, which were previously discussed on chapter 3, depend on several estimations. In particular the 1/2 factor on (4.1). In this sense different expressions of the aforementioned quantities may be seen through the bibliography. Nevertheless, we want to point for now that $I_{sat}^{+} \propto n\sqrt{T_e}$ (4.1 and 4.2), and that $V_f \approx V_p - 3K_\beta T_e$ (4.3).

Fig. 4.1 shows samples of measured signals (during the flat top of the first cycle of alternating current regimes) for I_{sat}^{+} and V_f. Both signals were probed at r=80 mm.

In the remaining of this chapter it's presented the average radial profiles of I_{sat}^{+}, V_f and V_p on 4.2. On 4.3 an initial characterization of the fluctuations, followed by a frequency resolved analysis on 4.4. Finally, on sections 4.5 and 4.6 it's computed the fluctuations poloidal velocity and the induced particle flux, respectively. For every discharge (radial location), an individual study of the previous subjects was done in six individual alternating current cycles (positive or negative I_p). This analysis builds on previous works on ISTTOK where the boundary plasma was characterized [2–5], with a significantly extended analysis performed in this thesis.

4.2 Average profiles

This section presents the radial profiles of I_{sat}^{+}, V_f and V_p (mean values) at the edge/SOL of ISTTOK. The radial profiles are computed with measurements taken during different discharges, in-between each the probe system is radially displaced by a driving mechanism.
The profiles were determined first from the discharges characterized on Fig. 3.4 (shot lists A and B) and secondly for the ones in Fig. 3.5 (shot lists C and D). The first figure referring to two shot lists in which the dependency on the plasma current value was studied. While the second referred to discharges for which the dependency on the neutral density and gas puffing conditions was observed.

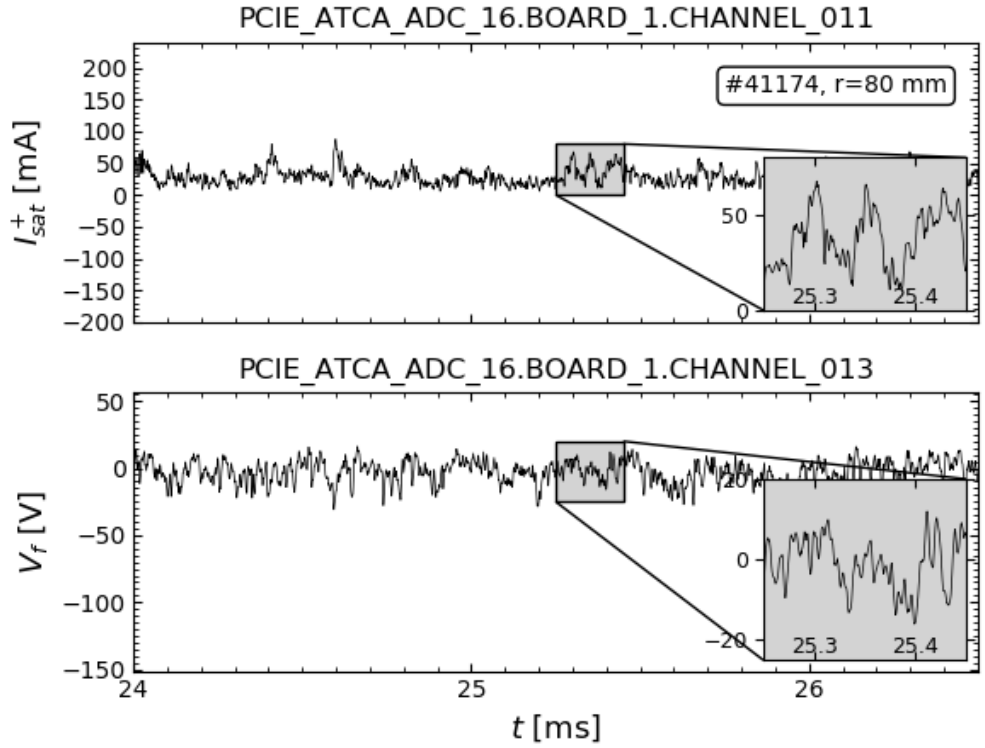

Figure 4.1 Langmuir Probe time recordings of the ion saturation current and floating potential, at the edge of the ISTTOK tokamak (r = 80 mm), for #41174. The time series were obtained with the sampling rate of 2 MHz. It is shown the overall intermittent character of the edge fluctuations in the ISTTOK tokamak, and an enlargement on the burst-events temporal structures.

On Figs. 4.2, 4.3, 4.4 are computed the I_{sat}^{+}, V_f and Vp radial profiles for discharges with $I_p = 4$ kA (shot list A) and $I_p = 4.7$ kA (shot list B). The plasma potential is determined from the definition on 4.3, using the floating potential profile on Fig. 4.3 and ISTTOK's temperature profile on Fig. 3.8 (previously obtained).

Tokamak plasmas tend to be hot and dense in the core with values decreasing towards the walls. In the SOL the plasma temperature and density profiles are expected to decrease exponentially mainly due to the strong parallel losses to the limiter, if assuming a simple SOL model. One can see from the I_{sat}^{+} radial profile on Fig. 4.2 that in the SOL ($r \geq r_L = 85$ mm) I_{sat}^{+} decreases with radius. However an exponential decay may no apply to the entire SOL region. An exponential fit to the data from shot list A (where $I_p = 4$ kA), can be seen in the figure along with the determined radial decay constants, τ. There is a fair agreement with an expo-

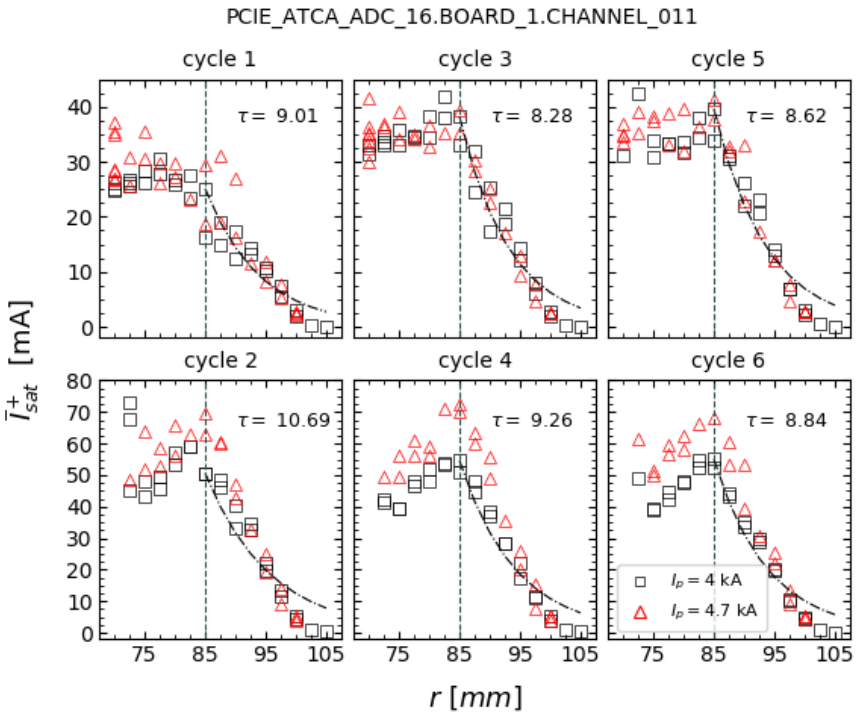

Figure 4.2 Radial profile of the ion saturation current (mean values), taken with Langmuir probe recordings at the edge and SOL of the ISTTOK tokamak. The radial measurements represent the mean values for probe samples of about $\sim 3-5$ ms, with the sampling rate of 2 MHz. The results from shot list A (black squares) were taken for $I_p = 4$ kA, while the results from shot list B (red triangles) with $I_p = 4.7$ kA, Fig. 3.4. The remaining device/plasma parameters were kept for all discharges.

nential decay of I^+_{sat} while $r \lesssim 100$ mm. From this position outwards I^+_{sat} decreases much faster, which is understandable given that it's the location of the wall. The exponential decay length determined, $0.9 \lesssim \lambda \lesssim 1.2$ cm, is according to what is expected for the SOL length at ISTTOK.

The plasma potential has a maximum just before the limiter, as seen on Fig. 4.4. For positive cycles it is observed $V_{p_{max}} \sim 80$ V around r=75 mm, and for negative cycles $V_{p_{max}} \sim 43$ V near r=80 mm. During positive plasma current cycles it is observed a near linear decrease towards both the confined and the SOL regions. The inversion of the slop of V_p corresponds to the change in the sign of the radial electric field E_r. From the plot in Fig. 4.4 the magnitude of E_r seems to be similar in the confined region and in the SOL, and in the order of 2.5 kV/m. For negative plasma cycles the plasma potential maximum is slightly lower and all probing positions have the same sign for E_r in Fig. 4.4. For negative cycles one sees only a decrease from the maximum towards the SOL. The profile of V_p was determined with previous radial temperature measurements of ISTTOK. The temperature was measured for positive cycles and

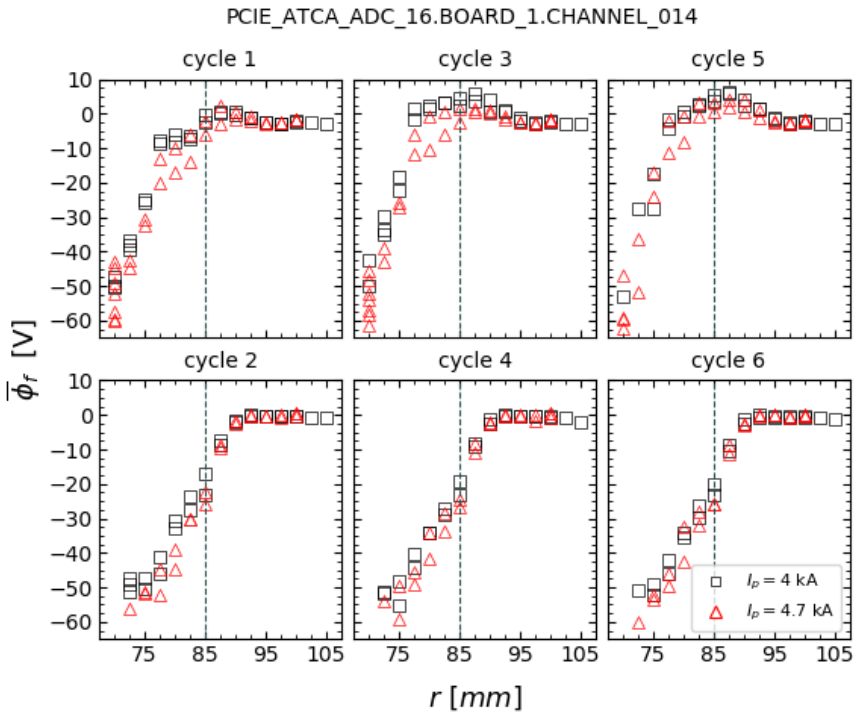

Figure 4.3 Radial profile of the floating potential (mean values), taken with Langmuir probe recordings at the edge and SOL of the ISTTOK tokamak. The radial profiles are computed in the same way as proceeded for the plots in Fig. 4.2. The results from shot list A (black squares) were taken for $I_p = 4$ kA, while the results from shot list B (red triangles) with $I_p = 4.7$ kA, Fig. 3.4.

therefore may not be suitable for the negative ones. The profile computed for positive cycles is very coherent with the inversion of the poloidal velocity of fluctuations.

On the other hand, the radial profiles of the floating potential are coherent to expected results on ISTTOK, [5], and independent of temperature estimations. The radial profile of the floating potential is typically observed to reach a maximum near the limiter's position, decreasing slowly towards the SOL and sharply towards the core plasma, as observed in Fig. 4.3. As expected from the changes in the radial plasma position, the V_f profiles for negative current cycles start to decay slightly further out than for positive cycles.

4.2.1 Alternating current regimes

In this subsection the aim is to consider the radial profiles computed on Figs. 4.2, 4.3 and 4.4 independently of the magnitude of I_p. In order to observe for the same shot list (A or B), in which the same plasma/device parameters are taken, the dependency on the plasma current regime (direction of I_p).

As illustrated in Fig. 3.7, the plasma position typically moves down by about 3 cm from positive to negative cycles, and radially slightly further out by ~ 5 mm. As will be seen, the measurements for negative current cycles have always a very systematic result among themselves, and for most parameters a very distinctive behavior is shown from positive current cycle measurements (also showing a very systematic behavior among themselves).

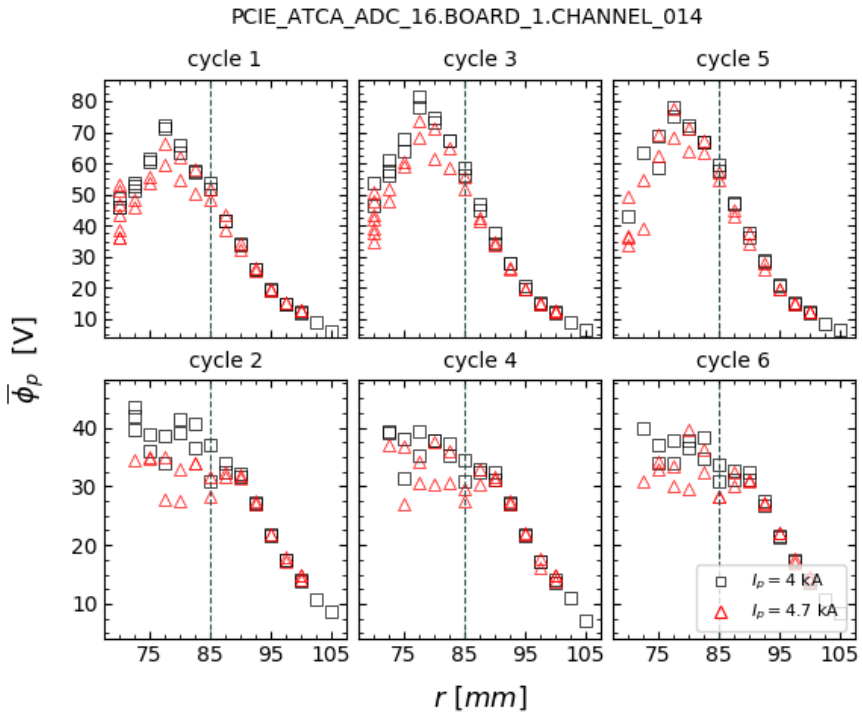

Figure 4.4 Radial profile of plasma potential. Computed from the measurements of the floating potential profile on Fig. 4.3 along with the temperature profile for typical ISTTOK discharges, on Fig. 3.8, according to 3.2.. The results from shot list A (black squares) were taken for $I_p = 4$ kA, while the results from shot list B (red triangles) with $I_p = 4.7$ kA, Fig. 3.4.

Individual analysis for every current regime of each discharge were determined taking time periods of ∼3-5 ms. The time periods were chosen in the discharges flat top in stationary phases, avoiding therefore transient periods. Since the data set of probe measurements used here includes a large number of discharges, the selected time intervals may vary from discharge to discharge. The intervals were carefully chosen for more steady plasma conditions. While corroborating general results of tokamak devices, the analysis throughout the AC cycles of ISTTOK gives an understanding of edge plasma physics on the operation of a tokamak in an alternating plasma current regime.

On Fig. 4.2, during both positive and negative cycles the ion saturation current mean value decreases as expected with radial position in the SOL ($r \gtrsim r_L$). However, the measurements taken also suggest a considerable decrease of the ion saturation current mean value ($\Delta I_{sat}^{+} \sim 30$ mA) for negative cycles, and a slight one for positive cycles ($\Delta I_{sat}^{+} \lesssim 20$ mA), for $r \lesssim r_L$, thus implying a decrease in density into the core (about 1.5 cm) of ISTTOK.
The local maximum exhibit on the radial profiles of density is not anticipated and contradicts the expected plasma losses towards the wall. This result may be explained by the large negative values of floating potential (-60 V) in the innermost positions, Fig. 4.3. As the floating potential takes these large negative values the applied voltage to the probes (-180 V) may not be large enough to completely repel the electrons and drive the probe current into the ion saturation mode. In this case the flux into the probe is not restrictive to ions, but instead results in a net of both ion and electron currents, and therefore for $r \lesssim r_L$ there is no guaranties that the probe current corresponds to a correct measurement of I_{sat}^{+}. It is observed an increase in the maximum value of I_{sat}^{+} between cycles having a positive current regime relative to cycles having a negative current regime ($\Delta I_{max} \sim 30$ mA). This is most probably due to the fact that the plasma position is further out in negative cycles than in positive ones, leading to larger density and temperatures values near the limiter's position ($r_L = 85$ mm). However the exponential decay in the SOL ($r \gtrsim r_L$) is identical for both positive and negative cycles, with exponential decay lengths of $0.9 \lesssim \lambda \lesssim 1.2$ cm.

Overall, the main cause of the differences observed in the averaged radial profiles on Figs. 4.2 to 4.4, across cycles having either positive or negative plasma current regimes, is due to the evolution of the plasma position. The radially outwards displacement of the plasma column during negative cycles is reflected on an increase of the plasma density further out.

4.2.2 Dependency on plasma current

Concerning the dependency on the plasma current (Figs. 4.2 and 4.4), during positive cycles no significant changes are seen for either I_{sat}^{+} and V_p between measurements taken with $I_p = 4$ kA or $I_p = 4.7$ kA. For negative cycles I_{sat}^{+} presents a small increase, and V_p a small decrease with plasma current. These differences may be justified by the fact that on ISTTOK only ohmic heating is available. Therefore as the plasma current is increased the heating power is also typically increased leading to larger temperatures, more ionization and higher densities.

4.2.3 Dependency on the neutral density

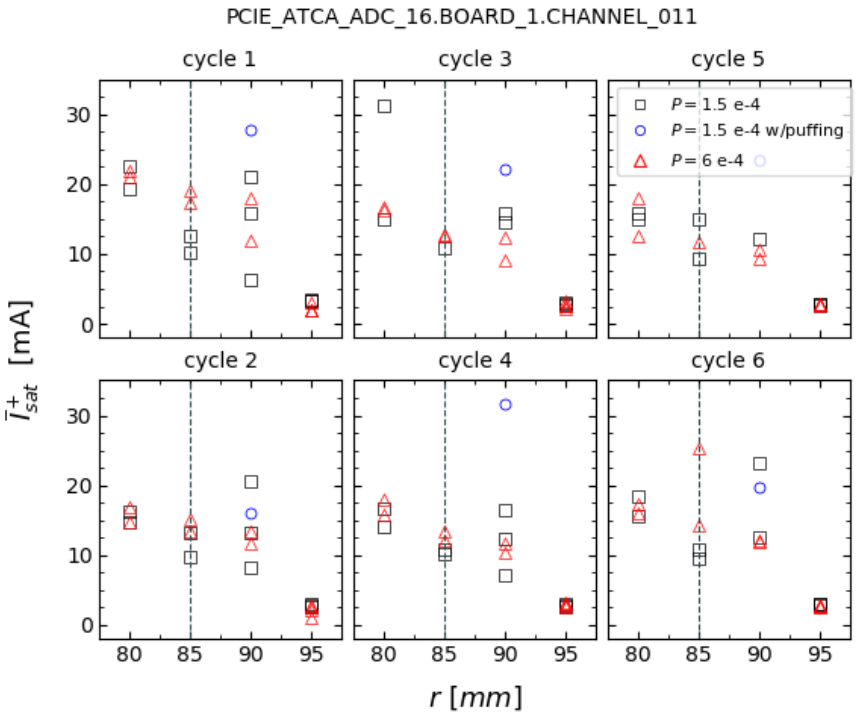

Figure 4.5 Radial profile of the ion saturation current (mean values) for shot lists C and D. The radial profiles are computed in the same way explained for Fig.4.2. The results from shot list C (black squares and blue circles) were taken for $p \sim 1.5e^{-4}$ torr, while the results from shot list D (red triangles) with $p \sim 6.0e^{-4}$ torr, Fig. 3.5.

Tokamaks are often characterized by having a large clearance between the plasma and the wall, achieved for instance by the shaping of the magnetic field surfaces. In the far SOL filaments propagate into a region where the background plasma density is very low but with a high neutral pressure. The interaction of the filaments with neutrals may lead to changes in the properties of the filaments. The plasma ionization source is partially defined by the neutral density. By changing the neutral pressure in the vacuum chamber the density of the neutrals in contact with the plasma can be modified. This is a new research topic with very little information available in the literature, stressing the relevance of this study.

The dependency on the neutral denstity at ISTTOK was studied trough the work pressure estabished during discharges. For shot list C was taken $p \sim 1.5 \times 10^{-4}$ torr, while for shot list D $p \sim 6.0 \times 10^{-4}$ torr, Fig. 3.5. The remaining device/plasma parameters were kept for all discharges. The data set on shot list C still includes a discharge with additional gas puffing injections. On Figs. 4.5 and 4.6 are shown the radial profiles of I^{+}_{sat} and V_f mean values for

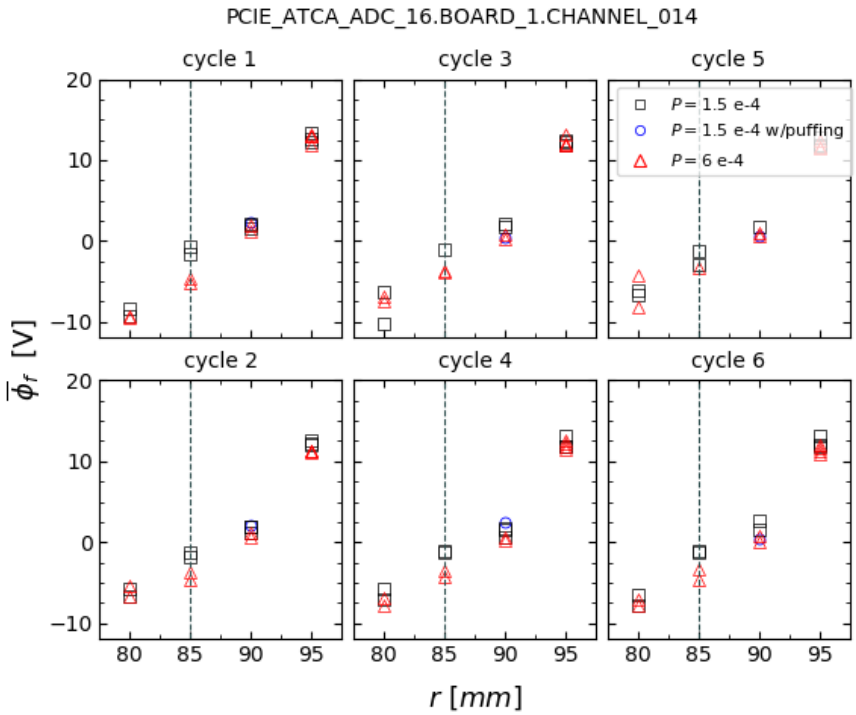

Figure 4.6 Radial profile of the floating potential (mean values) for shot lists C and D. The radial profiles are computed in the same way explained for Fig.4.2. The results from shot list C (black squares and blue circles) were taken for $p \sim 1.5e^{-4}$ torr, while the results from shot list D (red triangles) with $p \sim 6.0e^{-4}$ torr, Fig. 3.5.

shot lists C+D.

As illustrated in Figs. 4.5 and 4.6, the neutral pressure does not seem to change significantly the SOL profiles, although results suggest that the scatter of the data increases at low pressures. Only when gas is puffed along the discharge (large amounts of gas injected for short periods, ~ 2 ms, along the discharge) a clear change in the plasma parameters is observed. In tokamaks the neutral fluxes are defined mainly by the fuel externally injected in the vacuum vessel. However, a particle flux from the wall (limiter and vacuum vessel) also exists (resulting from the fuel retained in the plasma facing components). The flux from the wall will have a direct impact on the ionization sources. However, the particle fluxes from the wall are difficult to control, as they depend on the wall particle inventory that is defined by the history of the previous discharges and cleaning process in between discharges. On ISTTOK the plasma extends all the way until the wall and therefore the ionization sources will be strongly influenced by the particle fluxes from the limiter and vacuum vessel. The fact that no significant change of the plasma properties is seen with neutral pressure may indicate that the fluxes from the wall are dominant on ISTTOK. This is consistent with the observation of a larger data scatter at low pressure, as the wall fluxes may vary significantly from discharge to discharge.

4.3 Properties of the fluctuations

Given that $I_{sat}^{+} \propto n\sqrt{T_e}$ (4.1 and 4.2), and also that $V_f \approx V_p - 3K_\beta T_e$ (4.3) it's assumed that the fluctuations of plasma density $\tilde{n}$ and potential $\tilde{V}_p$ are given by,

$$\tilde{n} \approx \tilde{I}_{sat}^{+} \tag{4.4}$$

$$\tilde{V}_p \approx \tilde{V}_f \tag{4.5}$$

, neglecting the temperature fluctuations, as previously discussed in chapter 3.

Finally, the fluctuations are obtained from the directly acquired probe data, $y(t)$, by subtracting the averaged value of the signals $\bar{y}_N$,

$$\tilde{y}(t) \approx y(t) - \bar{y}_N(t) \tag{4.6}$$

, where the mean signal in time $\bar{y}_N(t)$ is determined by a Moving Average technique, which creates a series of averages of different subsets of the full data set (N data points). The subset averages are calculated typically in a time scale in the order of 1 ms. In this study was set $\Delta t = 0.5$ ms so that there were considered 1000 points for every subset (given the sampling frequency of 2MHz).

The fluctuations statistical properties have been studied with results presented trough Figs. 4.7-4.11. First it is shown the standard deviation for I_{sat}^{+} ($\sigma_{I_{sat}^{+}}$) along with the fluctuation levels ($\sigma_{I_{sat}^{+}}/\bar{I}_{sat}^{+}$, where $\bar{I}_{sat}^{+}$ is the time average) in Fig. 4.7 for shot lists A+B. In Figs. 4.8 and 4.9 are considered the skewness and kurtosis of I_{sat}^{+} and V_f for the same discharges. Lastly, the discrete probability density function is computed for I_{sat}^{+} and V_f on Figs. 4.10 and 4.11, respectively. The PDFs along with the values of skewness and kurtosis will give a broader understanding of the distinct statistical characteristics of turbulent plasma regions.

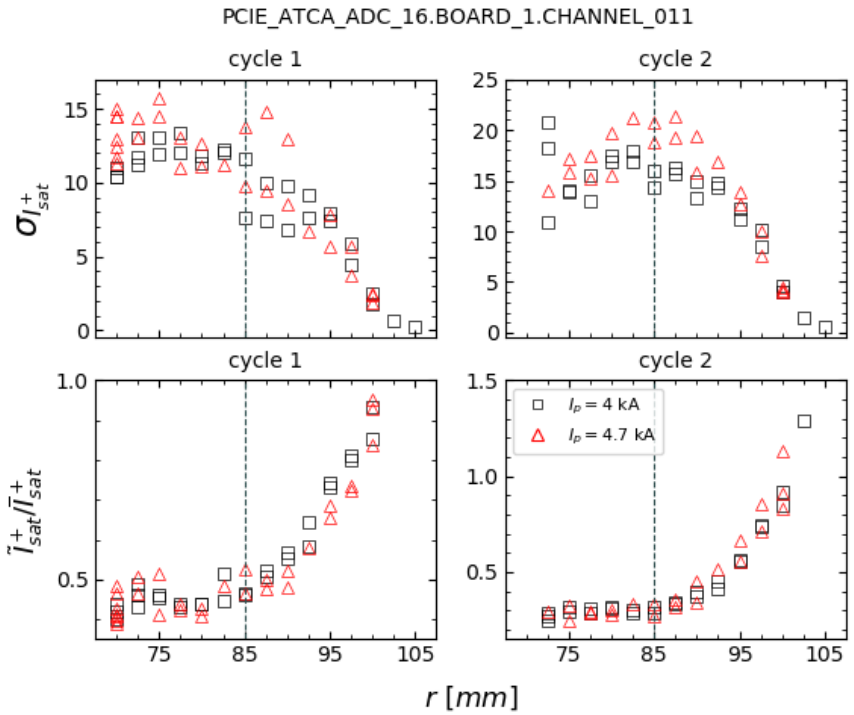

Figure 4.7 Radial profile of the standard deviation ($\sigma_{I_{sat}^+}$) and fluctuation level ($\sigma_{I_{sat}^+}/\bar{I}_{sat}^+$) of the fluctuating ion saturation current. The results from shot list A (black squares) were taken for $I_p = 4$ kA, while the results from shot list B (red triangles) with $I_p = 4.7$ kA, Fig. 3.4.

On Fig. 4.7 one can see that the standard deviation of the I_{sat}^+ fluctuations decreases with radius as for the mean values, because filaments also exhibit losses by parallel transport to the limiter's structures. However, this radial variation is slower than for the mean values (Fig. 4.2), leading to an increase of the fluctuation level with radius. This is a typical result observed in most devices where fluctuation levels in the order of 100% are observed at the far SOL, although on ISTTOK values are often even larger, with fluctuation levels up to 150% observed (see Fig. 4.7). This result indicates that the SOL plasma is dominated by fluctuations and most probably induced by the filamentary structures.

As referred on chapter 2 the intermittent fluctuations of plasma quantities are reflected in a deviation from a Gaussian distribution for the quantities' time series. For the plasma density fluctuations, the higher density blob-filaments result in positive bursts, which are reflected in positive skewness with increasing values towards more turbulent plasma regions in the far-SOL. Similar observations made for the distribution of $\tilde{V}_p$ could indicate overall higher values of the filament's potential, when compared to the background plasma.

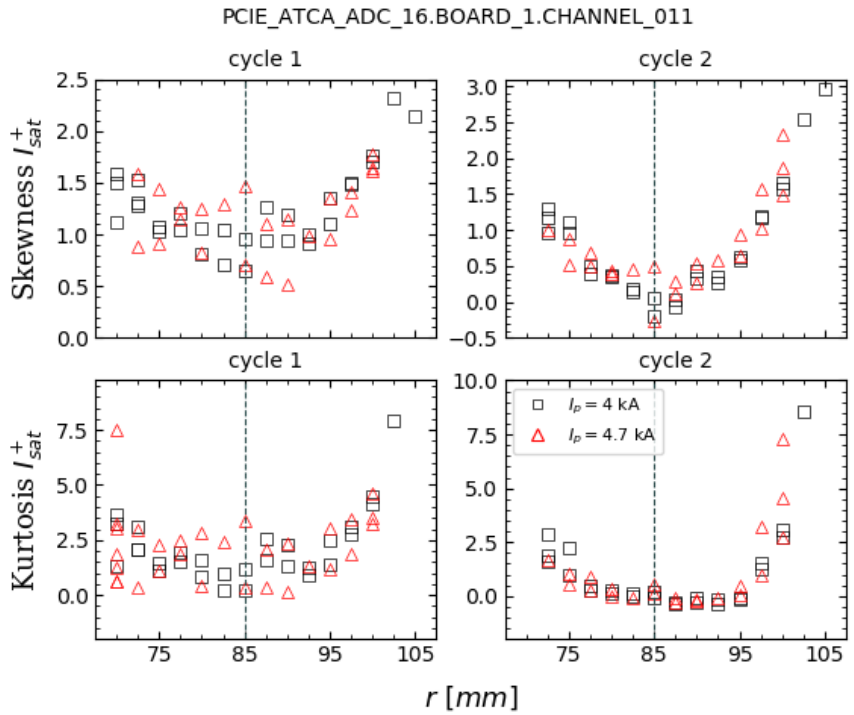

Figure 4.8 Radial profile of the skewness and kurtosis of the ion saturation current. The results from shot list A (black squares) were taken for $I_p = 4$ kA, while the results from shot list B (red triangles) with $I_p = 4.7$ kA, Fig. 3.4.

The skewness and kurtosis should increase with radius at the edge/SOL since the importance of the filaments increases as well. This fact is corroborated in this work for ISTTOK SOL studies. In Figs. 4.8 and 4.9 are computed the skewness and kurtosis radial profiles for both I_{sat}^{+} and V_f, where it's observed an increase with radius at the SOL ($r \geq 85$ mm). A minimum in the skewness is typically observed near the limiter and an increase inwards. The minimum observed may be related to the velocity shear layer position, which can possibly influence the filaments and their propagation.

The higher asymmetry and peakeness of the distributions (measured by the skewness and kurtosis, respectively) are graphically shown by the discrete PDFs on Figs. 4.10 and 4.11. Fig. 4.10 illustrates clearly that the PDF of the I_{sat}^{+} fluctuations in the far SOL is peaked and exhibits a long positive tail, confirming that fluctuations are dominated by intermittent structures.

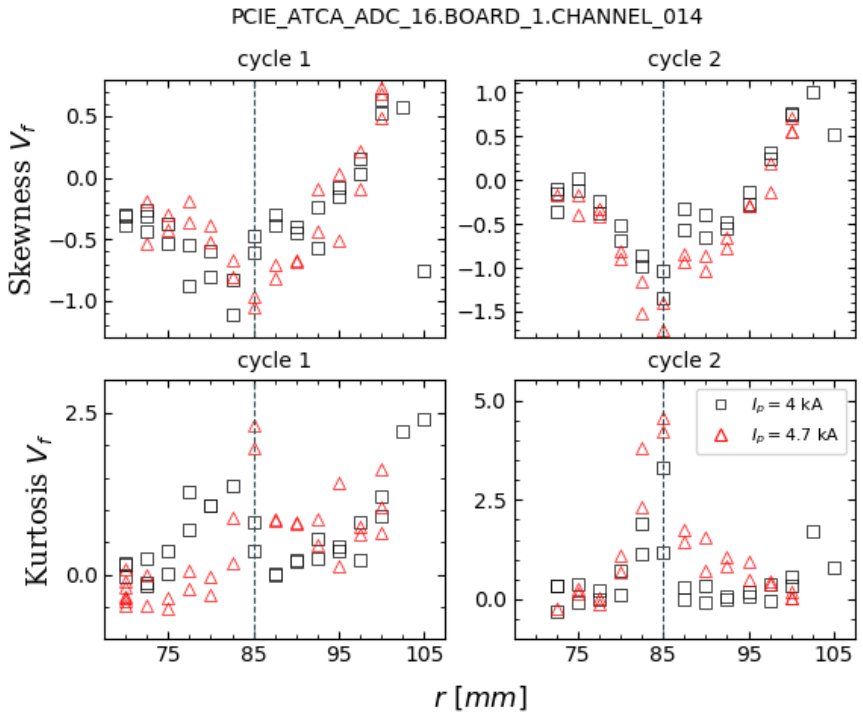

Figure 4.9 Radial profile of the skewness and kurtosis of the floating potential. The results from shot list A (black squares) were taken for $I_p = 4$ kA, while the results from shot list B (red triangles) with $I_p = 4.7$ kA, Fig. 3.4.

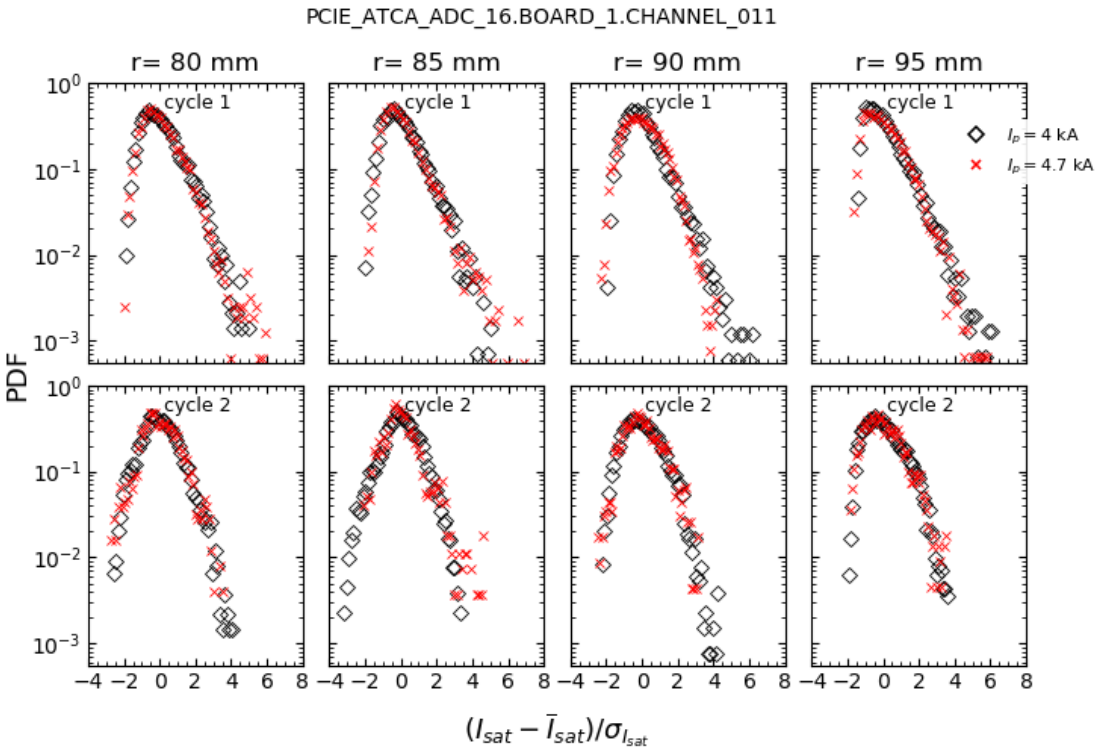

Figure 4.10 PDF of the ion saturation current time series. The distributions were computed for Langmuir probe recordings of about $\sim 3-5$ ms. The results presented were taken for the discharges #41174, #41172, #41169 and #41167, with $I_p = 4$ kA from list A, and #41219, #41216, #41214, and #41212 with $I_p = 4.7$ kA from list B, Fig.3.4.

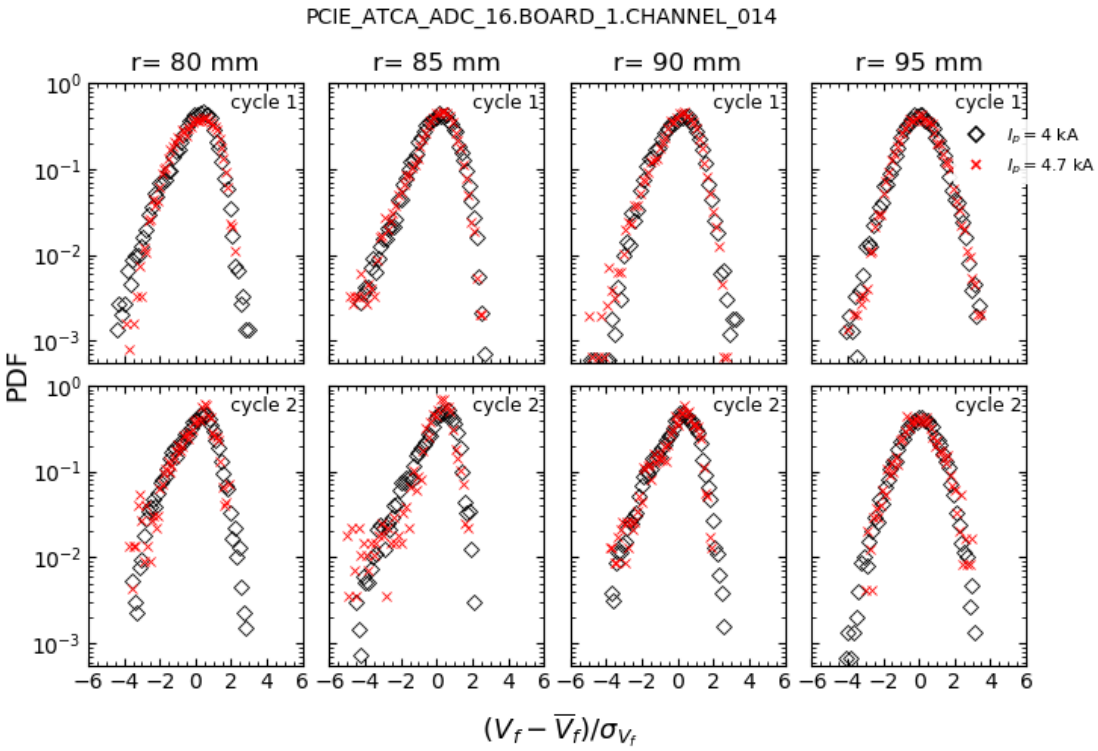

Figure 4.11 PDF of the floating potential time series. The distributions were computed for Langmuir probe recordings of about $\sim 3-5$ ms. The results presented were taken for the discharges #41174, #41172, #41169 and #41167, with $I_p = 4$ kA from list A, and #41219, #41216, #41214 and #41212 with $I_p = 4.7$ kA from list B, Fig.3.4.

4.4 Frequency resolved measurements

To further characterize the fluctuations properties the frequency power spectra of the $\tilde{I}^+_{sat}$ and $\tilde{V}_f$ signals has been computed for the different radial locations r=80, 85, 90 and 95 mm, with $I_p = 4$ kA (discharges #41174, #41172, #41169 and #41167 from list A).
The frequency power spectra is very broad extending above 100 kHz, generally not exhibiting any coherent structure (not clear frequency component), with the power displaying a small variation with frequency up to ~ 100 kHz, and then a fast decay often with a power law of f^{-C}.

For each of the four locations, the spectra of both I^+_{sat} and V_f were constructed from time periods of about $\sim 3-5$ ms. During this section it will be considered the first and second plasma current cycles, therefore having the characterization for a positive and negative plasma current cycle, respectively. The spectras were determined using the Welch method, and finally the frequencies were normalized according to the σ of each series.

In Fig. 4.12 the computed power spectra for I^+_{sat} and V_f (from list A with $I_p = 4$ kA)

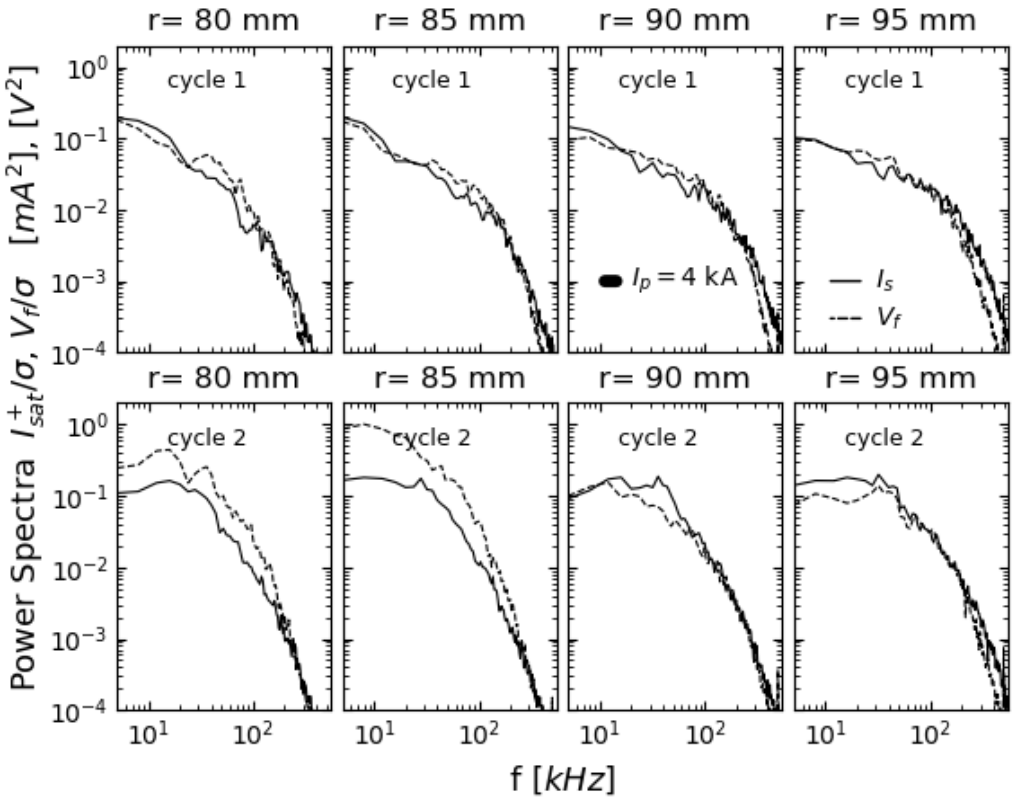

Figure 4.12 power spectra (PS) of the ion saturation current (solid lines) and floating potential (dashed lines) time series at the edge/SOL of the ISTTOK tokamak. For each quantity was computed the PS for $I_p = 4$ kA (#41174, #41172, #41169 and #41167 from list A, Fig.3.4). The frequencies were normalized according to the factor $1/\sigma$ of each time series. The PSs' shape supports what was described in chapter 2 (see Fig.2.9).

display a similar shape, despite having a broader range of dominant frequencies and a higher power amplitude maximum for I_{sat}^+. This fact is coherent with the overall higher intermittent character of the ion saturation current signals.

Outside the confined region the differences between the power spectra computed for the two quantities shows to be more contrasting with each other. Nevertheless, both power spectra exhibit a strong dependence on frequency at high frequencies, rapidly decaying with $1/f^C$, where C is a constant that varies for the different segments of the power spectra.

The value of the constant C has been determine for the I_{sat}^+ spectra on Fig. 4.12 (at r=80 mm, during cycle 1), taken the frequency intervals shown on table 4.1. The faster decay for higher frequencies, is shown by higher values for C on table 4.1. At lower frequencies the spectral power shows a more modest dependency on frequency. This can be concluded both from Fig. 4.12 and the power law f^{-C} dependency on table 4.1.

Table 4.1 Determination of the decay with f^{-C} for the I_{sat}^{+} spectra on Fig. 4.12 (at r=80 mm, during cycle 1). The constant C has been seen to take different values in different segments of the curve.

Δ_f (kHz)		f^{-C} fit to PS(I_{sat}^{+}/σ) (mA^2)
f_i	f_f	C
20	50	0.304 ±0.005
50	100	0.372 ±0.006
100	150	0.422 ±0.004
150	200	0.462 ±0.004
200	250	0.513 ±0.004

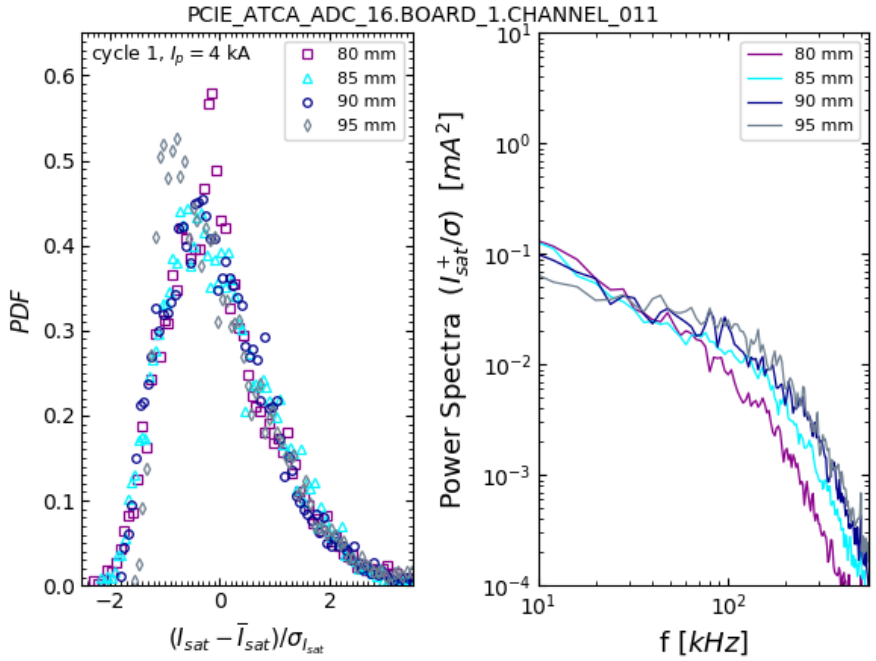

Figure 4.13 PDF and PS of the I_{sat}^{+} fluctuations. Comparison of the PDF and power spectra results shown on Fig.4.10, Fig.4.11 and Fig.4.12. The fluctuations PDF shows a higher asymmetry (higher skewness) for the outwards locations. Most clrear for r=95 mm. While for the PS, the relative importance of the lower frequencies decreases with radius and broader spectras are observed.

Still from Fig. 4.12, and clearly on Fig. 4.14, one can see that the fluctuations' power spectra has a broader extent for outer positions r=90, 95 mm, which indicates an increase of the higher frequency components of the fluctuations near the wall. For outer radial locations the relative

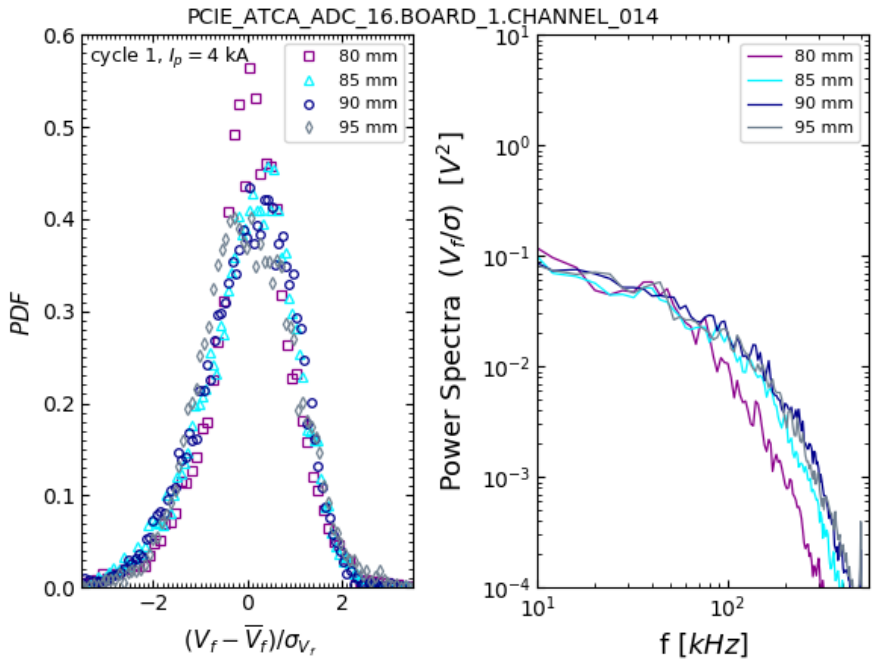

Figure 4.14 PDF and PS of the V_f fluctuations. Comparison of the PDF and power spectra results shown on Fig.4.10, Fig.4.11 and Fig.4.12. The relative importance of the lower frequencies decreases with radius and broader spectras are observed.
Its known from Fig. 4.9 that the asymmetry of the PDF of $\tilde{V}_f$ increases with radius, although the changes are not very perceptible in this figure.

importance of the lower frequencies decreases.

The evolution of the fluctuations with a time scale smaller than 1 ms was studied by applying a Savitzky-Golay (SG) filter ([42, 43]) to the original signals of I_{sat}^{+} and V_f. The method uses a sliding window of $n = L + R + 1$ points, with L and R being the left and right neighbors of a center point x_i. For each iteration i a polynomial of order M, f_M, is approximated to the n data points. The smoothed value at x_i corresponds to the result of the fit, $f_M(x_i)$. On the other hand, the remaining values of f_M are discarded for the i^{th} iteration. It was taken $n = 1001$ in order to consider the fluctuations evolution with time scale of ~ 0.5 ms (signals with sampling frequency of 2 MHz). The SG filter choice of appropriate parameters is not usually obvious, and some visual optimization was needed in choosing M=4. In Fig. 4.15 its shown the SG filter result for I_{sat}^{+} and V_f.
This smoothing technique of the fluctuating signals was introduced with the aim of suppressing the highest frequencies of the fluctuations, but not so severe that we would completely lose track of the intermittency appearing in the data. SG filters are commonly used to smooth signals with

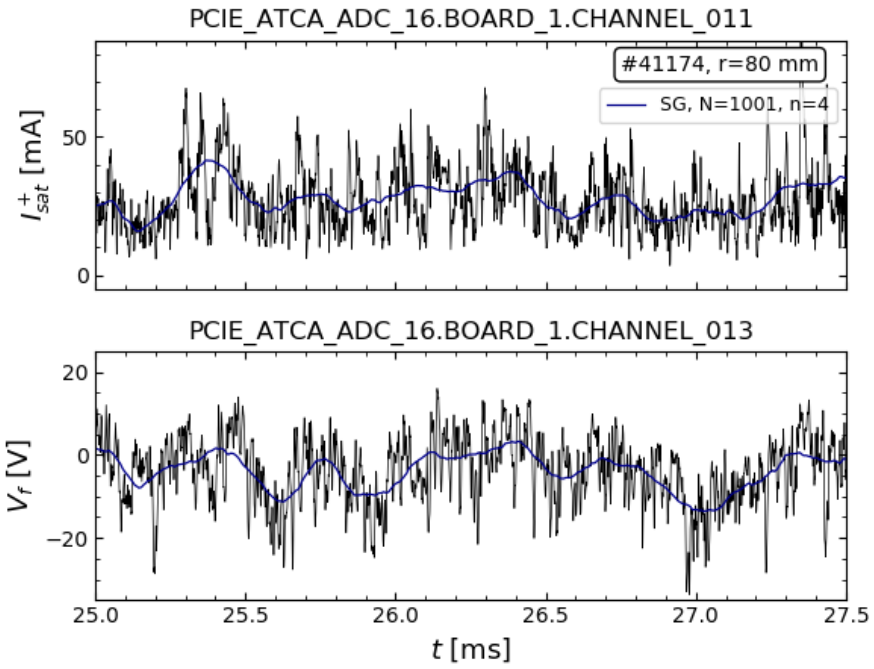

Figure 4.15 Smoothing result of a Savitzky-Golay filter (n=1001, M=4) on the initial recordings of the ion saturation current and floating potential ($r = 80$ mm, $f = 2$ MHz), for #41174. The technique ended up revealing in this case a possible trend for the structures first introduced in the zoom-in in Fig. 4.1 (at r=80 mm).

a large frequency span, as for the broad PS seen for the edge/SOL fluctuations.

The technique ended up revealing in this case a possible trend for the structures first introduced in the zoom-in in Fig. 4.1 (at r=80 mm). Filaments with usual structures around $10 - 100$ μs ($10 - 100$ kHz) are in good agreement with the observed PS of fluctuations. Furthermore, we can see that the intensity of these bursts is modulated in a time scale $0.1 - 1$ ms ($1 - 10$ kHz), Fig. 4.15. The apparent modulation of the intermittency intensity is probably associated with a variation in the mechanisms driving the filaments at ISTTOK.

4.5 Cross-correlation

Electrostatic probes allow the measurement of the velocity of the turbulence moving in the plasma, along with their characteristic time and spatial structures. The correlations between different pin measurements are strongly influenced by the propagation and characteristic structures of the turbulence. The correlations between the several pin measurements allow to determine the velocity of the induced fluctuation structures in the direction of the probe array. For the

set-up in this experiment it will allow to determine the poloidal velocity. Simultaneously, one can approximate the characteristic time of the fluctuations by taking the auto-correlation time (time for which the auto-correlations decays by 1/e). The determination of the poloidal velocity along with the temporal structure of the fluctuations are finally used to estimate their spatial structure in the poloidal direction.

4.5.1 Poloidal velocity of the fluctuations

To determine the poloidal velocities were taken from two different probe pins (of either I_{sat}^{+} or V_f) measurements with the same time period (typically $\sim$ 5 ms), for each location. The time lag of the maximum value of the cross correlation between two poloidally shifted probe measurements i and j, $n_{\max_{i,j}}$, has been used to determine the poloidal propagation velocity of the fluctuations as defined bellow,

$$v_\theta = \frac{n_{\max_{i,j}}}{\Delta\phi_{i,j}}, \tag{4.7}$$

$$n_{\max_{i,j}} = lag \text{ for } \max(f[k]_{\text{probe i}} \star g[k]_{\text{probe j}}), \tag{4.8}$$

where $\Delta\phi_{i,j}$ corresponds to the poloidal shift between the considered pin probes, i and j.
The cross correlation between the time series of one pin by itself, i.e., the auto-correlation, has a maximum value at lag=0, and was used as a reference when determining the lag between the cross correlations of different pin signals.

The poloidal velocities determined are shown on Fig. 4.16 using the cross correlations of both ion saturation current and floating potential signals, and show the reverse of the filaments poloidal velocity around the limiter. The slope of the plasma potential radial profile changes sign around the limiter's position (Fig. 4.3) so we expect the plasma rotation due to the $\vec{E_r} \times \vec{B}_\phi$ drift to reverse around the same position, usually referred to as the velocity shear layer.

As illustrated in Fig. 4.16 in both sides of the velocity shear layer are seen similar magnitudes of v_θ, in the order of 5-10 km/s. The cross-correlation gives the similarity between the signals of two different pins in function of the time delay between them. Here the time delay between the series is limited to multiples of the acquisition system resolution. The filaments poloidal

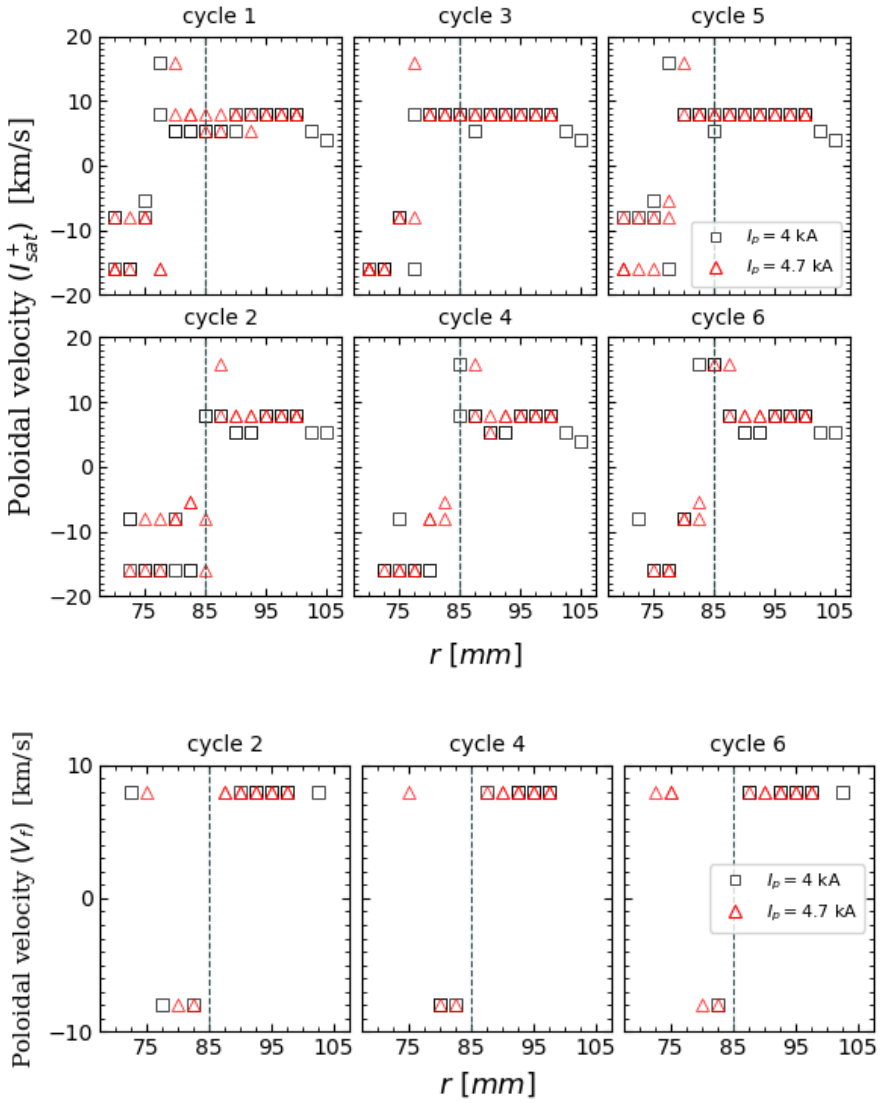

Figure 4.16 Radial profile of the blobs' poloidal velocity, $\|\vec{v}_\theta\|$, determined according to (4.7), where it is used the cross correlations of both ion saturation current and floating potential signals. The blob-filaments propagate with opposing direction across the shear layer ($\sim r_L$), however in both sides of the velocity shear layer are seen similar magnitudes.

propagation and time structures can be smaller than the discrete time delays that arise from the finite resolution of the acquisition system (0.5 μs). In this sense, the discrete time delays possible may not be enough to resolve the poloidal displacement of the filaments, resulting in similar determinations through the SOL.

The propagation velocity of the fluctuations is generally small in the plasma frame and therefore the $\vec{E}_r \times \vec{B}_\phi$ velocity should dominate the measurements. To confirm this assumption,

the $\vec{E_r} \times \vec{B_\phi}$ drift velocity can be estimated from the plasma potential profile at both sides of the limiter (see Fig. 4.4) and compared with the poloidal velocity obtained here. From Fig. 4.4 a radial electric field in the order of 2.5 kV/m is obtained both in the SOL and in the confined region resulting in a drift velocity of 5 km/s. This is in reasonable agreement with the estimate obtained from the plasma fluctuations taking into account the limitations of the cross-correlation method. The plasma potential profile has a similar decay on both sides of the shear layer with a near constant decay, which should also be a major factor in the similar results obtained.

4.5.2 Characteristic structure of the fluctuations

The auto-correlation time (for which the auto-correlations falls by 1/e) gives an approximation of the characteristic temporal structure of the filaments (locally). It is assumed here that the living time of the turbulent structures is larger than the time taken by the filaments to cross a probe, and therefore the filament duration as seen by the Langmuir pin will be given by its poloidal dimension and velocity.

The example on Fig. 4.17 shows the auto-correlation for an I_{sat}^{+} measurement from ch 11 at $r = 80$ mm. From this example it's concluded that the characteristic time of the fluctuations at $r = 80$ mm is ~ 7.3 μs. On Fig. 4.17 it's shown a radial profile of the duration of the turbulent structures, estimated from the remaining discharges in shot list A (for cycles 3 (pos.) and 4 (neg.)). The remaining data is computed in the same way for the auto-correlation of the measurements of ch 11. It's not shown in the figure, but the results using measurements from ch 12 (also I_{sat}^{+}) have the same exact values. The distance between the two pins (8 mm) is relatively smaller that the characteristic spatial structure of the fluctuations (a few centimeters).

It is observed that structures have a duration of ~ 5 μs from $r = 70$ mm growing until ~ 13 μs just inside the limiter during positive cycles. For negative cycles the growth for the temporal structures is slightly lower from ~ 5 μs to ~ 9 μs. Further out the auto-correlation time decreases from ~ 5 μ at the limiter to $2 - 3$ μs at $r = 105$ mm.
The smaller correlation times in the far-SOL probably result from the fact that the plasma is more turbulent near the wall than inside the limiter. More turbulent plasma regions display smaller time structures (as seen by the probes), i.e., higher intermittency.

The profiles of the characteristic time structures, along with the poloidal velocities (Fig. 4.16) were used to estimate the characteristic poloidal spatial structures, 4.18.
During both negative and positive current cycles are seen in the SOL poloidal structures ranging

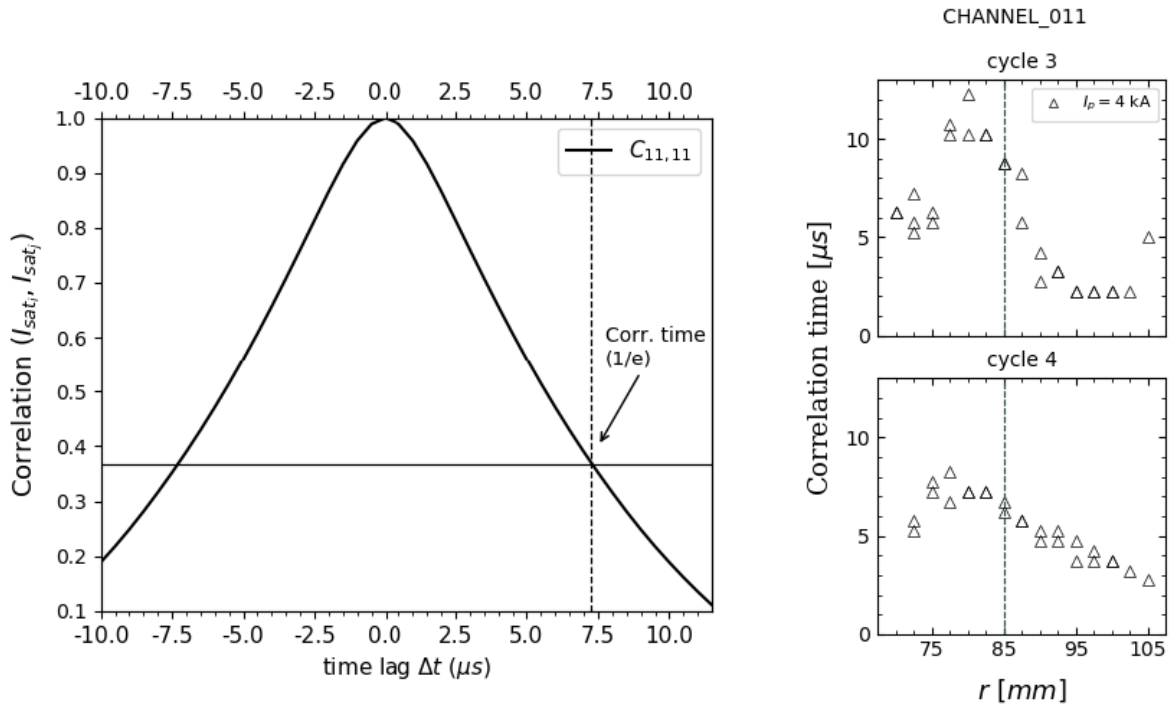

Figure 4.17 Time delay analysis. The auto-correlation time for the I_{sat}^{+} measurements from ch 11 were used to estimate the characteristic time structures of the fluctuations.

from $\sim 1-6$ cm. The decrease of the poloidal dimension of the turbulent structures from the edge to the SOL confirms again that the SOL plasma is dominated by filamentary structures, with a poloidal dimension in the order of a few centimeters.

4.6 Transport induced by fluctuations

In this section we hope to further emphasize the consequences of the fluctuations on the edge and SOL of ISTTOK by determining the radial profile of the induced particle transport, $\bar{\Gamma}_r$. The radial profile of $\bar{\Gamma}_r$ (mean values), was determined for the positions listed on Fig. 3.4 (shot lists A and B). Once again the profile is computed for the individual alternating plasma current cycles. The results for each location represent the mean values for time periods of about $\sim 3-5$ ms, during stationary periods of the flat top of each plasma current cycle.

As expressed on 2.1 the turbulent particle flux is given by $\bar{\Gamma}_r =< \tilde{n}(t) \cdot \tilde{\vec{E}}_\theta(t) > /B$ (where the angular brackets denote a time average). The plasma density fluctuations are estimated from the fluctuating ion saturation current, 4.4. The poloidal electric field fluctuations, $\tilde{\vec{E}}_\theta$, estimated from two floating potential signals, 4.5.

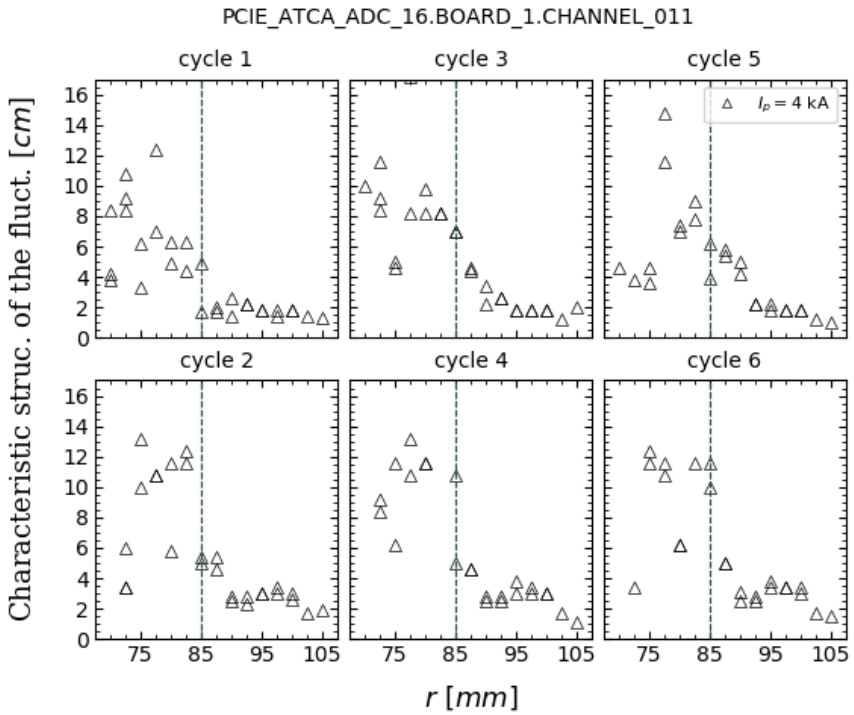

Figure 4.18 Characteristic spatial structures of the fluctuations.

Recall that $I_{sat}^{+} = en_e c_s A_{pr}/2$, 4.1. Given the probe area of $A_{pr} = 1 \times 10^{-6}$ m^2, and $C_s = \sqrt{2T_e/m_i} = 1 \times 10^4 \sqrt{T_e}$ (hydrogen nuclei), follows for the fluctuating density

$$\tilde{n} = \frac{1.25 \times 10^{21}}{\sqrt{T_e}} \tilde{I}_{sat}^{+}. \tag{4.9}$$

It has been used the ion saturation signal obtained from channel 11, and the temperature is determined in function of r from 3.8.

The fluctuating poloidal field is determined from two floating potential signals $\Delta_\theta = 2$ mm apart, measurements from channels 13 and 14,

$$\tilde{E}_\theta(t) = \frac{\tilde{V}_{f1} - \tilde{V}_{f2}}{2 \times 10^{-3}}. \tag{4.10}$$

Finally the toroidal magnetic field is $B = 0.5$ T.

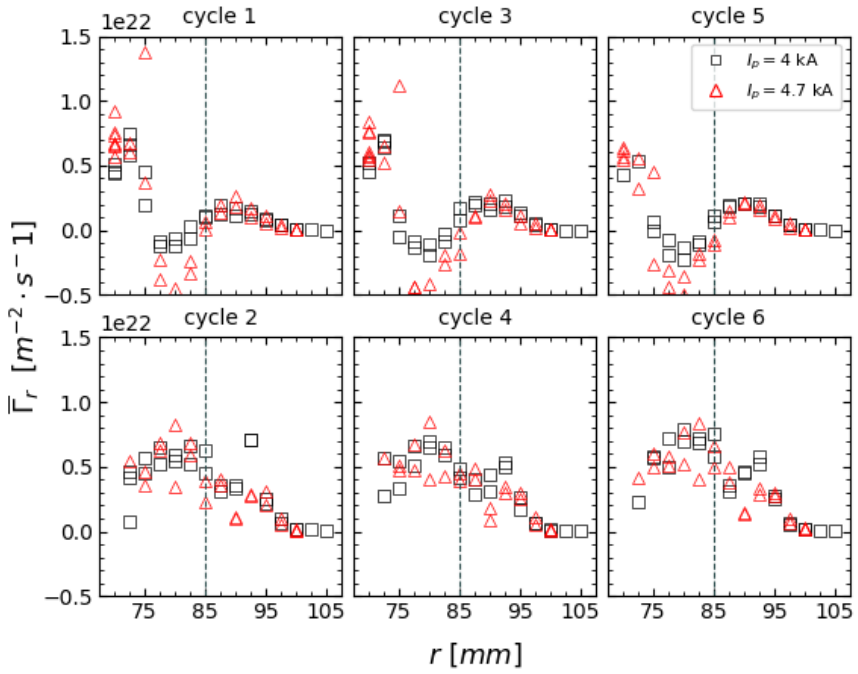

Figure 4.19 Radial profile of the turbulent particle flux, $\bar{\Gamma}_r =< \tilde{n}(t) \cdot \tilde{\vec{E}}_\theta(t) > /B$. The plasma density is estimated from fluctuating ion saturation current (channel 11), and the poloidal electric field fluctuations, $\tilde{\vec{E}}_\theta$, estimated from two floating potential signals $\Delta_\theta = 2$ mm apart, (measurements from channels 13 and 14).

In this way,

$$\bar{\Gamma}_r = 1.25 \times 10^{24} \frac{< \tilde{I}^{+}_{sat}(t) \cdot (\tilde{V}_{f2}(t) - \tilde{V}_{f1}(t)) >}{\sqrt{T_e}}. \tag{4.11}$$

On Fig. 4.19 is shown the profile of the turbulent particle flux computed as just explained, for $[\bar{\Gamma}_r] = m^{-2}s^{-1}$.
The profile shows an increase from the confined region towards the inner SOL. For the negative AC cycles the induced transport shows a systematic maximum just around the limiter's position, and rapidly decreasing towards the wall, since the density should be considerably smaller.
The inner displacement of the plasma for the positive cycles, is shown on Fig. 4.19 as a inner displacement of the behavior profile observed for the negative cycles. The maximum induced transport is seen around $r = 70$ mm, while around the wall position the decreasing profile takes values near zero.

Fluctuations induce by plasma turbulence, and in particular by filaments, cause radial trans-

port. In the SOL, apart from radial transport, there are fast parallel losses to the limiter surfaces and therefore it is expected that the turbulence flux decay radially as observed. In the confined region the ionization sources may exist but because there are no parallel losses (field lines are closed) the particle flux should increase with radius up to the limiter position. This is observed in the region just inside the limiter but not for $r < 80$ mm, suggesting again that I_{sat}^{+} data may not be valid in this region.

At ISTTOK the particle confinement time is in the order of $\tau = 0.2$ ms, [3]. The confinement time can be estimated from 4.12.

$$\tau = \frac{N}{\bar{\Gamma}_T A}, \tag{4.12}$$

where $N = \bar{n}V$ is the total number of particles in the chamber, Γ_T the total particle flux ($\bar{n}$ and V are the average density, and volume of the torus), and A the surface of the torus. At ISTTOK follows that,

$$\begin{cases} \bar{n} \sim 4 \times 10^{18} & [m^{-3}], \\ V = 2a^2\pi^2 R_0 \sim 0.066 & [m^3], \\ S = 4a\pi^2 R_0 \sim 1.544 & [m^2]. \end{cases} \tag{4.13}$$

From the quantities at 4.13 and the expression on 4.12 one estimates that the total particle flux at ISTTOK is in the order of $10^{21} m^{-2} s^{-1}$. The average particle flux induced by the edge/SOL fluctuations, estimated in Fig. 4.19, is in the same order of magnitude as the total flux at ISTTOK, of $\sim 10^{21} m^{-2} s^{-1}$. As mentioned throughout this work the particle transport induced by the edge/SOL fluctuations dominates the losses in most fusion devices. Here at ISTTOK we have estimated the losses induced by fluctuations to be in the same order of magnitude than the total particle flux (given by the measured confinement time).

Chapter 5
Conclusions & Future Work

5.1 Conclusions

This thesis aimed to further understand the presence of blob-filaments and the induced fluctuations on plasma quantities at the boundary plasma of the ISTTOK experiment, while emphasizing the major importance of the radial transport induced by fluctuations.
The diagnosis of the plasma edge/SOL (up to 1.5 cm inside the LCFS) is achieved with high resolution at ISTTOK with a Langmuir probe system coupled to a ATCA DAQ system.

An initial assessment for discharges with two distinct plasma current values $I_p = 4$, 4.7 kA showed slightly higher values for the average $I_{sat}^{+} \propto n$ (chapter 4) and slightly lower values for the average V_p in the same conditions. This observation (clear during negative plasma current cycles) may result from the fact that only Ohmic heating is available on ISTTOK. The gain in plasma current usually sets a gain in the heating power leading to larger temperatures, more ionizations and higher densities. During the characterization of the fluctuations no relevant differences were seen, with neither a suppression or a more intermittent character with the 0.7 kA gain in I_p.

It also was intended to investigate how the properties of filaments were influenced by the interactions with the neutrals by changing the neutrals pressure. It's a new research topic and little was known to start with. The results for discharges with the different work pressure values $p = 1.5$, 6×10^{-4} torr didn't show a significant change for the average SOL profiles (on chapter 4). More important, for the different values of p, the characterization of the fluctuations showed similar results (from the fluctuation levels, skewness, kurtosis and PDF of these discharges).

During this work we didn't got to realize discharges with a broader range of either plasma current or neutral pressure values. However, an extensive and comprehensive characterization of the plasma fluctuations was carried out. Density and potential fluctuations measurements were performed with a high radial (2 mm) and temporal (0.5 μs) resolution. By applying different analysis techniques, ranging from statistical analysis to correlation techniques and spectral analysis, the fluctuations where characterized with a contribution to a better understanding of the physics associated with the plasma filaments and its impact on the radial transport.

We have seen in chapter 4 edge/SOL fluctuation levels increasing from $\sim 25\%$ inside the LCFS to $\sim 150\%$ at the far SOL, which indicates that the SOL plasma is dominated by fluctuations and most probably induced by the filamentary structures. The SOL fluctuations were shown to have a distribution consistent with a high presence of intermittent events. The filamentary structures in the SOL should result in the intermittency of plasma quantities and a deviation from a Gaussian distribution, due to their different properties from the background plasma. High skewness values should be seen for the density fluctuations, for example, given the higher density of the filaments. We concluded in this work this hypothesis for the negative and positive plasma current cycles that ISTTOK operates on. Longer positive tails were also found in the density fluctuations ($\tilde{I}^{+}_{sat}$) PDF at the far SOL (r=95 mm), confirming that fluctuations are dominated by intermittent structures at this region.
Overall the fluctuation levels, skewness and kurtosis should increase with radius at the edge/SOL, since the importance of the filaments increases as well. The importance of the induced fluctuations in the edge region near the limiter has severe consequences in degrading the plasma confinement, therefore restraining the machine performance.

We were able to show the frequency resolved fluctuation measurements at the edge and SOL of ISTTOK, and corroborate a common result in most fusion devices. The computed power spectra (using the Welch method) as expected showed to be very broad extending above 100 kHz. It was seen that the relative importance on the lower frequencies decreases going near the wall, where there is an increase of the higher frequency components of the fluctuations. Therefore, at the far SOL are seen even broader spectras. Overall the fluctuations power shows a modest dependency with frequency for $f \lesssim 100$ kHz, and then a fast decay often with a power law f^{-C}. The faster decay of the power from $f \sim 100$ varies for different frequency ranges, as displayed for the values of C estimated on chapter 4.

Filaments with usual structures around $10 - 100$ μs ($10 - 100$ kHz) are in good agreement

with the observed PS of fluctuations. In addition a Savitzky-Golay smoothing technique end up revealing that the intensity of these bursts may be modulated in a time scale $0.1 - 1$ ms ($1 - 10$ kHz), Fig. 4.15, probably associated with a variation in the mechanisms driving the filaments.

Afterwards, the poloidal velocities of the fluctuations were determined. In the poloidal direction the filaments are expected to rotated along with the background plasma, since the $E_r \times B_\phi$ drift should be dominant over the smaller velocity of the fluctuations. This hypothesis is in good agreement with our observation as the poloidal velocity derived both from the fluctuation and the radial electric field profile are in the order of 5-10 km/s. Similar magnitudes were obtained in both sides of the velocity shear layer, coherent with similar magnitudes of the radial electric field.

The probe array system installed at ISTTOK allowed to determine the induced particle flux from simultaneous measurements of the ion saturation and poloidal electric field fluctuations. We have concluded an induced particle flux in the same order of magnitude as the total particle losses of ISTTOK, of $10^{21} m^{-2} s^{-1}$. The flux showed to increase in the edge boundary plasma, from $r = 75$ mm to $r \sim 85$ mm. These observations are of major importance in the performance of devices such as ISTTOK, where the turbulence in the confined edge plasma (near the LCFS) results in dominant losses of particles and energy, degrading the confinement conditions and energy output. Hopefully the previous characterization of the turbulence induced fluctuations are a significant addition in understanding the conditions in which these mechanisms arise and in solving some of the constrains observed in the edge plasma of fusion devices.

The results through chapter 4 are in agreement with previous observations at ISTTOK, and are a good addition to the existent literature for the edge/SOL plasma not only at this experiment but for fusion devices in general. Given that ISTTOK operates with AC plasma current cycles to allow longer discharges, trough out this entire work we also added an analyses of the fluctuations and induced transport conditions in six consecutive AC cycles of the experiment.

5.2 System Limitations & Future Work

During this work the machine conditions did not allow to realize discharges with a broader range of either plasma current or neutral pressure values. For example, the maximum achievable plasma current on ISTTOK strongly depends on the machine vacuum and wall conditions. Following a ISTTOK shutdown, typically only after one month of operation plasma currents above 5 kA are achieved, requiring not only good vacuum condition (in the order of 2×10^{-7}

mbar) but also conditioned walls (low level of surface and retained impurities). In this condition, the low impurity content in the plasma will result in lower plasma resistivity, therefore offering the possibility to achieved higher plasma currents. As the machine was not fully conditioned during our experiments, the maximum achieved plasma current in stationary conditions was limited to about 4.7 kA. Future work to understand the influence of both the plasma current and neutral density on the plasma fluctuations would consist on performing more experiments in function of a broader range of these parameters, when the machine conditions permit so.

Across this work some uncertainties were mentioned about the I_{sat}^{+} measurements on chapter 4. In future experiments it is also necessary to make sure that the I_{sat}^{+} data is valid by applying a large bias voltage.

Bibliography

[1] H. Fernandes, J. Cabral, C. Varandas, and C. Silva, "20 years of isttok tokamak scientific activity," in *Presented at the 24th IAEA Fusion Energy Conference. San Diego, USA, October 8–13*, 2012.

[2] H. Fernandes, C. Varandas, and J. Cabral, "Role of the tokamak isttok on the euratom fusion programme," *Brazilian journal of physics*, vol. 32, no. 1, pp. 100–106, 2002.

[3] C. Silva, H. Figueiredo, I. Nedzelskiy, B. Gonçalves, and C. Varandas, "Control of the edge turbulent transport by emissive electrode biasing on the tokamak isttok," *Plasma physics and controlled fusion*, vol. 48, no. 6, p. 727, 2006.

[4] C. Silva, H. Figueiredo, P. Duarte, and H. Fernandes, "Characterization of the poloidal asymmetries in the isttok edge plasma," *Plasma Physics and Controlled Fusion*, vol. 53, no. 8, p. 085021, 2011.

[5] C. Silva, H. Fernandes, H. Figueiredo, C. Varandas, J. Cabral, C. Hidalgo, M. Pedrosa, and E. Sanchez, "Plasma fluctuations and reynolds stress measurements on the tokamak isttok," *Czechoslovak Journal of Physics*, vol. 49, no. suppl. S3, pp. 29–34, 1999.

[6] M. G. Sevillano, I. Garrido, and A. J. Garrido, "Sliding-mode loop voltage control using astra-matlab integration in tokamak reactors," *International Journal of Innovative Computing, Information and Control*, vol. 8, no. 9, pp. 6473–6489, 2012.

[7] "Tokamak- Wikipedia, the free encyclopedia," https://en.wikipedia.org/wiki/Tokamak, accessed: 2019-05-30.

[8] "An introduction to operational regimes in limiter and divertor tokamaks, Mitglied der Helmholtz-Gemeinschaft Institut für," https://slideplayer.com/slide/10998174/, accessed: 2019-05-30.

[9] "AP C - UNIT 9 Magnetic Fields and Forces," https://slideplayer.com/slide/273794/, accessed: 2019-05-30.

[10] A. A. m. i. t. J. b. Presented by GuoshengXu and transport teams, "Blob/hole formation and zonalflow generationin the jet edge plasma presentation, tfe meeting," 2009.

[11] R. Maqueda, D. Stotler, S. Zweben, and N. The, "Intermittency in the scrape-off layer of the national spherical torus experiment during h-mode confinement," *Journal of nuclear materials*, vol. 415, no. 1, pp. S459–S462, 2011.

[12] J. A. Boedo, D. Rudakov, R. Moyer, S. Krasheninnikov, D. Whyte, G. McKee, G. Tynan, M. Schaffer, P. Stangeby, P. West *et al.*, "Transport by intermittent convection in the boundary of the diii-d tokamak," *Physics of Plasmas*, vol. 8, no. 11, pp. 4826–4833, 2001.

[13] J. A. Boedo, D. L. Rudakov, R. A. Moyer, G. R. McKee, R. J. Colchin, M. J. Schaffer, P. Stangeby, W. West, S. L. Allen, T. E. Evans *et al.*, "Transport by intermittency in the boundary of the diii-d tokamak," *Physics of Plasmas*, vol. 10, no. 5, pp. 1670–1677, 2003.

[14] D. D'Ippolito, J. Myra, and S. Zweben, "Convective transport by intermittent blob-filaments: Comparison of theory and experiment," *Physics of Plasmas*, vol. 18, no. 6, p. 060501, 2011.

[15] G. Y. Antar, G. Counsell, Y. Yu, B. Labombard, and P. Devynck, "Universality of intermittent convective transport in the scrape-off layer of magnetically confined devices," *Physics of Plasmas*, vol. 10, no. 2, pp. 419–428, 2003.

[16] S. Zweben, J. Boedo, O. Grulke, C. Hidalgo, B. LaBombard, R. Maqueda, P. Scarin, and J. Terry, "Edge turbulence measurements in toroidal fusion devices," *Plasma Physics and Controlled Fusion*, vol. 49, no. 7, p. S1, 2007.

[17] C. Silva, "Plasma diagnostic techniques, lectures, ist," 2017.

[18] "The Shift Project, Breakdown of Electricity Generation by Energy Source," http://www.tsp-data-portal.org/Breakdown-of-Electricity-Generation-by-Energy-Source#tspQvChart, accessed: 2019-05-30.

[19] J. P. Freidberg, *Plasma physics and fusion energy*. Cambridge university press, 2008.

[20] "Iter: A brief history of fusion."

[21] F. F. Chen, *Introduction to plasma physics and controlled fusion*. Springer, 1984, vol. 1.

[22] D. Rudakov, J. Boedo, R. Moyer, S. Krasheninnikov, A. Leonard, M. Mahdavi, G. McKee, G. Porter, P. Stangeby, J. Watkins *et al.*, "Fluctuation-driven transport in the diii-d boundary," *Plasma physics and controlled fusion*, vol. 44, no. 6, p. 717, 2002.

[23] D. Rudakov, J. Boedo, R. Moyer, P. C. Stangeby, J. Watkins, D. Whyte, L. Zeng, N. Brooks, R. Doerner, T. Evans *et al.*, "Far sol transport and main wall plasma interaction in diii-d," *Nuclear fusion*, vol. 45, no. 12, p. 1589, 2005.

[24] J. Boedo, D. Rudakov, R. Colchin, R. Moyer, S. Krasheninnikov, D. Whyte, G. McKee, G. Porter, M. Schaffer, P. Stangeby *et al.*, "Intermittent convection in the boundary of diii-d," *Journal of nuclear materials*, vol. 313, pp. 813–819, 2003.

[25] I. Garcia-Cortes, R. Balbin, A. Loarte, J. Bleuel, A. Chankin, S. Davies, M. Endler, S. Erents, C. Hidalgo, G. Matthews *et al.*, "Turbulent transport studies in the jet edge plasmas in limiter configuration," *Plasma physics and controlled fusion*, vol. 42, no. 4, p. 389, 2000.

[26] J. A. Boedo, D. L. Rudakov, R. A. Moyer, G. R. McKee, R. J. Colchin, M. J. Schaffer, P. Stangeby, W. West, S. L. Allen, T. E. Evans *et al.*, "Transport by intermittency in the boundary of the diii-d tokamak," *Physics of Plasmas*, vol. 10, no. 5, pp. 1670–1677, 2003.

[27] D. D'Ippolito, J. Myra, and S. Zweben, "Convective transport by intermittent blob-filaments: Comparison of theory and experiment," *Physics of Plasmas*, vol. 18, no. 6, p. 060501, 2011.

[28] S. Krasheninnikov, D. D'ippolito, and J. Myra, "Recent theoretical progress in understanding coherent structures in edge and sol turbulence," *Journal of Plasma Physics*, vol. 74, no. 5, pp. 679–717, 2008.

[29] D. Russell, J. Myra, and D. D'Ippolito, "Collisionality and magnetic geometry effects on tokamak edge turbulent transport. ii. many-blob turbulence in the two-region model," *Physics of Plasmas*, vol. 14, no. 10, p. 102307, 2007.

[30] T. Carter, "Intermittent turbulence and turbulent structures in a linear magnetized plasma," *Physics of plasmas*, vol. 13, no. 1, p. 010701, 2006.

[31] O. Grulke, J. Terry, B. LaBombard, and S. Zweben, "Radially propagating fluctuation structures in the scrape-off layer of alcator c-mod," *Physics of Plasmas*, vol. 13, no. 1, p. 012306, 2006.

[32] A. Melnikov, L. Eliseev, T. Estrada, E. Ascasibar, A. Alonso, A. Chmyga, C. Hidalgo, A. Komarov, A. Kozachek, L. Krupnik *et al.*, "Changes in plasma potential and turbulent

particle flux in the core plasma measured by heavy ion beam probe during l–h transitions in the tj-ii stellarator," *Nuclear Fusion*, vol. 53, no. 9, p. 092002, 2013.

[33] A. Melnikov, L. Krupnik, L. Eliseev, J. Barcala, A. Bravo, A. Chmyga, G. Deshko, M. Drabinskij, C. Hidalgo, P. Khabanov *et al.*, "Heavy ion beam probing—diagnostics to study potential and turbulence in toroidal plasmas," *Nuclear Fusion*, vol. 57, no. 7, p. 072004, 2017.

[34] J. Boedo, D. Gray, L. Chousal, R. Conn, B. Hiller, and K. Finken, "Fast scanning probe for tokamak plasmas," *Review of scientific instruments*, vol. 69, no. 7, pp. 2663–2670, 1998.

[35] B. LaBombard, M. Umansky, R. Boivin, J. Goetz, J. Hughes, B. Lipschultz, D. Mossessian, C. Pitcher, J. Terry *et al.*, "Cross-field plasma transport and main-chamber recycling in diverted plasmas on alcator c-mod," *Nuclear Fusion*, vol. 40, no. 12, p. 2041, 2000.

[36] W. West, N. Brooks, G. Jackson, A. Leonard, M. Mahdavi, T. Osborne, T. Petrie, M. Schaffer, R. Stambaugh, M. Wade *et al.*, "Impurity enrichment and radiative enhancement using induced sol flow in diii-d," *Journal of nuclear materials*, vol. 266, pp. 44–50, 1999.

[37] A. Filippas, "Av filippas, rd bengtson, gx li, ma meier, cp ritz, and ej powers, phys. plasmas 2, 839 (1995)." *Phys. Plasmas*, vol. 2, p. 839, 1995.

[38] C. Varandas, J. Cabral, J. Mendonça, M. Alonso, P. Amorim, B. Carvalho, C. Correia, L. Cupido, M. Carvalho, J. Dias *et al.*, "Engineering aspects of the tokamak isttok," *Fusion Technology*, vol. 29, no. 1, pp. 105–115, 1996.

[39] "Isttok tokamak, cfn, ist."

[40] "Isttok: Real-time control of ac discharges."

[41] M. Endler, "Turbulent sol transport in stellarators and tokamaks," *Journal of nuclear materials*, vol. 266, pp. 84–90, 1999.

[42] H. H. Madden, "Comments on the savitzky-golay convolution method for least-squares-fit smoothing and differentiation of digital data," *Analytical chemistry*, vol. 50, no. 9, pp. 1383–1386, 1978.

[43] P. A. Gorry, "General least-squares smoothing and differentiation by the convolution (savitzky-golay) method," *Analytical Chemistry*, vol. 62, no. 6, pp. 570–573, 1990.